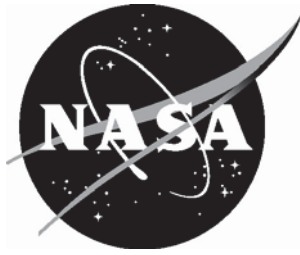


NASA/TP-2014-218554



# Open Circuit Resonant (SansEC) Sensor Technology for Lightning Mitigation and Damage Detection and Diagnosis for Composite Aircraft Applications

*George N. Szatkowski, Kenneth L. Dudley, and Laura J. Smith  
Langley Research Center, Hampton, Virginia*

*Chuantong Wang and Larry A. Ticatch  
National Institute of Aerospace, Hampton, Virginia*

---

November 2014

## NASA STI Program . . . in Profile

Since its founding, NASA has been dedicated to the advancement of aeronautics and space science. The NASA scientific and technical information (STI) program plays a key part in helping NASA maintain this important role.

The NASA STI program operates under the auspices of the Agency Chief Information Officer. It collects, organizes, provides for archiving, and disseminates NASA's STI. The NASA STI program provides access to the NTRS Registered and its public interface, the NASA Technical Reports Server, thus providing one of the largest collections of aeronautical and space science STI in the world. Results are published in both non-NASA channels and by NASA in the NASA STI Report Series, which includes the following report types:

- **TECHNICAL PUBLICATION.** Reports of completed research or a major significant phase of research that present the results of NASA Programs and include extensive data or theoretical analysis. Includes compilations of significant scientific and technical data and information deemed to be of continuing reference value. NASA counter-part of peer-reviewed formal professional papers but has less stringent limitations on manuscript length and extent of graphic presentations.
- **TECHNICAL MEMORANDUM.** Scientific and technical findings that are preliminary or of specialized interest, e.g., quick release reports, working papers, and bibliographies that contain minimal annotation. Does not contain extensive analysis.
- **CONTRACTOR REPORT.** Scientific and technical findings by NASA-sponsored contractors and grantees.

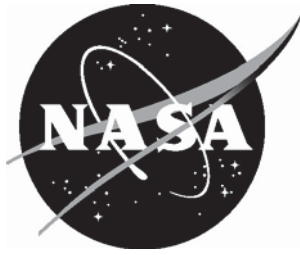
- **CONFERENCE PUBLICATION.** Collected papers from scientific and technical conferences, symposia, seminars, or other meetings sponsored or co-sponsored by NASA.
- **SPECIAL PUBLICATION.** Scientific, technical, or historical information from NASA programs, projects, and missions, often concerned with subjects having substantial public interest.
- **TECHNICAL TRANSLATION.** English-language translations of foreign scientific and technical material pertinent to NASA's mission.

Specialized services also include organizing and publishing research results, distributing specialized research announcements and feeds, providing information desk and personal search support, and enabling data exchange services.

For more information about the NASA STI program, see the following:

- Access the NASA STI program home page at <http://www.sti.nasa.gov>
- E-mail your question to [help@sti.nasa.gov](mailto:help@sti.nasa.gov)
- Phone the NASA STI Information Desk at 757-864-9658
- Write to:  
NASA STI Information Desk  
Mail Stop 148  
NASA Langley Research Center  
Hampton, VA 23681-2199

NASA/TP-2014-218554



# Open Circuit Resonant (SansEC) Sensor Technology for Lightning Mitigation and Damage Detection and Diagnosis for Composite Aircraft Applications

*George N. Szatkowski, Kenneth L. Dudley, and Laura J. Smith  
Langley Research Center, Hampton, Virginia*

*Chuantong Wang and Larry A. Ticatch  
National Institute of Aerospace, Hampton, Virginia*

National Aeronautics and  
Space Administration

Langley Research Center  
Hampton, Virginia 23681-2199

November 2014

## **Acknowledgments**

Document edited by Robert T. Neece, Rheal P. Turcotte and Stan Dehaven.

Available from:

NASA STI Program / Mail Stop 148  
NASA Langley Research Center  
Hampton, VA 23681-2199  
Fax: 757-864-6500

## TABLE OF CONTENTS

1.0	ABSTRACT.....	4
2.0	INTRODUCTION.....	4
3.0	ACRONYMS AND SYMBOLS.....	7
4.0	SANSEC SENSOR BASIS.....	11
	4.1 Theory of Operation.....	11
	4.2 Design Factors.....	13
	4.3 Inductance Value.....	13
	4.4 Capacitance Value.....	14
	4.5 Resisitance Value.....	14
	4.6 Design Geomtry.....	14
5.0	MATHEMATICAL MODEL for SANSEC STRUCTURE and SUBSTRATE.....	15
6.0	INVESTIGATION of DAMAGE DETECTION CAPABILITY.....	27
	6.1 Damage Detection Simulations on Fiberglass Reinforced Composite Substrates.....	28
	6.2 Skin Depth Analysis.....	30
	6.3 SansEC Operation on Carbon Composite Materials.....	32
	6.4 Damage Detection Simulations on Carbon Fiber Reinforced Composite Substrates.....	34
	6.5 Damage to the SansEC Sensor.....	38
7.0	SANSEC EXPERIMENTAL RESULTS.....	39
	7.1 Magnetic Field Response Recorder.....	40
	7.2 Experimental and CEM Parametric Study on Square SansEC Configurations.....	42
	7.3 SansEC Experiments on Carbon Composite Materials.....	47
	7.4 Damage Detection Experiments on Carbon Fiber Reinforced Composite Substrates.....	48
8.0	SANSEC SENSOR LORENTZ FORCE EFFECTS ON LIGHTNING ATTACHMENT.....	50
	8.1 SansEC Sensor’s Influence on the Electrical Breakdown of Air.....	52
9.0	LIGHTNING MITIGATION.....	52
	9.1 Universal Common Practice Guide to Conduct Lightning Energy Transfer Characterizations.....	53
	9.2 Lightning Test Results on FRC Test Panels.....	57
	9.3 Lightning Attachment and Propagation on SansEC Sensor FRC Test Panels.....	60
	9.4 Lightning Strike Test Results on Carbon Fiber Composite Substrates.....	68
	9.5 Lightning Attachment on SansEC Sensor CFRP Test Panels.....	73
10.0	CFRP DAMAGE ASSESSMENT COMPARISONS.....	76
11.0	CFRP SHIELDING EFFECTIVENESS COMPARISONS.....	77
12.0	RELAVENCE TO NASA AVIATION SAFTEY PROGRAM.....	79
13.0	FUTURE RESEARCH.....	81
14.0	CONCLUSIONS.....	82
15.0	APPENDIX A.....	84
16.0	REFERENCES.....	173

**This page intentional left blank.**

## 1.0 ABSTRACT

Traditional methods to protect composite aircraft from lightning strike damage rely on a conductive layer embedded on or within the surface of the aircraft composite skin. This method is effective at preventing major direct effect damage and minimizes indirect effects to aircraft systems from lightning strike attachment, but provides no additional benefit for the added parasitic weight from the conductive layer. When a known lightning strike occurs, the points of attachment and detachment on the aircraft surface are visually inspected and checked for damage by maintenance personnel to ensure continued safe flight operations. A new multi-functional lightning strike protection (LSP) method has been developed to provide aircraft lightning strike protection, damage detection and diagnosis for composite aircraft surfaces.

The method incorporates a SansEC sensor array on the aircraft exterior surfaces forming a “Smart skin” surface for aircraft lightning zones certified to withstand strikes up to 100kA peak current. SansEC sensors are open-circuit devices comprised of conductive trace spiral patterns sans (without) electrical connections. The SansEC sensor is an electromagnetic resonator having specific resonant parameters (frequency, amplitude, bandwidth & phase) which when electromagnetically coupled with a composite substrate will indicate the electrical impedance of the composite through a change in its resonant response. Any measureable shift in the resonant characteristics can be an indication of damage to the composite caused by a lightning strike or from other means. The SansEC sensor method is intended to diagnose damage for both in-situ health monitoring or ground inspections.

In this paper, the theoretical mathematical framework is established for the use of open circuit sensors to perform damage detection and diagnosis on carbon fiber composites. Both computational and experimental analyses were conducted to validate this new method and system for aircraft composite damage detection and diagnosis. Experimental test results on seeded fault damage coupons and computational modeling simulation results are presented. This paper also presents the shielding effectiveness along with the lightning direct effect test results from several different SansEC LSP and baseline protected and unprotected carbon fiber reinforced polymer (CFRP) test panels struck at 40 and 100 kA following a universal common practice test procedure to enable damage comparisons between SansEC LSP configurations and common practice copper mesh LSP approaches. The SansEC test panels were mounted in a LSP test bed during the lightning test. Electrical, mechanical and thermal parameters were measured during lightning attachment and are presented with post test nondestructive inspection comparisons. The paper provides correlational results between the SansEC sensors computed electric field distribution and the location of the lightning attachment on the sensor trace and visual observations showing the SansEC sensor’s affinity for dispersing the lightning attachment.

## 2.0 INTRODUCTION

NASA Langley Research Center has developed a new multifunctional technology for aircraft lightning strike protection, damage detection and damage diagnosis for aerospace composite structures. The concept is to apply a SansEC sensor array, as shown in Figure 2.1, to an aircraft surface forming a “Smart Skin” layer as the external composite protective covering. The SansEC Sensor array includes a number of individual SansEC sensors each of which is an open-circuit resonant conductive spiral pattern sans (without) electrical connections. For applications on exterior aircraft surfaces, the sensor must be designed to perform the required lightning strike protection in addition to damage detection and diagnosis.

With a promising new technology, a new multifunctional sensor concept, a solid theory of operation, and the desire within the Aviation Safety Program (AvSP) coupled with an interest by entities in Integrated Vehicle Health Management (IVHM) to assess the current and future health state of the composites in an aircraft, the High Intensity Radiated Fields (HIRF) laboratory at NASA Langley Research Center was tasked to establish an experimental capability for the investigation and development of applying SansEC sensors to the problem of lightning strike protection, enhanced shielding effectiveness, and damage detection and damage diagnosis of composite aerospace materials. The laboratory is used to develop SansEC test articles and conduct proof of concept experiments. The laboratory is equipped with measurement instrumentation, tools, hardware, material resources, and various means of fabrication. Additional resources such as autoclaves and specialized equipment exist at the Research Center that can sometimes be leveraged for use.

A SansEC sensor is an electric-magnetic resonator having specific resonant characteristics. The length and width of the conductive trace as well as the gap separation between adjacent turns determines the inductance, resistance and capacitance of the LRC circuit and its associated resonant response. When the sensor is placed on a composite substrate, the electric impedance of the substrate is reflected in the sensor's resonant response thus enabling it to detect permittivity and conductivity changes associated with composite damage. Damage in composite material is generally associated with a localized change in material permittivity and/or conductivity. These changes are sensed using SansEC. Unique electrical signatures are used for damage detection and diagnosis. The source cause of the in-service damage (lightning strike, bird strike, impact damage, material fatigue, etc.) to the aircraft composite is not relevant. The sensor will detect damage independent of the cause. The unique electrical signatures (amplitude, frequency, bandwidth, and phase) are used for damage detection and diagnosis. SansEC sensors can be designed in various shapes and sizes depending on the application.

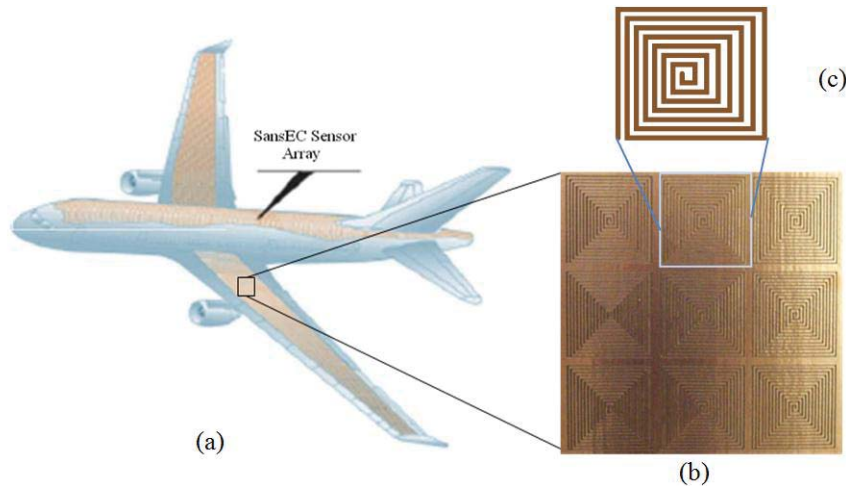


Figure 2.1. Aircraft “Smart Skin” concept using surface tiling array of SansEC Sensors.

An aircraft incorporating a SansEC smart skin technology could be realized from two different approaches. The first approach is for the in-situ measurement where the sensors are interrogated through antennas embedded on the composite or by direct wiring to the sensors themselves with instrumentation on board to quantify the health state of the aircraft. In this method, the sensor response is monitored in real-time during the flight. After a lightning strike occurs, the interrogation system could scan the sensor array and compare the scanning result with the nominal baseline stored in a database or utilize an algorithm capable of determining a damage state without baseline reference to determine the health state of the vehicle. The second approach would allow the interrogation system to be external to the aircraft for ground inspection crews or maintenance personnel to conduct the structural health measurement. The second method is for routine health checks post flight when specific incidents such as a suspected or known lightning strike occur. In this method SansEC sensors are used to assess and detect potential damage and assist the visual inspections.

Traditional methods for lightning protection for composite aircraft rely on a metal mesh or expanded metal foil embedded on or within the composite skin. This provides the required lightning protection and enhanced shielding effectiveness for the composite aircraft, but provides no other benefit for the parasitic weight. The SansEC sensor smart skin technology provides lightning strike protection, shielding effectiveness, and opportunity to achieve in-situ damage detection and diagnostics for aerospace composite structures along with other potential beneficial functions not available from the standard LSP method. Table 2.1 summarizes the functions a SansEC sensor array could provide versus the functions performed by the traditional metal mesh LSP. Additional examples include measuring aerodynamic loads or wind gusts, detecting moisture egress or hail damage in the composite and detecting ice buildup on the structure, all of which are normal atmospheric hazards to aviation safety. The SansEC sensor could also be developed for internal aircraft uses such as wireless fuel quantity measurements to eliminate wires from entering the fuel cells thus vastly reducing the complexity of failure conditions to further improve flight safety from lightning hazards. SansEC sensor smart skin technology provides a revolutionary new approach to mitigate lightning strike attachment and propagation on composite aircraft and offers a new paradigm for future LSP system designs.

This will enable future aircraft LSP designers to reexamine the approach used today of covering the structure to make it resemble an Aluminum aircraft and provide greater flexibility in future LSP designs.

The advantages of composite materials to the design, construction, and operation of modern aircraft have led to a transformation in the aerospace industry. The benefits of composites are found in weight reduction, superior strength, durability, and corrosion-free reliability over traditional metals. These benefits promise to lead to reduced maintenance costs and lower necessity for in-service inspections. To fully leverage the advantages of composites in new aerospace vehicles and applications requires continuous investigation of novel technologies beyond the current state-of-the-art.<sup>[1]</sup>

Table 2.1. Functionality Comparison of SansEC Sensor Array with Traditional Metal Mesh.

Functions	SansEC Sensor	Metal Mesh	Comments
Lightning Protection	Yes	Yes	Zone 2B Lightning Mitigation
Shielding Effectiveness	Yes	Yes	Approximately 10 dB at 10 GHz
In-situ Damage Detection	Yes	No	Delaminations and Rips
Aerodynamic Load Measurements	Yes	No	Potential Function
Fuel Quantity Indication	Yes	No	Potential Function
Ice Detection	Yes	No	Potential Function

The increased use of composites in aircraft structures also means an increased potential for damage and/or failure of those composites. It can be difficult to predict the degree of composite damage or incipient faults while an aircraft is in use. This can be especially significant when the aircraft encounters a lightning environment. Statistics on lightning strikes indicate that in a typical year of operation, a transport aircraft is likely to receive one or two lightning strikes. Depending on geographical regions, flight altitudes, routes, and traffic patterns, the frequency of strike occurrences can be higher than the average. Lightning strikes are a safety hazard to aircraft and can be especially so for those with a considerable amount of composite material structure.<sup>[2]</sup> When a lightning strike occurs on an aircraft, the points of attachment and detachment on the aircraft surface must be found by visual inspection, and then assessed for damage by maintenance personnel to ensure continued safe flight operations. A means of in-situ health monitoring of aircraft composite materials for damage detection in real time would be highly desirable for enhancing aircraft safety.<sup>[3-6]</sup>

The capability to assess the current or future state of the health of an aircraft to improve safety, availability, and reliability while reducing maintenance costs has been a continuous goal for decades. Many companies, commercial entities, and academic institutions have become interested in Integrated Vehicle Health Management (IVHM) and a growing effort of research into “smart” vehicle sensing systems has emerged. Methods to detect damage to aircraft materials and structures have historically relied on visual inspection during pre-flight or post-flight operations by flight and ground crews. More quantitative non-destructive investigations with various instruments and sensors have traditionally been performed when the aircraft is out of operational service during major scheduled maintenance. Through the use of reliable sensors coupled with data monitoring, data mining, and data analysis techniques, the health state of a vehicle can be detected in-situ.

To show compliance with FAA certification airworthiness standards, composite substrates are subjected to lightning direct-effect electrical waveforms to determine performance characteristics of the lightning strike protection conductive layers used to protect composite substrates. Test results collected from independent LSP studies are often incomparable due to variability in test procedures & applied practices at different organizations, which impairs performance correlations between different LSP data sets. Under a NASA supported contract, The Boeing Company developed technical procedures and documentation as guidance in order to facilitate a test method for conducting universal common practice lightning strike protection test procedures. The procedures foster conformity in future lightning strike protection evaluations to allow meaningful performance correlations across data sets.

This universal common practice guidance provides the manufacturing specifications to fabricate carbon fiber reinforced plastic (CFRP) test panels, including finish, grounding configuration, and acceptable methods for pre-test nondestructive inspection (NDI) and post-test destructive inspection. The test operations guidance elaborates on the provisions contained in SAE ARP5416<sup>[7]</sup> to address inconsistencies in the generation of damage protection

performance data, so as to provide for maximum achievable correlation across capable lab facilities. In addition, the guidance details a direct effects test bed design to aid in quantification of the multi-physical phenomena surrounding a lightning direct attachment supporting validation data requirements for the development of predictive computational modeling. The lightning test bed is designed to accommodate a repeatable installation procedure to secure the test panel and eliminate test installation uncertainty. It also facilitates a means to capture the electrical waveform parameters in 2 dimensions, along with the mechanical displacement and thermal heating parameters which occur during lightning attachment. Descriptions of the common practice CFRP test articles, LSP test bed fixture, and monitoring techniques to capture the electrical, mechanical and thermal parameters during lightning attachment are presented here.

Lightning-direct effect current tests were conducted on SansEC LSP FRC and CFRP test panels following the Universal Common Practice test procedures to evaluate and compare their ability to withstand the incident lightning energy and protect the underlying composite. The test results indicated several SansEC sensor geometric configurations demonstrated an intrinsic ability to attach the lightning current along specific sensor traces and propagate the current in a directed fashion. To investigate this phenomenology, electromagnetic computational simulations were conducted to calculate the electric field distribution on the SansEC sensor's conductive trace to determine if the associated electromagnetic radiation preceding lightning attachment establishes modal structures on the conductive trace which predisposition the attachment and direction of the current flow. The simulations provide a means to visualize the trace's modal structure and identify high electric field regions residing on the sensor. This paper presents a correlation between the SansEC sensor's computed high electric field distributions with the heat signature images from infrared (IR) thermography which is indicative of the lightning attachment and propagation for several SansEC sensor configurations. Visual observations from high speed video and time lapse photography showing the SansEC sensors affinity at dispersing the lightning attachment are also discussed and presented in this paper.

Keywords: Lightning Mitigation, Lightning Strike Protection, Damage Detection, Composites, Integrated Vehicle Health Monitoring (IVHM), Aviation Safety, SansEC Sensors, Computational Electromagnetic Modeling

### 3.0 ACRONYMS AND SYMBOLS

AC	alternating current
AEST	Atmospheric Environment Safety Technologies
ARP	<i>Aerospace Recommended Practice</i>
AvSP	Aviation Safety Program
BW	Bandwidth
CAD	Computer Aided Design
CEM	Computational Electromagnetic
CFRP	Carbon Fiber Reinforced Polymers/Plastics
CRES	Corrosion resistant Steel
CW	continuous wave
DC	Direct Current
DN	Drawing Note
DUT	Device Under Test
ECF	Expanded Copper Foil
EDM	electron discharge machining
EM	Electro Magnetic
EMF	electromotive force
ESB	Electromagnetics & Sensors Branch
FAA	Federal Aviation Administration
FEKO	Feldberechnung für Körper mit beliebiger Oberfläche (Field Calculations for Bodies with Arbitrary Surface)
FLIR	Forward Looking Infra Red
FRC	Fiberglass Reinforced Composites
FRP	Fiberglass Reinforced Polymers
HIRF	High Intensity Radiated Fields

IR	Infra Red
IVHM	Integrated Vehicle Health Management
KCL	Kirchhoff's Current Law
KVL	Kirchhoff's Voltage Law
KNK	Klik-N-Kut
LaRC	Langley Research Center
LRC	inductive-capacitive-resistive
LSP	Lightning Strike Protection
LTI	Lightning Technologies, Inc.
MoM	method of moments
NASA	National Aeronautics and Space Administration
NCAMP	National Center for Advanced Materials Performance
NDE	Nondestructive evaluation
NDI	Nondestructive inspection
NDT	Non Destructive Test
NIAR	National Institute for Aviation Research
NMS	NCAMP Material Specification
NPS	NCAMP Process Specification
NTS	National Technical Systems
OML	Outer Mold Line (smooth Tool Side of Lay-up, this side is painted, and is also the side to be directly exposed to simulated lightning currents)
PEC	perfect electrical conductor
PNA	Performance Network Analyzer
RF	Radio Frequency
SansEC	Without (Sans) Electrical Connection (EC)
SAE	Society of Automotive Engineers
SRF	self resonance frequency
SHM	structural health monitoring
SURF	Surfacer
TTU	through transmission ultrasonic
UV	Ultra Violet

## SYMBOLS

A	ampere, complex scalar, area
a	Wire radius
B	Magnetic Flux Density, Magnetic Field
$B_{Air}$	Magnetic Flux Density in air
C	Capacitance
$C_S$	total effective capacitance of the SansEC sensor
$C_{S0}$	Capacitance value in air
E	Electric Field
$E_{r1}$	reflected energy
$E_{i1}$	injected energy on port 1
e	complex exponential
F, f	frequency
F	Lorentz force, force
G	trace gap
H	Magnetic Field, substrate thickness
I	Current
$I_0$	maximum current amplitude
$I_1$	current in the antenna circuit
$I_2$	sensor current
$I_3$	current in material
$I_{enc}$	Current enclosed by loop

$i, j$	imaginary unit
$J(r)$	current density
$J$	current distribution function
$L$	Inductance
$L_A$	inductance of the loop antenna
$L_M$	material inductance
$L_S$	total effective inductance of the SansEC sensor
$l$	trace length
$M$	mutual inductance
$M_1$	mutual inductance between the sensor and the antenna
$M_2$	second mutual inductance
$N$	Number of turns
$Q$	Quality Factor, particle electric charge
$q$	charge density
$q_0$	maximum charge density
$R$	Resistance, Radius
$R_A$	Intrinsic resistance
$R_M$	material resistance
$R_S$	Intrinsic resistance of the sensor trace
$r, r'$	distance vector
$S, S_{11}$	refection coefficient
$s$	complex parameter
$t$	time
$\text{Tan}\delta$	Dielectric Loss Tangent
$V$	voltage
$V_0$	voltage source
$v$	velocity
$W$	length of side, trace width
$X$	distance
$Z$	complex impedance
$Z_A$	antenna impedance
$Z_L$	total load impedance
$Z_M$	material impedance
$Z_S$	SansEC sensor impedance;
$\mathcal{E}$	Electromotive force (EMF), permittivity
$\epsilon_0, \epsilon_0$	Free Space Permittivity
$\epsilon_r$	Relative Permittivity
$\mu_{\text{eff}}$	effective permeability
$\mu_0$	Permeability of free space ( $4\pi \times 10^{-7}$ )
$\mu_r$	Relative permeability
$\delta$	skin depth
$\sigma$	conductivity
$\Phi_B, \Phi_m$	magnetic flux
$\rho$	charge distribution function, resistance, charge density
$\rho(r)$	charge density
$\omega$	angular frequency
$\Sigma$	open surface
$\pi$	Pi

#### UNITS

msec	millisecond
$\mu\text{sec}$	microsecond
kA	kilo amps

kHz	kilohertz
MHz	megahertz
GHz	gigahertz
dB V/m	Electric Field in Decibels
dB A/m	Magnetic Field in Decibels

## 4.0 SANSEC SENSOR BASIS

### 4.1 Theory of Operation

The SansEC Sensor is an open circuit resonant sensor technology framework originally developed by Dr. Stanley Woodard and his research team at NASA Langley Research Center. The SansEC sensor is a planar resonant spiral or helix structure configured as an open circuit sensor without (Sans) electrical connection (EC) to any recording instrumentation. It is composed of conductive material and formed in a manner such that the natural response of the geometry is to self-resonate when impinged upon by an external electro-magnetic field. Through additional focused research this sensor concept has been developed for the specific purpose of in-situ detection and diagnostics of damage in non-conductive and conductive aerospace composite materials. Our development team in the SansEC Laboratory at NASA LaRC has leveraged the technology for this specific application to aircraft lightning protection and intelligent vehicle health monitoring.

The sensor baseline design is a single physical component of geometric design constructed of conductive material. There is no single point on the sensor that if damaged destroys the functionality of the circuit. The resonant sensor is essentially an electrical inductor in the form of a planar spiral. Figure 4.1 illustrates a square spiral resonant sensor. The sensor does not utilize a distinct built in discrete capacitor or resistor, but rather the inherent capacitance and resistance of the geometric design. The inductance (L) is the sum of all the self and mutual inductances of the individual trace interactions. In the simplest model the capacitance (C) is an inherent result of the gap between the spiral traces and substrate dielectric. The resistance (R) is the ohmic loss along the length of the conductive trace material and loss in the dielectric substrate.

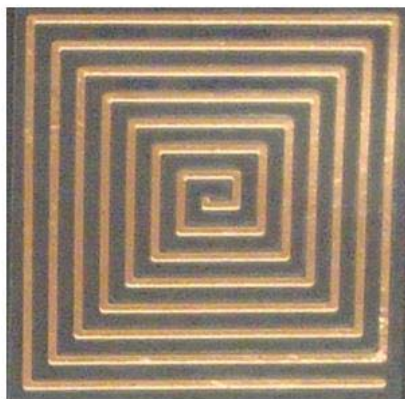


Figure. 4.1. A generic open-circuit SansEC Sensor.

Figure 4.2 is the schematic representation. If the sensor itself is damaged, such as torn or punctured, it still functions but with a different frequency response. Depending on the failure and its location, a single sensor or multiple coupled sensors will now exist and still maintain function.<sup>[8]</sup> This robustness of functionality makes these types of sensors highly effective in detecting and diagnosing damage.

Placing the sensor upon a non-conductive substrate material, such as a composite panel, alters the sensor's resonance characteristics of frequency, amplitude, and bandwidth. The substrate material on which the sensor is placed or attached acts as a dielectric. Any changes of this modified baseline characteristic can be used to detect changes physically to the sensor or the substrate upon which it is placed or embedded. Comparisons of these changes from the baseline frequency, amplitude, or bandwidth response produce unique signatures that can be correlated to the detection of damage.

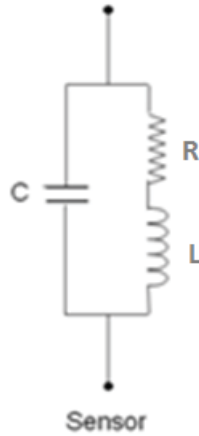


Figure 4.2. Schematic representation of sensor.

The baseline frequency corresponds to the resonant frequency of the sensor. The resonant frequency is determined by the interaction of the overall inductance and capacitance of the sensor. As seen by equation 4.1, the equation for resonant frequency of a LC circuit, resonance is inversely proportional to the square root of either L or C.<sup>[9]</sup>

$$f = \frac{1}{2\pi\sqrt{LC}} \quad \text{Eq. 4.1}$$

Where  $f$  is the frequency in hertz, C is capacitance in farads, and L is inductance in henrys. The resonant frequency increases as the inductance decreases. The same effect is true if capacitance varies with inductance remaining constant.

The resistance of the resonant sensor has the greatest effect on the selectivity or quality factor (Q) of the sensor which in turn affects the bandwidth. The simple definition of Q is the amount of energy stored over the energy loss in one cycle. In terms of inductors, Q becomes the ratio of peak magnetic energy to peak electric energy. The inductance is also a factor in determining the Q, but resistance exerts a greater influence with inductance playing a greater role on the center frequency. The higher the quality factor the sharper the response curve at the resonant frequency. This sharper response curve in turn results in a smaller bandwidth (BW). The Q of a circuit can be determined by calculation or using measured data. When using measured data, the Q can be found using equation 4.2.<sup>[10]</sup>

$$Q = \frac{f}{\Delta f} \quad \text{Eq. 4.2}$$

Where  $Q$  is the quality factor,  $f$  is the resonant frequency, and  $\Delta f$  is the difference in frequency at the 3dB power points. The theoretical calculation of the quality factor takes into account the resistance of the circuit and is determined using equation 4.3.<sup>[4]</sup>

$$Q = \frac{2\pi fL}{R} \quad \text{Eq. 4.3}$$

Where  $Q$  is the quality factor,  $f$  is the resonant frequency in hertz,  $L$  is the inductance in henrys, and  $R$  is the resistance in ohms. The effect the Q factor has on the sharpness of the resonant frequency and the bandwidth can be seen in figure 4.3. A higher Q factor results in a narrower bandwidth with the opposite true for a low quality factor.

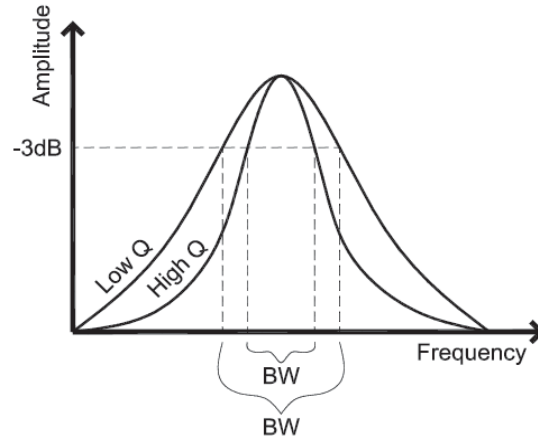


Figure 4.3. Relationship of Q value to BW.

The conductivity of the substrate also has an effect on the Q value. A semi-conductive substrate will tend to couple more energy to the substrate material as the frequency increases. This coupling to the substrate causes losses in the inductor.<sup>[11]</sup> The frequency where this begins to occur is dependent on the size of the spiral inductor.

## 4.2 Design Factors

The theoretical design of resonant sensors is an involved process. In addition to the sensor's characteristics, the substrate's physical properties must be known to include not only the physical layout, but also permittivity and permeability. The key parameters must be known to accurately make calculations and modeling. The full electrical characterization over the operational frequency bandwidth of both the sensor and the substrate on which it is to be placed or embedded must be well defined. The key sensor parameters are inductance, capacitance, and resistance. This is also the case for the substrate material or materials. The sensor inductance is a factor of the conductive spiral geometry including the number of turns, the overall trace dimensions (length and width), and the magnetic permeability of the conductive trace material. The substrate inductance is primarily related to its relative magnetic permeability. The sensor capacitance is primarily produced by the space between the traces and the relative permittivity of the material between the traces. The relative permittivity of the substrate material will also influence the capacitance seen by the sensor.

In this paper we focus on using the SansEC sensor for aircraft lightning strike protection and damage detection after a lightning strike. We concentrate on exploring the effects of design factor variables that most impact the ability of the sensor to provide good lightning strike protection. However, in understanding the design factors beyond the lightning protection application, SansEC sensors might also be applied to provide other potential functions to an aircraft. Examples include the measuring of aero dynamic loads, wind gust, and fuel quantity indication. By detecting variations in the permittivity due to water, moisture detection and hail damage detection would also be possible. The conductivity of the sensors would add to the electromagnetic shielding effectiveness as well. Knowing the physical characteristics of the sensor and the properties of the surrounding substrate leads to a broader design space, sensor functionality, and new aerospace applications.

## 4.3 Inductance Value

The open circuit resonant sensor, as stated earlier, is a planar spiral and essentially an inductor. As with any inductor, the inductance value is composed of self and mutual inductance. The self-inductance is a measure of the magnetic field generated by a time-varying current. Mutual inductance is the measure of mutually coupled magnetic fields of adjacent traces with current flowing in the same direction. There are various empirical formulas that exist for calculating the inductance of a planar spiral.<sup>[12-17]</sup> The Missouri Electromagnetic Compatibility Laboratory presented several simplified equations for various geometries. Equations 4.4 and 4.5 are for a circular spiral and a square spiral, respectively.<sup>[18]</sup>

$$L_{circle} \approx N^2 R \mu_0 \mu_r \left[ \ln \left( \frac{8R}{a} \right) - 2.0 \right] \quad \text{Eq. 4.4}$$

$$L_{square} \approx N^2 \frac{2\mu_0 \mu_r w}{\pi} \left[ \ln \left( \frac{w}{a} \right) - 0.774 \right] \quad \text{Eq. 4.5}$$

Where N is the number of turns, R is the outer radius in centimeters, a is the wire radius in centimeters,  $\mu_0$  is the permeability of free space,  $\mu_r$  is the relative permeability of the medium conductor, and w is the length of one side in centimeters. These are approximations and have a tolerance of 20% range as determined by comparison of calculated and measured data. These calculations are based upon the spiral in free space.

#### 4.4 Capacitance Value

The capacitance is an inherent result of the width between the spiral traces and the interaction with the substrate which acts as a dielectric. The capacitance is considered to be parasitic and is minimal in a basic geometric spiral in free space or with a non-conductive substrate. As with the calculation of the inductance values, several equations exist for the calculation of the capacitance.<sup>[16,18-20]</sup> To accurately calculate the capacitance of the sensor when placed upon a substrate the permittivity of the panel must be known.

The sensors for this project were tested in free space and on fiberglass and Carbon Fiber Reinforced Polymer composite panels. The fiberglass panels used were nonconductive and therefore the capacitance was considered to be minimal and more parasitic in both cases. The capacitance of the sensor was determined mathematically by manipulating the resonant frequency equation, equation 4.1.

#### 4.5 Resistance Value

The total resistance of a planar spiral is a combination of series and parallel resistance. Series resistance is both dependent and independent on the frequency. The independent portion is essentially the direct current (DC) resistance of the wire, or in this case the trace, and is largely dependent on the total length. The frequency dependent portion of the overall resistance is due to the effects of eddy currents. The parallel resistance is a result of the finite resistance between the substrate material and the spiral conductor. Several equations exist to calculate the series and parallel resistance.<sup>[13,16]</sup>

#### 4.6 Design Geomtry

The overall dimensions of the resonant sensor along with its trace width, trace spacing (gap width), and total length establish the inductance, capacitance, and resistance and corresponding operational characteristics. The thickness and conductivity of the composite material under test will also influence the sensor operation and influence the design geometry. Thicker substrates require lower frequency resonances to adequately couple deeper into the substrate while thinner substrates may have adequate coupling at higher frequencies.

Sensors for this project were initially designed to operate on nonconductive structural fiberglass substrates. The sensors were designed in various sizes in the shape of polygonal spirals which included triangular, square, hexagonal, and circular geometries and placed as appliques on top of the substrate. The spiral sensors were measured to characterize their resonant structure for relative performance comparison and evaluated at low level lightning currents to obtain a first look at their lightning strike protection attributes. Figure 4.4 illustrates the four geometric shapes that were initially evaluated. The square sensor geometry was observed to have desirable characteristics in both resonant performance and lightning strike protection and selected for further study.

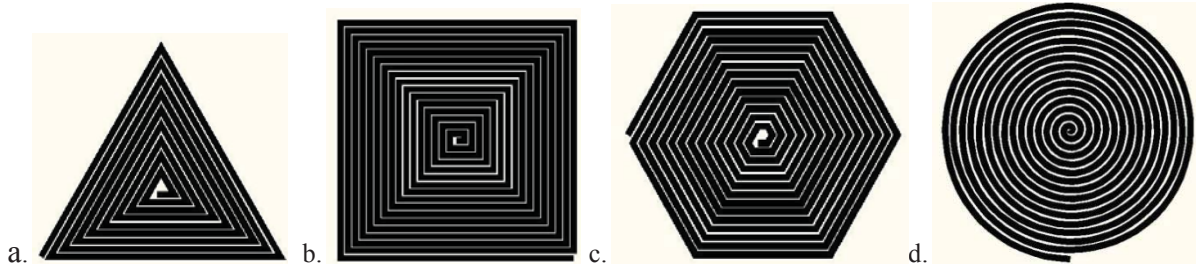


Figure 4.4. Spiral geometries utilized for the resonant sensors: (a) triangular, (b) square, (c) hexagonal, and (d) circular.

## 5.0 MATHEMATICAL MODEL for SANSEC STRUCTURE and SUBSTRATE

There are many kinds of important mathematical formalisms in establishing a rigorous theory of operations. The simplest of these that still maintain a formal consistency are algebraic and first-order theories. All first-order theories may be developed into a framework whereby all possible models of objects in the theory may be explored. The format of a first-order theory is of central interest for specialists in a field of research. In electrical engineering, objects or elements, such as resistance, inductance, capacitance, which are elementary formal labels can be evaluated in connection and relation with other types of objects, elements, or physical phenomena. Collections of objects and their formal relations form structures (i.e. planar resonant spirals that we call SansEC Sensors). These structures of distributed inductances, capacitances, and resistances and their relational interactions with charges, currents, materials, and electromagnetic fields allows for investigations of a fundamental nature. Operations of such structures can be deduced and evaluated based on established axioms and lists of variables which specify object types and their values.<sup>[19]</sup> The principles and axioms of electrical engineering and electromagnetic theory are well established. Ohm's Law, Kirchhoff's Laws, Thévenin's Theorem, Maximum Power Transfer Theorem, Biot-Savart's Law, Ampere's Law, Faraday's Law, Maxwell-Faraday's Law, Maxwell's Equations, and the Lorentz Force Law are all such axioms that taken collectively together completely describe the operation of SansEC sensors. Each axiom is a closed formula expression that facilitates the construction of logically consistent mathematical models and a theory of SansEC sensors that is without contradiction. In this paper we will not derive any of the axioms, but present the relevant Laws and Theorems and how they relate to the SansEC sensor technology framework.

Charge is the fundamental property of matter. Electric charge is the physical property of matter that causes it to experience a force when close to other electrically charged matter. Objects of matter are either negatively charged, neutral and therefore uncharged, or positively charged. Like charges repel and opposite charges attract. Charge is quantized with relative values of -1, 0, +1 or integer multiples thereof. Charge is a relativistic invariant. This means that any particle that has charge  $Q$ , no matter how fast it goes, always has charge  $Q$ . This is known as Charge conservation. The total electric charge of an isolated system remains constant regardless of changes within the system itself. This law is inherent to all processes known to physics. All moving charged particles produce magnetic fields. There are many ways of carrying an electric current, including: a flow of electrons; a flow of electron "holes" that act like positive particles; and both negatively and positively charged particles (ions or other charged particles) flowing in opposite directions in an electrolytic solution or plasma. Moving point charges, such as electrons, produce complicated but well known magnetic fields that depend on the charge, velocity, and acceleration of the particles.<sup>[18]</sup> Magnetic field lines form in concentric circles around a cylindrical current-carrying conductor, such as a length of wire. The direction of such a magnetic field can be determined by using the "right hand rule". The strength of the magnetic field decreases with distance from the wire. The motion of electrons in conductive metals in a specific direction is known as electric current.

$$I = \frac{dQ}{dt} \quad \text{Eq. 5.1}$$

In formulating a theory of SansEC sensors we must start with Ohm's Law. Ohm's law is the most important, basic law of electrical engineering. It defines the relationship between the three fundamental electrical quantities, current,

voltage, and resistance. When a voltage is applied to a circuit containing only resistive elements (i.e. no inductors), current flows according to Ohm's Law, which is given below;

$$I = \frac{V}{R} \quad \text{Eq. 5.2}$$

Where;

$I$  = current (Amperes)

$V$  = voltage (Volts)

$R$  = resistance (Ohms)

Ohm's law states that the electrical current,  $I$  flowing in a circuit is proportional to the voltage,  $V$  and inversely proportional to the resistance,  $R$ . Therefore, if the voltage is increased, the current will increase provided the resistance of the circuit does not change. Similarly, increasing the resistance of the circuit will lower the current flow if the voltage is not changed.<sup>[20]</sup> The formula can be reorganized so that the relationship can easily be seen for all of the three variables.

$$I = \frac{V}{R} \quad \text{or} \quad V = IR \quad \text{or} \quad R = \frac{V}{I} \quad \text{Eq. 5.3}$$

Ohm's Law is valid for both direct current (DC) circuits and alternating current (AC) circuits. In time-invariant AC circuits the flow path consists purely of resistive (real) elements, the voltage and current are always in phase with each other and Ohm's Law is realized exactly as described for DC circuits. In time-variant AC circuits reactive (imaginary) elements such as capacitors and inductors are involved and the voltage and current are no longer in phase with each other. In circuits where the inductive element is dominant the voltage leads the current in time. In circuits where the capacitive element is dominant the current leads the voltage. The variables of the elements are generalized to complex numbers and the relationship between voltage and current becomes the solution to a differential equation in the form of;

$$Ae^{st}$$

where:

$A$  is a complex scalar

$e$  is the complex exponential

$s$  is a complex parameter

$t$  is time

In this form currents and voltages can be expressed with the same  $s$  parameter as the input to the system, allowing the time-varying complex exponential term to be canceled out and the system described algebraically in terms of the complex scalars in the current and voltage waveforms.<sup>[20]</sup>

For the common case of a steady sinusoidal AC waveform, the  $s$  parameter is taken to be  $j\omega$ , corresponding to a complex sinusoid  $Ae^{j\omega t}$ .

The complex generalization of resistance is impedance, and denoted by  $Z$ ;

For an inductor,

$$Z = sL \quad \text{Eq. 5.4}$$

or

$$Z = j\omega L \quad \text{Eq. 5.5}$$

and for a capacitor,

$$Z = \frac{1}{sC} \quad \text{Eq. 5.6}$$

or

$$Z = \frac{1}{j\omega C} \quad \text{Eq. 5.7}$$

We can now write the generalized form of Ohm's Law as;

$$I = \frac{V}{Z} \quad \text{Eq. 5.8}$$

where  $V$  and  $I$  are the complex scalars of voltage and current respectively and  $Z$  is the complex impedance. When  $Z$  is purely real, it is the same as  $R$ , in the simpler form of Ohm's Law. When  $Z$  is complex, only the real part is responsible for dissipating heat, and the imaginary part represents the energy storage term. For the capacitor, energy is stored in the electric field and later returned to the circuit as the voltage dissipates. For the inductor, energy is stored in the magnetic field as the current builds and later returned to the circuit as the current falls. The real parts of such complex current and voltage waveforms describe the actual sinusoidal currents and voltages in a circuit, which can be out of phase due to the different complex scalars. In the general AC circuit,  $Z$  varies strongly with frequency as does the relationship between voltage and current.<sup>[20]</sup>

The principle of conservation of electric charge is defined by Kirchhoff's Current Law (KCL) and implies that: At any node (junction) in an electrical circuit, the sum of currents flowing into that node is equal to the sum of currents flowing out of that node, or: The algebraic sum of currents in a network of conductors meeting at a point is zero.<sup>[20]</sup>

Recalling that current is a signed (positive or negative) quantity reflecting direction towards or away from a node, this principle can be stated as:

$$\sum_{k=1}^n I_k = 0 \quad \text{Eq. 5.9}$$

$n$  is the total number of branches with currents flowing towards or away from the node.

This formula is valid for complex currents:

$$\sum_{k=1}^n \tilde{I}_k = 0 \quad \text{Eq. 5.10}$$

The law is based on the conservation of charge whereby the charge (measured in coulombs) is the product of the current (in amperes) and the time (in seconds).

Kirchhoff's Voltage Law (KVL) states that the sum of all the voltages around a closed loop is equal to zero. A closed loop is a closed conducting path of an electrical circuit that allows the current to flow through. This is the principle of conservation of energy applied to electric potentials. The algebraic sum of the products of the resistances of the conductors and the currents in them in a closed loop is equal to the total electromotive force (EMF) available in that loop.

$$\sum_{k=1}^n V_k = 0 \quad \text{Eq. 5.11}$$

Similarly to KCL, it can be stated as:

Where,  $n$  is the total number of voltages measured. The voltages may also be complex:

$$\sum_{k=1}^n \tilde{V}_k = 0 \quad \text{Eq. 5.12}$$

This law is based on the conservation of energy whereby voltage is defined as the energy per unit charge. The total amount of energy gained per unit charge must equal the amount of energy lost per unit charge, as energy and charge are both conserved.<sup>[20]</sup>

In the low-frequency limit, the voltage drop around any loop is zero. This includes imaginary loops arranged arbitrarily in space – not limited to the loops delineated by the circuit elements and conductors. In the low-frequency limit, this is a corollary of Faraday's law of induction. However, it is important to point out the limitations to

Kirchhoff's laws. KCL and KVL both depend on the lumped element model. This model of electrical objects makes the simplifying assumption that the attributes of the circuit inductance, resistance, and capacitance are concentrated into idealized discrete electrical components connected by perfect electrical conductors. When actual circuit and device cannot be modeled by discrete elemental components KCL and KVL laws cannot be applied directly. Therefore, it is important to consider using the equivalent lumped parameters of the SansEC sensor to model its electrical behavior. One version of a lumped element model of a SansEC sensor circuit is presented in Figure 5.1.

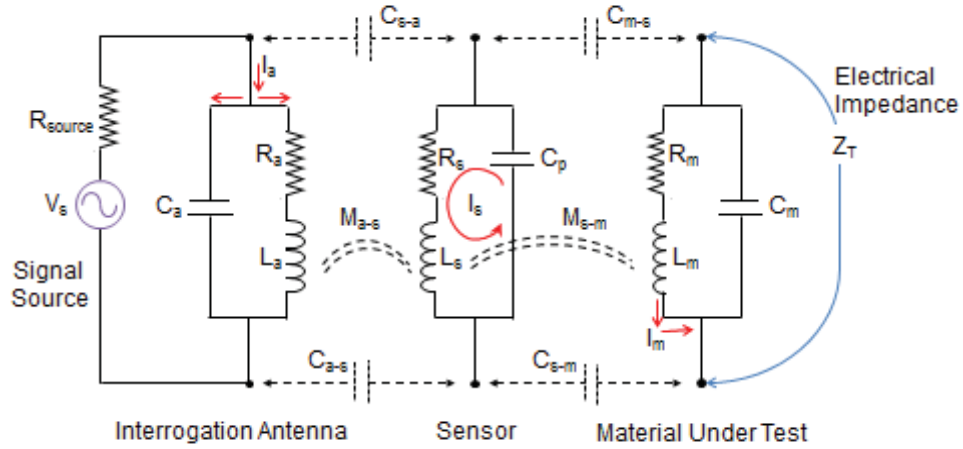


Figure 5.1. One version of a lumped element model for a SansEC Sensor System.

In the low-frequency limit, SansEC sensors are inherently open circuit devices (there are no closed loops to consider) so there is no current flow possible and KCL or KVL currents and voltages become zero. KCL, in its usual form, is dependent on the assumption that current flows only in a conductor and that whenever current flows into one end of a conductor it immediately flows out the other end. In high-frequency AC circuits, where the lumped element model is usually no longer applicable,<sup>[20]</sup> we can make it applicable for KCL solutions by considering "parasitic capacitances" distributed along the conductors.<sup>[21]</sup> This again is very important because the functioning and operation of any SansEC sensor is critically dependent upon the distributed parasitic capacitances in the geometry of the spiral conductor. At high frequencies, parasitic capacitances are established in the gap between the conductive trace of the SansEC spiral. Charge can flow in the boundary gap between the traces through this capacitance region creating a closed loop resonant circuit (LC circuit) with the larger inductive component of the spiral. In other words, at sufficiently high frequencies a seemingly opened circuit SansEC sensor becomes a closed circuit and KCL becomes valid as the total electric charge remains constant in the loop created by the spiral's inherent inductance and parasitic capacitance. This can be simply modelled in a lumped element fashion with a properly applied parasitic capacitance element. The most common approach is to roll up all the distributed capacitance into one lumped element in parallel with the inductance and resistance of the coil. More accuracy could be achieved with the complexity of a distributed element model using many more spatially distributed capacitive elements but this is unnecessary for a first-order representation of SansEC sensor functions and operations.

KVL is based on the assumption that there are no fluctuating magnetic fields linking the closed loop. This is not a safe assumption for high-frequency (short-wavelength) AC circuits.<sup>[22]</sup> In the presence of a changing magnetic field the electric field is not conserved. Therefore the path integral of the electric field around the loop is not zero, directly contradicting KVL. It is possible to improve the applicability of KVL by considering "parasitic inductances" particularly mutual inductances distributed along the conductors.<sup>[22]</sup> These are treated as imaginary circuit elements that produce a voltage drop equal to the rate-of-change of the flux.

A more accurate model requires series resistance elements with the inductance elements. This model is fairly difficult to deal with in simple calculations and for the most part is avoided. The usual practice is to simply measure (or specify) an overall  $Q$  for the inductor without associating a specific equivalent circuit.<sup>[23]</sup>

The Biot–Savart Law is used for computing the resultant magnetic field  $B$ , at position  $r$ , generated by a steady current  $I$ , flowing in a SansEC sensor. Shaping the geometry of a current-carrying conductor into a loop concentrates the magnetic field inside the loop while weakening it outside. Bending a conductor into multiple closely spaced loops to form a coil or spiral enhances this effect. The strength of the field and the polarity are determined by the current flowing through the shaped conductor. The magnetic field generated by the constant flow of electrons in a steady current  $I$  is given by;

$$B = \frac{\mu_0 I}{4\pi} \int_{wire} \frac{d\ell \times \hat{r}}{r^2} \quad \text{Eq. 5.13}$$

where the integral sums over the wire length and  $d\ell$  is the infinitesimal vector line element with direction in the same sense as the current  $I$ ,  $\mu_0$  is the intrinsic magnetic permeability of free-space,  $r$  is the distance between the location of  $d\ell$  and the location at which the magnetic field is being calculated, and  $\hat{r}$  is a unit vector in the direction of  $r$ .<sup>[24]</sup>

The description of the magnetic field may be generalized through Ampere’s Law;

$$\oint B \cdot d\ell = \mu_0 I_{enc} \quad \text{Eq. 5.14}$$

where the line integral is over any arbitrary loop and  $I_{enc}$  is the current enclosed by that loop. Ampère's law is always valid for steady currents and can be used to calculate the magnetic field for certain highly symmetric situations such as an infinite wire or an infinite coil.<sup>[24]</sup>

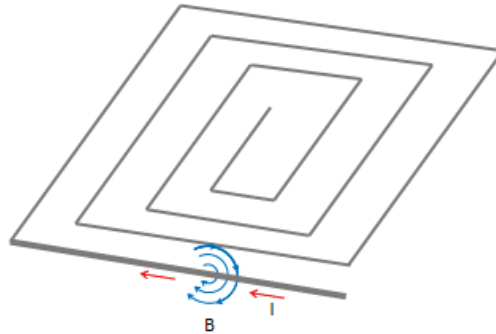


Figure 5.2. A current flowing in a SansEC sensor with the direction of the red arrows produces a magnetic field shown by the blue arcs.

Ampere’s Law relates magnetic fields to the electric currents that produce them. Using Ampere's law, one can determine the magnetic field associated with a given current or the current associated with a given magnetic field, providing there is no time changing electric field present. In a modified form that accounts for time varying electric fields, Ampère's Law can be re-written as one of four Maxwell’s equations that describe electricity and magnetism. We will see the importance of this for SansEC sensors a bit later in this report when we describe Maxwell’s extension to Ampere’s Law.

A changing magnetic field moving through a conducting loop or coil, generates an electric force that tends to drive a current through the loop or a coil. This is known as Faraday's law. Mathematically, Faraday's law is:

$$\mathcal{E} = - \frac{d\Phi_m}{dt} \quad \text{Eq. 5.15}$$

where  $\mathcal{E}$  is the electromotive force (*EMF*) or the voltage generated around a closed loop. The EMF is given by the time rate of change  $dt$ , of the magnetic flux,  $\Phi_m$ . Magnetic flux is the surface integral of the perpendicular

component of the magnetic field  $\mathbf{B}$  passing through that surface.<sup>[25]</sup> The negative sign in equations 5.15 and 5.16 represents the fact that any current generated by a changing magnetic field in a coil produces a magnetic field that *opposes* the change in the magnetic field that induced it. This phenomenon is known as Lenz's Law.<sup>[25-26]</sup>

The integral formulation of Faraday's law follows;

$$\mathcal{E} = \oint_{\partial\Sigma} (\mathbf{E} + \mathbf{v} \times \mathbf{B}) \cdot d\boldsymbol{\ell} = -\frac{d\Phi_B}{dt} \quad \text{Eq. 5.16}$$

Where again  $\mathcal{E}$  is the electromotive force (*EMF*) and  $\Phi_B$  is the magnetic flux through the open surface  $\Sigma$ , and  $\partial\Sigma$  is the boundary of the open surface  $\Sigma$ . The electromotive force is induced along this boundary and we should note that the surface, in general, may be in motion and deforming, and so is generally a function of time. Along the boundary contour  $\partial\Sigma$  of the open surface,  $d\boldsymbol{\ell}$  is the infinitesimal vector element we saw previously in Ampere's Law,  $\mathbf{v}$  is the velocity of the boundary  $\partial\Sigma$  if it is in fact moving.  $\mathbf{E}$  is the electric field and  $\mathbf{B}$  is the magnetic field.<sup>[24-26]</sup>

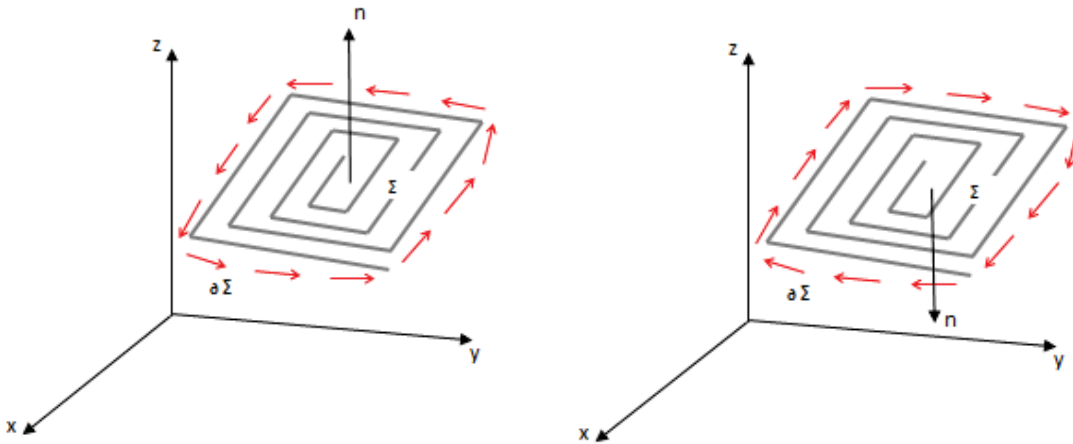


Figure 5.3. Path integral around a SansEC surface  $\Sigma$  and its boundary contour  $\partial\Sigma$  with orientation  $\mathbf{n}$  normal to the surface set by the right-hand rule.

For a tightly wound inductive coil composed of a number,  $N$  identical turns, each with the same  $\Phi_B$ , Faraday's law of induction states that;

$$\mathcal{E} = -N \frac{d\Phi_B}{dt} \quad \text{Eq. 5.17}$$

where  $N$  is the number of conductor turns and  $\Phi_B$  is the magnetic flux through a *single* loop.

The above formulation is for inductors with loops of identical geometry. There are algebraic formulations of Faraday's law of induction that have been specifically derived for various geometries of inductive coils and spirals. We will describe formulations for planer spiral inductors that we will apply specifically to SansEC sensors later in this report. Algebraic variants for planer spirals are of the form seen in equations 4.4 and 4.5 earlier in this report. The integral formulation of Faraday's law is equivalent to the differential form, which applies under slightly different conditions. This form is covered as one of Maxwell's equations which fully describe the behavior of both the electric and magnetic fields, as well as their interactions with matter which extends the phenomenon from the electrical to the electromagnetic.<sup>[24-26]</sup>

The Maxwell-Faraday version of Faraday's Law describes how a *time varying* magnetic field creates or induces an electric field. Maxwell's modification of Ampere's law states that magnetic fields can be generated in two ways: by electric current (this was the original "Ampère's law") and by changing electric fields (this was "Maxwell's addition"). Maxwell's addition to Ampère's law is particularly important as it shows that not only does a changing magnetic field induce an electric field, but also a changing electric field induces a magnetic field.<sup>[18]</sup> Maxwell's completion of Ampère's Law together with the Maxwellian form of Faraday's law of induction allow self-sustaining electromagnetic waves to travel through empty space. The speed calculated for electromagnetic waves exactly matches the speed of light.<sup>[27]</sup>

Maxwell-Faraday's law is given as;

$$\nabla \times \mathbf{E} = -\frac{\partial \mathbf{B}}{\partial t} \quad \text{Eq. 5.18}$$

where  $\nabla \times$  is the curl operator and again  $\mathbf{E}$  is the electric field and  $\mathbf{B}$  is the magnetic field. These fields can generally be functions of position  $\mathbf{r}$  and time  $t$ . The Maxwell formulation is critically important in the creation and propagation of electromagnetic waves.<sup>[24]</sup>

There are no magnetic charges or monopoles. The magnetic field in a resonating SansEC sensor is given by a configuration called a dipole. Magnetic dipoles resemble positive and negative magnetic charges analogous to electric charges, however they are inseparably bound together, having no net magnetic charge.<sup>[24-26]</sup> Gauss's law for magnetism, in terms of field lines, states that magnetic field lines neither begin nor end but make loops that extend to infinity and back. Figure 5.4 provides an illustration of the magnetic field lines generated from current flowing along SansEC sensor trace at a resonant frequency.

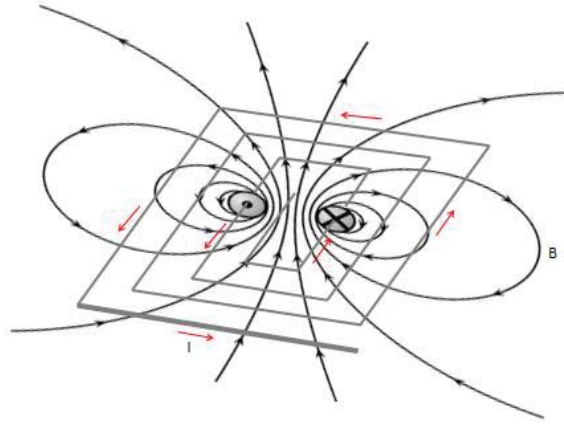


Figure 5.4. Theoretically magnetic field lines never begin nor end but form loops that extend to infinity as shown here with a magnetic field due to current flow in a SansEC at resonance.

The sum total magnetic flux through any Gaussian surface is zero,

$$\nabla \cdot \mathbf{B} = 0 \quad \text{Eq. 5.19}$$

Gauss's law relates the electric flux through any closed Gaussian surface to the enclosed electric charge. The number of field lines that pass through the sensor surface yield the total charge enclosed by the surface divided by the intrinsic permittivity of free space. If the sensor is in contact with a material other than free space then the charge due to the polarization of the material is included, that is the permittivity of the material. This is to say that the distribution of electric charge in a SansEC sensor is given by;

$$\nabla \cdot \mathbf{E} = \frac{\rho}{\epsilon_0} \quad \text{Eq. 5.20}$$

where  $\nabla \cdot \mathbf{E}$  is the divergence of the electric field,  $\epsilon_0$  is the intrinsic electric permittivity of free space, and  $\rho$  is the total electric charge density.<sup>[24-26]</sup>

Maxwell's addition to Ampère's law is particularly important to SansEC sensors as it shows that not only does a changing magnetic field induce an electric field, but also a changing electric field induces a magnetic field.<sup>[24-26]</sup> Therefore, these equations allow self-sustaining electromagnetic waves to travel through empty space and interact with SansEC sensors from a distance.

$$\nabla \times \mathbf{B} = \mu_0 \mathbf{J} + \mu_0 \epsilon_0 \frac{\partial \mathbf{E}}{\partial t} \quad \text{Eq. 5.21}$$

Magnetic fields can be generated in two ways, by electrical current as in the original Ampère's law and by changing electric fields as described by Maxwell's addition to the law.<sup>[24-26]</sup> Early development of SansEC sensors concentrated on near-field excitation of a magnetic field response on the resonant sensors. Maxwell's equations show that a magnetic field response on the SansEC can be generated from the far-field using electromagnetic waves.

Again the Maxwell-Faraday equation version of Faraday's law describes how a time varying magnetic field creates or induces an electric field.

$$\nabla \times \mathbf{E} = -\frac{\partial \mathbf{B}}{\partial t} \quad \text{Eq. 5.22}$$

This aspect of electromagnetic induction<sup>[24-26]</sup> is a major operating principle behind SansEC sensors as an interrogation loop couples a changing magnetic field to the spiral sensor which induces an electric field that is coupled into the material space in the vicinity of the SansEC.

The magnetic field can be defined in several equivalent ways based on the effects it has on its environment. Often the magnetic field is defined by the force it exerts on a moving charged particle. It is known from electrostatic experiments that a particle of charge  $q$  in an electric field  $\mathbf{E}$  experiences a force  $\mathbf{F} = q\mathbf{E}$ . However, in other situations, such as when a charged particle moves in the vicinity of a current-carrying wire, the force also depends on the velocity of that particle. Fortunately, the velocity dependent portion can be separated out such that the force on the particle satisfies the *Lorentz force law*,

$$\vec{\mathbf{F}} = q(\vec{\mathbf{v}} \times \vec{\mathbf{B}}_X + \vec{\mathbf{E}}_X) \quad \text{Eq. 5.23}$$

Here  $\mathbf{v}$  is the particle's velocity and  $\times$  denotes the cross product. The vector  $\mathbf{B}$  is termed the magnetic field, and it is *defined* as the vector field necessary to make the Lorentz force law correctly describe the motion of a charged particle.<sup>[29]</sup>

The Lorentz force law is critical to understanding how SansEC sensors can function as an advanced lightning strike protection layer on aerospace vehicles. This will be more fully described in Section 8 of this report comprising the lightning mitigation technique.

The four Maxwell's equations (including the Maxwell-Faraday equation), along with the Lorentz force law, are a sufficient foundation to derive *everything* in classical electromagnetism.<sup>[25-27, 29]</sup> These in conjunction with the earlier fundamental electrical principles and equations described are the mathematical tools that allow a fuller understanding of SansEC sensors to engineer future design applications.

Electromagnetic resonance theory is well established for classical electromagnetic resonators such as resonant cavities, dielectric resonators, and LCR (inductive-capacitive-resistive) resonant circuits or structures.<sup>[30-32]</sup> The open-circuit resonator used as a sensor is a technology having unique features and applications. It is interrogated by a magnetic near field. It self resonates at a specific fundamental frequency. It has useful harmonics so can operate at

additional frequencies. It has high power exchange efficiency. It responds to perturbations within its self-resonant field with detectable shifts in frequency, amplitude, phase, and resonance bandwidth.<sup>[33]</sup> This is the foundation for using open-circuit resonators for sensing purposes.

The electro dynamic process of the open-circuit resonator is governed by Maxwell's equations with zero current boundary conditions at both ends of the resonant spiral. The free electrons carried by the conductor are uniformly distributed along the conductive trace when no external source is applied, but when driven by an oscillating electromagnetic field the induced electromotive force (EMF) pushes the electrons carried by the conductor into the resonant state where the electrons move back and forth along the conductive trace. Figure 5.5 shows the electric current distribution on the SansEC sensor trace when excited at its fundamental resonance. The current must go to zero at the ends of the trace to satisfy Maxwell's boundary conditions.

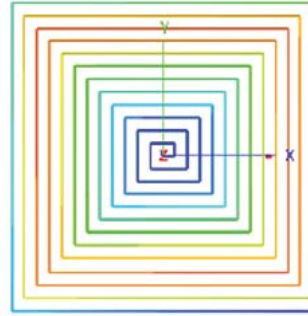


Figure 5.5. Illustration of the Dominant Mode Current Distribution on an Open-Circuit Resonant Spiral (blue: lowest currents to red: highest currents) when excited at its fundamental resonance.

The time-dependent current profile along the conductive trace has the form:

$$I = I_0 \cos\left(\frac{\pi x}{l}\right) e^{-i\omega t} \quad \text{Eq. 5.24}$$

Where,  $x \in [-l/2, l/2]$  is the parameterization coordinate along the length of the conductive trace;  $l$  is the trace length;  $I_0$  is the maximum current amplitude; and  $\omega$  is the angular frequency with  $t$  as time. The induced current along the conductive trace has a cosine distribution with the peak magnitude at the middle part of the trace and zero values at both ends of the trace. During each oscillation cycle, the total current will reach the peak magnitude twice (in opposite directions) and at these moments the energy stored in the resonator is in the form of the magnetic field.

From the continuity equation, the charge density profile has the following form:

$$q = q_0 \sin\left(\frac{\pi x}{l}\right) e^{-i(\omega t + \frac{\pi}{2})} \quad \text{Eq. 5.25}$$

Where,  $q_0$  is the maximum charge density value. The charge is a sine distribution along the trace and creates the potential difference and consequently induces the electric field between the different localized segments of the trace. During each oscillation cycle, the electric field reaches its peak magnitude twice and at these moments the energy is stored in the electric field.

When resonating, the open-circuit sensor produces both electric and magnetic fields which occupy the space between the conductive traces and also penetrates into the space near the resonator. For the planar spiral sensor, the magnetic field and electric field will penetrate into the space beyond the planar surface of the sensor. This is an important feature for sensing purposes because it allows the sensor to measure the properties of the materials placed in close proximity.

Any physical quantity that affects the material's permittivity, permeability, or conductivity will affect the sensor's resonant parameters and therefore can be measured. Electric theory describes the LCR resonator by its lumped parameters of inductance  $L$ , capacitance  $C$ , and resistance  $R$ . For the self-resonant coil, the equivalent lumped parameters can be calculated based on the distributed parameters, as shown in equation 5.26 and equation 5.27, where  $\mu_0$  is the free space permeability,  $\mu_r$  is the relative permeability,  $\epsilon_0$  is the free space permittivity,  $\epsilon_r$  is the relative permittivity, and  $\mathbf{J}(\mathbf{r})$  and  $\rho(\mathbf{r})$  are the current and charge density functions along the conductive trace.<sup>[33]</sup>

$$L = \frac{\mu_0 \mu_r}{4\pi |I_0|^2} \iint \frac{\mathbf{J}(\mathbf{r}) \cdot \mathbf{J}(\mathbf{r}')}{|\mathbf{r} - \mathbf{r}'|} d\mathbf{r} d\mathbf{r}' \quad \text{Eq. 5.26}$$

$$C^{-1} = \frac{1}{4\pi \epsilon_0 \epsilon_r |Q_0|^2} \iint \frac{\rho(\mathbf{r}) \cdot \rho(\mathbf{r}')}{|\mathbf{r} - \mathbf{r}'|} d\mathbf{r} d\mathbf{r}' \quad \text{Eq. 5.27}$$

However, the current and charge density functions are not measurable in actual experiments. Therefore, the equivalent inductance and capacitance values of a self-resonant coil are the calculated values and are used only for principle analysis. From equation 5.26 and equation 5.27, it can be clearly seen the dependency of inductance and capacitance upon the material's relative permeability  $\mu_r$  and relative permittivity  $\epsilon_r$ . If the material in the electric and magnetic field changes its permeability and/or permittivity, the resonator equivalent LC value will change correspondingly, so will the resonance parameters. It is notable that equation 5.26 and equation 5.27 are for the cases where the resonant sensor trace is totally embedded in the material having isotropic properties. For most actual applications, for example, the material is put on one side of the resonant sensor, the dependency function between the sensor parameters and the material properties is not obvious and needs to be characterized and calibrated by experiments or computational methods.<sup>[33]</sup>

Essentially, a SansEC sensor is an electromagnetic resonator and therefore its circuit level behaviors can be modelled with the well-developed circuit theory using lumped circuit parameters, more specifically, using the LCR resonant circuit model. Figure 5.6 presents the circuit model for the coupled impedance including a loop antenna, a SansEC sensor, and a substrate being measured. The substrate material can be conductive, dielectric, or semi-conductive. For conductive material, the material impedance is modeled by LC circuit as shown in Figure 5.6 where,  $L_M$  is inductance and  $R_M$  is the resistance. For non-conductive material the material impedance is modeled by the complex permittivity as shown in equation 5.31, and where  $\epsilon_r$  is the complex permittivity of the material.

The impedance of the loop antenna is:

$$Z_A = R_A + j\omega L_A \quad \text{Eq. 5.28}$$

where,  $R_A$  is the intrinsic resistance and  $L_A$  is the inductance of the loop antenna. The  $\omega = 2\pi f$  is the angular frequency.

The SansEC sensor is modeled using a serial LCR circuit model with its impedance expressed as following:

$$Z_S = R_S + j\left(\omega L_S - \frac{1}{\omega C_S}\right) \quad \text{Eq. 5.29}$$

where,  $R_S$  is the intrinsic resistance of the sensor trace and  $L_S$  is the total effective inductance of the SansEC sensor, and the  $C_S$  is the total effective capacitance of the SansEC sensor.

The substrate impedance is modeled based on its conductive property. When a conductive material is hit by an oscillating magnetic field, the current will be induced on and near the surface of the conductive material. Therefore, its impedance includes a resistive part and an inductive part, as shown in the following equation:

$$Z_M = R_M + j\omega L_M \quad \text{Eq. 5.30}$$

Driven by an oscillating voltage/current source, the loop antenna produces an oscillating magnetic field, which is coupled to the SansEC sensor's inductance through the mutual inductance between the sensor and the antenna  $M_1$ . The SansEC sensor receives energy from the oscillating magnetic field generated by the antenna and turns into resonant state in which it generates its own oscillating magnetic field (and electric field). The sensor generated magnetic field is coupled to the substrate material through the second mutual inductance  $M_2$ , as illustrated in figure 5.6. Physically, there is a third mutual inductance  $M_3$  between the antenna and the substrate but it is not a focus for our measurement objective here.

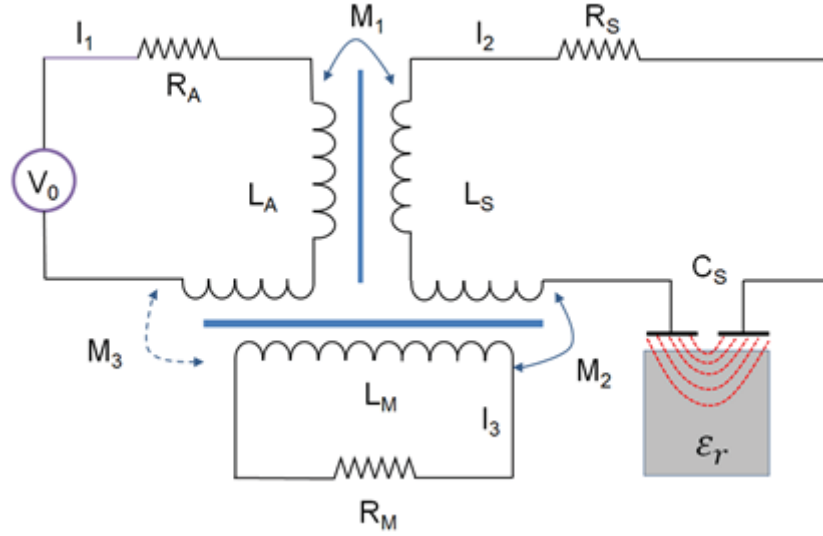


Figure 5.6. Impedance model of SansEC sensor circuit (Loop antenna, sensor, conductive and dielectric material).

For non-conductive substrate material, the eddy current phenomenon can be ignored and the material impedance should be modeled using the complex permittivity model.

$$\hat{\epsilon}_r = \epsilon_r'(\omega) + j\epsilon_r''(\omega) \quad \text{Eq. 5.31}$$

where,  $\epsilon_r'$  is the real part of the permittivity, which is related to the stored energy within the medium;  $\epsilon_r''$  is the imaginary part of the permittivity, which is related to the dissipation (or loss) of energy within the medium. The SansEC sensor is coupled to the non-conductive substrate material through the electric field and its total capacitance is correlated to the permittivity of the material as following:

$$C_S = f(C_{S0}, \hat{\epsilon}_r) \quad \text{Eq. 5.32}$$

where,  $f$  is the dependency function of sensor's total capacitance;  $C_{S0}$  is the capacitance value in air;  $\hat{\epsilon}_r$  is the complex permittivity of the material. In the simplest case of a parallel capacitor with uniform dielectric material between the electrode plates, the equation 5.32 is simplified into

$$C_S = C_{S0} \cdot \epsilon_r \quad \text{Eq. 5.33}$$

For semi-conductive material, the total impedance will include both inductive coupling and the capacitive coupling.

Applying the Kirchhoff's voltage law (KVL) on the circuit model as shown in figure 5.6., we can get the KVL equations as following:

$$\begin{cases} Z_A \cdot I_1 + j\omega M_1 \cdot I_2 + j\omega M_3 \cdot I_3 = V_0 \\ j\omega M_1 \cdot I_1 + Z_S \cdot I_2 + j\omega M_2 \cdot I_3 = 0 \\ j\omega M_3 \cdot I_1 + j\omega M_2 \cdot I_2 + Z_M \cdot I_3 = 0 \end{cases} \quad \text{Eq. 5.34}$$

where,  $Z_A$  is the antenna impedance;  $Z_S$  is the SansEC sensor impedance;  $Z_M$  is the material impedance;  $I_1$  is the current in the antenna circuit;  $I_2$  is the sensor current;  $I_3$  is the current in material;  $V_0$  is the voltage source. The above equations can be expressed in matrix form as following:

$$\begin{bmatrix} Z_A & j\omega M_1 & j\omega M_3 \\ j\omega M_1 & Z_S & j\omega M_2 \\ j\omega M_3 & j\omega M_2 & Z_M \end{bmatrix} \begin{bmatrix} I_1 \\ I_2 \\ I_3 \end{bmatrix} = \begin{bmatrix} V_0 \\ 0 \\ 0 \end{bmatrix} \quad \text{Eq. 5.35}$$

Solving the equations in 5.35, we can get the total load impedance of the circuit as following:

$$Z_L = \frac{V_0}{I_1} \quad \text{Eq. 5.36}$$

Figure 5.7 illustrates the circuit model for reflection coefficient S11 of 1-port system.  $Z_L$  is comprised of the antenna, sensor and substrate.

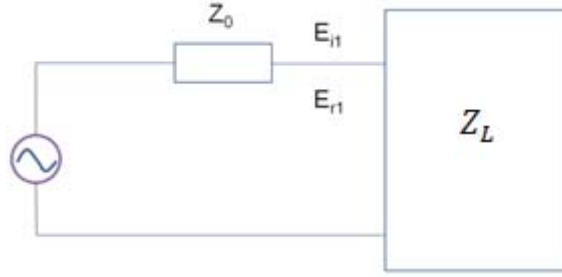


Figure 5.7. Reflection coefficient (S11) of 1-port system

The S11 equation is as follows:

$$S_{11} = \frac{E_{r1}}{E_{i1}} \quad \text{Eq. 5.37}$$

where,  $E_{r1}$  is the reflected energy;  $E_{i1}$  is the injected energy on port 1. Given the output impedance and the load impedance of DUT (Device-Under-Test), the S11 can be expressed as following:

$$S_{11} = \frac{Z_L - Z_0}{Z_L + Z_0} \quad \text{Eq. 5.38}$$

To summarize, the principles and axioms of electromagnetic theory have been presented to build the mathematical foundation used to develop the impedance model illustrated in equations 5.28 to 5.38 and establish the theoretical frame and conceptual roadmap to enable SansEC sensors to perform damage detection and diagnosis. It can give us a clear consequence path for how a physical change in substrate or sensor body will be reflected in the measurable outputs, such as the S11 parameter. For the conductive substrate material, structural damage will lead to a change in the material electrical characteristic properties including  $R_M$  and/or  $L_M$ . Depending on the specific situation, the mutual inductance between the sensor and material,  $M_2$ , may also be potentially influenced by the damage. All these changes are reflected in the impedance coupling equations, and eventually, in the total load impedance of the circuit  $Z_L$  and the reflected coefficient S11 parameter. For the non-conductive substrate material, the structural damage influence on material properties will be reflected on the material's complex permittivity  $\hat{\epsilon}_r$ , mostly on the dielectric constant  $\epsilon'_r$ , which is the real part of  $\hat{\epsilon}_r$ . The SansEC sensor is coupled to the material through the electric field generated by the sensor's capacitive part. The capacitance value of the sensor is directly correlated to the material permittivity through equation 5.33. The change in the sensor's capacitance will lead to a shift in the resonant frequency of the sensor which will be reflected in the impedance equations and the measurable reflected coefficient S11 parameter.

## 6.0 INVESTIGATION of DAMAGE DETECTION CAPABILITY

A major challenge in structural health monitoring (SHM) is to be able to detect damage beneath the surface of the composite substrate. In general, composite structural damage is accompanied by a localized change of the material properties and electrical impedance, including permittivity, permeability, and conductivity in the damaged areas. Computational Electromagnetic (CEM) simulations provide an invaluable tool to evaluate SHM techniques which rely on changes in the composite electrical impedance to detect damage beneath the substrate surface. We have developed CEM simulations to support our research using the **FEKO** software, "FEldberechnung für K rper mit beliebiger OBERfl che" or "Field Calculations for Bodies with Arbitrary Surface", a commercial computational electromagnetic software package capable of modeling our open-circuit resonant sensors.<sup>[34]</sup> The FEKO computational electromagnetic modeling software supports the method of moments (MoM) to perform a full wave solution to Maxwell's integral equations in the frequency domain. Special extensions were configured to the MoM formulation to enable the modeling of complex dielectric media associated with the simulated and real aerospace composite materials. Planar Green's functions were considered for some substrates.<sup>[35]</sup>

To simulate a planar SansEC resonant sensor on a composite substrate as a fundamental sensing element in the CEM tool, the sensor on the surface of the composite along with a square loop antenna positioned above was modeled as a three dimensional object. A combination of FEKO and MATLAB were used to build parametric features into the model. The sensor/material model was constructed such that physical dimensions of the sensor system were variable. As shown in Figure 6.1, the copper trace width  $W$  could easily be set to new design values. The copper materials were initially modeled as perfect electrical conductor (PEC) and later as real copper materials. The edge to edge separation distance, or trace gap  $G$ , between the conductive legs of the spiral could be adjusted. The composite dielectric substrate thickness  $H$  could be changed. The electrical material properties of the substrate were modifiable thus making it possible to simulate other composite materials or fatigue stresses and damage within the material by altering the relative value of the electric permittivity  $\epsilon_r$ , and/or the electric loss tangent  $\tan \delta$ . The length of the trace of a square spiral resonant sensor is further parameterized by the area  $A$ . This determines the sensor size which directly relates to the design operation frequency and the amount of composite material surface that the sensor covers. Also the number of turns  $N$  that comprise the inductive loops of the sensor is parameterized. The square loop antenna used to excite the sensor and read back the response was model with a stand-off parameter  $S$ , so that the height of the antenna above the sensor/material structure could be adjusted.

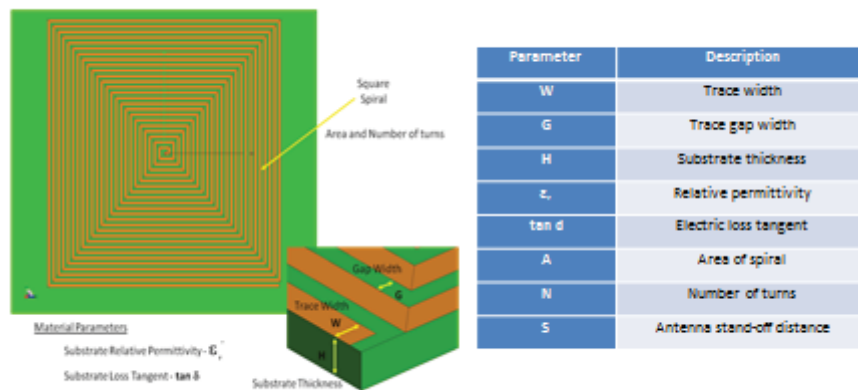


Figure 6.1 Square spiral resonant sensor model with several parameterized features.

In addition to supporting the full parametric creation of the models, FEKO was used to mesh the geometry, and to specify other solutions, settings, and calculation requirements in the graphical environment. The geometries were meshed as frequency dependent triangles, segments, and connection points. The geometrical data numerical results were processed by the software as the one-port S-parameter  $S_{11}$  (converted to return loss), which allowed comparison to the experimental network analyzer measurements that were similarly configured. The matrix elements were stored in memory and the calculation of the elements using the method of moments provided a vector

solution to the linear set of Maxwell's equations. The matrix was decomposed, and a backwards substitution provided a determination of the surface currents, impedances, and power amplitudes as a function of frequency.<sup>[2, 35]</sup>

The binary output files were read in FEKO and then the results were displayed in the form of  $S_{11}$  S-parameter plots. These return loss data offered the best comparison of computational modeling results to the experimental measurements. Three dimensional views of the sensor and substrate geometries were also available to display surface currents and electric or magnetic fields. The meshed geometry and optimization results were viewable. The 3-D views allowed researchers to gain a functional perspective on the interaction of the sensor with the simulated composite substrate. These examinations aid in the next generation design or modification of a sensor's geometry for improved sensing capabilities. Studies of field penetrations into a particular substrate will be of great future benefit in optimizing sensor/composite systems.

### 6.1 Damage Detection Simulations on Fiberglass Reinforced Composite Substrates

Figure 6.2 shows a 3D cross-section of a SansEC sensor on a FRC substrate modeled in FEKO. The substrate is shown with a free space slot to represent inner structural damage from a delamination defect. The slot has a size of 2.54 mm × 50.8 mm × 50.8 mm (0.1 inches × 2 inches × 2 inches) and is 2.54 mm (0.1 inches) from the substrate top surface. The localized permittivity change will alter the effective permittivity of the substrate and alter the resonant response of the sensor.

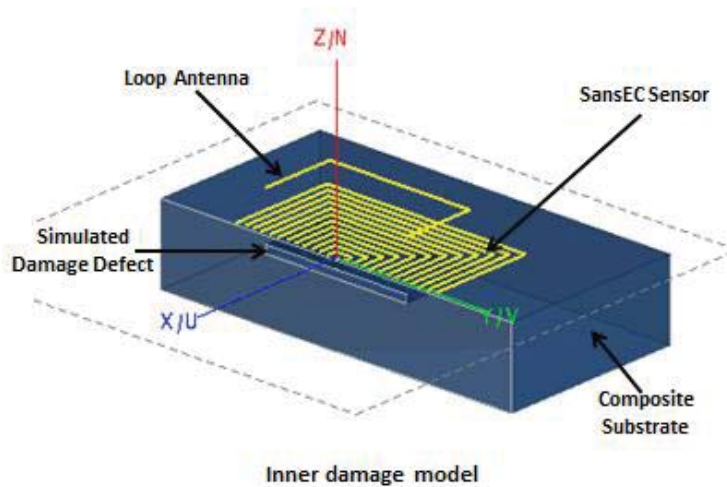


Figure 6.2. Computational model showing a 3D cross-section of a SansEC sensor on a dielectric composite with simulated internal damage.

Figure 6.3 presents the reflection coefficient resonances of the sensor on the substrate with and without the inner damage slot. The resonant frequency of the sensor is shifted from 52.8643 MHz to 54.9254 MHz. The presence of damage in this case shifts the resonance signature by about 2 MHz. In measuring this frequency shift, the inner damage of the composite substrate can be effectively identified. The Y axis is the reflected power in terms of reflection coefficient and is unitless. The maximum value 1 represents total reflected power and 0 indicates no energy reflected. The x axis shows the reflection coefficient as a function of frequency in Megahertz. These computed scales are different than the ones used later in measurements. In physical experiments using the network analyzer the y scale is shown as Return Loss in dBm referencing power to 1mW output from the interrogating source. Reflection Coefficient and Return Loss are similar and both are consider the S-Parameter  $S_{11}$ . A conversion from reflection coefficient to return loss may be achieved by  $20\text{Log}(\text{Reflection Coefficient})$ .

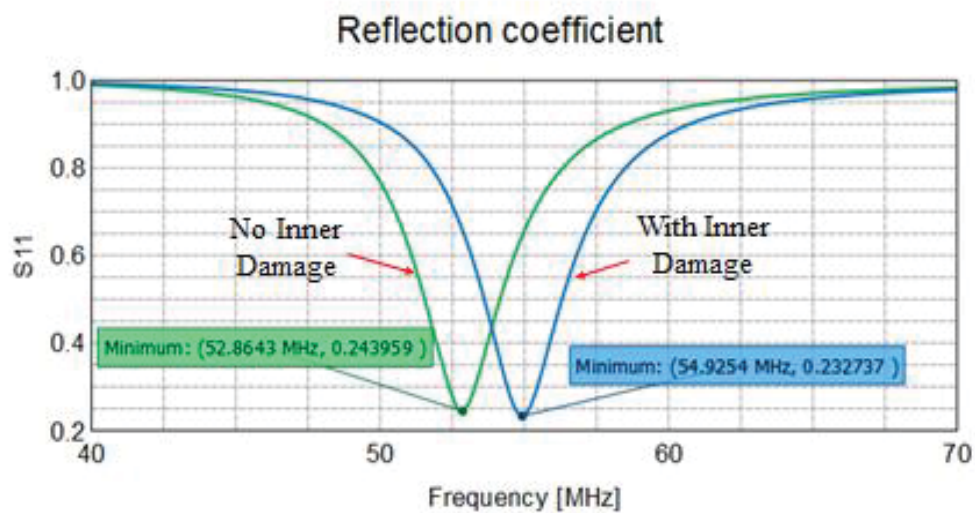


Figure 6.3. S-Parameter plot depicting resonances for substrates with and without damage.

Figure 6.4 shows a cross-section of the electric field distributions of the sensor without the inner damage activated in the model. Figure 6.5 shows the electric field distributions of the sensor with the simulated inner damage activated.

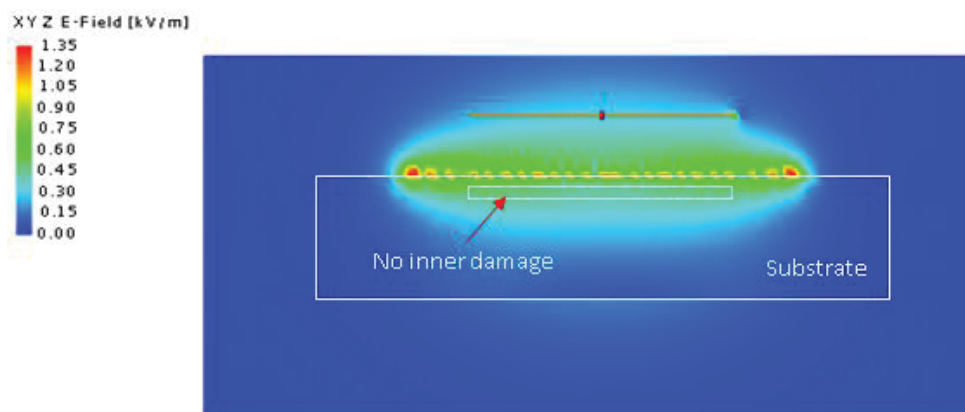


Figure 6.4. Computational model of the electric field penetration from a SansEC Sensor into a non-damaged dielectric composite.

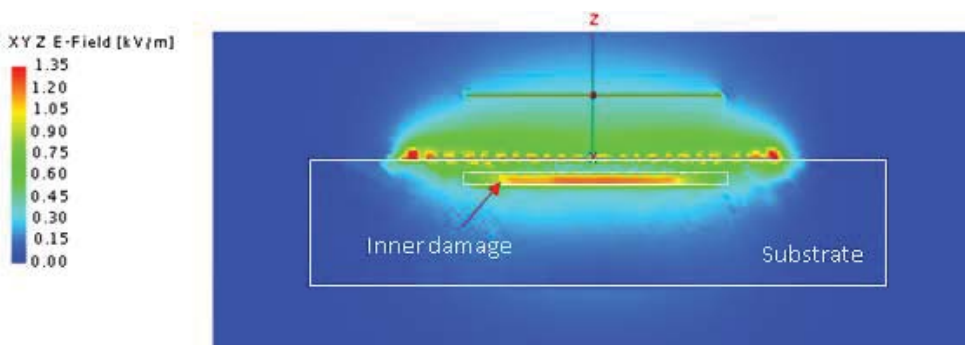


Figure 6.5. Computational model of the electric field penetration from a SansEC Sensor into a damaged dielectric composite.

The electric field has an obvious higher than normal density in the slot area. This is a great computational visualization that gives clear understanding of the electric field mechanism that allows the sensing of subsurface defects. This addresses realistic damages such as voids, delaminations, broken fibers, and heat damage in real composites.<sup>[27]</sup> This is so, because in these types of damages a localized dielectric change occurs that can be made representative by the geometry of a simple slot.

The initial laboratory computations proved that a SansEC sensor placed on a material surface is capable of determining physical characteristics and qualities about the material upon which it is placed.<sup>[36]</sup> The detection of the differences in frequency and amplitude of the induced currents within a material substrate offers a means of detecting damage or changes to the state and condition of the material substrate.

## 6.2 Skin Depth Analysis

Materials such as carbon-fiber-reinforced polymers (CFRP) are conductive materials. When an oscillating magnetic field hits a conductive material, the magnetic field can penetrate only a limited distance described by the “skin depth” effect. The skin depth is defined as the depth below the surface of the conductor at which the current density has fallen to  $1/e$  of the current at the surface. For a general dielectric material with conductivity, the skin depth  $\delta$  is governed by the following equation:

$$\delta = \frac{1}{\omega} \left\{ \left( \frac{\mu\epsilon}{2} \right) \left[ 1 + \left( \frac{\sigma}{\omega\epsilon} \right)^2 \right]^{1/2} - 1 \right\}^{-1/2} \quad \text{Eq. 6.1}$$

For conductors having high conductivity which satisfies  $\sigma \gg \omega\epsilon$ , the skin depth equation can be simplified to:

$$\delta = \frac{1}{\sqrt{f\pi\mu\sigma}} \quad \text{Eq. 6.2}$$

Skin effect describes the tendency of a time varying electric current to distribute its largest current density near the surface of a conductive or semi-conductive material. The current density decreases with greater penetration into the material. As a result, the electric current flows mainly at and near the "skin" or surface of the material. The skin depth is thus defined as the depth below the surface of the material at which the current density has fallen to  $1/e$  or about 37% of the density at the surface. When an oscillating magnetic field impinges on the surface, the skin effect is caused by the opposing currents induced by the oscillating magnetic field. Induced currents circulating in planes perpendicular to the magnetic flux travel parallel to the SansEC sensor trace and flow is limited to the area of the inducing magnetic field. The induced currents concentrate near the surface adjacent to the exciting SansEC sensor and the strength decreases with distance from the sensor as shown in the image of Figure 6.6. Current density decreases exponentially with depth.

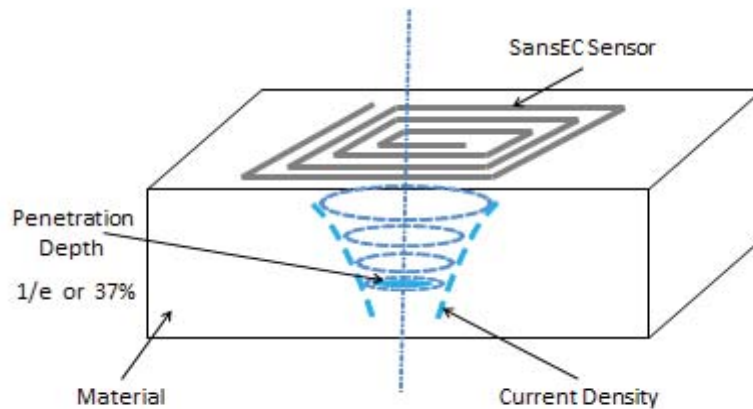


Figure 6.6. Skin effect and induced current in conductive material.

For a SansEC sensor on a highly conductive material, the skin depth is defined as following:

$$\delta = \sqrt{\frac{2\rho}{\omega\mu_r\mu_0}} \quad \text{Eq. 6.3}$$

where,  $\delta$  is the skin depth and  $\rho$  is the resistance. Equation 6.3 is a variation of equation of equation 6.2. From the equation it can be shown that the skin depth of a material is determined by the permeability and resistance of the material and the frequency of the electromagnetic excitation.

For the materials which are less conductive, a variation of equation 6.1 provides a more accurate prediction of the skin depth, from which it can be shown that the skin depth is related to the operation frequency and the material's resistance, permeability and permittivity.

$$\delta = \frac{1}{\omega} \left\{ \frac{\mu_0\mu_r\varepsilon_0\varepsilon_r}{2} \left[ 1 + \left( \frac{1}{\rho\omega\varepsilon_0\varepsilon_r} \right)^2 \right]^{1/2} - 1 \right\}^{-1/2} \quad \text{Eq. 6.4}$$

The SansEC sensors currently used in this research have a frequency range of 100 kHz to 200 MHz. Aircraft composite structures have a typical conductivity of  $2.54 \times 10^4$  S/m.<sup>[37]</sup> With the given frequency range and conductivity, the parameters satisfy the condition of  $\sigma \gg \omega\varepsilon$  and equation 6.2 can be used to calculate the skin depth. Figure 6.7 shows the skin depth as a function of frequency. The y axis is the penetration depth in units of meters and the x axis is the frequency in Hertz. The frequency curves for the material conductivity of  $1 \times 10^3 \sim 1 \times 10^5$  S/m. The red curve is for the typical conductive composite structures having the conductivity of  $2.54 \times 10^4$  S/m. It can be seen that the maximum skin depth is 10 mm at frequency of 100 kHz which is toward the lower frequency limit. At frequencies of 1 MHz, 10 MHz, and 100MHz, the skin depth values are 3 mm, 1 mm, and 0.3 mm, respectively. Figure 11 provides a roadmap for designing SansEC sensors on composite structures for different conductivities. Given specific conductivity and the penetration depth requirement, the sensor's working frequency can be determined. For example, if a penetration depth of 5 mm is required for the composite having conductivity of  $2.54 \times 10^4$  S/m, the sensor should be designed to resonate at the frequency of 400 KHz. It is notable that the skin depth is defined by the factor of  $1/e$  which is about 36.8% amplitude attenuation. The actual magnetic field penetrates deeper than the skin depth defined in this manner into the material and decreases exponentially. For sensing purpose, the detectable depth may be extended beyond the skin depth, for example, to  $2\delta$  or  $3\delta$ .

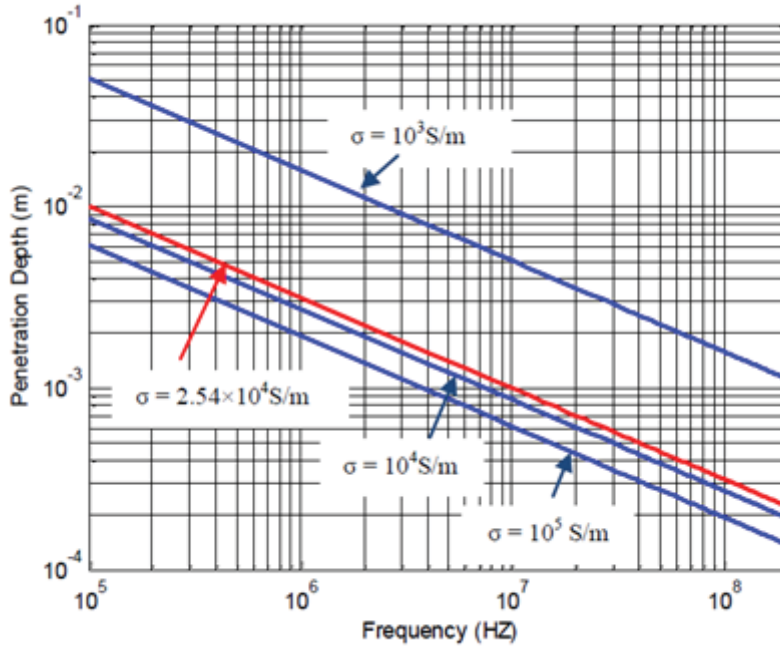


Figure 6.7. Skin depth for the conductivity of  $1 \times 10^3$ ,  $1 \times 10^4$ ,  $2.54 \times 10^4$ , and  $1 \times 10^5$  S/m within the frequency ranges of 100kHz~200MHz.

In general, higher frequency will lead to smaller skin depth and therefore smaller penetration depth from the SansEC sensor into the material. It is a general strategy to use lower frequency sensors to achieve better penetration depth. However, the frequency of the sensor is limited by its geometric parameters. A lower frequency will typically require larger sensor size which has larger effective capacitance and inductance. It is an important task to design the sensor having a balanced geometric size and resonant frequency for the specific application. To overcome this challenge, we proposed a solution using a high magnetic permeable material (high  $\mu$  material) layer to improve the electromagnetic coupling between the sensor and the CFRP material which will be discussed in the following section.

### 6.3 SansEC Operation on Carbon Composite Materials

When the composite substrate has high conductivity, the conductive surface of the substrate may absorb all of the electromagnetic field energy and render the sensor's response non-detectable. For example, if a SansEC sensor made of copper is put on the surface of a copper substrate, the sensor's response characteristics will be non-detectable. As an electromagnetic resonator, a SansEC sensor relies on the external oscillating magnetic field to excite its self-resonance and establish the associated sensor produced electromagnetic fields. An obvious application limitation of the sensor in its basic configuration is that it cannot be applied directly on or put very close to a conductive substrate because the conductive substrate will shield and absorb the electromagnetic energy making the sensor non-functional. The goal of this research was to develop SansEC applications for use on CFRP materials, which have a conductivity in the range of [ $10^3 \sim 10^5$  S/m]. This is a much more challenging application than sensing on nonconductive dielectric substrates.

To solve this problem, we propose a new method that incorporates a high permeability material between the sensor and the conductive substrate to control the field coupling and enable sensor operation. The depth that induced currents can penetrate into a material is affected by the frequency of the excitation current, and the conductivity and magnetic permeability of the substrate material. While the depth of penetration decreases with increasing frequency and increasing conductivity and magnetic permeability, the degree of penetration can in principle be increased by the creating a saturation magnetic field. SansEC sensors that incorporate magnetic shielding constructed from materials with high magnetic permeability can generate this saturation magnetic field to enable their operation. The general configuration consists of stacking the SansEC sensor over a thin electrical isolating dielectric over a high permeability material layer placed over the CFRP substrate. The high permeability material layer is used to concentrate the magnetic field inside the high permeability material to enable the sensor to self-resonate. By partially covering the sensor area with high permeability material, the current density can be increased at the interface of the CFRP surface allowing the magnetic field to be more effectively coupled. The high permeability materials are typically thin metallic films composed of a nickel-iron alloy and are commonly referred to as mu metals or high  $\mu$  materials. The high  $\mu$  material allows a region of low magnetic reluctance to enable the self-resonate electromagnetic fields to be sustained to make the sensor operational.

The high  $\mu$  material has a natural capability of concentrating magnetic flux density and that is why it is typically used as the core material in transformer coils. The high  $\mu$  material performs two functions at improving the sensor response. The first function is to increase the magnetic field produced by the sensor and correspondingly increasing the penetration depth of the magnetic field into the CFRP material. The second function of the high  $\mu$  material is to reserve a high density magnetic flux in a very narrow space (which is the thickness of the high  $\mu$  material layer) to sustain the oscillating magnetic fields (both the external driving magnetic field and the sensor produced magnetic field) from being totally shielded and absorbed by the conductive surface.

As we know, when a solenoid inductor is immersed in a material with relative permeability  $\mu_r$ , the magnetic flux density will be increased proportionately by the amount of  $\mu_r$ .

$$B = \mu_r \cdot B_{Air} \quad \text{Eq. 6.5}$$

where,  $B_{Air}$  is the magnetic flux density when the solenoid is put in air. However, in most cases, the inductor is not immersed in a higher permeability material, but rather some portion of the space around the solenoid has the high permeability material and the rest is in free space air, as shown in Figure. 6.8. In this scenario, the full effect of the

high permeability material will be reflected as an effective permeability  $\mu_{eff}$  which is in the range of  $1 \leq \mu_{eff} \leq \mu_r$ . Similarly, when high permeable material layer is used between the sensor and the conductive substrate, a portion of the space around the sensor inductor has higher permeability, as shown in Figure 6.8, and therefore the magnetic flux density will be increased by an effective permeability  $\mu_{eff}$  which is in the range of  $1 \leq \mu_{eff} \leq \mu_r$ . Though not shown here, SansEC sensors can also be configured using a high mu metal material between the traces as a means to sustain the magnetic flux when placed on a conductive substrate. In flat planer coils, this is known as a planer core.

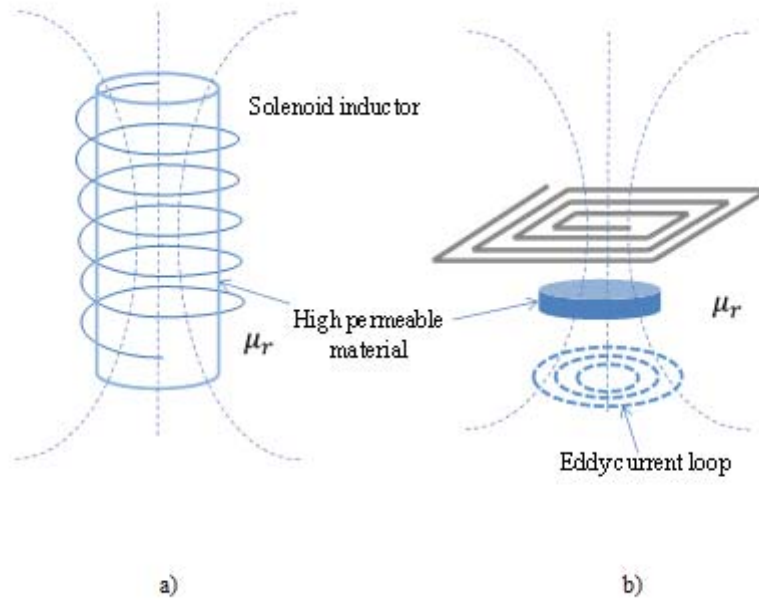


Figure 6.8. High permeable material enhancing the strength of the magnetic flux.

Figure 6.9 illustrates how the high  $\mu$  material concentrates and reserves the magnetic flux density within it. This is a method for impedance matching the sensor to the substrate. A portion of the magnetic field flux is reserved within the high  $\mu$  material and the rest is used to couple induced currents into the conductive substrate. There is an obvious optimization and tradeoff required to determine how much magnetic field energy should be reserved within the  $\mu$  material and how much should be coupled into the conductive substrate to penetrate the substrate as deeply as possible for damage detection and resonate strongly enough for accurate characterization. Various geometric configurations are possible to optimize the sensor-to-substrate interface for a conductive composite. From the damage detection perspective, the magnetic field coupling with the CFRP is expected to be as strong as possible and the penetration depth is expected to be as deep as possible. However, a very strong magnetic field coupling between the sensor and CFRP will absorb most of the energy from the oscillating magnetic field and render the sensor non-resonant. Therefore, we need to carefully balance the tradeoff to preserve a portion of the energy in the form of oscillating magnetic field strong enough to keep the sensor resonant, and at the same time, have an acceptable penetration depth of measurement. The research needed to achieve this proper balance is still ongoing.

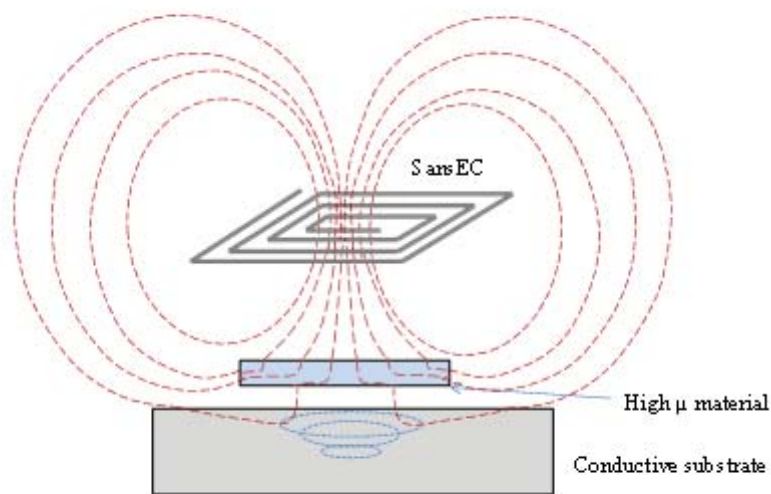


Figure 6.9. High permeable material concentrates magnetic flux density.

The high  $\mu$  material layer has different impedance characteristics with different geometric designs. Figure 6.10 shows the high  $\mu$  material layer geometric design used in our simulations. The impedance of the geometric design must be appropriately matched to the impedance of the SansEC sensor and to the impedance of CFRP composite to effectively control the coupling coefficient tradeoff as discussed above.

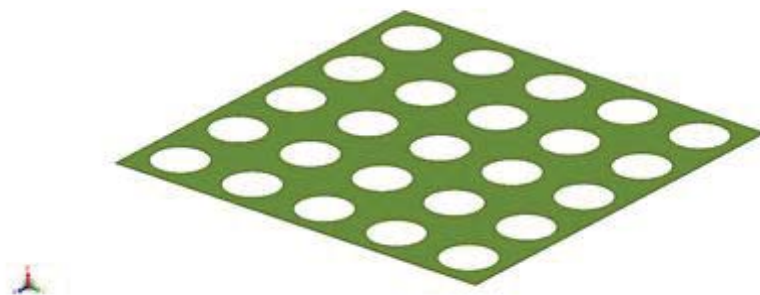


Figure 6.10 Example of high permeable material structural design.

#### 6.4 Damage Detection Simulations on Carbon Fiber Reinforced Composite Substrates

A new CFRP model was developed using the Surface Modeling Method in FEKO to simulate the complexity inherent in a realistic aerospace composite skin. The model is based on Hexcel carbon fiber test panels that were fabricated as composite panel test articles for lightning strike research. Based on these panels we also designed panels as physical test coupons that included known seeded faults. These experimental test panels were fabricated with a single top layer Hexcel Hexply 8552/A193-PW.3K-70-PW plain weave fabric as seen modeled in Figure 6.11 and five “clocked” or rotated layers of Hexcel Hexply 8552/AS4 unidirectional tapes shown modeled in figure 6.12.

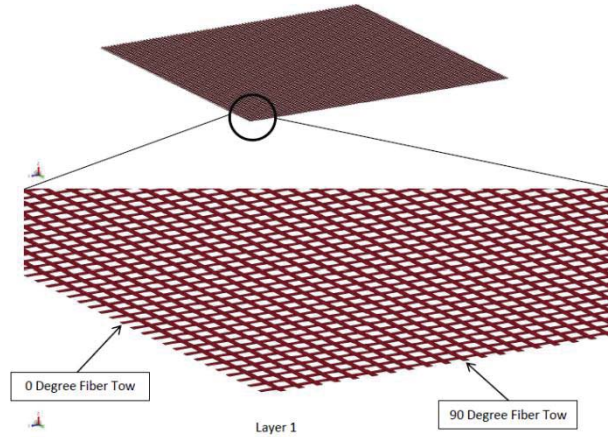


Figure 6.11. CFRP Model Plain Weave Fabric Top Layer.

The top plain weave layer was modeled at the fiber tow level. The fiber tows were oriented at 0 degrees and 90 degrees. The next five layers in the stack consisted of the unidirectional tapes. They were oriented or “clocked” at +45 degrees, +90 degrees, -45 degrees, 0 degrees, and back to +45 degrees respectively. The ply thicknesses were nominally 0.15 mm (6 mils) thick. The ply thicknesses were nominally 0.15 mm (6 mils) thick.

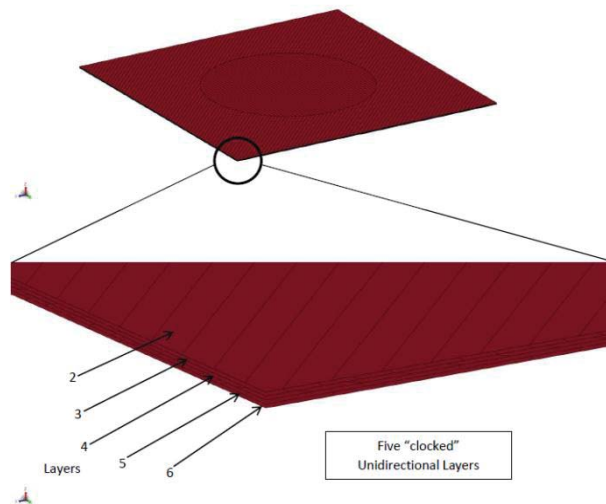


Figure 6.12. CFRP Model Unidirectional Tape Stack Layers.

The CFRP modeling is much more complicated and computer intensive than for the ideal dielectric FRC models. Techniques were developed to minimize the demand on computing resources for both meshing and calculating the solution. The geometry of the fiber tow in this model is parameterized such that control of the complexity of the model and the detailed micro-structure in the CFRP is realized. This enables the use of modest computing resources and the capability to attack complex problems and still converge to high fidelity solutions. For this modeling effort, the configuration of the computational models was matched to the expected experimental CFRP panels. The model included a SansEC sensor stacked above a thin electrical isolating dielectric placed over a perforated high permeability material layer placed over the CFRP substrate. Figure 6.13 shows the model geometry of the perforated high permeability material layer used in the investigation along with the interrogating loop antenna. This piece of the model was stacked over the CFRP model (illustrated in Figures 6.11 and 6.12) in a series of computational electromagnetic modeling tests. The modeling effort enables an intuitive understanding of the electromagnetic field penetration interactions with the carbon fiber composite plies and corresponding damage within the plies. These insights were used to inform the experimental design and testing of actual seeded fault test panels for the purpose of sensing and diagnosing damage.

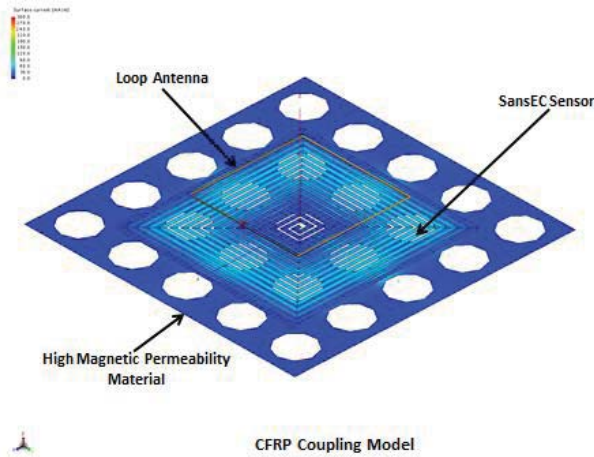


Figure 6.13. SansEC CFRP Impedance Coupling Model.

The simulations were conducted on a baseline panel structure representative of a realistic aircraft skin, and repeated on the same structure with seeded faults. The models and simulations were configured and run with damage faults of various sizes and at various ply depths. Table 6.1 presents the SansEC CFRP damage detection computational electromagnetic model test matrix. For delamination faults, the fabric or unidirectional tape ply separations were small 0.05 mm (2 mils), medium 0.5 mm (20 mils), and large 1.0 mm (40 mils). The delamination damage fault were simulated one ply deep beneath the top CFRP plain weave layer, three plies deep beneath the top layer, and five plies deep beneath the top. Machined core damage faults were developed for two different sized damage cores cut at various layers. A 37.5 mm core was removed from the unidirectional tape layer at one ply, three plies and 5 plies beneath the top CFRP plain weave layer. Likewise a larger 75 mm core was incorporated in the model in the same fashion.<sup>[38-39]</sup>

Table 6.1. SansEC CFRP Damage Detection Computational Electromagnetic Model Test Matrix

Computational Electromagnetic CFRP Damage Model Test Matrix		
Damage Type	Folder	Damage Model
No Damage	Baseline	Baseline
Delamination	Delamination 1	PlyDepth1 Damage 0.05mm
		PlyDepth1 Damage 0.5mm
		PlyDepth1 Damage 1.0mm
	Delamination 2	PlyDepth3 Damage 0.05mm
		PlyDepth3 Damage 0.5mm
		PlyDepth3 Damage 1.0mm
Delamination 3	PlyDepth5 Damage 0.05mm	
	PlyDepth5 Damage 0.5mm	
	PlyDepth5 Damage 1.0mm	
Machined Core	Core 37.5mm	PlyDepth1 Core 37.5mm
		PlyDepth3 Core 37.5mm
		PlyDepth5 Core 37.5mm
	Core 75mm	PlyDepth1 Core 75mm
		PlyDepth3 Core 75mm
		PlyDepth5 Core 75mm

Figure 6.14 presents the computational results for the simulated S parameter reflection coefficient value versus frequency for a baseline simulation model with no delamination (red curve), delamination simulation beneath the first ply with a .5mm gap (blue curve) and delamination simulation beneath the first ply with a 1mm gap (green curve). Four resonances are clearly visible in all 3 curves. The two delamination curves show an increasing shift in both amplitude and resonant frequency at their respective higher order harmonic resonances. Figure 6.15 presents the same plot with a different xy axis to show the structure at the primary resonant frequency. The amplitude and frequency shift are clearly present at the primary resonance.

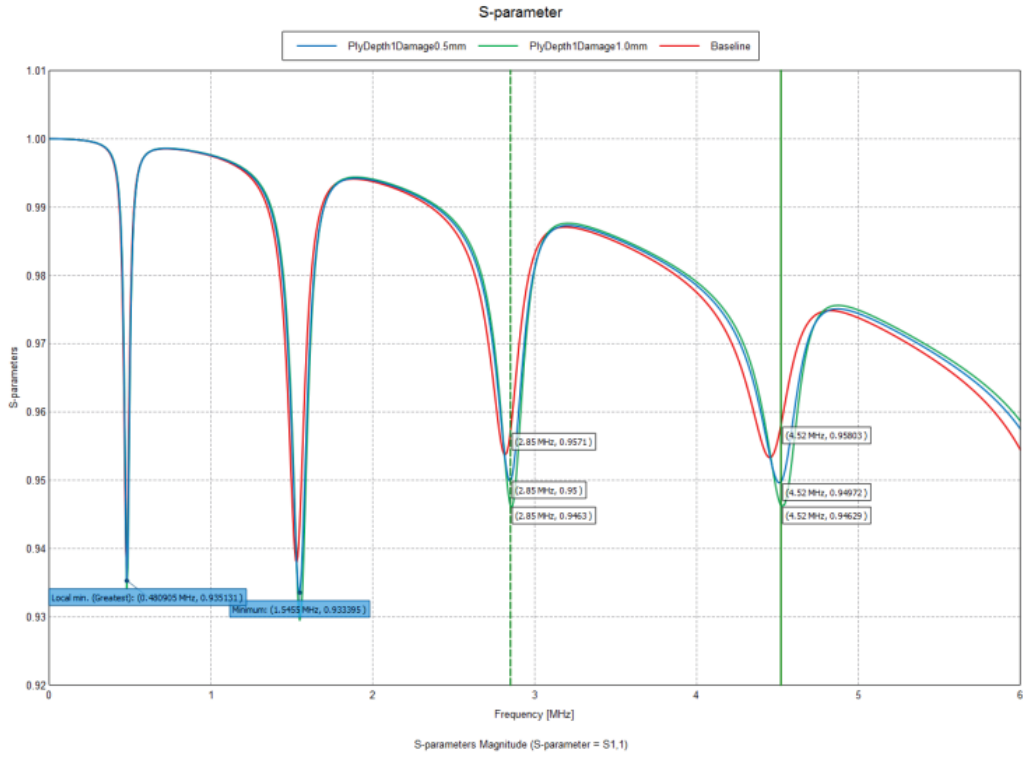


Figure 6.14. CEM data of SansEC Sensor on conductive composite (CFRP) using high permeability material.

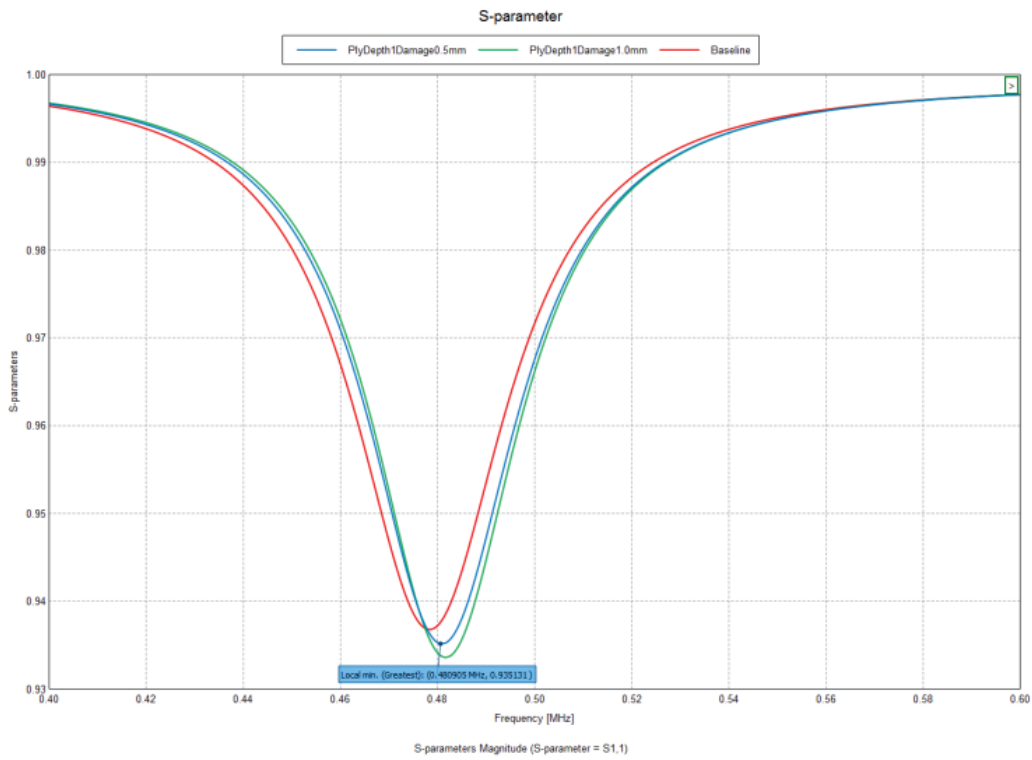


Figure 6.15. Frequency zoomed in on the first resonance shown in Figure 6.14.

Electric field and magnetic field maps were generated as part of the computational solution to visualize the field penetration into the CFRP substrate. Figure 6.16 presents a cross sectional visualization of the computed electric

field residing on a SansEC sensor placed above an un-damaged CFRP substrate. The top most horizontal line with the red square is the interrogation loop antenna used in the simulation. The SansEC sensor and high permeability layer are shown just above the CFRP. In Figure 6.17, the electric field visualization depicts the SansEC sensor's electric field on a panel with a CFRP delamination just beneath the top plain weave layer. Figure 6.18 shows the electric field on a SansEC sensor with a CFRP substrate having a puncture. The electric field bulging through the bottom of the test panel is very obvious. Finally in Figure 6.19 we see the cross sectional visualization of the electric field on the SansEC sensor influenced by a void in the inner-ply layers of the CFRP substrate.

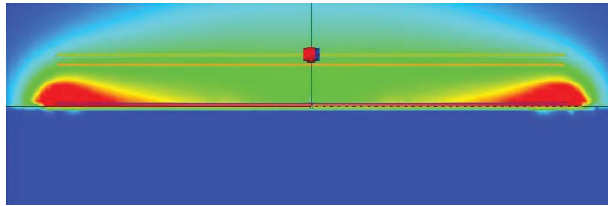


Figure 6.16. Cross-section electric field visualization of SansEC on CFRP with no damage.

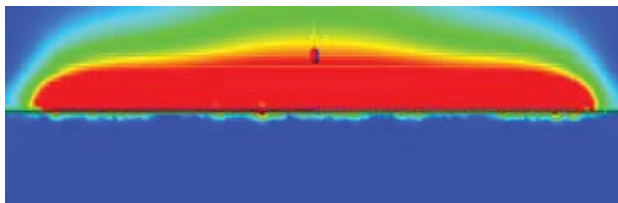


Figure 6.17. Cross-section electric field visualization of SansEC on CFRP with delamination damage.

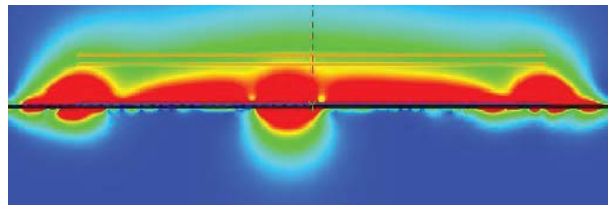


Figure 6.18. Cross-section electric field visualization of SansEC on CFRP with puncture damage.

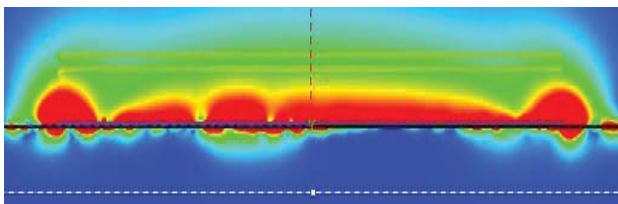


Figure 6.19. Cross-section electric field visualization of SansEC on CFRP with void damage.

This modeling confirms the feasibility of using high permeability material to control the electromagnetic field coupling between the sensor and the composite substrate. The SansEC sensor coupled to a high permeability material can effectively reduce the attenuation effect on the electromagnetic field making it possible to measure changes in the physical value of permeability and permittivity within a conductive CFRP to detect and diagnose damage in a CFRP substrate.

## 6.5 Damage on the SansEC Sensor

For aerospace smart skin applications, the SansEC sensor is expected to be placed on the surface of the composite substrate to provide the necessary lightning strike protection and exposing it to potential damage. In the event the sensor is impacted by damage, be it from lightning, hail or from other mechanical impacts, the sensor needs to be rugged enough to continue its normal function. The SansEC sensor can still function if enough isolated trace loops remain intact. If only a portion of the sensor trace is damaged, the remaining sensor traces will operate at different

resonate frequency. In addition, any damage to the sensor itself can be effectively used to detect an impact to the aerospace structure. In the operational scenario, once the damaged sensor pattern is redefined, a new baseline can be established enabling it to continue to function as a SHM sensor. Figure 6.20 shows a representative computational model of a damaged sensor, depicting one of many possible damage patterns. In this example, the sensor is damaged at one of its corners having four broken traces.

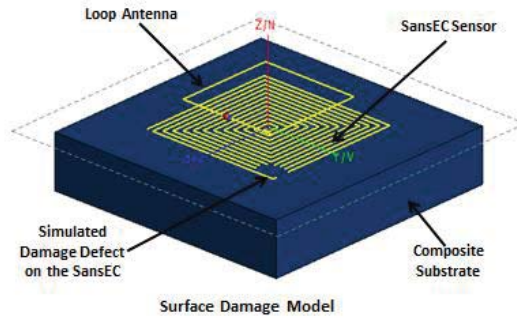


Figure 6.20. Computational model showing surface damaged SansEC sensor on a dielectric composite.

There is no single point on the sensor that if damaged will render the sensor non-functional. Each time the sensor is damaged, for example, by a puncture or partial split on the sensor body, it shifts the sensors self-resonant frequency to a new frequency range. Figure 6.21 presents the calculated reflection coefficient from the simulation modeled. The Y axis is the reflected power in terms of reflection coefficient and is unitless. The maximum value 1 represents total reflected power or 100% reflection. A minimum value 0 would indicate no energy reflected. The x axis shows the reflection coefficient as a function of frequency in Megahertz. The resonant frequency has shifted from 52.8571 MHz (depicted by the resonance on the left, labeled showing frequency and amplitude) to 112.374 MHz after the damage to the sensor (depicted by the resonance on the right, labeled showing frequency and amplitude).

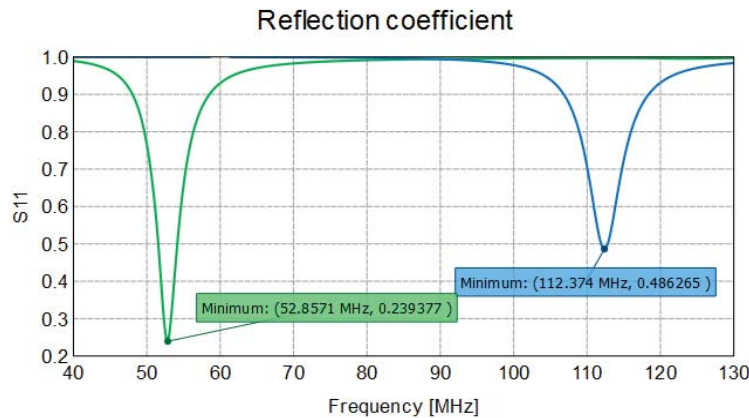


Figure 6.21. S-Parameter plot depicting resonances for a SansEC sensor with and without damage.

## 7.0 SANSEC EXPERIMENTAL MEASUREMENT RESULTS

The experimental SansEC sensor research was conducted in the NASA Langley HIRF Laboratory. The laboratory has three network analyzers that together cover frequency ranges from 10 kHz to 50 GHz. Figure 7.1 illustrates an Agilent E8364C Performance Network Analyzer (PNA) used in a system to interrogate a SansEC sensor. The PNA

is a vector network analyzer capable of generating and measuring the frequency, magnitude, and phase of an electromagnetic wave. It is shown here connected to a near-field square loop antenna.<sup>[40]</sup> The loop antenna is used to radiate or “interrogate” the SansEC sensor with a broadband continuous wave (CW) frequency sweep from the network analyzer and then used to “listen” or receive the electromagnetic response from the SansEC sensor.

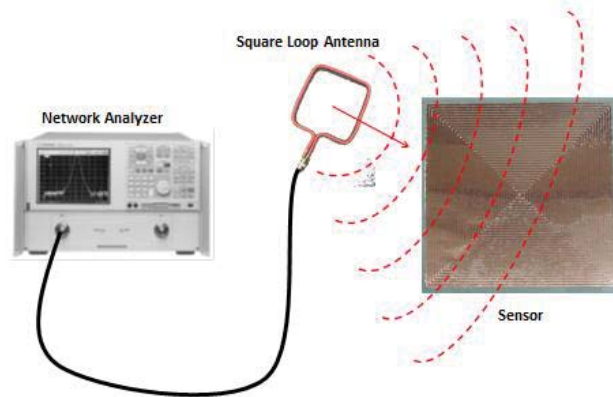


Figure 7.1. RF Network Analyzer connected to loop antenna illuminating a SansEC Sensor.

The transmitted energy from the loop antenna establishes the sensors’ self-resonate state in a wireless, passive mode. The operational bandwidth of the resonant response comprises both fundamental and harmonic resonances dependent on the geometry of the SansEC sensor and associated substrate under test. The loop antenna is coupled to the SansEC sensor through its magnetic near field creating induced currents in the SansEC sensor. At resonant state, the energy absorption of the SansEC sensor reaches its maximum value. The return loss S-parameter,  $S_{11}$ , is the reflection coefficient and is displayed on the network analyzer as a function of frequency. The resonant frequencies of the sensor are indicated by the minimum amplitudes of the reflection coefficient at the terminals of the loop antenna. Figure 7.3 is an example of an S-parameter plot and shows the resonance signature of a representative SansEC sensor operating in Free Space (green trace) and the same SansEC sensor placed on the surface of an undamaged dielectric composite substrate (blue trace). Note the 14 MHz frequency resonance shift occurring on the blue curve as a result of the SansEC sensor operating on the dielectric composite substrate.

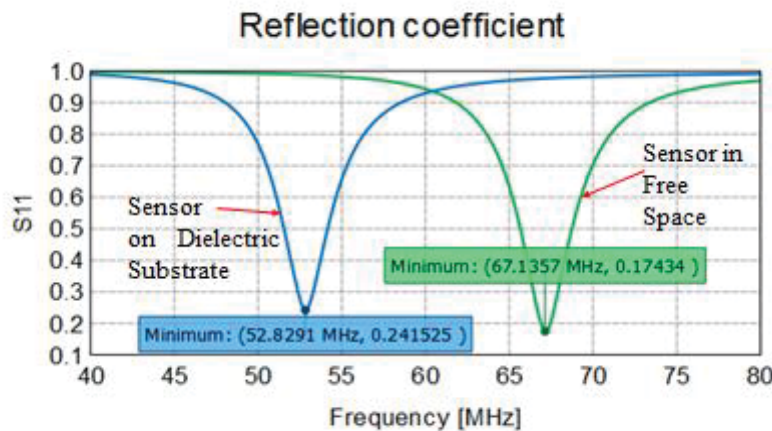


Figure 7.3. S-Parameter plot depicting resonances from two SansEC Sensor experiments.

## 7.1 Magnetic Field Response Recorder

The SansEC sensor can also be interrogated by means other than with a Network Analyzer. A NASA Langley developed magnetic field response recorder has been used extensively in previous SansEC research studies. It is a user friendly programmable self-contained portable unit to power and interrogate SansEC sensors and any other

passive inductive-capacitive sensors. Within a prescribed frequency range, the response recorder produces a sequence of magnetic fields on specific harmonic frequencies that are used to power the sensors that in-turn respond with their own magnetic fields. With appropriate bandwidth design, multiple sensors can be powered and interrogated using the same response recorder. A picture of the response recorder unit is shown in figure 7.4.



Figure 7.4. Magnetic field response recorder unit.

The basic function of the response recorder is to transmit a magnetic field harmonic to power the sensor, switch to a receiving mode and then rectify and store the magnetic field response amplitude from the sensor. For each harmonic, an antenna electrically coupled to an oscillating current (whose frequency is that of the harmonic) produces an oscillating magnetic field. Figure 7.5 illustrates a schematic of the control logic and antenna signals during transmission and reception. During transmission, the microcontroller places an antenna into transmission mode and submits a binary code to the frequency synthesizer. The frequency corresponding to this code is stored. The synthesizer converts the code into a square wave whose frequency is dependent upon the code. A high-speed amplifier then amplifies the square wave. All frequencies that are higher than the prescribed frequency are then attenuated using a low pass filter. The signal is then applied to the antenna for a prescribed number of cycles of the wave. The signal to the antenna results in a time varying magnetic field. When the cycles are completed or after a set time duration is completed, the microcontroller switches the antenna to a receiving antenna. During the transmission, the magnetic field response sensor is being electrically excited. The sensor's magnetic field decays when the antenna is placed in the receiving mode. This interrogation technique provides an alternative method to network analysis and may be beneficial for some applications.

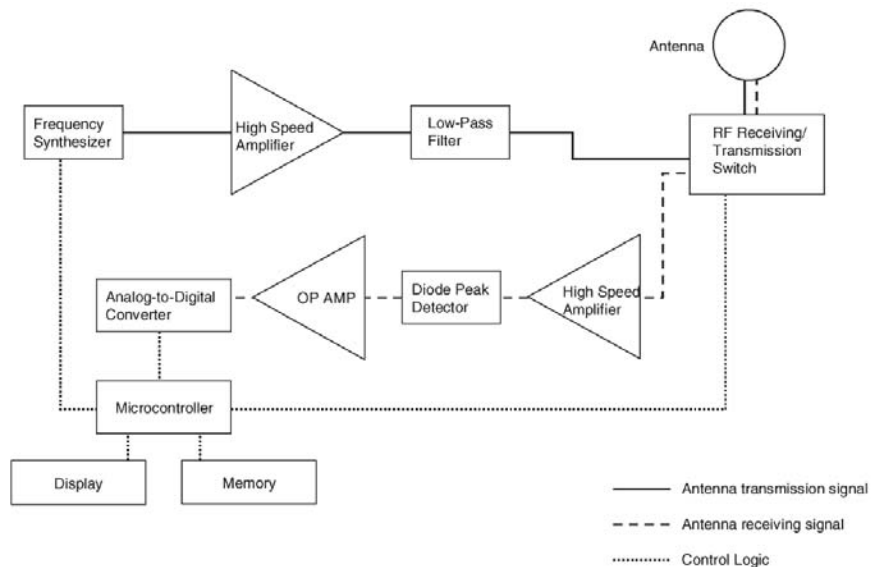


Figure 7.5. Schematic of control logic and antenna signals of magnetic field response recorder unit.

The magnetic field response recorder adopts a transmission and reception interrogation method, which is illustrated in figure 7.6. In transmitting stage, the response recorder first generates a signal lasting for  $N$  cycles through the frequency synthesizer and high speed amplifier circuit, which drive the antenna to generate oscillating magnetic fields on the corresponding frequency. The sensor captures energy from the oscillating magnetic field, goes into an external driven resonant state, and stores a portion of energy within the sensor in form of magnetic field and electric field. Then, the response recorder turns off the signal and switches to listening model. Without the external driving magnetic field, the sensor turns to a damped resonant state which generates a decaying oscillating magnetic field. The sensor-produced magnetic field is captured by the response recorder's antenna and the damped resonant signal is obtained from which the sensor resonant parameters such as amplitude and resonant frequency, can be calculated. The response recorder uses a frequency sweeping method to generate a series of transmitting signal and then it measures and compares the response amplitude of the sensor. The frequency that generates the highest response amplitude on the sensor is the corresponding resonant frequency, which can be accurately measured with this "transmission-reception" method.<sup>[41]</sup>

One clear advantage of this "transmission-reception" method is the high measurement speed and limited amount of electromagnetic emissions radiated during the transmission. For the measurement where the sensor resonant frequency range is pre-determined, the response recorder can complete the measurement in several transmission-reception cycles, which is much faster than the traditional impedance measurement instrument such as network analyzer.

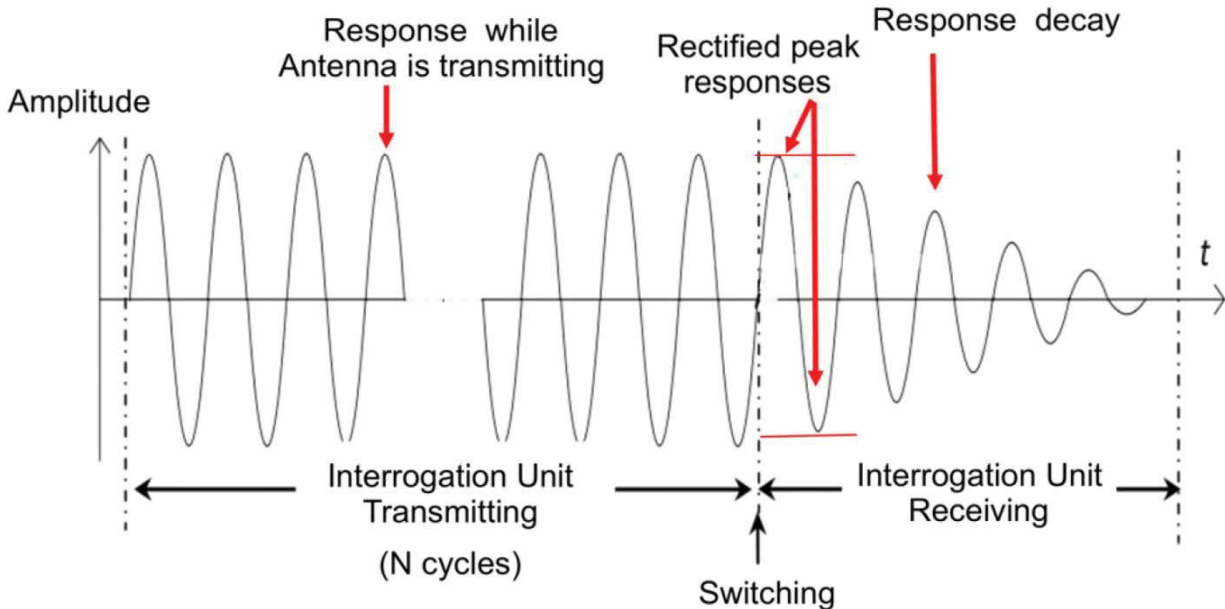


Figure 7.6. Signal sequence of transmission and reception interrogation method.

## 7.2 Experimental and CEM Parametric Study on Square SansEC Configurations

Eight planar square SansEC resonant spiral sensors were fabricated and characterized using a network analyzer. These experimental measurements were used to verify and validate equivalently modeled sensors simulated in the FEKO computational electromagnetic code. The sensors varied in size from 2 to 9 inch squares as depicted in Figure 7.7. The fabricated sensors were made from copper metal foils that had a thickness of 1.25 mils. Each sensor consisted of a copper metal trace that formed a continuous square spiral that started at the center and ended at an outer corner. The copper traces were 93.75 mils wide with a gap between the spiral traces of 31.25 mils. The copper metal foil trace of each individual sensor was encapsulated within a low dielectric 30 mil thick plastic clear film lamination.

An Agilent E8364C 10 MHz to 50 GHz Performance Network Analyzer (PNA) system was used to measure the  $S_{11}$  of each of the eight test sensors. After calibration, port 1 of the network analyzer was connected to a four inch square loop antenna, which illuminated the sensor-under-test with a broadband frequency swept electromagnetic

field from 10-300 MHz. The transmitted energy from the loop antenna was incident upon the sensor-under-test and excited resonant modes in the sensor. The sensor response was received through the same loop antenna and 10001 data points were recorded. Figure 7.8 presents experimental measurement S11 data plots for 2" thru 9" SansEC sensors. The y axis is S11 in dB and the x axis shows the frequency in MHz. The resonant structure and number of detectable resonates varies significantly from one sensor to another. The resonant harmonic bandwidth is shown to decrease with increasing sensor size.

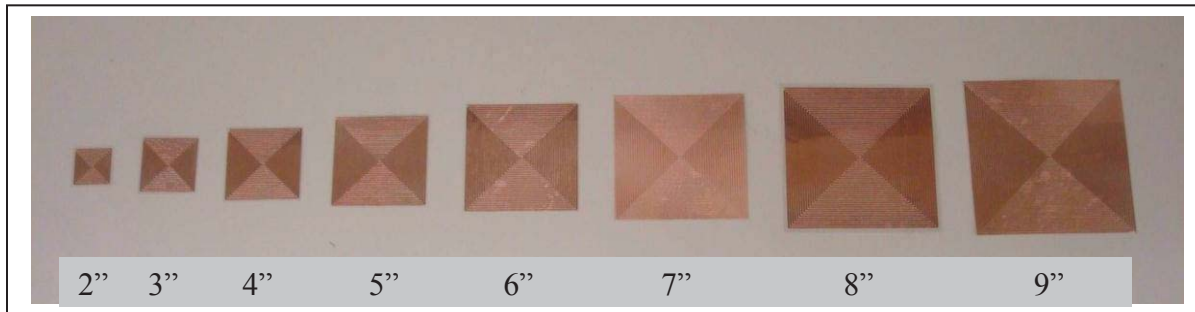
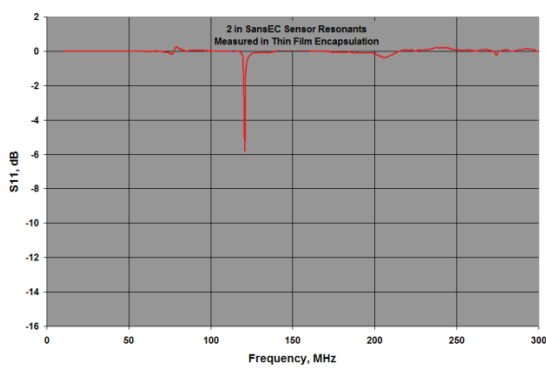
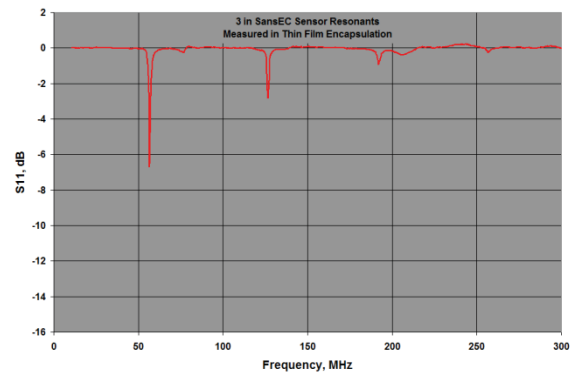


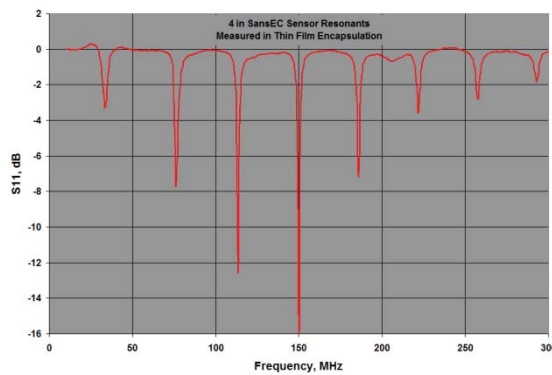
Figure 7.7. A series of square spiral resonant SansEC Sensors.



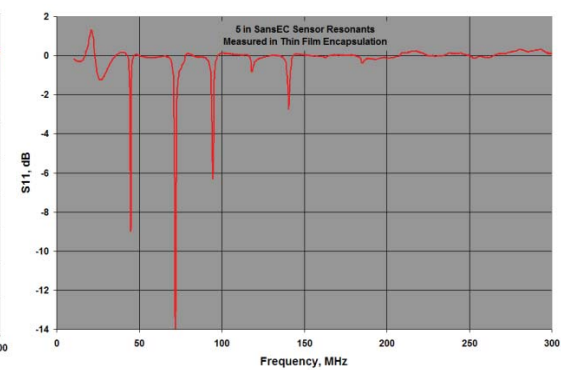
(a) 2" SansEC Sensor.



(b) 3" SansEC Sensor.



(c) 4" SansEC Sensor.



(d) 5" SansEC Sensor.

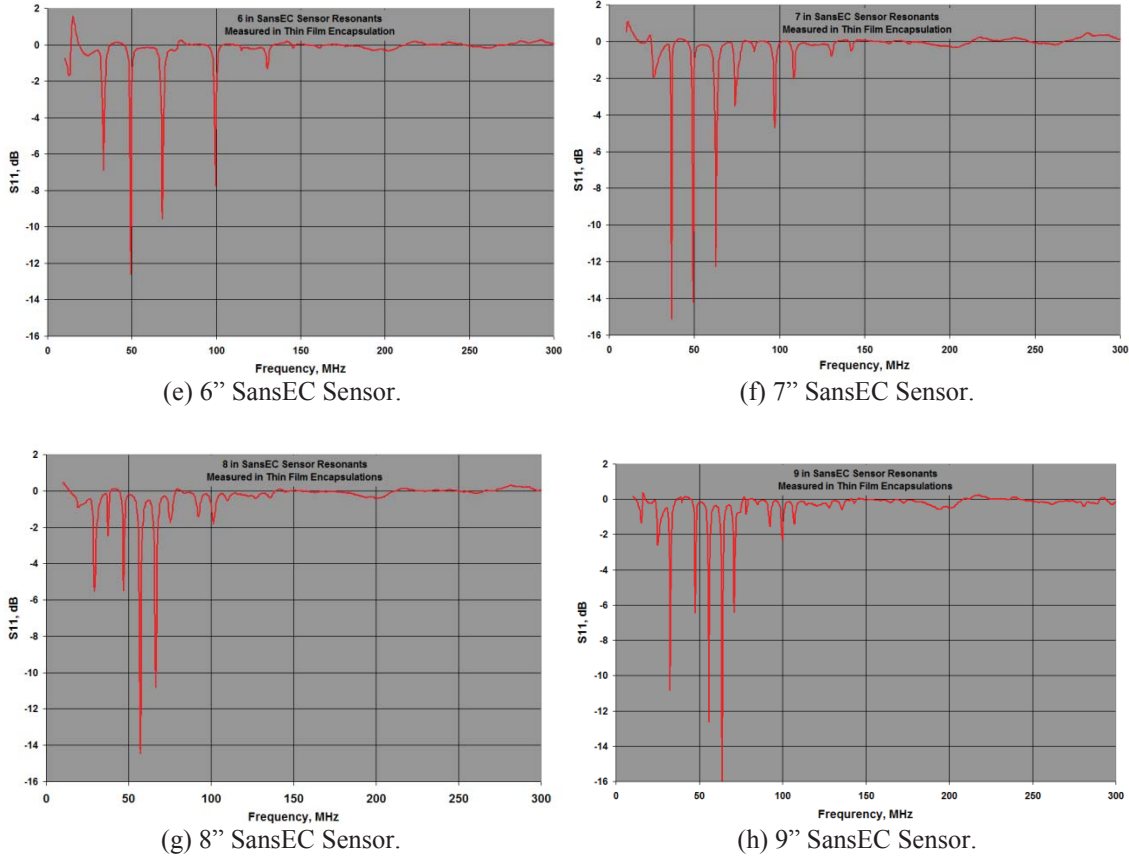
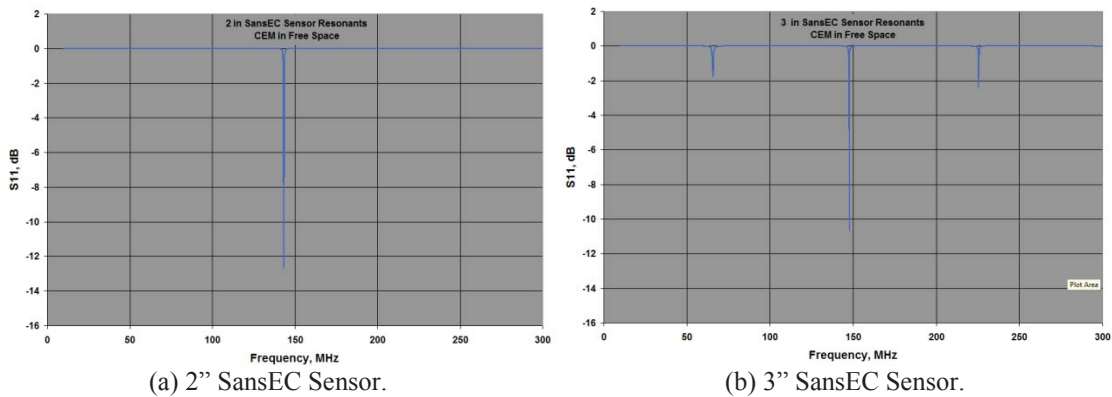


Figure 7.8. Measured SansEC Sensor resonant data. Measurement made in thin film encapsulation.

The same eight square SansEC sensor geometries were modeled in the FEKO computational electromagnetic software to calculate their free space resonant response. The CEM simulation models did not have the 30 mil thin film dielectric used in the experimental measurements to encase the sensors. Figure 7.9 present the CEM measurement S11 data plots for 2 inch thru 9 inch SansEC sensors. The y axis displays the S11 amplitude in dB and the x axis shows the frequency in MHz. The resonant structure and number of detectable resonates again varies significantly from one sensor to another as in the experimental data. The resonant harmonic bandwidth also decreases with increasing sensor size following the same trend as observed in the experimental measurements. The frequency between harmonics is directly related to the overall length of the sensor trace. Increasing the length of the sensor will correspondingly reduce the frequency span between harmonics.



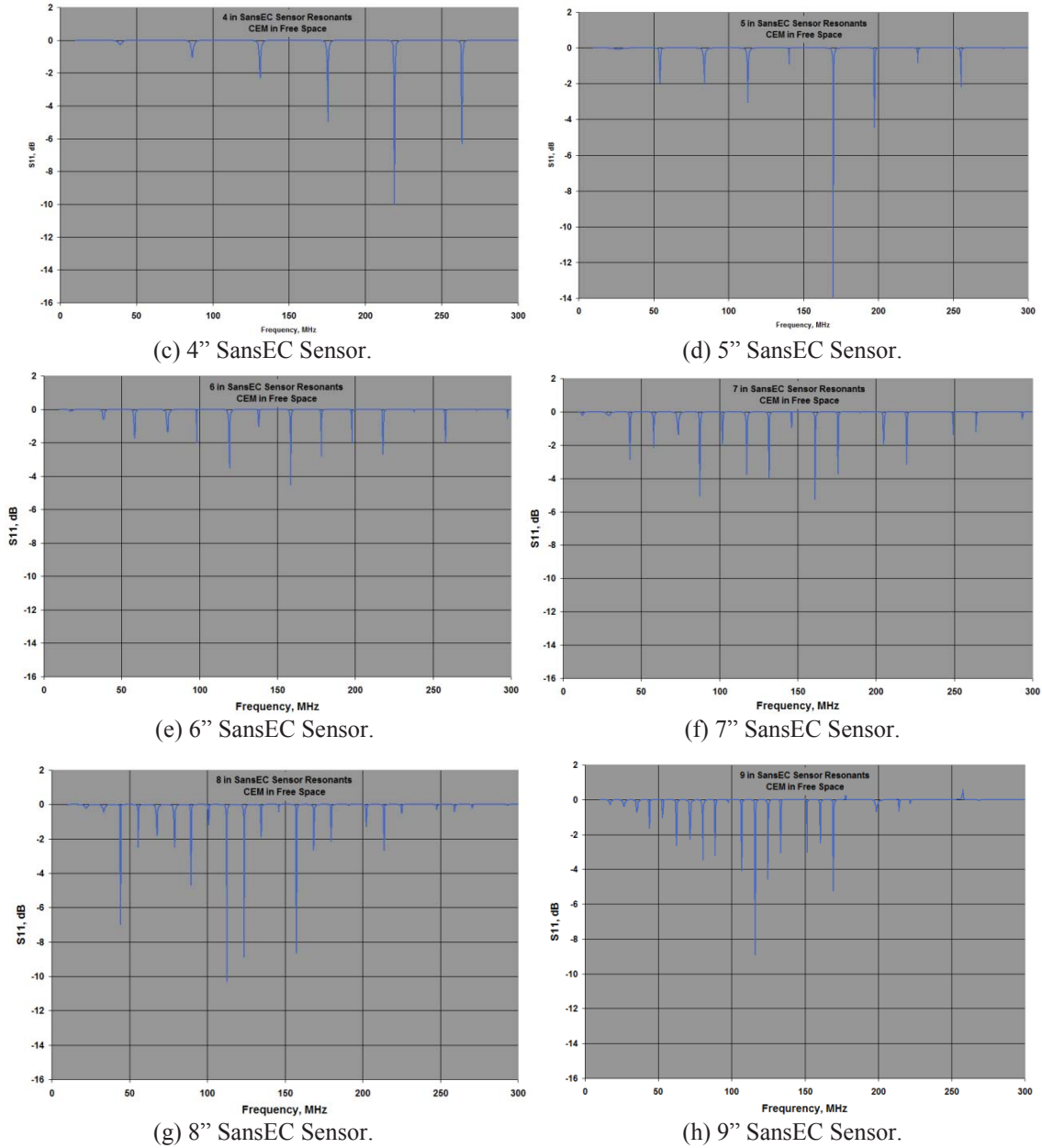


Figure 7.9. Computational SansEC Sensor resonant data. Calculation made in free space.

A side by side comparison of experimental and CEM measurement data for a 6 inch SansEC sensor on a .25" thick fiberglass substrate is shown in Figure 7.10. The x-axes represent the frequency (MHz) and the y-axes represent the  $S_{11}$  magnitude (dB). The red curve is the experimental data and blue curve is the CEM data. The two curves show some similarity in harmonic bandwidth but do not appear at first look to have a close correlation. However, these results do indicate the exactness necessary to develop comparison measurement data for resonant devices such as SansEC sensors. The sensitivity of the SansEC sensor response requires exact precision between the comparison methods to achieve reasonable correlation. The CEM model did not account for the laminate dielectric properties of the encapsulated sensor in the experimental measurement. The loop antenna parameters (size, standoff distance and impedance) were not tightly matched between the CEM and experimental measurements and have a significant effect on the overall resonant response. Non isotropic properties in the fiberglass substrate in the experimental measurement could also cause differences in the two patterns. This comparison was conducted as a quick look and was not conducted to the necessary exactness to achieve a high correlation. Future modeling efforts will begin

exploring more quantitative approaches that are expected to bring the experimental and CEM data in better agreement, but require substantial more preparation in carrying out the study.

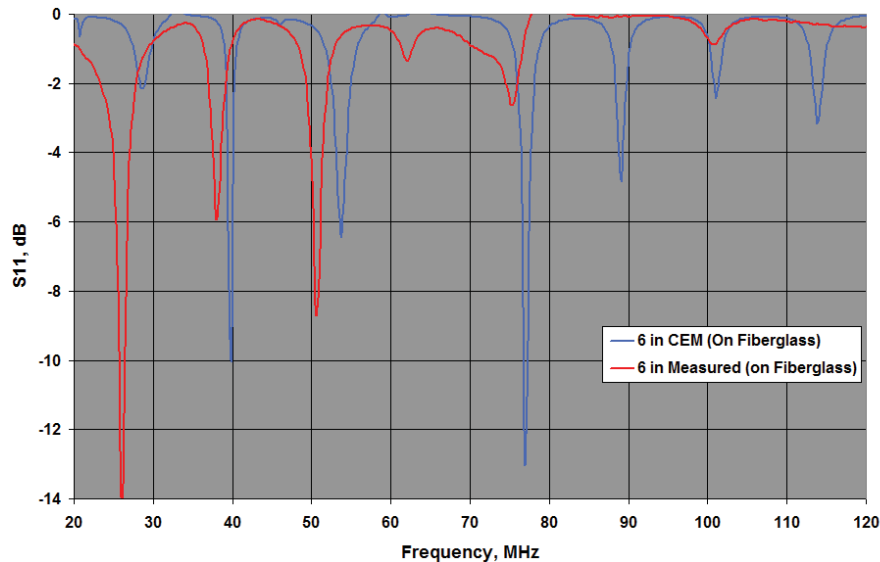


Figure 7.10. Comparison of calculated and measured resonant data for a 6 inch SansEC Sensor on a fiberglass substrate.

To improve correlation between CEM modeling and experimental measurements further refinements are needed. For very accurate computational models it is not sufficient to model the dielectric as an ideal dielectric. Not only is it critical to account for the actual dielectric value, but the dielectric is complex so the real and imaginary parts both play a role. The value of the dielectric storage component (the real part) and the value of the dielectric loss component (the imaginary part) must both be accurately accounted. This can be done by inputting the known values for the dielectric permittivity and the loss factor into the computational software. The loss factor can especially play a significant role in the amplitude response. The known values may be acquired through existing published data on the dielectric material or through direct electromagnetic material properties measurements. If published data or direct properties measurements are unavailable, then a well-designed parametric study must be embarked upon. In the parametric study, incremental changes in the values of the dielectric constant, both real and imaginary, should be run on the computational model. This will produce a family of curves representative of the effects in frequency and amplitude of the dielectric. A best fit can then be made to experimental data that is considered accurate.

Dielectric anisotropy is another consideration in real materials. Computational models, even ones that do not assume an ideal dielectric, should also consider that in real materials it may not be the case that the dielectric value is the same in all directions (x, y, and z). Non-uniform dielectric values in a material are known as dielectric anisotropy. If it is known or suspected that a material may be anisotropic, then this factor should be accounted for. In many cases for common engineered materials this is not an overwhelming concern, but still should be considered.

Differences in the geometry of the object being computationally modeled and the actual physical object must be accounted for. Usually great care is taken to insure that the physical geometric parameters are the same. In resonant devices this is critically important. Small differences in geometry can make big differences in computational comparisons. While great care has been taken in the CAD and construction of the SansEC Sensors a parametric sweep varying certain geometric features can yield great insights as to effects on frequency and amplitude of specific feature changes. We have fabricated and compared SansEC's with radius terminated trace ends versus flat terminated trace ends, and that little bit of difference is observable in measured data as well as measured versus computed data. In the real world fabrication of SansEC sensors, technique and equipment can play a factor in geometric feature tolerances. If features are not uniform or consistent throughout the loops of the SansEC spiral in actual fabrication, then they will affect the results of physical measurements and the computational comparison.

The interrogation antenna used in the physical experiments and simulated in the CEM modeling should match as close as possible. The antenna impedance, alignment and standoff distance are all critical factors that will influence the accuracy of the comparison. Measuring the actual antenna impedance and inputting that impedance into the simulation will further improve the comparisons. The SansEC sensor is asymmetric and chiral in nature and as such is sensitive to alignment and positioning. The standoff distance between the antenna and sensor will influence the electromagnetic coupling and greatly affect the sensor response characteristics. Future research to improve comparative data will need to carefully control all the parameters mentioned.

### 7.3 SansEC Experiments on Carbon Composite Materials

Physical experiments were conducted on CFRP substrates as a means to iterate proof of concept designs capable of measuring defects in composite substrates and to validate the CEM simulations to enable improved designs from further iterations in a feedback loop fashion. The first set of experiments were conducted to establish the efficacy of our approach using a high permeability material placed beneath the SansEC sensor and above the CFRP composite as a means to control the electromagnetic coupling into the CFRP and enable the sensor to generate a resonant response. Figure 7.11 a) show a photograph of the actual experimental setup used to establish efficacy of the mu metal approach. A schematic of the configuration is presented in Figure 7.11 b). In this experiment, the magnetic field response recorder was used to acquire the resonant frequency response. The magnetic fields produced by the sensor in the self-resonant state are captured in the time domain and are transferred into the frequency domain to obtain the sensor's resonant frequency response. In this experiment, the area of high permeability material used beneath the SansEC sensor was varied from full coverage, to half coverage and again to 20% coverage to study the coupling effect on the sensor's resonant response. The sensor area that was not covered by the high permeability material had a thin dielectric layer to electrically isolate the CFRP substrate from the SansEC sensor. The experimental measurement results showing the sensor's resonant frequency response are plotted in Figure 7.12. The resonant amplitude is shown on the y axis in dB. The frequency is displayed on the x axis in MHz. The red curve represents the resonant response collected with the high permeability material fully covering the surface beneath the sensor, the blue curve is 50% coverage and the green curve depicts the measurement data for the 20% coverage test. The data indicates increasing the amount of coverage increases the amplitude of the resonant response.

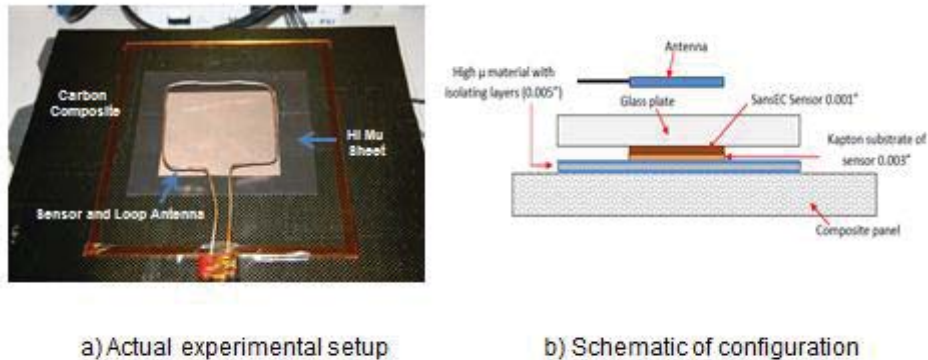


Figure 7.11. Experimental setup of SansEC sensor on carbon composite substrate.

As discussed in section 6.3, the high permeability material is used to concentrate a magnetic field flux around the sensor to allow it to sustain a self-resonate state. The high permeability material coverage area influences the impedance matching between the sensor and CFRP substrate and controls the magnetic field coupling into the CFRP to increase the depth of the coupled magnetic field. The data curve shows the obvious tradeoff with the varying area of coverage. The right balance of coverage would allow the sensor to self-resonant and yet provide enough coupling into the CFRP for measurement purposes. The larger the area of coverage, the stronger the sensor's signal response at the risk of having less magnetic field coupling into the CFRP for measurement purposes. Less area of coverage results in a lower sensor response, but allows for more of the existing magnetic field flux to be coupled for measurement purposes. This experiment verifies the use of high permeability materials to improve the resonant

response for CFRP applications, but also shows the balance required to preserve a portion of the energy in the form of oscillating magnetic field strong enough to keep the sensor resonant, and at the same time, have an acceptable penetration depth of measurement.

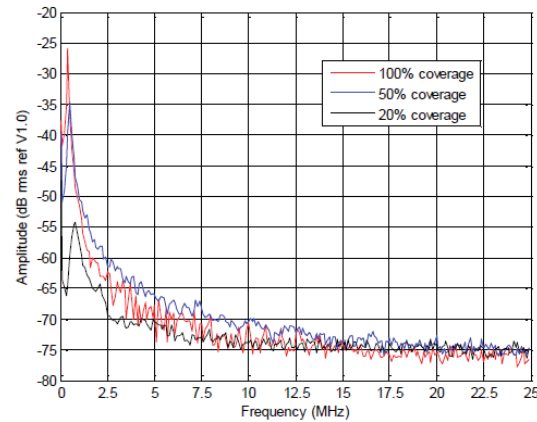


Figure 7.12. Experimental results of SansEC sensor on carbon composite substrate.

The magnetic field coupling between the sensor and composite substrate is a trade-off requiring an optimized engineering design. For measurement purposes, strong magnetic field coupling is needed to allow the field to penetrate as deeply as necessary into the composite substrate. However, if the coupling is too strong, it will render the sensor's response to be non-detectable. In order to maintain a sensor response with a reasonable signal-to-noise ratio, the coupling ratio must be controlled to an acceptable tolerance. The strategy of using high permeability material covering the sensor with appropriate area percentage is an effective solution to this problem. Further research is needed to achieve the proper balance to optimize this SansEC application.

#### 7.4 Damage Detection Experiments on Carbon Fiber Reinforced Composite Substrates

In conducting research with SansEC sensors for damage detection, diagnosis, and prognosis, the use of damage reference standards in setting up equipment is particularly important since signals are affected by many different variables and slight changes in equipment setup can drastically alter the appearance of a signal. As with most other nondestructive evaluation methods, the most useful information is obtained when comparing the results from an unknown object to results from a similar object or baseline with well characterized pristine features as well as known defects. In almost all cases initial inspection procedures require the equipment to be configured using reference standards.

For crack detection, voids, delamination, thinning, erosion, corrosion, and other material damage, reference standards are used to setup the equipment to produce a recognizable signal or set of signals from a defect or set of defects. In many cases, the appearance of a test signal can be related to the appearance of a signal from a known defect on the reference standard to estimate the size of a defect in the test component. Signals that vary significantly from the responses produced by the reference standard must be further investigated to determine the source and nature of the signal.

The reference standard should be of the same material as the test article. If this is not possible or practical, it should be of material that has the same electrical conductivity and magnetic permeability. Component features (material thickness, geometry, etc.) should be the same in the reference standard as those in the test region of interest. If the reference standard is the type with seeded fault defects, these defects should be as representative of actual defects in the test component as possible. The closer the reference standard is to the actual test component, the better. However, since cracks and corrosion damage are often difficult and costly to produce, artificial defects are commonly used. Narrow notches produced with electron discharge machining (EDM) and saw cuts are commonly used to represent cracks, and drilled holes are often used to simulate voids, porosity, and corrosion pitting, and inserts of Teflon or Kapton films to simulate layer separations and delaminations.

Common reference standards include:

- Dielectric standards (fiberglass composites).
- Semi-Conductive standards (carbon composites).
- Conductivity standards.
- Flat plate discontinuity standards.
- Flat plate metal thinning standards (step or tapered wedges).
- Hole (with and without fastener) discontinuity standards.

An experimental measurement based on the computational studies was conducted on the physical seeded fault test panel to demonstrate that a real SansEC sensor can detect delaminations in a real CFRP panel simulating an aircraft composite skin. A photograph of the test setup showing the loop antenna, sensor and perforated high permeability material layer is presented in Figure 7.13. Figure 7.14 presents the reflection coefficient measurement collected from the network analyzer for the baseline and 3 different delamination sizes. The y axis represents the reflection coefficient in dB and the x axis shows frequency in MHz. The most significant performance indicated the sensor could detect a 3 mil thick delamination down to the 5th ply of a carbon fiber composite with sufficient signal margins to indicate that the frequency resonance had shifted approximately 100 KHz between the baseline measurement (no delamination) and the measurement incorporating the delamination.<sup>[42]</sup> From the above results, it can be seen that the SansEC sensor with a high permeability material layer produced resonant responses, which confirmed that the high permeability material can be used on the conductive composite surface to reduce the effective attenuation and increase the sensor response amplitude. Even though the feasibility is confirmed, it is apparent from the experiment that more seeded fault test panels will be needed to thoroughly investigate the electrical characteristics of composite damage once an optimized SansEC CFRP is developed to achieve robust SansEC diagnostic capabilities.

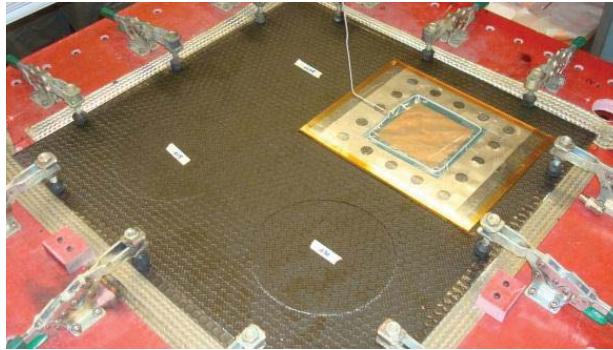


Figure 7.13. Experimental test setup showing the loop antenna, sensor and perforated high permeability material.

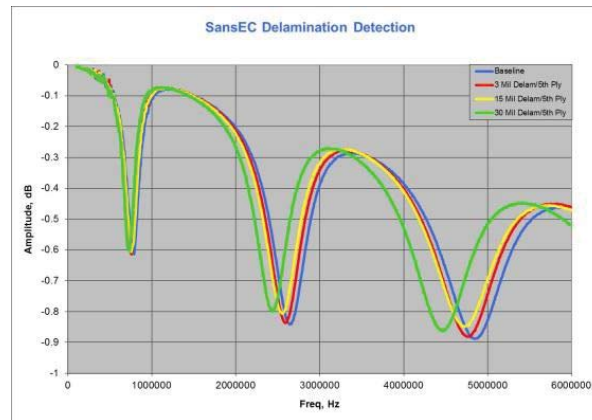


Figure 7.14. Reflection coefficient data from a baseline and 3 different delamination sizes.

## 8.0 SANSEC SENSOR LORENTZ FORCE EFFECTS ON LIGHTNING ATTACHMENT

The Lorentz force law is critical to understanding how SansEC sensors can function as an advanced lightning strike protection layer on aerospace vehicles. When a lightning leader propagates through the atmosphere in the vicinity of an aircraft, the lightning electromagnetic emissions generated from the moving electrical charge will radiate the aircraft surface long before the strike to the aircraft can occur. As the lightning leader propagates closer to the aircraft, the radiated emissions at the aircraft will grow stronger. The frequency bandwidth of the lightning radiated emission is generally accepted to be from a few Hertz to hundreds of MHz. SansEC sensors placed on the surface of the aircraft which are designed to resonant in the lightning spectrum frequency band will be passively powered by the external oscillating magnetic field of the lightning radiated emission. The SansEC sensor will then resonant and generate its own oscillating magnetic and electric fields. Figure 8.1 illustrates the magnetic and electric field on a selected point  $X$ , which is within the electromagnetic field generated by the self-resonant sensor. When the sensor resonates, it creates an electro dynamic process with time and space varying current and charge distribution along the sensor trace. At a specific moment, we choose an infinite small segment of the sensor trace,  $d\vec{l}$ , where the current vector is  $\vec{J}_f$ , as illustrated in Figure 8.1. Then, the magnetic field  $\vec{B}_X$  at the  $X$  point is the integration along the sensor trace  $l$ , as shown in the following equation:

$$\vec{B}_X = \frac{\mu_0}{4\pi} \int_0^l \frac{\vec{J}_f \times \vec{r}}{r^2} d\vec{l} \quad \text{Eq. 8.1}$$

where,  $\vec{J}_f$  is the current vector at the infinite small segment of sensor trace  $d\vec{l}$ ;  $\vec{r}$  is the vector from the sensor trace segment to the position of point  $X$ .

Correspondingly, the electric field at  $X$  point is shown as following:

$$\vec{E}_X = \frac{1}{4\pi\epsilon_0} \int_0^l \frac{\rho \times \vec{r}}{r^2} d\vec{l} \quad \text{Eq. 8.2}$$

where,  $\rho$  is the charge density along the sensor trace segment  $d\vec{l}$ .

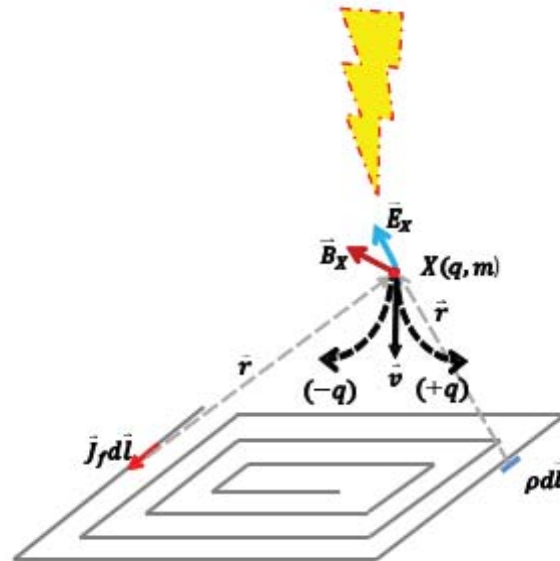


Figure 8.1. Sensor generated magnetic and electric field and Lorentz Force on charged particle.

Suppose at  $X$  point, a particle carrying charge  $q$  is moving toward the sensor surface with a speed of  $\vec{v}$ , the Lorentz force on the particle can be expressed in the following equation (in SI unit system):

$$\vec{F} = q(\vec{v} \times \vec{B}_X + \vec{E}_X) \quad \text{Eq. 8.3}$$

Under the Lorentz force, the particle will change its direction of movement following a superposition path of a circle, which is the effect of magnetic field, and the gradient direction of the electric field. The charge (positive or negative) of the particle will determine the direction of the force affecting the particle. The radius of the circle from magnetic field effect  $R$  can be calculated in the following equation:

$$R = \frac{m\vec{v}^2}{\vec{F}} \quad \text{Eq. 8.4}$$

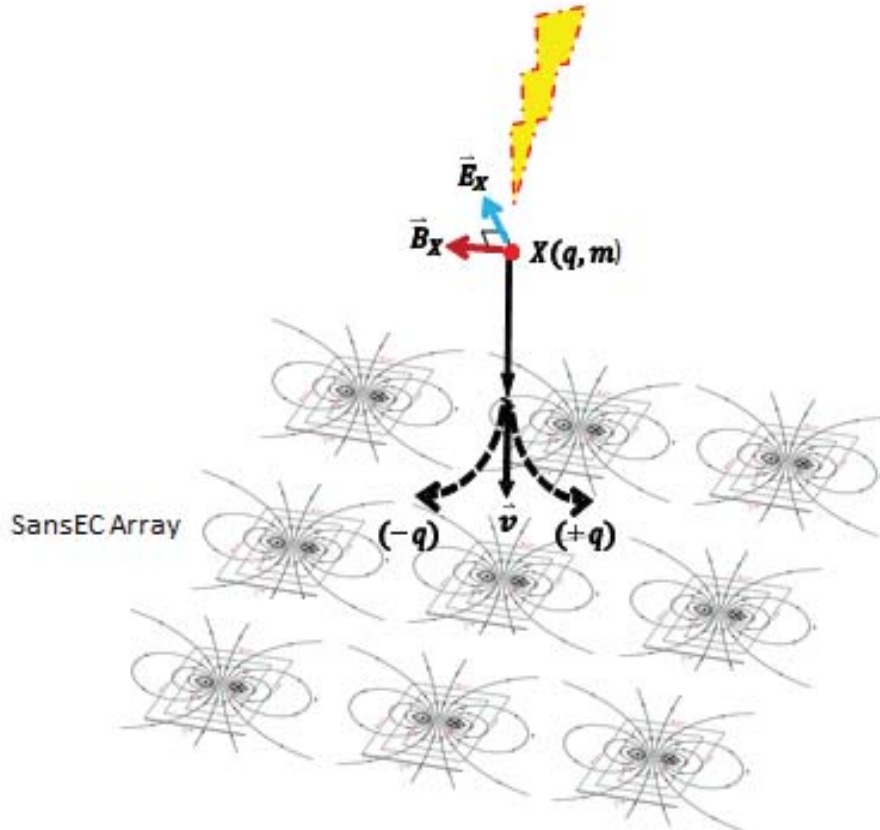


Figure 8.2. Sensor Array with combined magnetic and electric fields depicting the Lorentz Force on charged particle.

Here the superimposed magnetic fields of the collective array combine at a distance to effect the charged particle  $X(q,m)$  of the lightning stroke with a combined Lorentz force. This mathematical frame work establishes the potential usefulness of engineering Lorentz Force effects to alter the lightning attachment location using SansEC sensors to steer an oncoming attachment away from flight critical components. The time lapse photograph presented in Figure 8.3 shows a laboratory lightning generated waveform attaching to a SansEC array LSP FRC test panel. An interesting phenomenon is occurring at the attachment point that manifests in such a way to wiggle the arc column above the surface of the SansEC sensor trace. This phenomenon is believed to be a result of the Lorentz force effect caused by the SansEC sensor. Pursuing advanced LSP designs to take advantage of Lorentz force effects could provide revolutionary new approaches to manage or control lightning attachments for future composite aircraft.

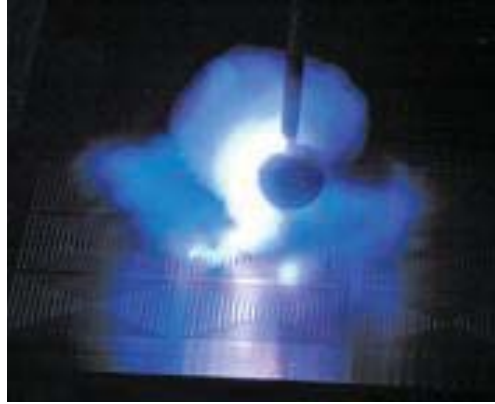


Figure 8.3. Time lapse photograph a lightning strike on a SansEC Array LSP FRC test panel.

### 8.1 SansEC Sensor's Influence on the Electrical Breakdown of Air

As discussed in the previous section, Lorentz force effects will influence the direction and momentum of the lightning attachment and influence where the strike point occurs on the aircraft. After the initial strike attachment occurs, the electrical breakdown voltage between the lightning leader and the aircraft will determine the next swept stroke attachment location. An aircraft that has arrays of SansEC sensors covering the fuselage could provide a unique means to establish where the electrical breakdown of air occurs to guide the swept stroke lightning attachment to a predetermined destination. The frequency band of operation and Q factor of the SansEC sensor can be designed to increase the electrical potential along the resonating sensor trace to be much higher than the external driving source potential coming from the induced electromotive force of the lightning leader radiated fields. The strong electrical field at the sensor location would help achieve the air breakdown threshold to establish the swept stroke location and improve the probability of attachment at these locations. The distance between the lightning leader and the sensor surface at the moment the sensor contributed air breakdown happens is influenced by both the electrical characteristics of the sensor and the lightning leader itself. The SansEC sensor's active contribution to the air electrical breakdown condition creates the least resistive path for the lightning leader to steer it to that location. Time lapse photographs of coronas on SansEC LSP test panels are shown in Figure 9.28

The traditional approach for providing LSP for composite aircraft is to cover the entire exterior surface with a conductive layer. If SansEC sensors were applied as the LSP instead of the traditional methods, the aircraft LSP design could be zoned into regions to utilize sensors with different impedances, resonant frequencies of operation and Q factor values to take advantage of Lorentz force effects and the electrical breakdown of air to establish locations with the highest probability of attachment and locations with the least probability of receiving a strike. This method of LSP could provide a significant improvement over traditional methods, especially on the fuselage where swept stroke attachments are most likely to occur.

## 9.0 LIGHTNING MITIGATION

To realize a SansEC smart skin application for composite aircraft, the sensor system must also function to mitigate lightning hazards. Today's composite aircraft perform this function by adding a thin conductor or inter woven wire to the outer layer of the carbon composite system. The LSP is designed to prevent major damage, but does not provide a means for determining the structural health of the vehicle. SansEC resonant sensors are uniquely suited to perform both functions: to provide the necessary lightning strike protection to prevent major damage and to enable sensing of the health state of the composite system.

To show compliance with FAA certification airworthiness standards, LSP composite substrate systems are subjected to lightning direct-effect electrical waveforms to determine how well they prevent damage in the composite substrate. To evaluate post strike performance damage metrics for SansEC LSP designs, relative comparisons were needed with a legacy FAA certified LSP solution as a baseline metric for acceptable damage performance. The

Boeing Company was contracted to develop the technical procedures and guidance documentation to facilitate a test method for conducting universal common practice lightning strike protection procedures and lightning strike damage assessments. The procedures were developed to ensure conformity in lightning strike protection evaluations to allow meaningful performance correlations across future data sets.<sup>[43-47]</sup> The universal common practice guidance included the definition of the legacy FAA certified LSP test article, fixturing to hold the test article and test methods used to carry out the actual lightning strike evaluations. By abiding by the universal common practice test procedures, NASA ensured the SansEC LSP performance metrics could be correlated with the performance metrics from an FAA certified LSP method. The test documentation procedures will be beneficial in evaluating emerging LSP technology, such as carbon nanotube bucky paper, graphene sheets, conductive coatings or other techniques to enable cross correlation to identify performance metrics. Descriptions of the test documents are provided in following sections.

The universal common practice procedures were demonstrated during three lightning direct effect tests at the National Technical Systems' (NTS) Lightning Technologies (LTI) facility in Pittsfield, MA. In February, 2012 over 30 different SansEC LSP designs were evaluated on FRC substrate panels to evaluate the performance of the test bed in obtaining damage mechanism data and to down select follow on designs for further testing on carbon fiber test panels. Baseline lightning test assessments were obtained for protected and unprotected CFRP test panels along with a limited set of SansEC LSP designs without mu metal in September, 2012 and again in July, 2013 with mu metal as part of the SansEC system. The lightning test bed was successfully used to capture the electrical, mechanical and thermal damage mechanism parameters during lightning strike attachment to the SansEC FRP, Baseline CFRP & SansEC CFRP test panels. Lightning test data results including damage mechanism metrics and damage assessments are presented later in this report.

## **9.1 Universal Common Practice Guide to Conduct Lightning Energy Transfer Characterizations**

Manufacturing procedures to fabricate protected and unprotected Carbon Fiber Reinforced Plastic (CFRP) test panel configurations that can be employed for the purposes of evaluating the protection capabilities of lightning strike protection materials are documented in NASA DOC-128694.<sup>[43]</sup> The composite test panels are intended to provide consistent behavior in their response to simulated lightning strikes at pre-defined levels when tested by a capable vendor according to a test procedure written to enable consistent results. It is expected that commercial vendors of existing and emerging LSP materials and concepts would use the behavior of this protected configuration as a baseline performance standard which they would try to meet or exceed.

The unprotected configuration consists of a cured CFRP laminate stack up of tape (Hexcel HexPly 8552/AS4) and fabric (Hexcel HexPly 8552 / A193-PW, 3K-70-PW) prepregs, coated with a typical aerospace primer (0.5-1.5 mils thick) and paint (4-6 mils thick) finishing scheme. The finished panels are attached to aluminum grounding bars intended to draw electrical current from the lightning attachment point to the panel edges to reach earth ground. The protected configuration contains a top LSP layer made up of Cytec Surfacermaster 905C Composite Surfacing Film above Dexmet 3CU7-100FA expanded copper foil and is included in the laminate stack up prior to cure. The laminates are to be designed per common aerospace industry practices (balanced, symmetric and sequence). The typical lightning strike panel will be quasi-isotropic in nature with a fabric ply on each side of the laminate. The laminate stack is defined as follows; 16 ply tape with 2 ply fabric (as follows):[(0/90F)/45/90/-45/0/45/90/-45/0/0/-45/90/45/0/ -45/90/45/(0/90F)].

The panels have countersunk fastening with 2 inch spacing. Each panel is fastened to four independent aluminum ground bars. Common steel or CRES fasteners are used to provide a conductive path from the panel to the frame to the test equipment ground. Figure 9.1 shows a test panel with ground bars attached.

To ensure manufacturing quality control of the CFRP tests panels, the panels must undergo nondestructive evaluation testing to quantify their pretest condition. NASA DOC-128695 defines an appropriate pre-test inspection of the panel to ensure integrity of post-strike test results.<sup>[44]</sup> This reference guidance states the cured panels will be examined with a through transmission ultrasonic (TTU) 'C' scan inspection at 5 MHz. An ultrasonic indication (flaw) is an area with ultrasonic attenuation that is at least 6dB larger than the attenuation of the adjacent areas without flaws or defects. An ultrasonic "defect" is an indication greater than 0.50 inch in diameter. Multiple



A test bed is used to secure the test article in a fixed position during test and constructed to minimize fixture-induced motion during the application of test current. The lightning test waveform is injected into the test article at the electrode with the aid of an initiator wire. Current injected into the test panel propagates to the panel and into the 4 ground bars on the perimeter of the test panel and is measured by current sensors. Additional test bed specifications will be discussed later in this paper. Figure 9.3 shows a CFRP test panel installed in the test bed. Kapton covers are used over the clamps to prevent lightning attachment to the clamps.

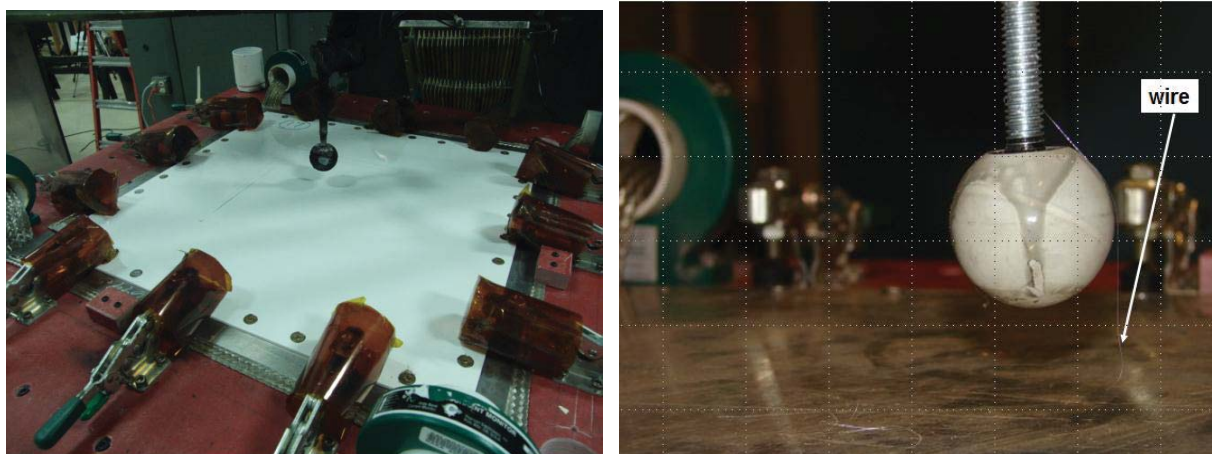


Figure 9.3. CFRP panel installed in test bed (left) and close-up view in the lightning initiator and wire (right).

NASA DOC-128697<sup>[47]</sup> defines the post-test non-destructive and destructive evaluations of CFRP test panels for the purpose of evaluating the protection capabilities of LSP materials.<sup>[5]</sup> This guidance defines pulse echo ultrasonic testing to determine the extent of non-visible damage in the post-strike CFRP test panel. Pulse echo testing should be performed on both sides of the panel. It uses a single transducer that transmits and receives longitudinal waves in the range of 0.5 to 20 MHz. An ultrasonic indication (flaw) is an area with ultrasonic attenuation that is at least 6dB larger than the attenuation of the adjacent areas without flaws or defects. Delaminations in composites are also exhibited as acoustic signal returns at depth levels less than the full thickness of a laminate.

Destructive assessment involves taper sanding of the damaged area of the panel to determine how deep the damage actually is since pulse-echo ultrasound techniques have difficulty finding damage regions laying deeper into a laminate than damaged regions laying closer to the surface contacting the ultrasonic transducer. The depth of damage provides a metric on how many plies deep into the composite will require repair, less depth corresponds to less damage and repair. The area of damage corresponds to how wide spread the surface damage is. Surface damage is often superficial damage and encompasses areas of paint blemishes or burns and does not equate directly to area in need of composite repair. Figure 9.4 shows a CFRP panel after the destructive assessment had been performed.

The final reference guidance belonging to the Universal Common Practice Guide to Conduct Lightning Energy Transfer Characterizations is the LSP Composite Substrate Test Bed Design, NASA DOC-128698. This document describes a method to acquire real time monitoring of mechanical, thermal, and electrical parameters during plasma flashover arcing events.<sup>[47]</sup> Specifications are provided to safely monitor electrical current, temperature, and mechanical shock with adequate detection thresholds to support direct effect lightning damage mechanism assessments and high fidelity damage modeling of composite structures.

The test bed implementation is necessarily subjective, but the general approach taken has been to design a test bed that provides features for testing and modeling that are as good as or better than any methods established in leading laboratories today. The instrumentation recommended was selected based on practicality and affordability for an ongoing lightning test operation. The procedures and specifications in the referenced document will enable a high degree of correlation of results between testers.

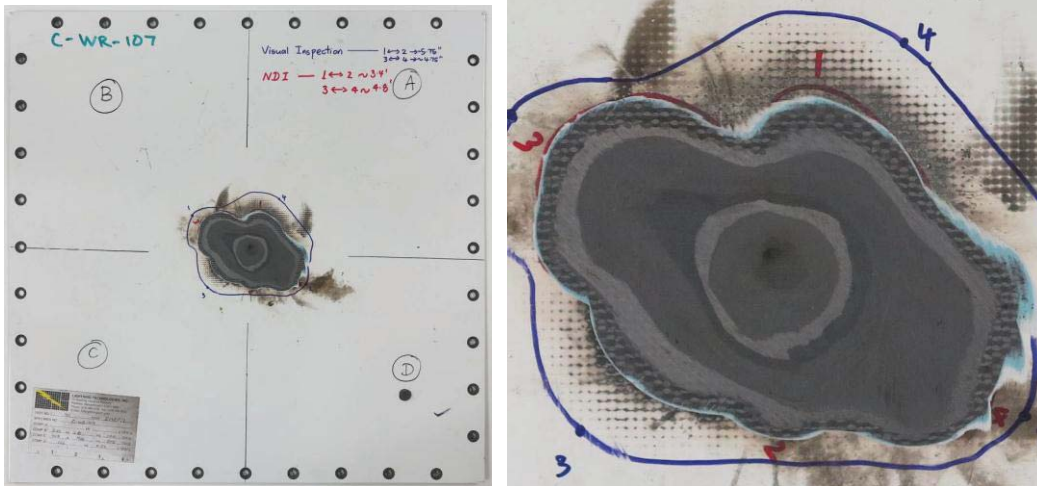


Figure 9.4. Photographs of CFRP panel after taper sanding.

The test bed fixture design allows leeway in construction provided the resulting structure has comparable rigidity and capability. The test panel is secured in position by toggle clamps which apply pressure to the panel's ground bars and ensures solid contact to the 4 grounding straps. Four Pearson 4418 Current Probes are used to monitor the electrical current on the 4 grounding straps. The test bed design allows all four edges of the test panel to be independently sensed and provides a means to study current propagation for asymmetric LSP designs. Figure 9.5(a) shows a picture of the NASA test bed assembly being used at the National Technical Systems' (NTS) Lightning Technologies (LTI) facility in Pittsfield, MA. A FLIR Systems SC645 IR camera is mounted 48 inches directly below the test panel to capture back side temperatures are shown in Figure 9.5(b). Thermal data can be used to quantify energy deposition on test panels to identify attachment location and propagation direction and provide validation data for damage computation modeling. The SC645 camera has adequate thermal range, speed and remote operation making it ideally suited to monitor back side temperatures. Mechanical displacement of the panel deflection is monitored using Keyence LK-G507 laser displacement sensors mounted 28" beneath the panel as shown in Figure 9.5(b). An accessory band pass Optical Filter (Keyence part OP-87110) is required to eliminate lightning flash interference on the optical detector. This sensor has adequate sampling speed and range resolution to capture the peak deflection and sense lower-order vibrations. The test bed design specifies up to 3 displacement sensors to allow displacement measurements from multiple locations if desired. Figure 9.5(b) shows the IR camera and laser displacement sensors mounted in the test bed.



(a) Test bed installed at LTI.

(b) IR camera and laser displacement sensors in the test bed.

Figure 9.5. Test bed fixture views.

## 9.2 Lightning Test Results on FRC Test Panels

The lightning test bed was first utilized at LTI in February, 2012 to evaluate approximately 30 different SansEC LSP designs on .25" thick standard grade structural FRC panels. The procedures defined in the universal common practice were adhered to except for the FRC panels substituted for CFRP panels and the corresponding pre and post-strike NDE assessments were not conducted. The FRC panels provided a quick and inexpensive way to check out the utility of the test bed instrumentation and provided a meaningful look at a broad arrangement of potential SansEC LSP concepts. The SansEC designs consisted of various geometric shapes and sizes, varying gap and trace widths, and varying first and second order discontinuities at the spiral corners. The geometries selected in the test matrix were taken from historical designs known to have good resonance responses and derivations from those to look for optimization trends and behaviors in the experimental data. The SansEC geometries were drawn using Autodesk AutoCAD, a computer-aided design (CAD) software tool. The CAD designs were exported to a Klick-N-Kut (KNK) machine for fabrication as shown in Figure 9.6. The resonance sensors were fabricated from adhesive backed 1.25 mil thick copper sheets. The KNK machine provided a rapid means of cutting the copper sheet for the various geometries with a high degree of accuracy and repeatability. The adhesive backing was used to secure the sensors to the fiberglass panels. The end point of the SansEC spiral trace was always positioned at the lower right corner with the trace proceeding in a clockwise manner to the center. (The panels were also oriented in the test bed so the outer end point of the sensor aligned at Channel 3). Self adhering 2" wide 1.25 mil 3M copper tape was placed around the perimeter of the sensor to form ground paths to the 4 perimeter grounding bars. The copper tape ground paths were isolated from the sensor and from each other to facilitate the independent 4 channel current measurements. The grounding configuration was designed to uncover any asymmetry in the behavior of the electric current propagation resulting from the sensor geometry. Most of the test panels were coated with aircraft primer and paint, but a few were left unpainted. A complete summary of the individual test data (pre and post panel photographs, reflection coefficient resonance response plots, electrical, mechanical and thermal data) are shown in Appendix A.

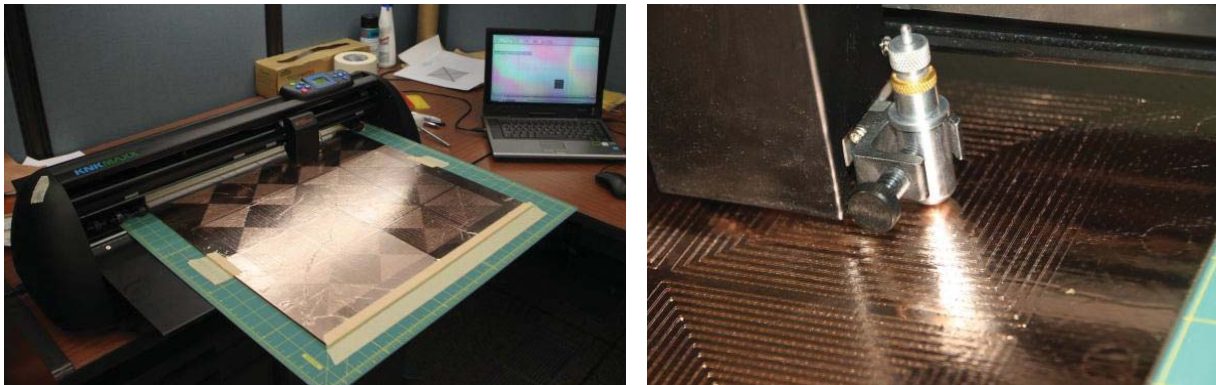
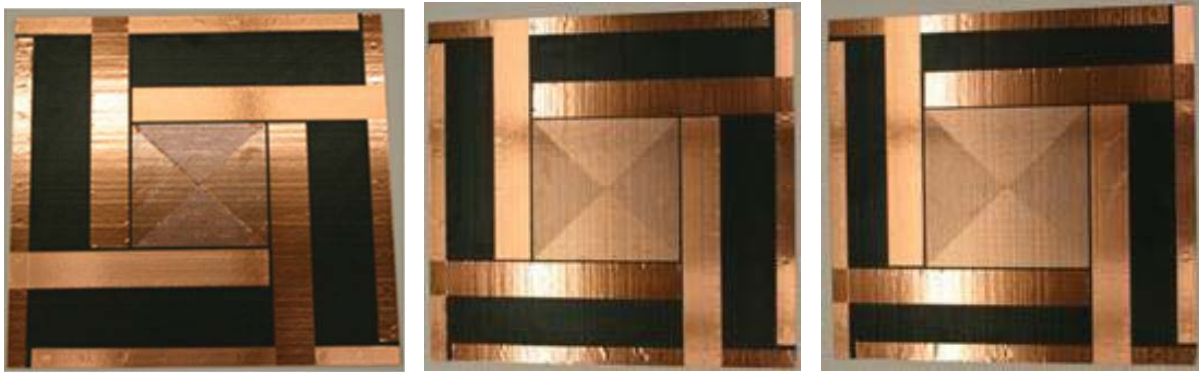


Figure 9.6. Klick-N-Kut Machine.

Figure 9.7 presents actual photographs for 3 of the lightning test panels showing details of the placement of the SansEC sensor and the ground path surrounding it before paint was applied for the 7", 8" and 9" configurations. The SansEC LSP test articles were mounted in the lightning test bed during strike to capture the induced damage mechanisms during strike. Electric currents were measured on the four sides of the test panel with Pearson 4418 Current Probes to determine the propagation direction of the electric current. The lightning electrode was positioned at the center of the test panel with the initiation wire pointing in the middle of the sensor for each test.

The test panels were evaluated at 40 kA peak current using combined component D, B and C\* waveforms based on pre-test set up calibration strikes on an Aluminum plate panel. The Component D waveform had a unipolar 40kA peak current lasting  $\leq 500$   $\mu$ sec. This waveform delivers the fast rise time, high current, high impact impulse to the test panel. The actual peak current delivered to the SansEC LSP panels were slightly less than 40 kA due to the higher impedance of the SansEC LSP FRC systems under test. Component B is an intermediate current waveform averaging 2 kA lasting  $\leq 5$  msec. Component C\* is a modified continuing current waveform averaging  $\geq 400$  A for close to 45 msec and is considered the long duration, slow burning lightning current. To evaluate the sensor's influence to direct the propagated current off the sensor, recording the power levels exiting the perimeter of the

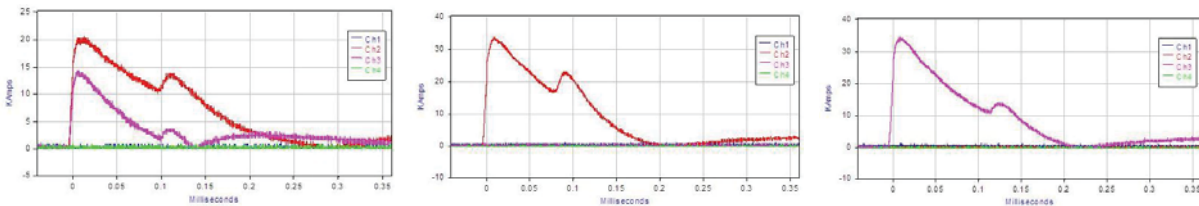
panel on the 4 ground channels was determined the most effective method. The electrical power delivered to the test panel is defined as the action integral. It is determined by integrating the square of the measured current incident on the panel over time. The action integral from the 4 channels were summed to generate a total calculated power level measured from the 4 output channel grounds. The power at each channel was divided by the total calculated power level value to determine the ratio of power along each of the 4 current paths. A fifth current probe stationed at the input cable before the lightning is injected into the test panel captured the total current waveform of Component D and resulting action integral.



(a) 7” SansEC test panel. (b) 8” SansEC test panel. (c) 9” SansEC test panel.

Figure 9.7. SansEC Sensor configured test panels (shown unpainted).

The measured electric current waveform data for the 7”, 8” and 9” SansEC LSP configurations are shown in Figure 9.8. The data plots show the current amplitude in kilo amps on the y-axis versus time in milliseconds on the x axis. For the 7 in configuration all the electric current is measured in channels 2 and 3 while in the 8 in and 9 in configurations all the current travels in one channel. The second amplitude peak visible in the unipolar waveform at 0.1 ms is an anomaly artifact of a resistor flashover short occurring in the lightning current generator resistor bank during the strike.



(a) 7” SansEC test panel. (b) 8” SansEC test panel. (c) 9” SansEC test panel.

Figure 9.8. Measured electric currents on SansEC Sensor configured panels.

Figure 9.9 presents photographs of post-strike test panels for the 4”, 5” and 6” SansEC configurations with graphical representation of the ground paths (4 thin black lines on photograph) to depict the position of the 4 current channels in relation to the sensor. The 4 ground bars surrounding the photograph of the sensor represent the 4 current channels, number 1 thru 4. The values shown on the ground bars represent the action integral ratio received in that channel. The 4” configuration shows power distributed in 3 different channels. In the 5” configuration the current followed channels 3 and 4. The current propagation on the 6” configuration exited the sensors bottom right corner and is measured in channel 2 and 3. The orientation of the test panel relative to the test bed was kept the same for each test to ensure the outer end of the sensor was always nearest to Channel 3.

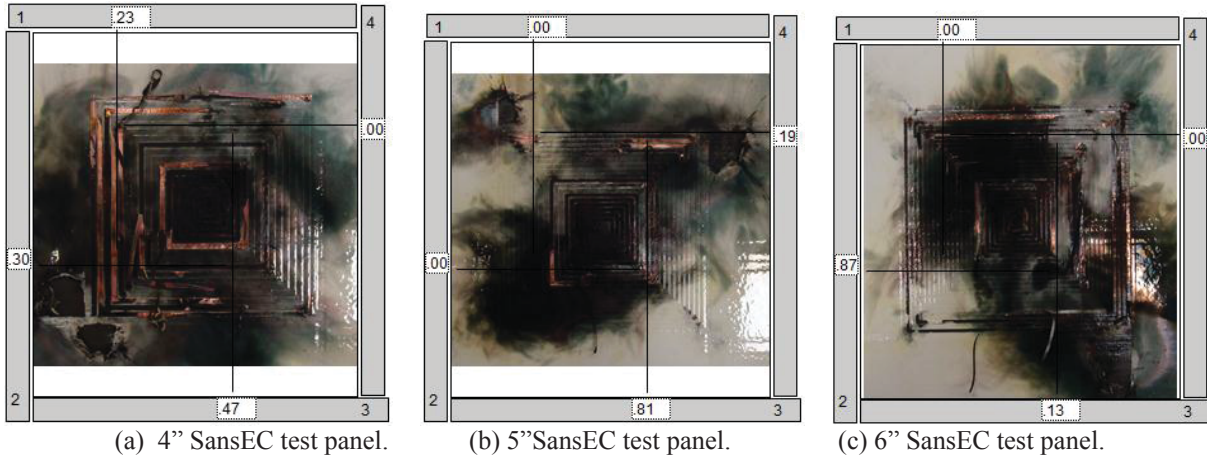


Figure 9.9. Photographs of post-strike test panels for 4", 5" and 6" SansEC panel configurations.

Table 9.1 presents a summary of the electrical data for the FRC lightning tests. The test configurations are shown in column one. The associated electric current power ratios measured on the 4 channels are shown in columns 2 thru 5. The 4 channels measure the current as it exits the panel and enters the facilities' earth ground. The remaining two columns in the table show the peak current and corresponding action integral measured just before the lightning is injected into the panel from a fifth current probe.

Table 9.1. Electric Power Channel Distribution Summary

SansEC Lightning FRC Panel Test Configuration	*Ratio of Action Integral (AI) at each Channel (CH)				Peak Current Measured at Injection Probe, kA	Action Integral Measured at Injection Probe, $\times 10^3 \text{ kA}^2\text{-sec}$
	CH 1 AI Ratio	CH 2 AI Ratio	CH 3 AI Ratio	CH 4 AI Ratio		
Unpainted 4in SansEC (A)	N/A	N/A	N/A	N/A	37.6	78
Unpainted 4in SansEC (B)	0.24	0.13	0.20	0.43	37.6	77
Painted 2in SansEC	0.26	0.24	0.50	0.00	37.6	77
Painted 3in SansEC	0.52	0.00	0.48	0.00	36.8	77
Painted 4in SansEC	0.23	0.30	0.47	0.00	37.2	77
Painted 5in SansEC	0.00	0.00	0.81	0.19	36.6	81
Painted 6in SansEC	0.00	0.87	0.13	0.00	35.6	84
Painted 7in SansEC	0.00	0.80	0.20	0.00	35.6	82
Painted 8in SansEC	0.00	1.00	0.00	0.00	35.0	84
Painted 9in SansEC	0.00	0.00	1.00	0.00	36.2	82
Painted 4in SansEC Quad Triangle	0.03	0.46	0.17	0.34	37.0	78
Painted 3in SansEC Taper Trace	0.47	0.22	0.05	0.26	37.2	75
Painted 3in SansEC Dual Trace	0.15	0.45	0.08	0.32	37.0	77
Painted Baseline Dexmet Cu Mesh	0.26	0.21	0.18	0.35	37.8	77
Baseline Plasma Spray Cu	0.27	0.19	0.19	0.35	37.0	76
Unpainted 4in Square Plasma Spray Cu	0.23	0.12	0.51	0.14	37.8	78
Unpainted 4in SansEC Plasma Spray Cu	0.22	0.12	0.63	0.03	37.8	78
Unpainted 4in Dexmet Cu Mesh SansEC	0.48	0.02	0.32	0.18	36.2	76
Painted 4in Gap Width SansEC	0.20	0.65	0.01	0.14	36.8	76
Painted 4in Trace Width SansEC	0.11	0.24	0.13	0.52	35.8	76
Painted 3in SansEC 1in Cu Impedance	0.45	0.30	0.25	0.00	37.0	77
Painted 3in SansEC 2in Cu Impedance	0.47	0.00	0.30	0.23	37.4	77
Painted 3in SansEC 2in AI Impedance	0.05	0.35	0.05	0.55	37.2	77
Unpainted 3in SansEC 45 deg Rotation	0.20	0.17	0.23	0.40	37.6	76
Unpainted 4in Triangular SansEC	0.15	0.26	0.35	0.24	37.8	77
Unpainted 4in Hexagonal SansEC	0.24	0.24	0.25	0.27	37.4	77
Unpainted 2in Octagonal SansEC	0.48	0.15	0.11	0.26	37.6	77
Unpainted SansEC Football Stars	0.01	0.63	0.10	0.26	37.2	76
Unpainted Carbon Composite MuMetal	0.02	0.33	0.34	0.31	37.6	76
Unpainted SansEC Spider Web	0.35	0.10	0.13	0.42	37.4	76
Unpainted SansEC Tight Trace	0.18	0.22	0.17	0.43	37.4	76

\* The Ratio of Action Integral (AI) is the AI of the measured ground current for each channel divided by the summed of all four channel AI.

Multiple test runs on the same test configuration panel were not acquired except for two unpainted 4" SansEC test runs. The instrumentation failed on the first test shown in the table and the electric current was not recorded. Having only one strike test for each configuration limits our ability to establish a statistical probability to reduce uncertainty in these quantitative results. However, the data does suggest the electrical impedance of the sensor can

vary significantly based on its size, and to lesser extent from the sensor geometry and trace and gap dimensions. This relative impedance change between test configurations is reflected in the values shown in the measured peak current observed in Table 9.1. The test voltage is held constant for each lightning strike, thus any variability in the peak current is a result of the impedance change between sensor configurations.

The capacitive charge in the lightning generation equipment was set at a constant 80 kV for each test. This ensures a repeatable charge was delivered in the lightning waveform. The electric current delivered to the test panel is inversely proportional to the impedance value of the total circuit. When the impedance value of the test panel increases, the peak current delivered to the test panel will decrease. The 5, 6, 7, 8 and 9 inch square SansEC sensor test configurations show a reduction in peak current over the smaller sized sensors. Table 9.1 shows an increase in the action integral values for these configurations due to the test anomaly mentioned earlier where the resistor bank shorted during current injection resulting in a secondary peak current which raised the delivered power. The action integral values should have reduced with lower peak power, but the test anomaly interfered with this expected trend. Table 9.1 also shows the 6, 7, 8 and 9 inch square SansEC sensors directed the lightning current propagation in one direction when used on the FRC substrate. This is a very significant discovery because this sensor demonstrates an ability to precondition the lightning current path and suggests this inherent characteristic of SansEC sensors could provide a revolutionary new approach to mitigate lightning strike hazards on composite aircraft. This will be discussed in detail in a following section.

The backside IR temperature and mechanical displacement data were also acquired on the FRC test panels. Appendix A provides the full set of available IR images over multiple time sequences (taken from video) and mechanical displacement versus time plots for the FRC test panels. The test setup of the IR camera and Keyence optical displacement sensors were described in the test bed description section of this report. The IR images for the 7, 8, and 9 inch SansEC sensor LSP configurations will be analyzed in detail in the following section. The peak values recorded in the mechanical displacement data for the FRC test panels were corrupted as a result of the brightness of the lightning flash interfering with the laser sensor reader. The sensor quickly recovered after the flash and recorded the damped oscillatory nature of the panel deflection, but the peak values were deemed suspect. Attempts were made to interpolate the peak values based on curve fitting algorithms and peak deflection estimations were acquired. However, there remained enough uncertainty in the results that reliable trends from this data are not possible. It was hoped the mechanical displacement data could be used to determine if any SansEC sensor geometries significantly changed the panel deflection. Optical filters were used to reduce the level of lightning flash reaching the sensor and allowed reliable mechanical displacement test data on future tests.

### **9.3 Lightning Attachment and Propagation on SansEC Sensor FRC Test Panels**

A propagating lightning channel generates a wide band electromagnetic emission with a radiation spectrum from near DC to beyond 100Mhz.<sup>[48]</sup> The amplitude of the radiated field is stronger the closer you are to the actual lightning channel. The operational frequency resonance of our tested SansEC LSP designs fall within the radiated emission of the lightning spectrum. When the sensor is excited by the radiated fields from an incoming lightning strike the modal structures (electric and magnetic field gradients present on the sensor trace) occurring at its resonance frequencies are established. The radiated emission from the lightning propagation, either from a laboratory generated lightning waveform or from naturally occurring lightning, will excite the SansEC sensor and establish a modal structure on the trace before lightning attachment occurs, preconditioning how the attachment will occur. This could be used to great advantage in designing future LSP mitigation designs to improve flight safety. For example, it is common practice to vent wing fuel tanks at or near the wing tip. If a passive, light weight surface treatment could be incorporated near the wing tip to reduce the possibility of lightning current entering the fuel cells, it would provide a significant safety improvement over today's practice.

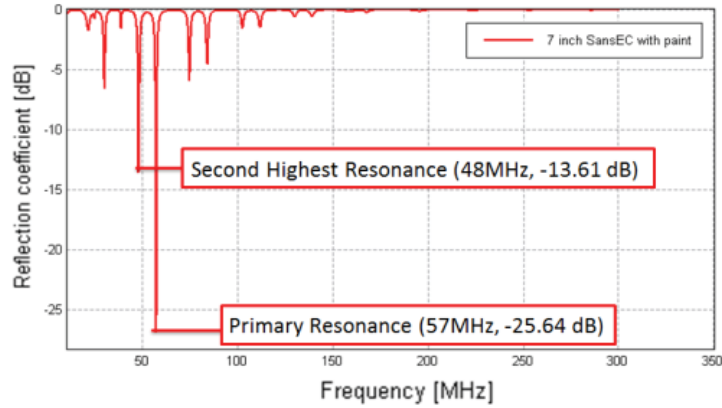
Aircraft surface areas and structures are classified or “zoned” according to the possibility of lightning attachment, dwell time and current conduction.<sup>[7]</sup> Not all surfaces of an aircraft need to be designed to survive the same lightning threat since the lightning attachment process does not expose the same lightning environment equally. The aircraft can be divided into different lightning strike zones to meet FAA airworthiness certification to optimize the required lightning protection across the entire aircraft. Lightning mitigation requirements are more stringent for aircraft zones which are expected to receive the first return stroke such as the nose, tail and wing tips. Zone definitions and methods of locating them on particular aircraft are given in SAE ARP5414.

It is widely accepted within the aircraft lightning community and standards committee that when a fast moving aircraft is struck by lightning, the attachment location sweeps backwards along the vehicle as the aircraft travels forward relative to the lightning channel. This movement of the attachment point typically progresses in a series of discrete irregular steps. The dwell time at any particular step is not likely to exceed 50 ms, being chiefly dependent on the nature of the surface and the velocity of the vehicle. When the lightning channel has swept back to a trailing edge, it can persist or “hang on”. The body of knowledge pertaining to lightning attachment reveals laboratory testing indicates the attachment point on aircraft models are influenced by the voltage waveform. Fast rising waveforms (in the order of a few microseconds) produce a relatively small number of attachment points, usually to the apparent high electric field regions on the model. Slow front waveforms (in the order of hundreds of microseconds) produce a greater spread of attachment points, possibly to include attachments to less high electric field regions. Because the SansEC sensor inherently generates high electric field regions on its conductive trace in the presence of the lightning radiated emission, applying them on an aircraft surface could potentially provide a means to influence lightning attachment which is not achievable from the LSP methods used today. This approach could improve upon existing lightning mitigation designs by narrowing down the probability of attachment to smaller regions of the aircraft that would then be designed more robust to lightning attachment to minimize or eliminate costly repairs and time out of service. If the use of SansEC sensors on an aircraft surface can be designed to regulate where the initial and swept stroke attachments occur, this would enable a means to change the statistical probability of attachment and resulting zoning requirements. As a result, less stringent design requirements could be realized that result in direct weight savings for the overall aircraft LSP system.

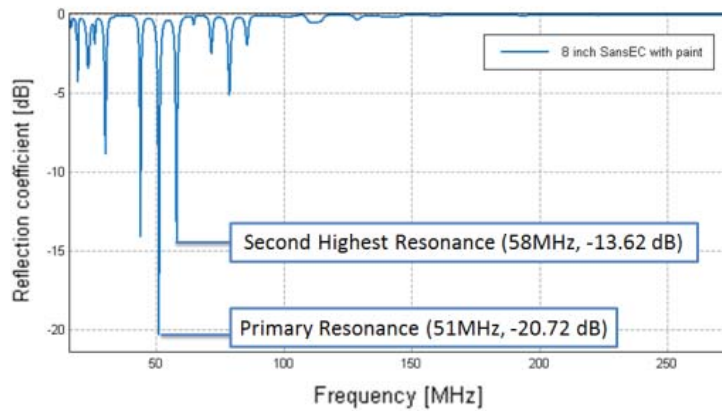
Analysis was conducted to investigate if the high electric field regions on the SansEC sensor could be shown to influence the location of lightning attachment and propagation based on the SansEC FRC lightning test results. CEM simulations were developed to generate the electric and magnetic field maps at peak resonant frequency for the 7, 8 and 9 inch square SansEC sensors to support this investigation. Electric current data for these 3 sensor configurations were shown earlier in the report in Figure 9.8. The simulations were generated to match the physical conditions of the lightning test panels and were modeled with the same perimeter ground path around the sensor. The electrical properties of the FRC substrate were also matched, but the substrate thickness was slightly thinner than actual to overcome a modeling issue. The sensor was interrogated with a 4 inch square loop antenna to establish the electromagnetic excitation.

Figure 9.10 presents the computed reflection coefficient frequency plot for the 7, 8 and 9 inch SansEC Sensors in decibel scale from 10 to 300 MHz. Figure 9.10(a) shows the primary resonance frequency is at approximately 57 MHz at a level of -26 dB for the 7” sensor. The second largest resonance occurs just below 48 MHz at -14 dB. These are fairly strong resonances and are more than adequate to perform sensing in a FRP. Strong resonance phenomena are diminished above 100 MHz. The 8” SansEC reflection coefficient frequency plot is shown in Figure 9.10(b). The primary resonance of the 8” SansEC sensor is -21 dB at approximately 51 MHz. The second highest resonance is about -14 dB at approximately 58 MHz. Strong resonance phenomena is again diminished above 100 MHz. The 9” SansEC reflection coefficient frequency plot is shown in Figure 9.10(c). The primary resonance of the 9 in SansEC sensor is -34 dB at approximately 52 MHz. The second highest resonance is around -15 dB at approximately 58 MHz. Again strong resonance phenomena are observed to be diminished above 100 MHz. These results demonstrate these sensor configurations contain multiple resonances in the lightning radiated emission band. Each unique resonance when excited simultaneously will establish a superimposed complex electric and magnetic field distribution on the trace geometry.

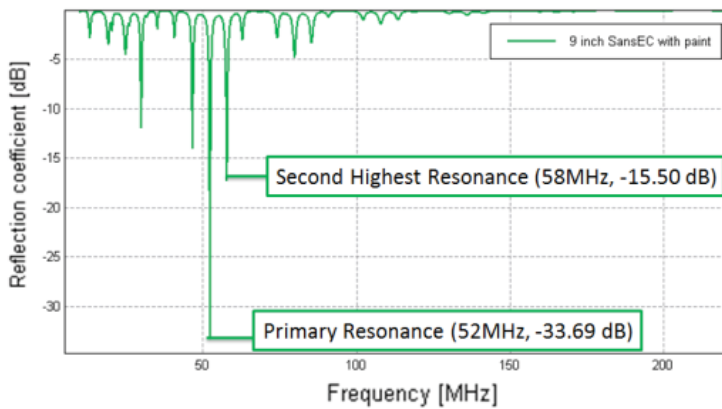
Figure 9.11 presents the electric and magnetic field distribution in dBV/m and dBA/m respectively for the 7” SansEC sensor. The simulation contained the full panel with grounds, but only the SansEC sensor fields are presented. The amplitude scales were selected to provide visual contrast between high field regions and low field regions. Figure 9.11(a) clearly shows five distinctive loops of high electric field at the primary resonance frequency (57 MHz). Figure 9.11(b) shows four distinct loops of high magnetic field also at the same frequency. Note both images have no significant field strength at the center of the spiral and at the outer end of the spiral. The open circuit nature of the SansEC sensor necessitates that no current flow occurs at the ends of the trace and thus the field strength diminishes to zero at the terminations. The electric and magnetic field maps shown in Figure 5.5 only depict the modal structure for one resonance frequency. In actuality, the modal structure present on the sensor from an impinging radiated lightning waveform is the superposition of all the resonances within band of the radiated emission.



(a) 7" SansEC Sensor.



(b) 8" SansEC Sensor.



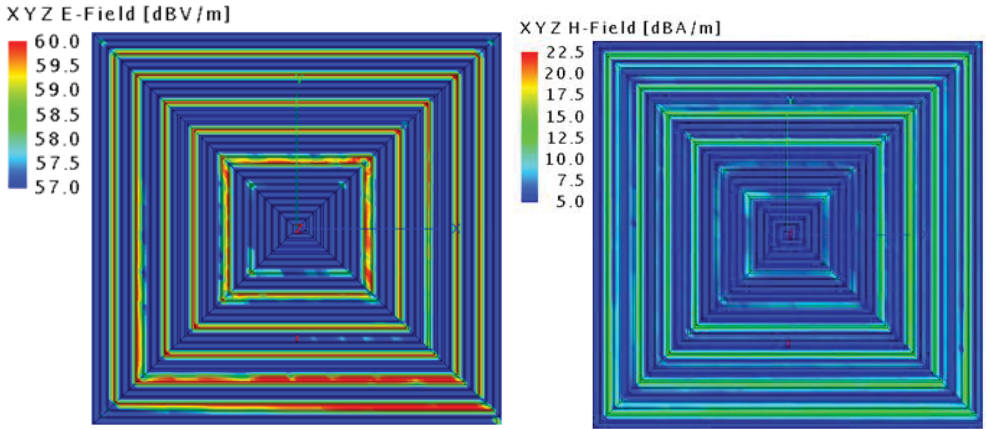
(c) 9" SansEC Sensor.

Figure 9.10. Reflection Coefficient for 7, 8 and 9 inch SansEC Sensor configurations.

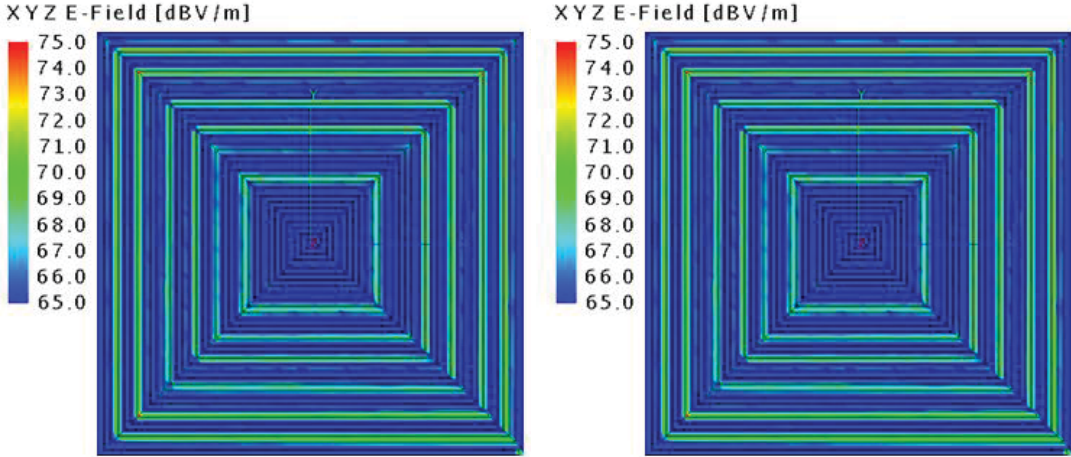
Figure 9.12 presents the electric and magnetic field distribution for the 8" SansEC sensor at 51 MHz in the same format as presented for the 7". The E-field distribution shows six loops with higher field while the H-field distribution shows five.

Figure 9.13 presents the electric and magnetic field distribution for the 9" SansEC sensor at 52 MHz in the same format as presented earlier. The E-field distribution again shows six distinctive loops with higher electric field. The H-field distribution does not show the distinctive loops of relatively higher magnetic field regions as was observed

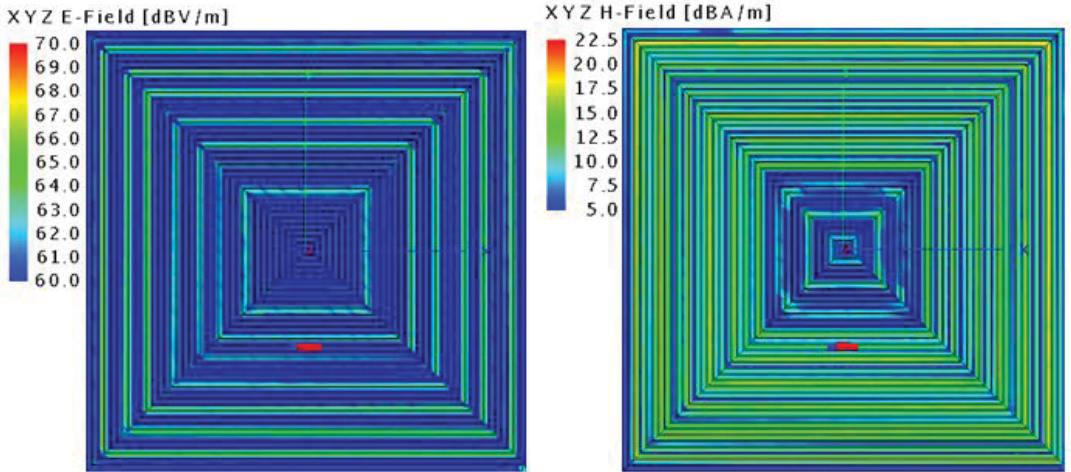
in the 7" and 8" sensors. Instead, it appears that nearly all of the traces of the 9" sensor generate magnetic field activity at the resonance frequency. The center of the spiral and outer edge are still shown to have minimal magnetic field.



(a) E-field of 7" SansEC Sensor at 57 MHz. (b) H-field of 7" SansEC Sensor at 57 MHz.  
Figure 9.11. Electric field and magnetic field distributions on a 7" SansEC Sensor.



(a) E-field of 8" SansEC Sensor at 51 MHz. (b) H-field of 8" SansEC Sensor at 51 MHz.  
Figure 9.12. E-field and H-field of 8" SansEC Sensor at fundamental resonance.

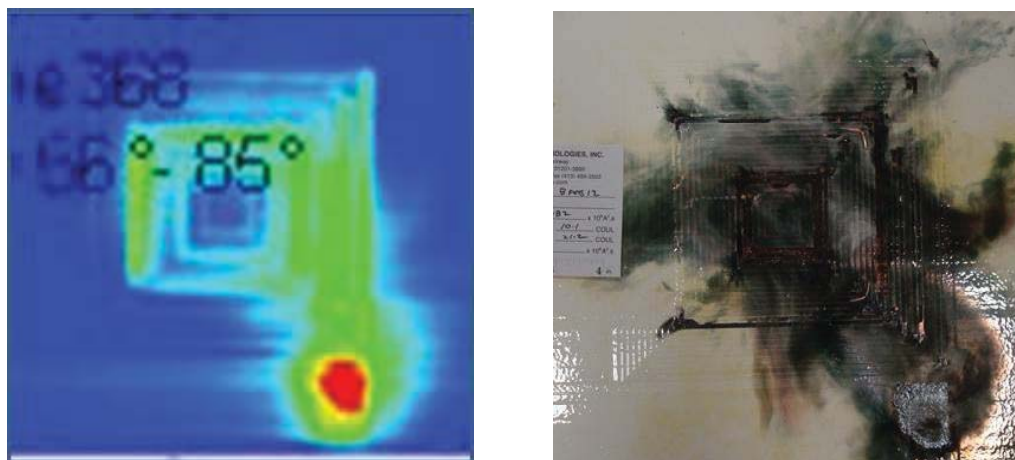


(a) E-field of 9" SansEC Sensor at 52 MHz. (b) H-field of 9" SansEC Sensor at 52 MHz.  
Figure 9.13. E-field and H-field of 9" SansEC Sensor at fundamental resonance.

IR video imagery was recorded during the FRC lightning test to capture the heat signature residing on the back side of the panel initiated from lightning attachment. The IR images will show higher temperatures at the lightning attachment locations and along the current pathways from resistive heating. A thermal image of the 7” SansEC LSP configuration taken 4 seconds after initial heating is detected is shown in Figure 9.14 along with the corresponding post-strike test panel photograph. The IR images shown in this report are inverted to represent the front side view, since the thermal data was collected from the back side of the strike. The hotter temperatures seen in the IR image correlate the location of lightning attachment and or current propagation. If a portion of the SansEC trace is immediately destroyed or removed from the panel during lightning insult, the IR image may not sense an increase in temperature at that location. Figure 9.14(a) shows higher temperatures at the intersection of the ground paths attached to channel 2 and 3 at the lower right corner of the SansEC sensor. Even though the sensor is electrically conductive everywhere, the resistive heating did not occur uniformly over the sensor trace. The IR image shows the right side of the sensor has five separate traces that appear to have higher temperature from lightning attachment on the 7” SansEC Sensor. Note the absence of resistive heating in the center of the sensor and at the upper, left and lower outer traces. Examination of post-strike test panel photographs often shows the center region of the trace is no longer present after the strike. Further investigations are needed to definitively determine the reason for this. It could be due to strong Lorentz forces acting on the traces in the center of the sensor and poor adhesion methods that were used to integrate the sensor to the test panel or from other causes. The post-strike photograph indicates the upper, left and lower outer traces have remained intact.

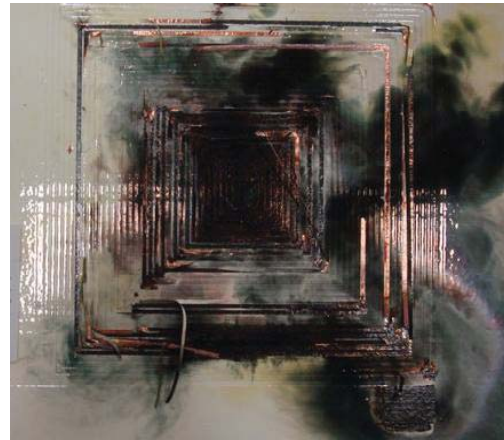
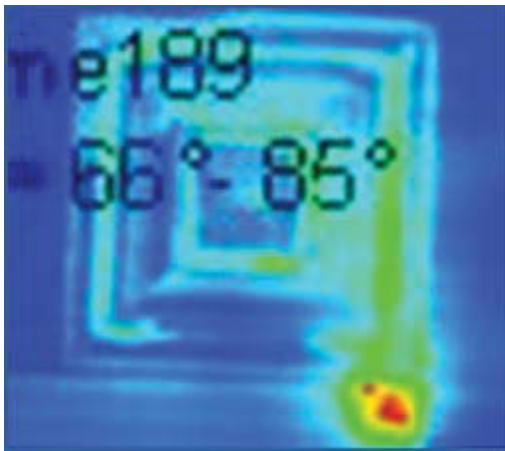
Figure 9.15(a) presents the IR image data taken 4 seconds after the onset of heating. The corresponding post-strike test panel photograph for the 8” SansEC sensor is shown in Figure 9.15(b). The current propagation was measured entirely on channel two and is corroborated with the heat signature seen on the channel 2 ground path in the IR image. The photograph shows burnt traces on the sensor aligning with the hotter traces in the IR image. The missing portion of the ground path conductor in the photograph on channel 2 is the highest temperature in the IR image. The 8” IR image is similar in nature to the 7” IR image but with six traces on the right side showing higher temperatures.

Figure 9.16(a) presents the IR image for the 9 in SansEC sensor 2 seconds after initial heating is detected. The corresponding post-strike photograph is shown in Figure 9.16(b). All the lightning current on the 9 in SansEC was measured in channel 3. The photograph shows burn marks at the upper right corner of the 9 in SansEC and bare substrate at the edge of where the ground path once was. The IR image is shown at 2 seconds for this sensor instead of at 4 seconds as in the other 2 cases. The heat signature in the 4 second image showed a uniform increase in temperature over the entire region making it impossible to determine which traces were attached at the onset of lightning initiation. The IR image at 2 seconds offered a little clearer definition as to which traces may have been attached to. The highest temperature is coming at the ground path on channel 3. The heat signature for the 9 in SansEC sensor is more dispersive than was seen on the 7 in or 8 in sensors and shows elevated heating in most of the traces in the upper right corner.

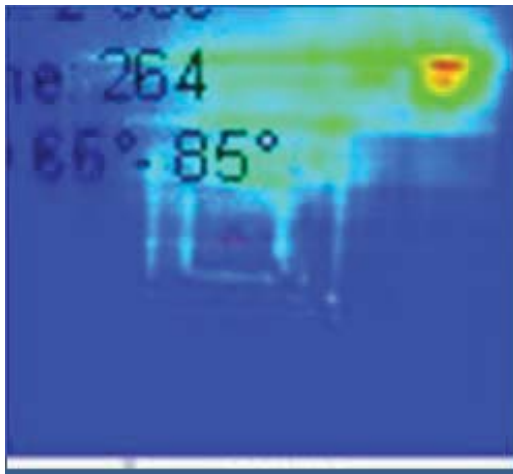


(a) Backside IR thermal image at 4 sec after strike. (b) Post strike photograph.

Figure 9.14. Data of a 7 in SansEC Sensor on FRC.



(a) Backside IR thermal image at 4 sec after strike. (b) Post strike photograph with.  
Figure 9.15. Data of an 8" SansEC Sensor on FRC.



(a) Backside IR thermal image at 4 sec after strike. (b) Post strike photograph.  
Figure 9.16. Data of a 9" SansEC Sensor of FRC.

To establish possible correlation between the high electric field regions excited on the sensor trace from the propagating lightning's radiated emission with the location of lightning attachment on the sensor, the computed electric field maps were compared to the IR images to determine any similarities. Figure 9.17 shows the 7" SansEC sensor E-field distribution at the primary resonance appropriately sized next to its IR image. A slice of the IR image from above the center line has been pasted over the E-field distribution to help visually align the location of the hotter traces with the higher E-field traces. The five high electric field traces on the right side of the E-field distribution seem to align well with the five higher temperature traces in the right side of the IR image. The area of lower electric field in the center of the E-field distribution appears to coincide with the area of lower temperature in the IR image. It should be noted once again the high E-field regions occurring at other resonance frequencies are not presented in this graphical representation of the E-field map, but they would play a role in the experimental IR results and conceivably will play a role in the preconditioning of the lightning attachment to the sensor. Although these results are not 100% conclusive, they do appear to have enough similarity to conclude there is some correlation.

The E-field distribution of the 8" SansEC at the primary resonance is shown appropriately sized next to its IR image in Figure 9.18. A slice of the IR image from above the center line has been pasted over the E-field distribution to help visually align the location of the hotter traces with the higher E-field traces. The six high electric field traces on the right side of the E-field distribution seem to approximate the location of the six higher temperature traces in the right side of the IR image. The area of lower electric field in the center of the E-field distribution is very close to the area of lower temperature in the IR image. This comparison would again suggest

there appears to be a correlation between the E-field distributions at the primary resonance with the heating observed in the experimental IR data.

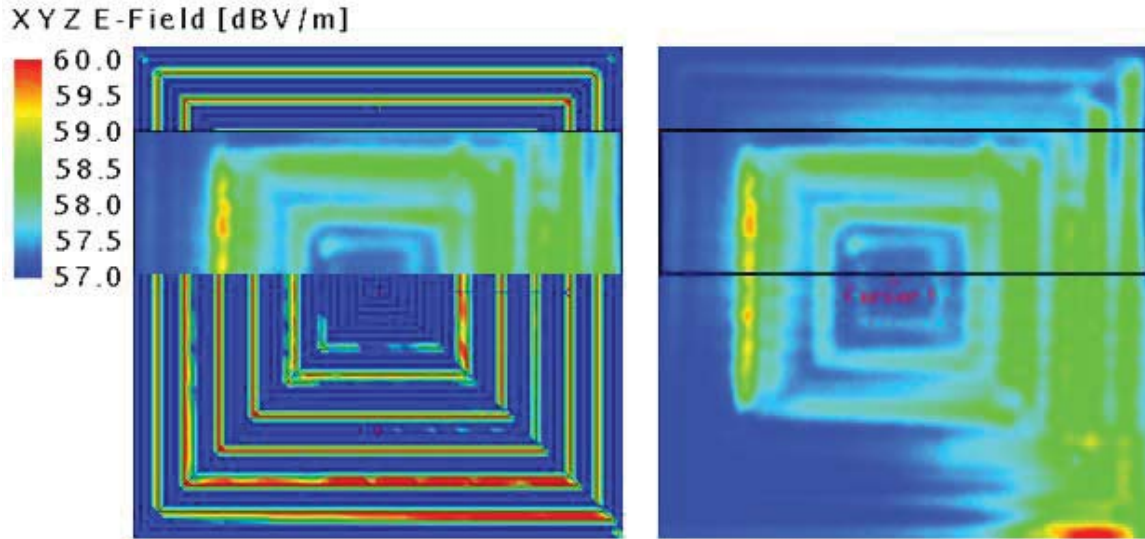


Figure 9.17. 7” SansEC Sensor E-field at 57 MHz (primary resonance) compared with IR image.

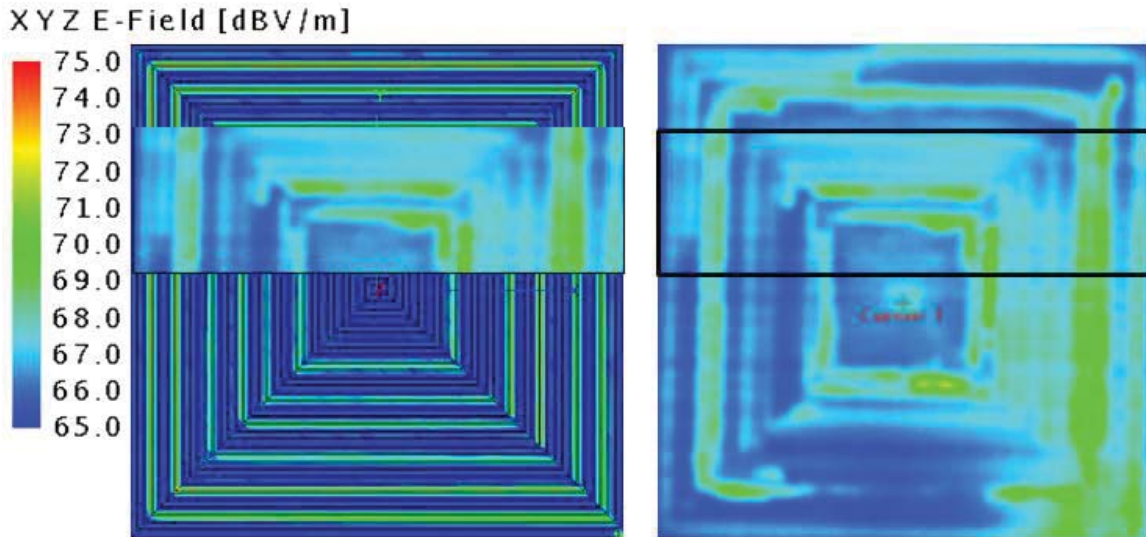


Figure 9.18. 8” SansEC Sensor E-field at 51 MHz (primary resonance) compared with IR image.

The E-field distribution of the 9” SansEC at the primary resonance is shown appropriately sized next to its IR image in Figure 9.19. A portion of the IR image from upper left corner has been pasted over the E-field distribution to help visually align the location of the hotter traces in this area with the higher E-field traces. The high E field traces above the center line align very well with the higher temperature traces. The area of lower electric field in the center of the E-field distribution again matches well to the area of lower temperature in the IR image. A second comparison of this data is shown in Figure 9.20 with a different dBV/m scale. The E-field scale has been compressed to highlight the higher field regions appearing at the upper right corner. A slice of the E-field distribution from the upper right corner is shown overlaid on the IR image. The E-field distribution shows higher relative field values at this corner and corresponds nicely to the higher temperatures shown in the IR image. These results also show a reasonable level of correlation and substantiate the proposed concept of incorporating SansEC sensors into aircraft smart skins as a means to manipulate the probability of lightning attachment to a specific area and correspondingly influence the zoning requirements to further optimize and reduce the weight of the overall LSP system for composite aircraft. Additional engineering of the SansEC sensor geometry could be concentrated to

effectively co-locate the superimposed high E field regions from multiple resonance frequencies to enhance and optimize this effect.

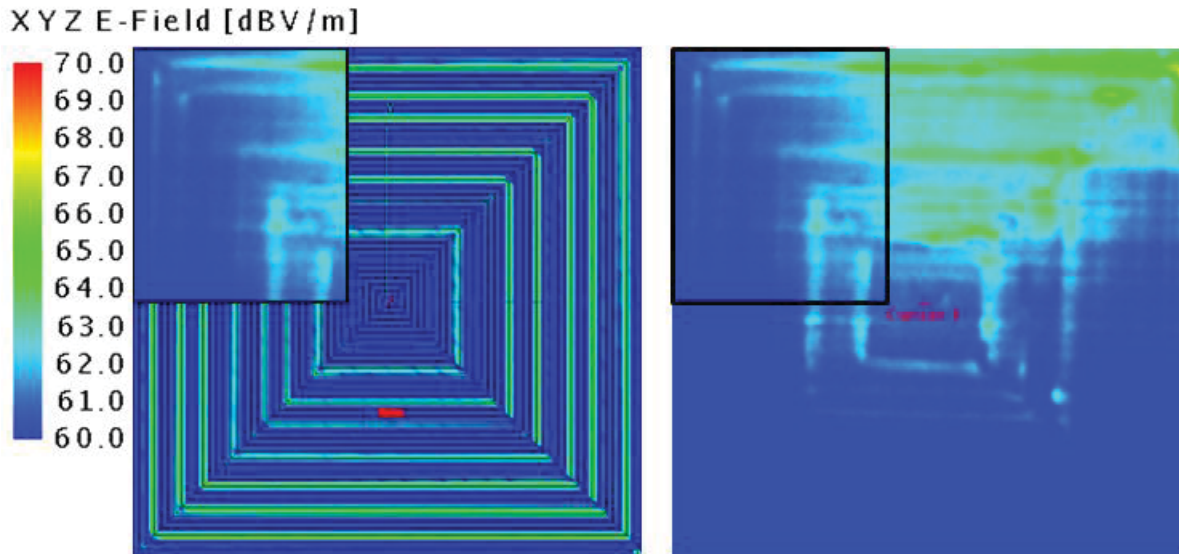


Figure 9.19. 9” SansEC Sensor E-field at 52 MHz (primary resonance) compared with IR image.

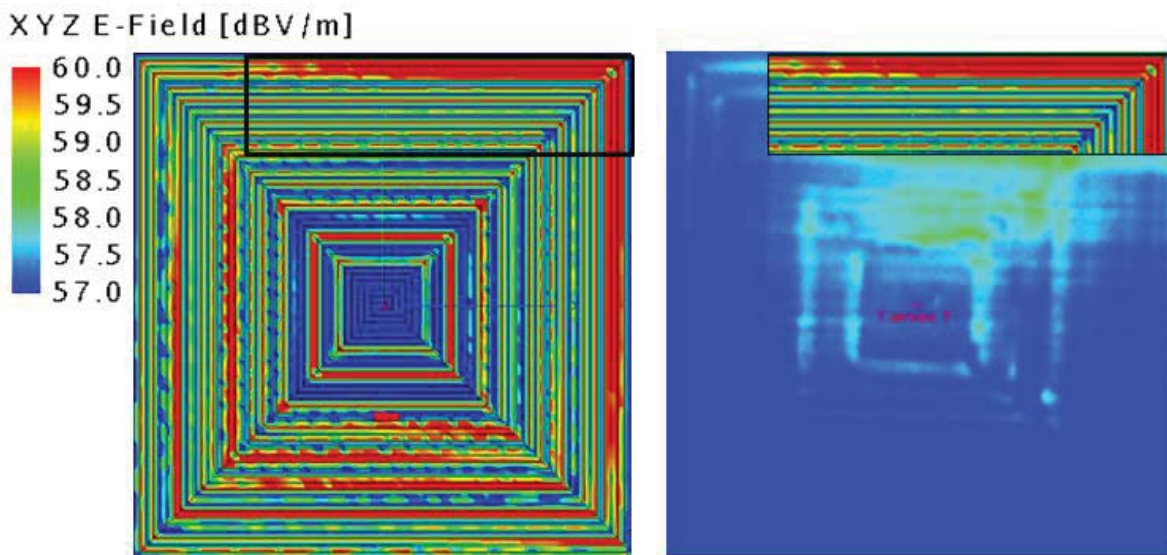


Figure 9.20. 9” SansEC Sensor E-field at 52 MHz (primary resonance) at different dBV/m scale compared with IR image.

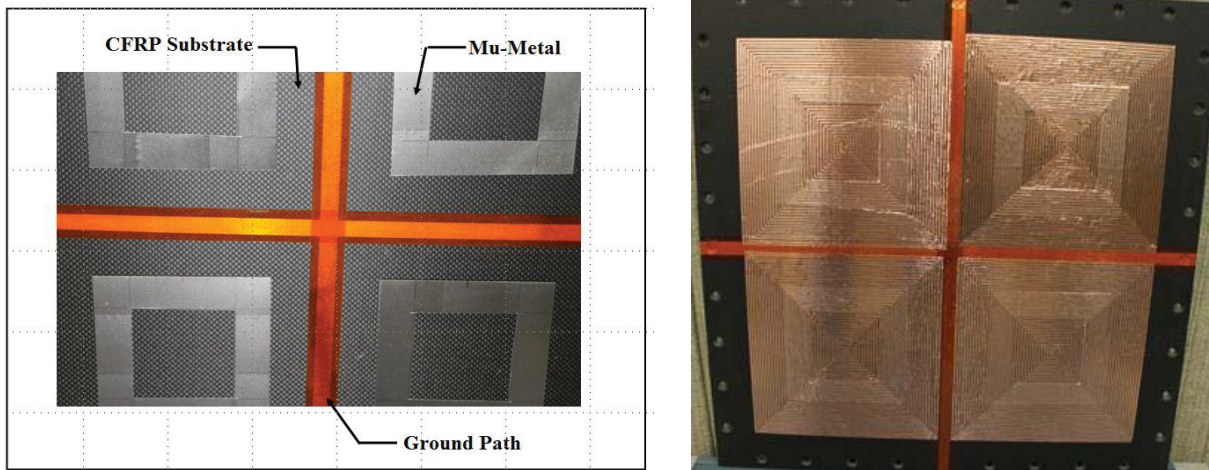
The discussion in this section thus far has focused on the SansEC sensor’s electric field characteristics and its influence on lightning attachment. This alone does not explain the observed phenomena shown by some SansEC sensor configurations to steer the lightning current in one direction. As discussed in above, the SansEC sensors magnetic field distribution acting above the plane of the trace has an intrinsic ability to steer charged particles following the principles found in the Lorentz equation. The 7” SansEC sensor magnetic field (H-field) map was shown prior in Figure 9.17. The computed H-field shows 4 loops of distinctly higher field values that seem to start and stop at the bottom right corner of the geometry and look strangely familiar to a split ring resonator. The measured current data for this configuration showed all the lightning current followed this same vector direction and exited the SansEC sensor along this corner. It is plausible to believe this phenomenon is a result of the asymmetric magnetic field present above the surface of the sensor inducing Lorentz forces on the charged particles biasing the electron flow along this vector. Figure 9.18 presented the magnetic field map for the 8” SansEC sensor. This configuration also showed the lightning current exiting the bottom right corner of the SansEC sensor. The H-

field map looks very similar to the 7” configuration in terms of its appearance, nature and orientation of the split ring resonator feature. Further analytical research is needed to determine the characteristic features of the SansEC sensor which can be engineered to develop optimal sensor geometries based on enhancing Lorentz force effects to direct the lightning path in a controlled manner. Initial observations based on this study suggest this phenomenon is real and could be developed into a revolutionary new lightning mitigation approach for composite aircraft.

#### 9.4 Lightning Strike Test Results on Carbon Fiber Composite Substrates

The procedures defined in the universal common practice were followed explicitly in executing the direct effect testing conducted at the Lightning Technologies test laboratory in September 2012 and again in July 2013. The purpose of these tests were to characterize baseline CFRP and SansEC LSP test panels to enable quantitative test metric comparisons to assess the performance of SansEC LSP configurations. The protected and unprotected CFRP panels were manufactured in accordance to guidance in NASA DOC-128694<sup>[43]</sup> by Cessna Aircraft Company under a NASA contract in March 2012. The baseline protected panels consisted of the Hexcel composite substrate with a 3 mil LSP layer of expanded copper foil (Dexmet 3CU7-100FA) and Cytec Surfamaster 905C Composite Surfacing Film. This LSP system is considered an acceptable method to protect composite substrates to achieve FAA airworthiness lightning protection standards. The weight of the Dexmet 3CU7-100FA is .040 lbs./sqft and the Surfamaster 905C Composite Surfacing Film weighs .035 lbs./sqft. The total weight of the baseline lightning strike protection configuration is .075lbs/soft.

The SansEC LSP CFRP test panels were manufactured by the NASA Langley Composites Fabrication Shop following the same manufacturing specifications which guided Cessna in building the baseline panels. The various SansEC LSP geometries were manufactured using a Klick-N-Kut machine to carve the spiral traces from 1.25 mil copper sheets. The 8” square SansEC sensor array which performed best in the damage assessment evaluation, consisted of a 3/16” trace width and 1/16” gap width. The weight of the 8” square copper SansEC sensor was .0194 lbs. To improve the SansEC’s electromagnetic coupling into the carbon composite, a layer of 5 mil Finemet flexible magnetic shielding was placed above the CFRP and below the SansEC sensor. The Finemet layer was 5 inches in outer dimension and 3 inches inner dimension centered at the midpoint of the sensor placement. The weight of the Finemet layer was .00578 lbs. The total weight of the 8” square SansEC LSP system was .0252 lbs. This equates to .0567 lbs./sqft. Figure 9.21(a) shows a photograph of the 8” SansEC array CFRP test panel with the Finemet layer before the sensor array was applied. Figure 9.21(b) shows the same test panel after the 8” SansEC sensor array was placed over the Finemet layer before being painted.



(a) Finemet layer on CFRP. (b) 8” SansEC Sensor array.  
 Figure 9.21. Photograph of 8” SansEC Sensor array CFRP test panel.

The baseline panels underwent pre-strike NDE inspections at Cessna under the provisions in NASA DOC-128695 to ensure the test panels were within design specifications. NASA Glenn Research Center conducted the pre-strike NDE on the SansEC LSP panels abiding by the same set of guidance documents. The NASA documents were effective in providing the detailed specifications necessary to manufacture and qualify the CFRP test panels without additional clarification.

The protected and unprotected baseline CFRP panels were subjected to Component D waveform at 20, 40 and 100 kA peak currents with follow on components B & C in a continuous lightning discharge in compliance with SAE ARP5416 following test procedures in NASA DOC-128696.<sup>[45]</sup> A minimum of 3 test panels were evaluated for each configuration and test condition during the September 2012 lightning test. In July 2013, 3 additional protected and 3 unprotected panels were retested at 100kA peak current to improve the statistical confidence in the baseline test results.

The SansEC LSP CFRP panels were tested at 100KA to obtain damage assessment metrics at the highest amperage. 7 SansEC LSP test panel configurations were evaluated during the September 2012 test and 12 more during the July 2013 test. To enable a broader look at various design details under a constrained set of test panels, each configuration was different and thus no statistical confidence can be established. The results and supposition are based off single test point observations. A total of 6 SansEC LSP test panels were evaluated thru damage assessment. 3 of these configurations will be highlighted in this paper showing their LSP performance.

The lightning test bed was used to collect the electric current propagation, mechanical deflection and back side IR temperatures to quantify the damage mechanism parameters present on the CFRP substrate during lightning insult. In addition, high speed video cameras were used to record the lightning attachment to provide additional quantifiable observational data.

The electric current on the 4 edges of the test panel were independently monitored during the lightning test as was done for the FRC testing. 4 Pearson 4418 current probes were used to monitor the electrical ground current off the edges of the CFRP panels. The 4 ground straps were installed with equal length and kept as short as possible. A quarter in thick Aluminum calibration test plate was installed in the test bed fixture and struck repeatedly to measure current flow at the 4 edges to ensure no significant bias was observed. For this isotropic calibration test plate it is expected each ground strap would receive approximately 25% of the total current. Table 9.2 presents the peak current data measured on the 4 Pearson probes identified as channel 1 thru channel 4 for the July 2013 lightning test for 3 repeated strikes to the Aluminum calibration test plate and 3 protected and 3 unprotected CFRP panels struck at around 100KA.

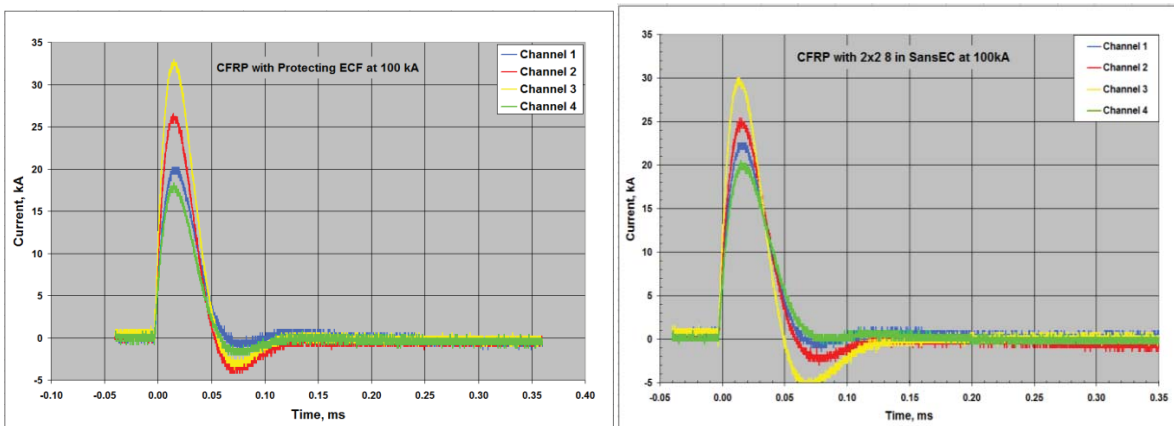
Table 9.2. Pearson Probe Current Data Collected July 2013

<b>Test Panel</b>	<b>Peak Input Current, kA</b>	<b>Channel 1</b>	<b>Channel 2</b>	<b>Channel 3</b>	<b>Channel 4</b>
Aluminum Plate	100	20.8	24.4	35.2	20.2
Aluminum Plate	100	21.6	24.4	35.2	20.2
Aluminum Plate	100	21.6	24.4	35.2	20.6
Unprotected CFRP	100	20.6	24.4	33.6	19.8
Unprotected CFRP	100	20.4	27.4	30.6	16.8
Unprotected CFRP	100	20.2	24.6	33.4	19.2
Protected CFRP	100	21.6	25.2	34	19.6
Protected CFRP	100	22.4	24.8	35.2	19.8
Protected CFRP	100	20.2	26.6	33	18.4

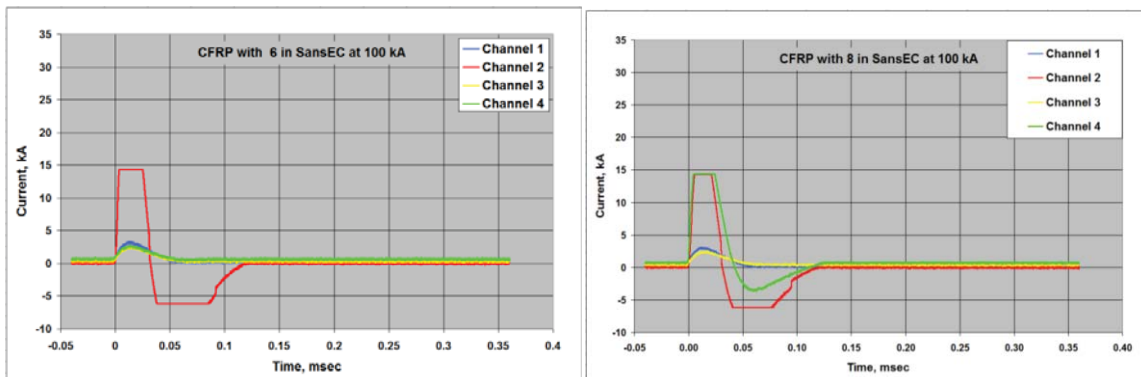
The test data show the peak electric current on each of the 4 ground straps is not distributed equally. Further investigation is needed to determine if adjustments to the length of individual ground straps could reduce the level of bias from the measurement or replacing the used braided copper ground strap with new straps would establish a more balanced equilibrium. The Pearson probes used in the test were within calibration specifications and were not suspect. The CFRP test panel data show similar bias as the Aluminum calibration plate with channel 3 typically measuring higher and channels 1 and 4 typically measuring lower. These results are believed to not have had any significant impact on the results for the protected and unprotected CFRP panels, but do affect our ability to have confidence in the evaluations of the asymmetrical SansEC LSP concepts, which require a more balanced distribution to develop conclusions based on the test results. Figure 9.22(a) shows the plotted 4 channel electric current waveforms measured from a protected baseline CFRP panel at 100KA. The y axis represents the current amplitude in kiloamps and the x-axis displays the time in milliseconds. Figure 9.22(b) shows a similar electric current plot from an 8” SansEC Array LSP CFRP test panel at 100kA. Both of these measurements were taken in

July 2013 and both show the same current distribution bias in the plots. Figure 9.23(a) and (b) present 4 channel current waveform data on a 6'' and 8'' SansEC LSP CFRP test panel taken during the September 2012 test. Even though the peak current values in both plots are clipped due to improper voltage settings on the test instrumentation, the curves do indicate SansEC sensor configurations on CFRP substrates can influence the current vector propagation as was observed on the FRC substrates.

The mechanical impact from a lightning strike caused by both a strong shock wave in the radial direction of the arc column and magnetic forces induced by the current circulation in the arc column can lead to breaking, delaminating and puncture to the composite system.<sup>[49]</sup> Mechanical displacement measurements were acquired to characterize this potential damage mechanism by using two Keyence LK-G507 laser displacement sensors to monitor the deflection at the center of the panel. A band pass Optical Filter (Keyence part OP-87110) was used in the July 2013 test to eliminate interference from the lightning flash. White spray paint was applied to the back side of the panels to compensate for the reduction in received laser power due to the optical filter. The sensors were mounted 28'' from the back surface of the panel and at 13.1 degrees off normal to prevent the sensors from blocking the IR camera view. The data is adjusted to compensate for the off normal measurement. The sensor was sampled at 100 microseconds. A fiber optic link was used to connect the laptop computer outside the test area with the Keyence controller inside the test facility to manually trigger data collection. The cables between the Keyence sensors and Keyence controller were wrapped in metal foil to prevent electromagnetic interference from the lightning strike. The controller buffers 65536 data points with each trigger. Approximately 6.5 seconds of data is collected for each strike. Automated triggering would ensure more reliable data collection from the Keyence sensors.



(a) CFRP protected with ECF. (b) CFRP protected with a 2 x 2 8'' SansEC Sensor array.  
 Figure 9.22. Current waveform at 100kA measured on the 4 edges of the protected baseline CFRP panel.



(a) CFRP protected with a 6'' SansEC Sensor. (b) CFRP protected with an 8'' SansEC Sensor.  
 Figure 9.23. Current waveform at 100kA measured on the 4 edges of the protected baseline CFRP panel.

Table 9.3 presents peak panel deflections at 100 kA for a painted and unpainted Aluminum plate, 2 protected and 2 unprotected baseline panels, and 3 SansEC LSP configurations. The data presented shows the Aluminum plate has a higher deflection with paint than without paint. It is common to see higher levels of damage on painted structures

than on the same unpainted structures. The paint adds a dielectric layer which focuses the lightning current preventing it from dispersing over a larger attachment area. The unprotected CFRP panels show about 1 mm higher deflection than protected panels. The 9" SansEC LSP had considerable less deflection than the 8" SansEC LSP. Based on this one test case, it suggests the sensor geometry can influence the mechanical impact. Further study is needed to determine how much reduction in mechanical impact could be achieved thru proper engineering of the SansEC sensor's magnetic field structure to mitigate the impinging magnetic force induced by the current circulation in the arc column. Any design will likely be less effective at mitigating the forces created by the strong shock wave in the radial direction of the arc column unless it totally prevents attachment to the aircraft.

Table 9.3. Mechanical Displacement Measured at Center of Test Panel

Test Panel	Peak Input Current, kA	Sensor 2 Peak Deflection, mm	Sensor 1 Peak Deflection, mm
Aluminum Plate	100	0.56	0.44
Aluminum Plate	100	0.57	0.62
Aluminum Plate with Paint	100	1.15	1.04
Unprotected CFRP	100	3.78	3.77
Unprotected CFRP	100	3.72	3.76
Protected CFRP	100	2.35	2.63
Protected CFRP	100	2.86	2.82
Protected CFRP with Single 8" SansEC	100	3.632	3.726
Protected CFRP with Single 9" SansEC	100	1.269	1.297
Protected CFRP with an Array of 2x2 8" SansEC	100	3.5912	3.5219

A data plot of mechanical displacement in millimeters (y-axis) versus time in seconds (x-axis) is presented in Figure 9.24 for an Aluminum plate with paint, and the protected and unprotected CFRP test panels at 100 kA. The data shows a typical damped sinusoidal response from the lightning impact on the test panel. If multiple lightning attachments happen to occur during the initial high current impulse, the peak deflection imparted to the panel could be influenced. It is important to acquire enough statistical data to establish confidence in the trends developed from the displacement data for future SansEC LSP research.

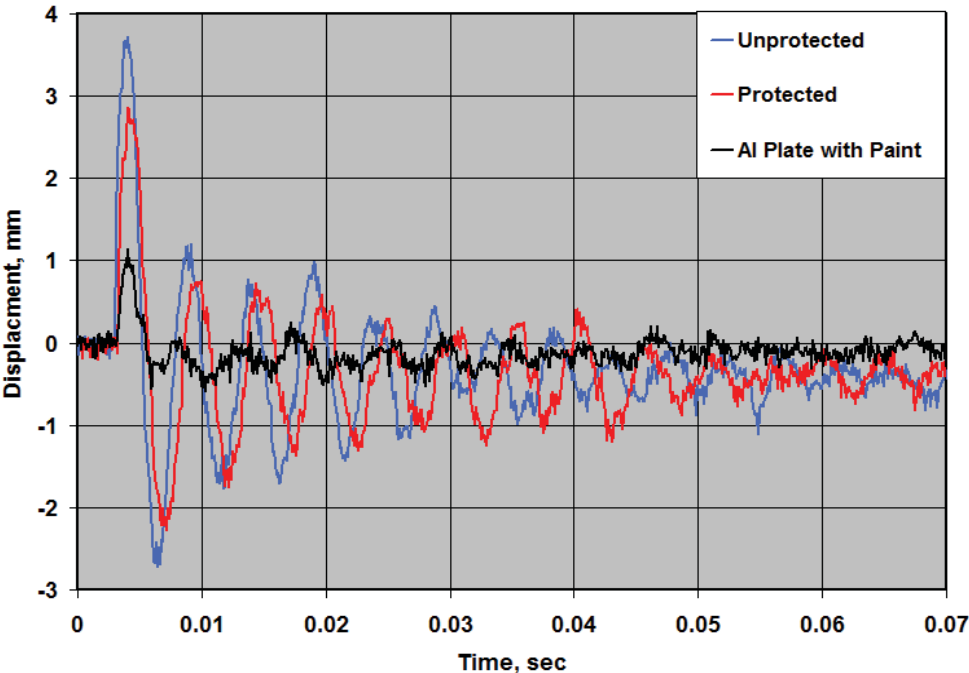


Figure 9.24. Displacement versus time plot of Aluminum Plate, unprotected and protected CFRP test panels at 100 kA. All panels were painted white.

Excessive heating from a lightning strike can cause melting or puncture at the attachment location from the direct plasma heat transfer and Joule heating in the CFRP material. A FLIR Systems SC645 IR camera was used to capture the temperature on the backside of the test panels during lightning strikes to quantify the thermal effects. The camera acquired 30 seconds of data at 25 Hz for each acquisition. This was adequate to capture the peak temperatures on the back side of the panel. The camera was mounted 48” directly below the test panel to capture back side temperatures. The IR camera was manually triggered with a fiber optic link connecting the camera to a laptop computer outside the test area. The camera power cable and Ethernet cable going to the fiber optic link were covered with metal foil to prevent upset. Automated triggering for the IR camera would ensure more reliable data collection.

IR cameras can accurately measure calibrated temperatures if the correct thermal emissivity of the measured object is known. The back side emissivity of the test panels were not measured but are assumed to be .95 based on an estimate of the emissivity of the paint applied to the back surface of the panel, which was needed to accommodate the mechanical displacement data collection. It is recommended that guidance be included in the Universal Common Practice to specify an appropriate white coating of known emissivity to be applied to the back side of the test panels to eliminate the need for additional emissivity testing to acquire calibrated temperatures.

Figure 9.25 presents the back side temperature profile curves for baseline protected and unprotected CFRP panels and the 8” SansEC array LSP CFRP test panel. The Fahrenheit temperature is on the y-axis and the time in seconds on the x-axis. The data curve time scales have been shifted to align the time point in which initial heating occurs to allow comparisons of the temperature profiles. The unprotected panels show higher rapid heating than the protected or SansEC array panels. The temperature profile for the SansEC array compared very well to the profile of the protected panels. Figure 9.26 presents additional temperature profile data collected in September 2012 on 2 baseline protected CFRP panels and 3 SansEC LSP CFRP configurations. The temperature rates of rise appear similar for all 5 test runs. The temperature setting on the IR camera was set to its low temperature range and thus failed to capture the peak temperature for some configurations. Peak temperatures usually occur during the long duration Component C\* waveform remaining stationary in one spot on the panel. If the lightning arc wanders on the test panel during the delivery of Component C\*, lower temperatures will be realized.

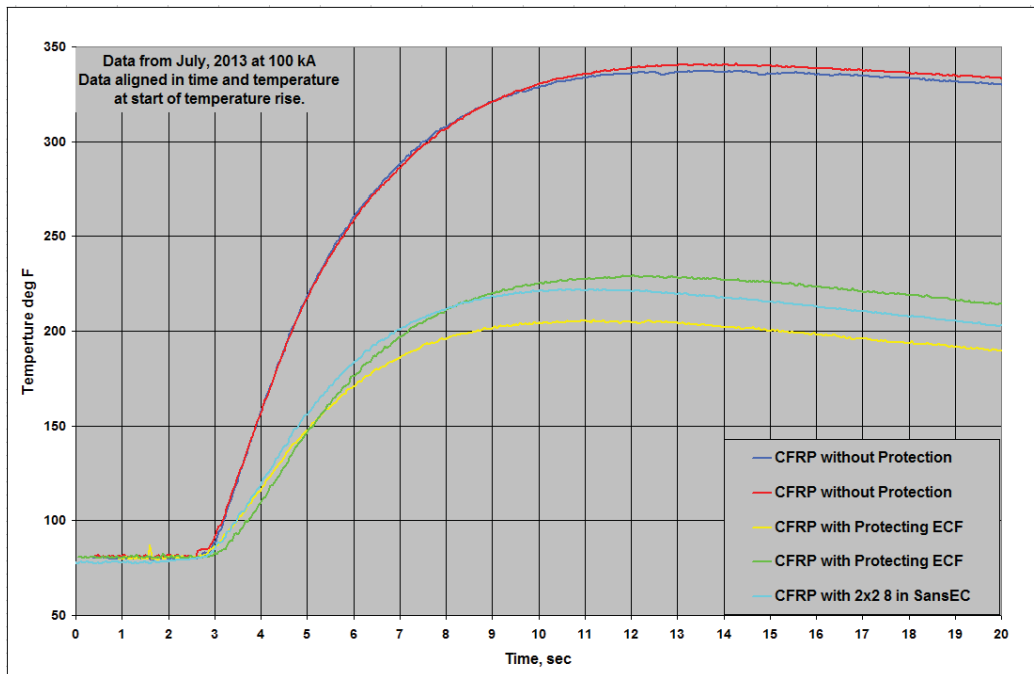


Figure 9.25. CFRP panel backside temperature profiles comparing unprotected, protected (ECF) and SansEC Sensor configurations. Data aligned in time and temperature at start of temperature rise.

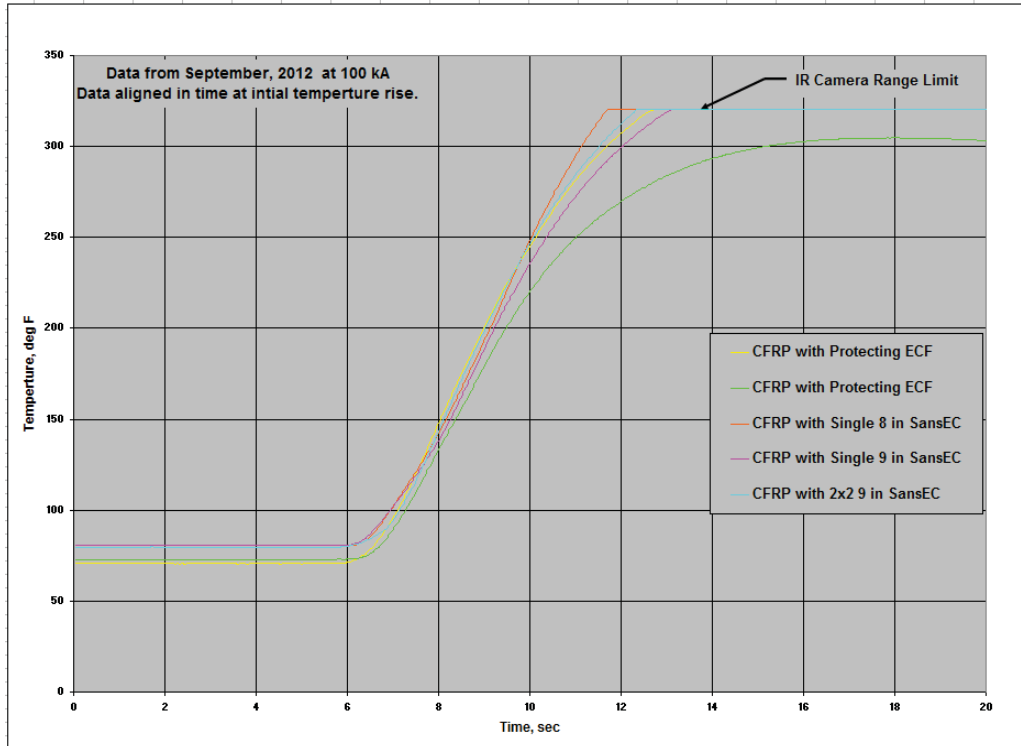


Figure 9.26. CFRP panel backside temperature profiles comparing protected (ECF) and SansEC configurations. Data aligned in time at start of temperature rise.

### 9.5 Lightning Attachment on SansEC Sensor CFRP Test Panels

High speed video imagery and time lapse photography were collected to provide additional insight into the lightning attachment phenomena on CFRP substrates. A 4 second shutter speed was used to collect the time lapse photography to observe the lightning strike attachments on the test panels. Figure 9.27(a) and (b) show the time lapse photography of lightning attachment to a painted aluminum plate and baseline protected CFRP test panel respectively. Figure 9.28(a), (b), and (c) present time lapse images of lightning attachment to the 6", 8" SansEC and 8" SansEC Array LSP CFRP test panels. The lightning attachments on the SansEC panels are shown to be more dispersive in nature with multiple attachment points visible in the images. The 8" SansEC Array LSP CFRP time lapse photo in Figure 9.28(c) shows the attachments occur outside the perimeter of the four SansEC sensors.

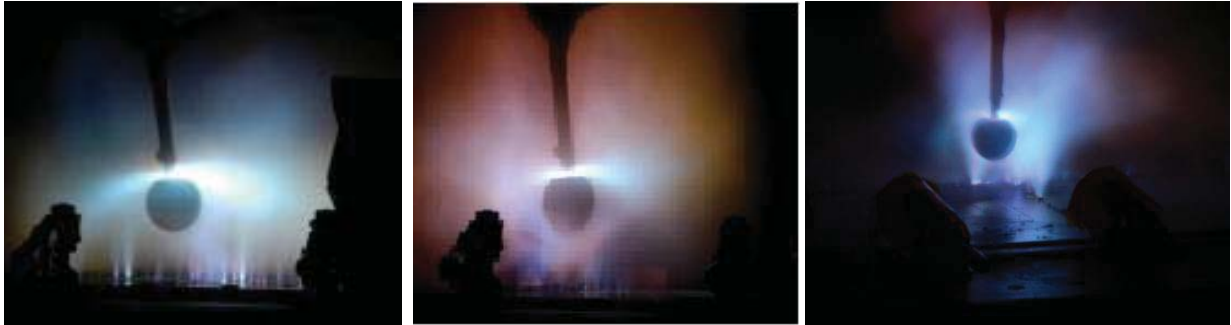


(a) Painted aluminum plate.



(b) Protected CFRP test panel.

Figure 9.27. 4 second time lapse photos of lightning attachment at 100 kA.

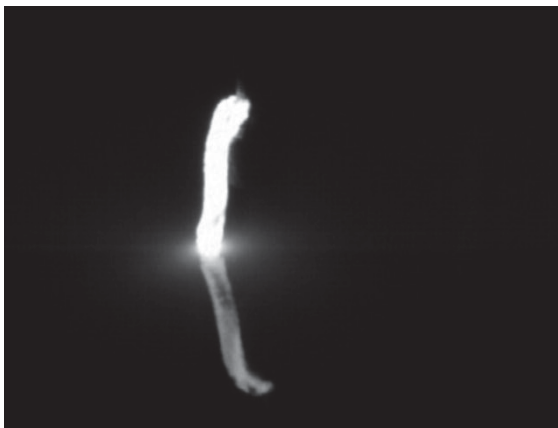


(a) 6" SansEC LSP on CFRP. (b) 8" SansEC LSP on CFRP. (c) 8" SansEC array LSP on CFRP.

Figure 9.28. 4 second time lapse photos of lightning attachment at 100 kA.

To further illustrate the SansEC sensors ability to disperse the lightning current we will compare the first few frames of the high speed video for the baseline protected panel and SansEC LSP configurations. Figure 9.29(a) and (b) presents the first and second high speed video frames for the baseline protected CFRP test panel collected at 35,000 fps. In Figure 9.29(a) the lightning arc column shows a well-defined attachment point. Figure 9.29(b) shows the next frame in the video 28 microseconds later. Notice the shock wave radiating from the attachment point. The lightning plume for the 8" SansEC LSP panel presented in Figure 9.30(a) shows significantly more spreading to the initial attachment than the baseline protected CFRP panel. Figure 9.30(b) shows the lightning attachment 100 microseconds later (video recorded at 10,000 fps) for the same 8 in SansEC LSP CFRP panel.

The 8" SansEC Array LSP panel's lightning attachment still images are shown in Figure 9.31(a) and (b). The video was recorded at 67,000 frames per sec. Figure 9.31 shows a well-defined initial lightning attachment striking the center of the panel on the ground path between the four 8" SansEC sensors. The lightning channel looks very similar to the strike occurring on the baseline protected CFRP panel since the attachment is to a copper ground and not on the sensors themselves. Figure 9.31(b) presents the image of the strike 15 microseconds later. Notice the damage occurring on the two ground paths bisecting the four sensors. A shock wave is also visible in the image. A photograph of the unpainted 8" SansEC Array LSP CFRP panel was presented earlier in Figure 9.21(a) depicting the two ground paths running perpendicular to each other between the 4 SansEC sensors.

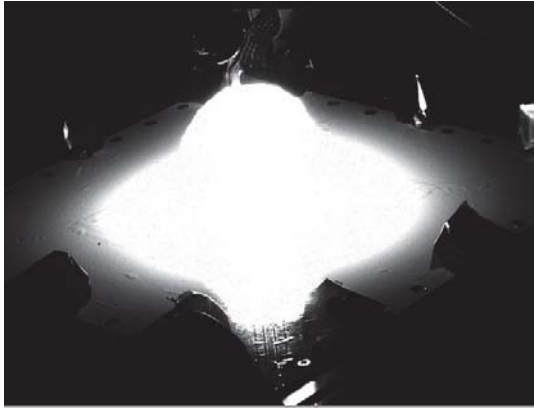


(a) First frame showing initial attachment.

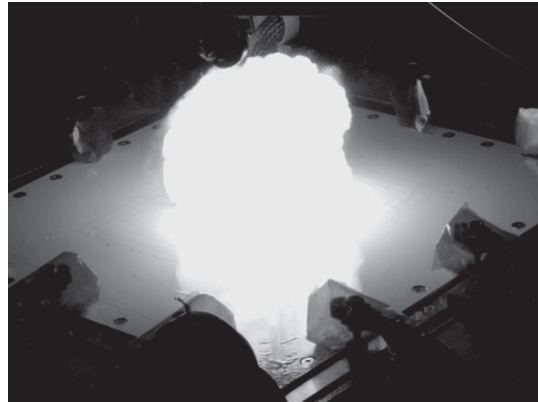


(b) 28 microseconds after attachment.

Figure 9.29. High speed video still images on baseline protected CFRP panel struck at 100 kA.

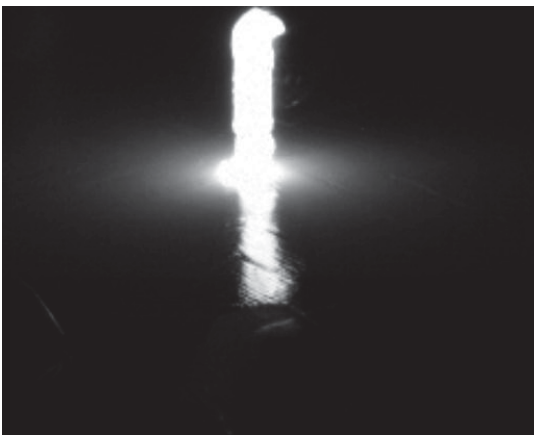


(a) First frame showing initial attachment.



(b) 100 microseconds after attachment.

Figure 9.30. High speed video still images on 8" SansEC LSP CFRP panel struck at 100 kA.



(a) First frame showing initial attachment.



(b) 15 microseconds after attachment.

Figure 9.31. High speed video still images of 8" Array SansEC LSP CFRP panel struck at 100 kA.

Figure 9.32 presents the IR image collected during the lightning strike for the same 8" SansEC Array LSP CFRP panel. The IR image confirms the lightning attachment at the center of the test panel and shows heating on the ground paths between the 4 SansEC sensors and also along a portion of the sensors perimeter. The hot spot shown in the top center of the image is from lightning attachment to a fastener attaching the aluminum ground bar to the CFRP panel.

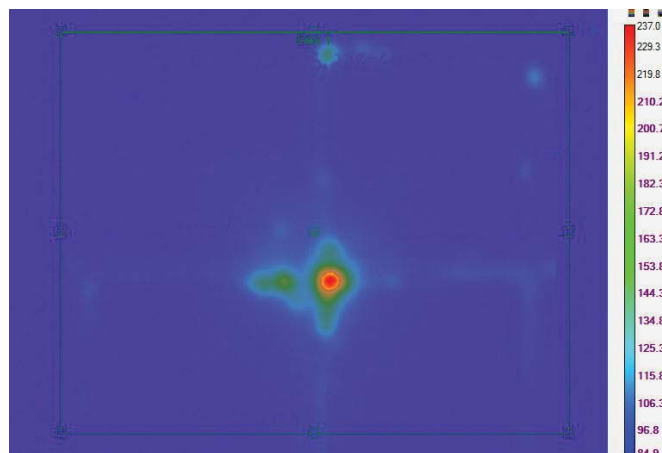


Figure 9.32. IR image of 8 in SansEC Array LSP CFRP panel.

A post-strike photograph of the 8” SansEC Array LSP CFRP panel is shown in Figure 9.33. The damage to the center of the panel is clearly obvious. The outer perimeter traces on three of the four SansEC sensors in the array show signs of lightning attachment with no visible current path on the surface. The logical explanation for this would suggest a portion of the lightning current injected during the high current pulse was pushed toward the perimeter of the sensor by Lorentz forces. The 4 fasteners bisecting the 4 sensor quadrants also show black smoke marks indicating lightning attachment and further supports this belief. High voltage lightning tests were not conducted on SansEC sensor panels. High voltage testing that incorporated an oscillatory charge would provide a better measure of the influence of the Lorentz forces and a more appropriate method to study lightning attachment.

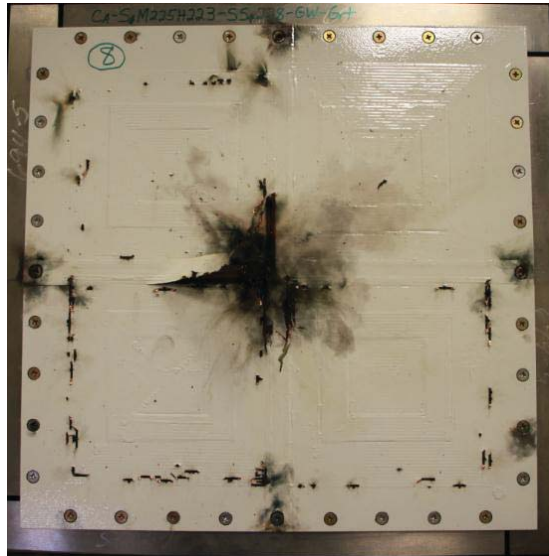


Figure 9.33. Photograph of post-strike 8” SansEC Array LSP CFRP panel.

## 10.0 CFRP DAMAGE ASSESSMENT COMPARISONS

Damage assessments were conducted on the post-strike CFRP panels in accordance to guidance in NASA DOC-128697 by the National Institute for Aviation Research (NIAR) at Wichita State University under a NASA contract established in May 2013. The NASA document was sufficient to enable NIAR to quote the task and perform the damage assessment without additional clarification. Table 10.1 presents a summary of the nondestructive damage assessment showing the pulse echo (PE) damage depth measurement and Through Transmission Ultrasound (TTU) damaged area measurements for protected and unprotected CFRP panels at 20, 40 and 100 kA strike currents and for 3 SansEC LSP configurations at 100 kA.<sup>[50]</sup> The data shows a fairly wide variation in damage depth and damage area within the same test configuration and current level. This is likely due to the long duration Component C\* waveform which can wander aimlessly along the top surface of the test panel resulting in variations in the damaged areas. Comparisons of like panels at the same current level typically show deeper damage depth and a smaller damaged area. Additional test panels are needed to increase the statistical data set to improve confidence in this data trend. The damage depth value quantifies the composite ply level and necessitates the severity of the composite repair.

Table 10.2 presents the averaged damage depth and damage area from data in Table 10.1 for each test scenario. The unprotected panels indicate deeper damage over a larger area than protected panels at the same current level. However, comparisons between the same panel configurations at different current levels does not show a meaningful trend as one would expect. This is likely the result of the long duration Component C\* waveform randomly wandering on the panel surface and further suggests additional test data are needed to improve statistical confidence. The lightning mitigation performance of three SansEC configurations compared very well to the averaged mitigation performance of the baseline protected CFRP panels at 100 kA. The average damage depth of the baseline protected CFRP panel was 0.041 in at 100 kA. The damage depth for the 3 SansEC test panels was 0.035, 0.022, and 0.013 inches at 100 kA respectively. The average damage area for the baseline protected panel was 5.97 inches at 100 kA. The damage area for the 3 SansEC configurations was 5.326, 8.668 and 8.140 inches at 100 kA respectively. The 8” SansEC LSP CFRP panel showed less damage depth and damage width and the 8”

SansEC Array LSP CFRP panel showed almost 70% less damage depth than the baseline protected CFRP panel average.

Table 10.1. Nondestructive Damage Assessment Summary

Test Panel	Peak Input Current, kA	Maximum Damage Depth per PE, in	Damage Area per TTU, in <sup>2</sup>
Unprotected CFRP	20	0.028	4.552
Unprotected CFRP	20	0.083	5.978
Unprotected CFRP	20	0.026	9.491
Unprotected CFRP	40	0.054	4.831
Unprotected CFRP	40	0.045	4.430
Unprotected CFRP	40	0.036	7.855
Unprotected CFRP	100	0.048	8.350
Unprotected CFRP	100	0.060	10.707
Unprotected CFRP	100	0.055	9.771
Protected CFRP	20	0.050	3.244
Protected CFRP	20	0.035	7.345
Protected CFRP	20	0.038	2.558
Protected CFRP	40	0.040	6.500
Protected CFRP	40	0.038	4.895
Protected CFRP	100	0.031	6.688
Protected CFRP	100	0.050	5.145
Protected CFRP	100	0.042	6.091
Protected CFRP with Single 8 in SansEC	100	0.035	5.326
Protected CFRP with Single 9 in SansEC	100	0.022	8.668
Protected CFRP with an Array of 2x2 8 in SansEC	100	0.013	8.140

Table 10.2. Averaged Nondestructive Damage Assessment

Test Panel	Peak I (kA)	Average Damage Depth per PE, in	Area per TTU, in <sup>2</sup>
Unprotected	20	0.056	6.67
Unprotected	40	0.045	5.7
Unprotected	100	0.054	9.61
Protected	20	0.041	4.38
Protected	40	0.039	4.24
Protected	100	0.041	5.97

## 11.0 CFRP SHIELDING EFFECTIVENESS COMPARISONS

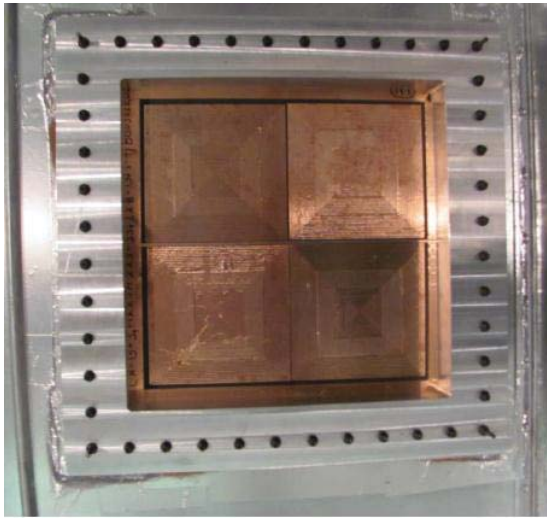
Shielding effectiveness measurements were conducted on the pretest CFRP (baseline protected, unprotected and SansEC sensor LSP configurations) test panels to quantify the performance metrics to enable comparison between baseline protected CFRP panels with SansEC LSP CFRP panels. The measurements were performed at the National Institute for Aviation Research (NIAR) at Wichita State University under a NASA contract established in May 2013.<sup>[51]</sup>

The shielding effectiveness measurements were carried out using a reverberation method from 100 MHz to 18 GHz. This was accomplished using two separate metal chambers (a transmit chamber and a receive chamber) attached only by an 18 in x 18 in (0.46 x 0.46 m) access panel to allow for complete isolation between the chambers. For this test fixture, the cutoff frequency is 328 MHz, meaning that the test fixture opening of 18” x 18” (0.46 m x 0.46 m) allows frequencies above 328 MHz to pass through without attenuation. The panels were tested at 20 frequencies per decade.

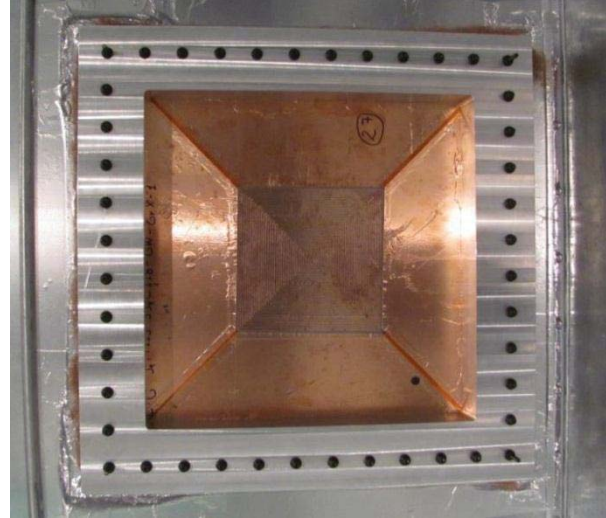
The reverberation method was selected due to its effectiveness at creating isotropic, uniform, randomly polarized fields. An electromagnetic field is created at random points inside the reverberation test chamber by a superposition of individual plane waves incident at numerous random angles. Each plane wave contains electric and magnetic components that are perpendicular to one another and to the direction of incidence. The direction of incidence of each plane wave changes with each movement of the chamber paddle wheel. This creates a change in the boundary condition of the resonant cavity (reverberation chamber). A full turn of the chamber paddle continuously changes the boundary conditions, therefore changing the incidence of each plane wave. A chamber that is sufficiently stirred by a paddle over one rotation creates a statistically uniform, randomly polarized, isotropic electromagnetic field at the face of each test panel.

Measurements were first taken without a panel installed in the test fixture. This provides the 0 dB attenuation reference that all panel data is referenced to. When determining the shielding effectiveness, an aluminum panel was considered the baseline for comparison with other panel materials. The difference between the aluminum panel measurement and the open-hole reference measurement determined the dynamic range that could be expected from the test setup. The aluminum panel provided enough shielding effectiveness when installed in the test fixture that a pre-amp connected to the receive antenna would be necessary from 1-18 GHz. After the open-hole measurement was made, a test panel was installed in the fixture. The difference between the open-hole reference measurement and the test panel measurement is considered the value of the shielding effectiveness of the material. The open-hole reference and test panel measurements both contain all chamber insertion losses, so when the difference between the measurements is taken the insertion loss was essentially cancelled out of the final shielding effectiveness value. Figure 11.1 shows photographs of SansEC LSP test panels installed in the chamber test fixture.

Figure 11.2(a) presents the calibrated shielding effectiveness data curves for the aluminum reference plate, protected and unprotected CFRP panels and three SansEC CFRP test panels. The shielding value is shown on the y axis from 0 to 150 dB in a linear scale. The x axis displays the frequency from 100MHz to 18 GHz on a logarithmic scale. The aluminum reference plate is shown to have highest shielding effectiveness values as expected. The three SansEC panel curves fall in the middle above the protected and unprotected CFRP panels. Figure 11.2(b) presents the linearized trends of the same data in Figure 11.2(a) generated from the linear curve fit function in Microsoft Excel. The protected and unprotected CFRP panel linear trend curves lie on one another and appear to be suspect. Because the protected and unprotected CFRP panels used to perform the shielding effectiveness testing were pre-strike LSP panels they had paint on them. The SansEC panels had not been painted yet, which created a tighter conductive seal to the chamber wall. The two painted panels did not have as tight a conductive seal and allowed radiation leakage to occur around the perimeter of the panels preventing accurate characterization. The manufacture of the Dexmet 3CU7-100FA LSP qualifies the shielding effectiveness of their product to be 10 dB at 10GHz. The shielding effectiveness of the unprotected panel is shown to be around 65 dB in the measurement and likely could be reduced another 5 dB with proper grounding to prevent leakage. It seems reasonable to make the assumption the approximate value of the shielding effectiveness of the CFRP is around 70 dB at 10GHz. A baseline protected panel would then expect to have around 80 dB shielding value. The SansEC shielding values at 10GHz fall plus or minus 3 dB around the 80 dB value.

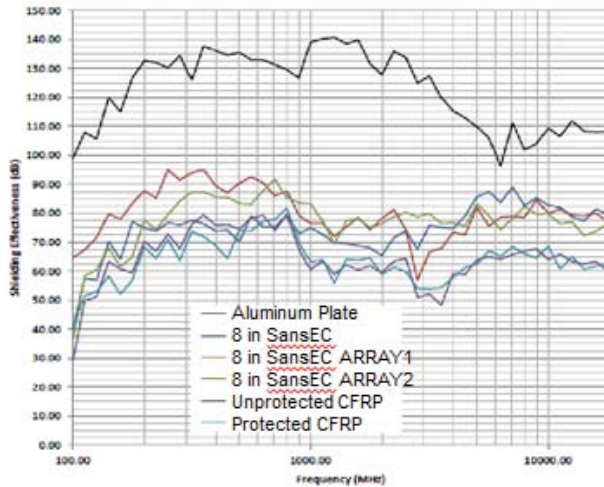


(a) 8 in SansEC Array LSP on CFRP.

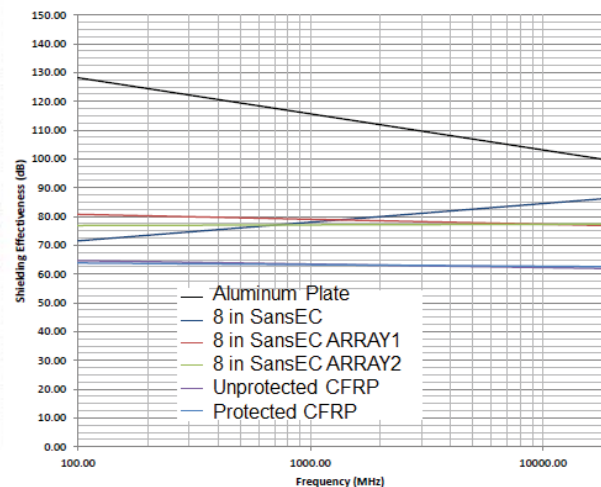


(b) 8 in SansEC Array on CFRP.

Figure 11.1. Photographs of SansEC LSP CFRP panels installed in chamber test fixture.



(a) Calibrated shielding effectiveness data curves



(b) Linearized shielding effectiveness data curves

Figure 11.2. Shielding effectiveness curves for aluminum, protected, unprotected and SansEC CFRP panels.

## 12.0 RELAVENCE TO NASA AVIATION SAFTEY PROGRAM

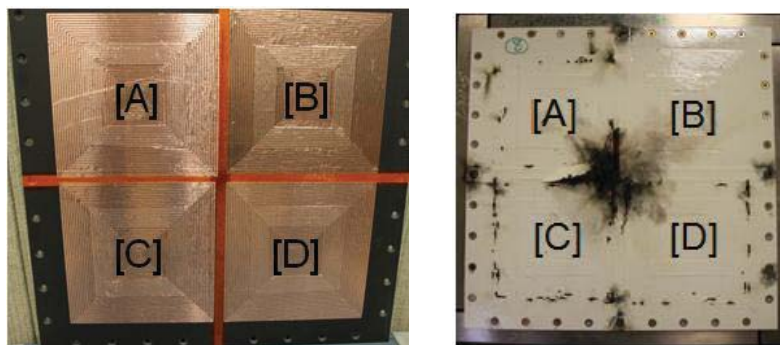
This research was established to demonstrate a multi-functional sensor for aircraft lightning protection capable of meeting lightning strike protection characteristics required in zone 2A (majority of aircraft surface, fuselage and wings per SAE 5414) with less weight compared to common practice conductive mesh technologies used on composite aircraft skins. In addition, the sensor should demonstrate the ability to detect & diagnose damage scenarios including delamination, punctures, and rips. Limited test data was developed to show successful completion of these two goals and further research is needed to optimize the performance characteristics for each of these metrics to realize the full potential the SansEC Sensor smart skin technology can offer.

The SansEC LSP CFRP test panels were subjected to lightning test conditions required for zone 2A and evaluated under strict accordance to the Universal Common Practice Lightning Energy Transfer Characterization guidance documents to enable direct comparison to a similarly tested flight certified baseline protected CFRP system. The 8” SansEC LSP CFRP panel showed less damage depth and damage width and the 8” SansEC Array LSP CFRP panel showed almost 70% less damage depth than the baseline protected CFRP panel averaged damage depth. These results demonstrate an equivalent level of protection as compared to an acceptable flight certified LSP system.

To demonstrate the SansEC Sensor LSP achieved zone 2A protection equivalency at a reduced weight over the common practice conductive mesh technologies (baseline protected CFRP panels) the materials used in fabrication of each type of panel were calculated based on manufacture specifications. The total weight of the baseline lightning strike protection configuration (3 mil layer of Dexmet 3CU7-100FA expanded copper foil LSP and Cytec Surfamaster 905C Composite Surfacing Film) equates to .075lbs/sqft. The total weight of the 8” square SansEC LSP (70% coverage of 1.25 mil copper with 15 square inches of 5 mil Finemet flexible magnetic shielding) system was .0567 lbs./sqft. Both calculations exclude the carbon fiber substrate and paint and only include the actual weight of the LSP system as tested. It is expected the weight of SansEC LSP systems can be further reduced through optimization of the SansEC sensor’s high permeability material, refinements in the sensor geometry, and utilization of materials to better match specification requirements. The SansEC LSP configuration was fabricated using off the shelf commercially available materials without expertise in best practice aircraft fabrication techniques.

Shielding effectiveness measurements were also conducted and test results indicated the shielding performance levels were comparable to the common practice metal mesh LSP at 10Ghz. Radiation leakage from around the perimeter of the painted baseline protected CFRP panel prevented accurate comparison; however manufacturer specifications were used to develop a reasonable estimation of the shielding value of the baseline protected panel and determined the SansEC LSP panels tested were very comparable in shielding performance values and thus not expected to reduce the aircraft’s overall shielding effectiveness, which is dominated by doors and windows. Further research should be conducted if the shielding value is critical to the specific aircraft design, such as for an unmanned aircraft system with sensitive avionics or instruments. If required, further reductions in the shielding effectiveness values could be achieved through design enhancements to the sensor geometry.

The same 8” SansEC Sensor Array LSP test panel which was shown to provide acceptable LSP performance for aircraft lightning zone 2B and had a comparable shielding effectiveness to common practice LSP metal meshes at a lower weight was also used as an operational composite damage detection system in a ground based demonstration. Figure 12.1(a) shows a photograph of the 8 in SansEC Sensor Array LSP test panel before being painted. The four 8” SansEC sensors are designated A thru D. Figure 12.1(b) shows a photograph of the 8” SansEC Sensor Array LSP test panel after lightning strike damage. The sensor designations A thru D area again provided for reference. Previous analysis in this paper showed the lightning attachment occurred at the center of the panel to the ground path bisecting the sensor quadrants.



(a) Test panel before paint was applied. (b) Test panel with strike damage.

Figure 12.1. Photographs of 8” SansEC Sensor Array LSP test panel showing sensor location A thru D.

Reflection coefficient measurement data acquired on the four sensors (A thru D) on the 8” SansEC Sensor Array LSP test panel before the lightning strike and after the lightning strike are shown in Figure 12.2 (a), (b), (c), and (d). The reflection coefficient magnitude is shown on the y axis from 0 to -2dB. The data is plotted for frequencies from 10KHz to 20MHz on the x axis. The plots are arranged to represent the same position as they occur on the actual test panel. Each plot contains the pre-strike (blue curve) and post-strike (red curve) data for comparison. The four sensors do not have the same pre-strike characteristic curves as one might expect. We believe this is due to both the natural characteristic of the SansEC sensor being an asymmetrical device. Each sensor couples differently with the neighboring sensor based on its position and orientation on the panel. Differences can also be introduced by inaccuracies in our ability to manufacture exact duplicate sensors and from alignment imperfections between the SansEC geometry and high permeability mu layer. The reflection magnitude is much lower than we

expect we will achieve with further optimization, but it is measurable. If we look at the change in the reflection magnitude for each sensor the plots do behave as expected. The lightning strike damage is visible in the photograph on sensor [A] and [C] as shown in Figure 12.1 (b) and these two curves correspondingly indicate a significant deviation from the pre-strike baseline curves. Sensors [B] and [D] show very little change in their post-strike measurements compared to the pre-strike baseline measurements. These data demonstrate our ability to use a SansEC LSP smart skin weighing less than common practice metal mesh to detect damage in a carbon fiber composite structure caused by a zone 2B lightning strike waveform.

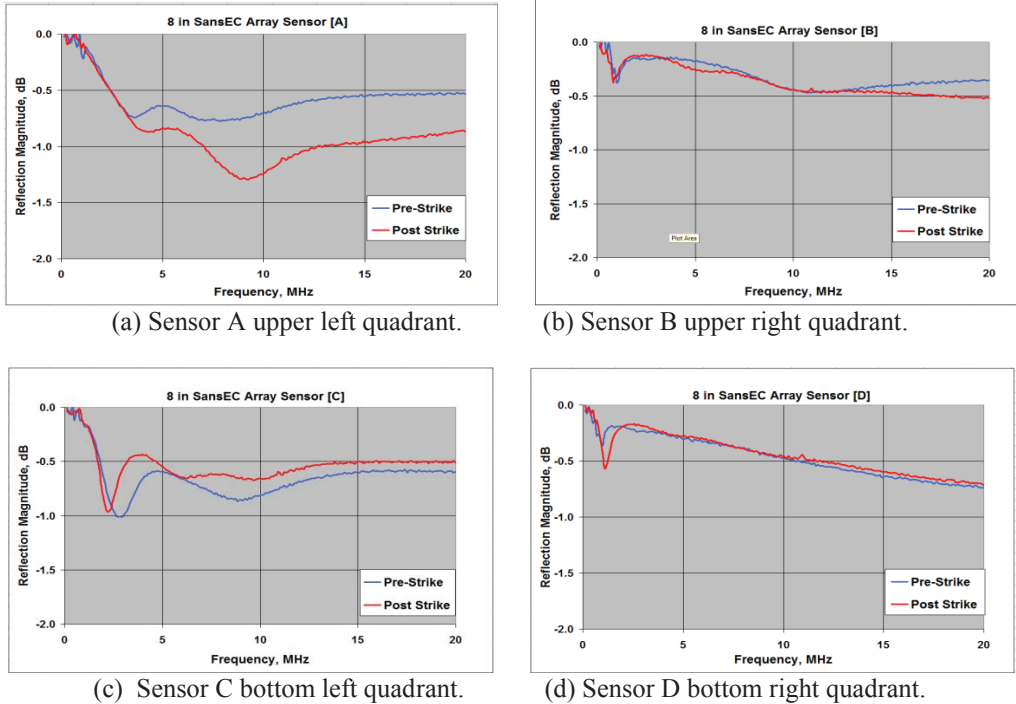


Figure 12.2. Reflection coefficient plots for the four sensors (A thru D) on the 8” SansEC Sensor Array LSP test panel pre and post lightning strike.

### 13.0 FUTURE RESEARCH

Significantly more work lies ahead to realize an operational SansEC smart skin technology ready for integration on a composite aircraft. The mathematical framework defined in this report will be used to optimize SansEC sensor design parameters for dielectric, non-conductive applications. Analytical trade studies will be conducted to develop performance curves to correlate the theoretical electrical parameters (Inductance, Resistance, Capacitance) with physical geometry variables (trace width, gap width and sensor trace length) for the square geometry. Once the free space (dielectric) sensor optimal design parameters have been determined, computational and theoretical analysis will focus on establishing the optimal high permeability parameters (numerical value of the permeability material, material thickness, material geometry and geometry beneath the SansEC sensor) to optimize the tradeoff between sustaining a measureable sensor response within the mu layer and amplifying the coupled magnetic field for deeper carbon composite penetration for damage sensing. Performance curves will be developed to correlate theoretical electrical parameters (Permeability, Inductance, Resistance, and Capacitance) of the coupled sensor/carbon composite system with the physical geometry variables (permeability, geometry, trace width, gap width and sensor trace length). Adequate computing resources are now available to the research team to enable an efficient effort to achieve these goals.

Once the design criteria to generate optimal square spiral sensors for detecting carbon composite damage have been established, the next phase of application development can begin. At this stage of development, a true determination of the sensor weight impact could be projected based on the makeup of the optimized sensor. With the optimized carbon composite SansEC sensor established, electrical impedance characterizations of common

composite damage modes can be conducted to develop data interpretation routines for the purpose of damage diagnosis. This will enable a determination of the maximum achievable damage detection threshold fidelity for expected fault type scenarios such as; barely visible impact damage (approx. 0.05 - 0.10-inch deep impression), impact damage in laminated structures not clearly visible from the exterior surface, heat exposure or aging composite damage including degradation of material properties due to extreme temperatures, moisture, or chemical exposure, matrix micro-cracking beneath painted surfaces and disbonds at composite-to-metal interfaces.

Computational and experimental analyses are needed to determine the full beneficial capabilities of designing SansEC arrays for lightning strike protection applications. Pursuing advanced LSP designs to take advantage of Lorentz force effects could provide revolutionary new approaches to manage or control lightning attachments for future composite aircraft. Research is needed to establish engineering approaches and investigations to quantify the expected achievable mitigation enhancements that could be obtained from designing sensors to manipulate the lightning propagation direction. Complementary research is needed to investigate the SansEC sensor's active contribution in establishing the condition for the electrical breakdown of air to occur on the sensor trace causing the lightning leader to be guided to that location. New experimental test procedures will need to be developed to quantify the influence of the sensor's electric field enhancement on lightning attachment. Existing test techniques commonly use static fields for high voltage long arc testing. Because the SansEC sensor requires an oscillatory waveform similar to a natural lightning waveform to establish the high electric fields at resonance, new test procedures will be required to adequately study lightning attachment zones. This research could eventually lead to less stringent zoning requirements for broader areas of the aircraft surface should sensor designs be shown to change the probability of lightning attachment. Less stringent zoning requirements in turn could realize a reduction in the overall aerial weight of the lightning strike protection system.

A number of significant challenging applications will become readily achievable within this technological framework. SansEC's passive wireless interrogation characteristics are highly sought for use in composite aircraft fuel quantity indicator systems to eliminate wires from protruding into the fuel cells. Wireless sensing will eliminate the potential lightning hazard from direct or induced lightning currents from igniting the fuel mixture. Certification procedures will be greatly simplified by having fewer potential fault scenarios to consider in identifying fault conditions. Wireless sensing the quantity of matter (gas, liquid, solid) in storage tanks and transfer pipelines is an immediate spin-off application resulting from this research. Integrating SansEC technology with advanced composite material developments should be considered as a means to further realize the benefits of smart sensing structures for future applications.

Thus far, the focus of the smart skin technology has been to provide LSP, damage detection and diagnosis. Additional smart skin functionality to improve situational awareness in harsh environments could potentially be achieved within this framework with further research. It is readily conceivable to expect the smart skin framework could be expanded to measure the humidity, temperature, and ice accumulation based on the huge dielectric difference among air, water and ice. Aerodynamic force and strain monitoring have already been demonstrated in prior related research. Quantifying the static charge in the surrounding clouds may be too ambitious a goal to realize within the confines of existing resources, but could provide a means dramatically improve the pilot's situational awareness of an imminent lightning threat. Through the acquisition and fusion of the environmental data parameters (humidity, temperature, pressure, air speed, cloud electrical charge, etc) imminent dangerous condition from weather related hazards such as icing and lightning could potentially be predicated before the flight condition becomes critical. The SansEC smart skin technology framework can support this type of evolution to achieve greater pilot situational awareness to further improve aircraft safety.

## **14.0 CONCLUSIONS**

The mathematical framework has been established to describe open circuit resonant sensors to verify the theoretical approach of their characteristic operation. Electromagnetic parametric equations were derived to optimize sensor designs to sense changes in the electrical impedance in FRC and CFRC substrates when placed in close proximity to the sensors near magnetic field. The foundational mathematical framework describing Lorentz Force effects from the SansEC sensors self-resonate radiation were also defined.

A new SansEC sensor configuration was developed to overcome the issue of electric field absorption from electromagnetic coupling into conductive carbon fiber composite substrates. The theory was established and

experimentally verified to prove a high permeability material thin film placed between the sensor and the conductive substrate could be used to control the field coupling and enable sensor operation on carbon composites. A portion of the magnetic field flux concentrated in the high permeability material is used to sustain the sensor self-resonant and the rest is used to couple induced currents into the conductive substrate to improve the penetration depth for damage sensing. The geometric design of the high permeability material establishes the impedance match between the sensor and carbon composite substrate and must be appropriately designed to effectively control the coupling coefficient. To achieve an optimal design for damage sensing, the tradeoff must be carefully balanced to preserve a portion of the energy in the form of oscillating magnetic field strong enough to keep the sensor resonate and at the same time, ensure the magnetic field coupling with the carbon composite is as strong as possible for maximum depth penetration. The research needed to achieve this proper balance is still ongoing.

Computational electromagnetic simulations were developed in the FEKO software suite to calculate the resonant response performance of SansEC designs on FRC and CFRC substrates. Electric field and magnetic field two dimensional plots were also calculated to visualize the concentration and distribution of the fields. Modeling on FRC substrates demonstrated the electric field enhancement in the area of a simulated delamination providing a visual substantiation as to the effective operation of the sensor. It was further shown on an FRC substrate the SansEC sensor will remain operational having damage on some broken traces. Computations were also demonstrated to evaluate one sensor configurations' ability to detect common damage faults of various sizes and at various ply depths in CFRP models. A CEM model was developed with a SansEC operating on a CFRP substrate and run repeatedly with various delamination depths modeled for each simulation. The data results showed a shifting of the sensor's resonant response demonstrating the efficacy of using SansEC sensors to detect and diagnose damage in CFRP substrates.

A universal common practice guide to conduct lightning energy transfer characterizations was developed by Boeing Research & Technology under NASA contract #NNL10AA05B to facilitate consistency in future carbon composite lightning strike protection evaluations. It provides the means to obtain performance correlations across data sets. The Universal Common Practice documents specify the processes required to manufacture (DOC-128694), inspect (DOC-12865), test (DOC-128696) and conduct post-strike damage assessments (DOC-128697) to compare LSP performance metrics on composite substrate test panels. The guidance also includes the LSP Composite Substrate Test Bed Design, NASA DOC-128698. This document describes a method to acquire real time monitoring of mechanical, thermal, and electrical parameters during plasma flashover arcing events. Specifications are provided to safely monitor electrical current, temperature, and mechanical shock with adequate detection thresholds to support high fidelity modeling of composite structures for direct effect lightning damage assessments. The procedures defined in the Universal Common Practice Guide were demonstrated and applied by NASA in two lightning direct effect tests conducted at the National Technical Systems' (NTS) Lightning Technologies (LTI) facility in Pittsfield, MA in September 2012 and July 2013 to quantify SansEC LSP performance metrics compared to those of a common practice LSP method to demonstrate comparable lightning strike protection attributes.

Baseline protected and unprotected CFRP lightning strike panels were subjected to the lightning direct effect Component D waveform at 20, 40 & 100 KA peak currents with follow on components B & C in a continuous lightning discharge in compliance with ARP5416. The electric current on the 4 edges of the test panels were independently monitored using current probes to acquire the current waveforms exiting the edges of the CFRP panel to characterize asymmetric current propagation. Laser displacement sensors were used to measure the peak deflection at the center of the panel during strike. Mechanical displacement data was collected to quantify LSP solutions to minimize damage caused by mechanical force from the lightning induced shock wave. The mechanical test data showed the unprotected CFRP panels have about 1 mm higher deflection than protected panels and calibration tests on an aluminum plate showed a higher deflection with paint than without paint. An IR camera was used to capture the temperature on the backside of the test panel during lightning strike to support lightning attachment and propagation analysis.

Damage assessments were conducted under a NASA contract in May 2013 by the National Institute for Aviation Research (NIAR) at Wichita State University on the struck CFRP panels in accordance to guidance in NASA DOC-128697. The unprotected test panels showed deeper damage over a larger area than protected panels at the same current level. However, comparisons between the same panel configurations at different current levels did not show a meaningful trend as one would expect and suggests additional test data are needed to improve statistical confidence.

Lorentz force effects generated from a resonant SansEC sensor can influence the direction and momentum of the lightning attachment and may provide a mechanism by which the aircraft strike point can be manipulated. After the initial strike attachment occurs, the electrical breakdown voltage between the lightning leader and the aircraft will determine the next swept stroke attachment location. The radiated emission from the lightning propagation, either from a laboratory generated lightning waveform or from naturally occurring lightning, will passively excite the SansEC sensor and establish a modal structure on the trace before lightning attachment occurs, preconditioning how the attachment will occur. An aircraft that has arrays of SansEC sensors covering the fuselage could provide a unique means to establish where the electrical breakdown of air occurs to guide the swept stroke lightning attachment to safer, predetermined destinations. A correlational study examined the location of heat signatures on IR thermal images resulting from lightning attachment and the two dimensional electric field distribution maps for the 7, 8 and 9 inch SansEC LSP test panels. A reasonable level of correlation existed, supporting the theory that high electric field regions on the SansEC trace during resonant state can influence where the electrical breakdown of air occurs at the onset of lightning attachment. High speed photography and time lapse images of lightning strikes to CFRP test panels were collected for SansEC LSP designs and baseline common practice LSP. These showed that the SansEC LSP altered the arc root dispersion attachment to the test panel. This is further evidence to suggest Lorentz force effects and the electrical breakdown of air are influenced by the SansEC sensor in its resonant state.

Limited lightning strike data was available to develop statistical confidence in the SansEC LSP performance but individual test cases showed very encouraging results. The 8 inch SansEC LSP CFRP panel showed less damage depth and damage width and the 8 inch SansEC Array LSP CFRP panel showed almost 70% less damage depth than the baseline protected CFRP panel average in side by side damage assessment comparisons. Direct weight comparisons of actual hardware used in the lightning tests showed the total weight of the baseline lightning strike protection configuration to be .075lbs/sqft and the total weight of the 8" square SansEC LSP system was .0567 lbs./sqft thus achieving the milestone weight metric. Even though the SansEC LSP test panel showed superior weight performance, additional optimization and fabrication techniques with realistic aircraft materials should further reduce the aerial weight of the SansEC LSP Array. The 8 inch SansEC Array LSP CFRP panel had 70% less damage depth than the baseline protected CFRP average. The SansEC Array also functioned as an operational sensor to detect damage on the panel. These results legitimize potential applications for a SansEC smart skin to provide lightning strike protection and damage detection on realistic fiber glass composite and carbon composite aircraft structures for zone 2A aircraft lightning strike protection (majority of aircraft surface, fuselage and wings per SAE 5414).

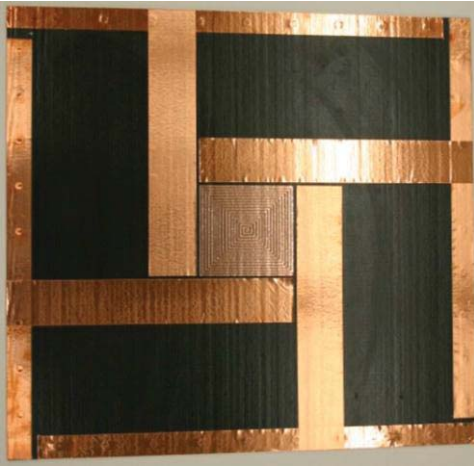
Shielding effectiveness measurements were conducted on the pretest CFRP (baseline protected, unprotected and SansEC sensor LSP configurations) test panels to quantify the performance metrics to enable comparison between baseline protected CFRP panels with SansEC LSP CFRP panels. The measurements were performed at the National Institute for Aviation Research (NIAR) at Wichita State University under a NASA contract established in May 2013. The baseline protected CFRP panel was calculated to have around 80 dB of isolation at 10GHz. The 8 in SansEC Array LSP shielding values at 10GHz are within plus or minus 3 dB around the 80 dB value.

## **15.0 APPENDIX A**

### **APPENDIX A**

#### **EXPERIMENTAL SANSEC SENSOR TEST DATA ON FIBERGLASS AND CARBON FIBER PANELS**

Fiberglass Panel - Configuration: Unpainted 4in SansEC (A)  
 Peak Current, kA: 40

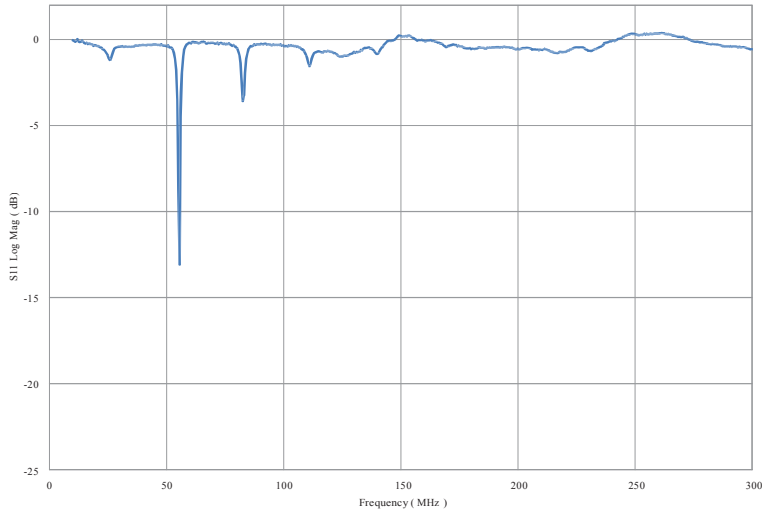


Pre Strike Photograph

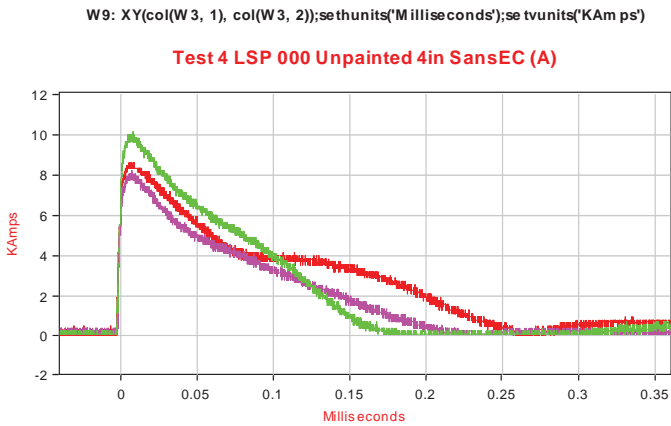


Post Strike Photograph

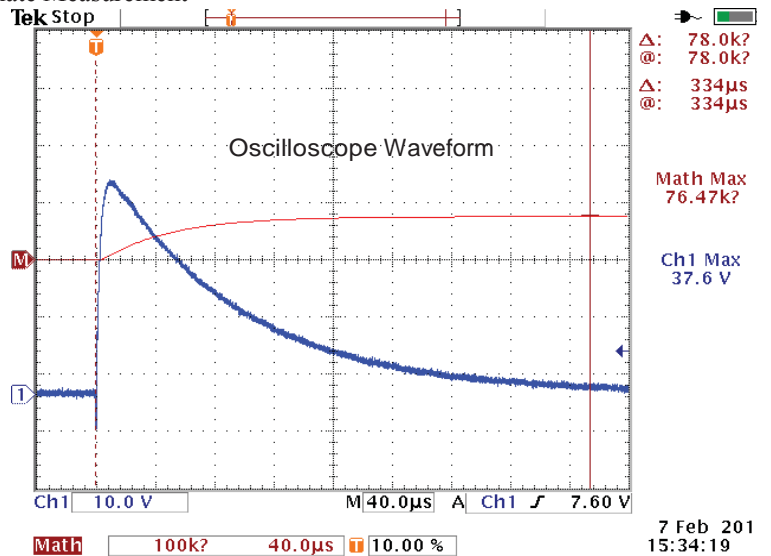
4 in SansEC LSP unpainted



Pre Strike Resonate Measurement



Channels 1-4 Ground Current

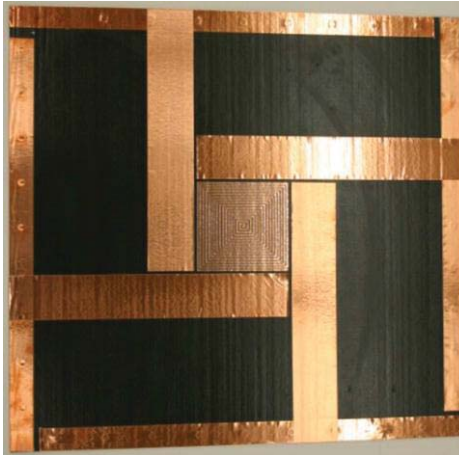


Input Current, kA verse Time, millsec

Figure A 1. Fiberglass substrate configuration performance. Configuration: Unpainted 4in SansEC (A)

# Fiberglass Panel - Configuration: Unpainted 4in SansEC (A)

Peak Current, kA: 40



Pre Strike Photograph



Post Strike Photograph

**Data not Available**

Panel Displacement: Displacement, mm verses Time, sec  
(This data is uncorrected for sensor placement angle. The scale factor for corrected data is 0.8572.)

**Data not Available**

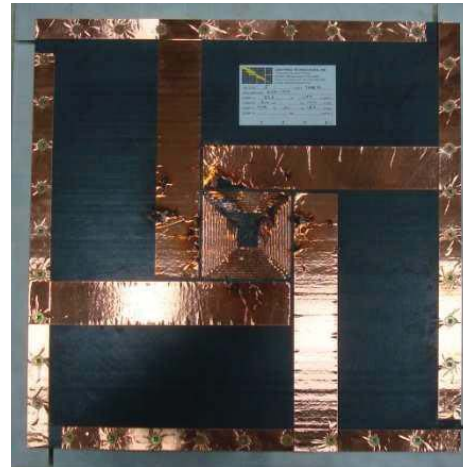
Panel backside IR image at sequential times. Note image has been flipped to provide a top side view.

Figure A 1. Concluded.

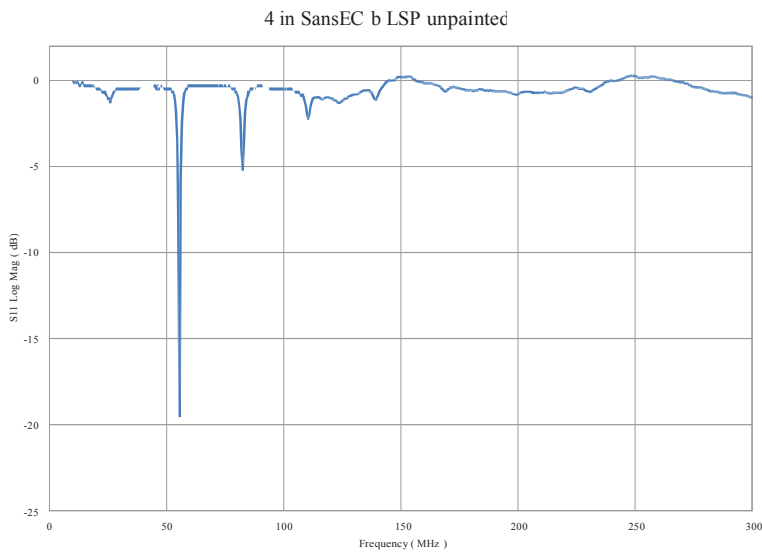
Fiberglass Panel - Configuration: Unpainted 4in SansEC (B)  
 Peak Current, kA: 40



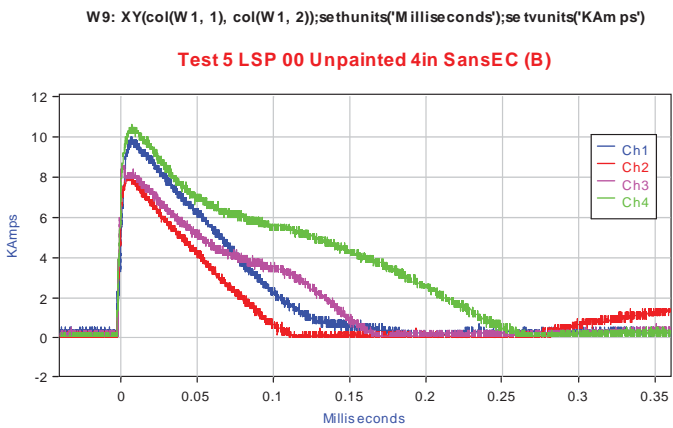
Pre Strike Photograph



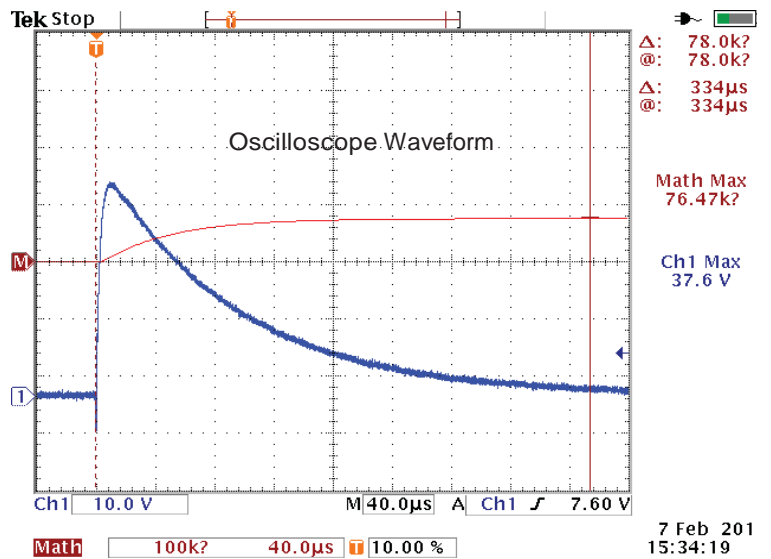
Post Strike Photograph



Pre Strike Resonate Measurement



Channels 1-4 Ground Current



Input Current, kA verse Time, millsec

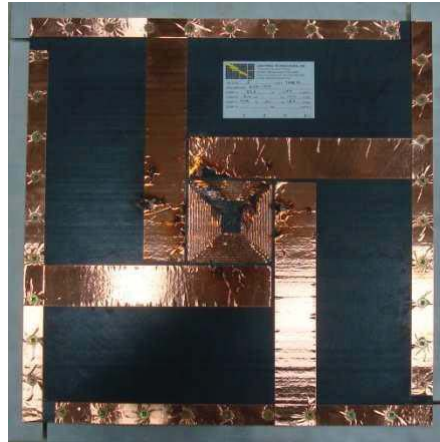
Figure A2. Fiberglass substrate configuration performance. Configuration: Unpainted 4in SansEC (B)

# Fiberglass Panel - Configuration: Unpainted 4in SansEC (B)

Peak Current, kA: 40



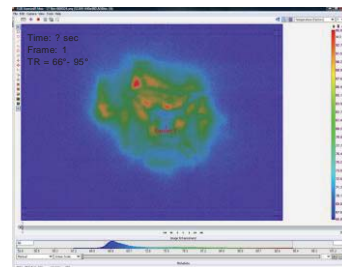
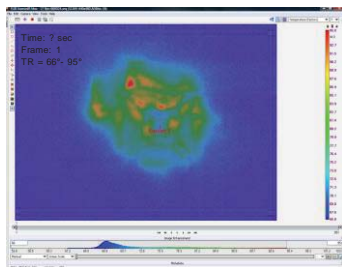
Pre Strike Photograph



Post Strike Photograph

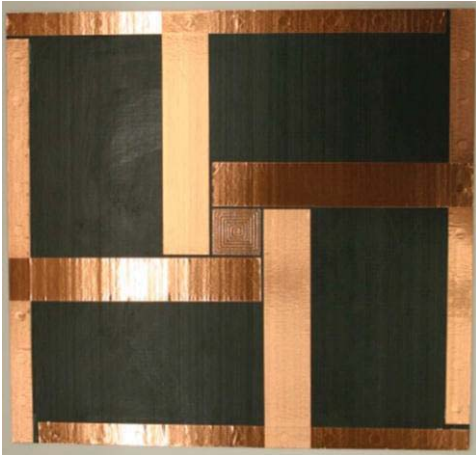
## Data not Available

Panel Displacement: Displacement, mm verses Time, sec  
(This data is uncorrected for sensor placement angle. The scale factor for corrected data is 0.8572.)



Panel backside IR image at sequential times. Note image has been flipped to provide a top side view.  
Figure A 2. Concluded.

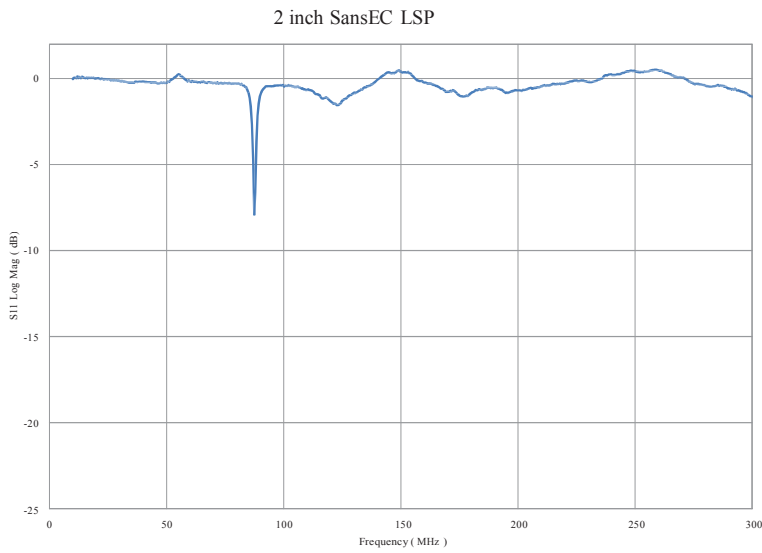
# Fiberglass Panel - Configuration: Painted 2in SansEC Peak Current, kA: 40



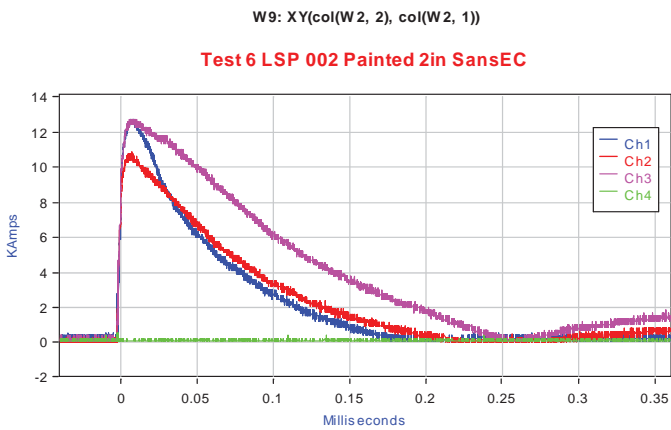
Pre Strike Photograph



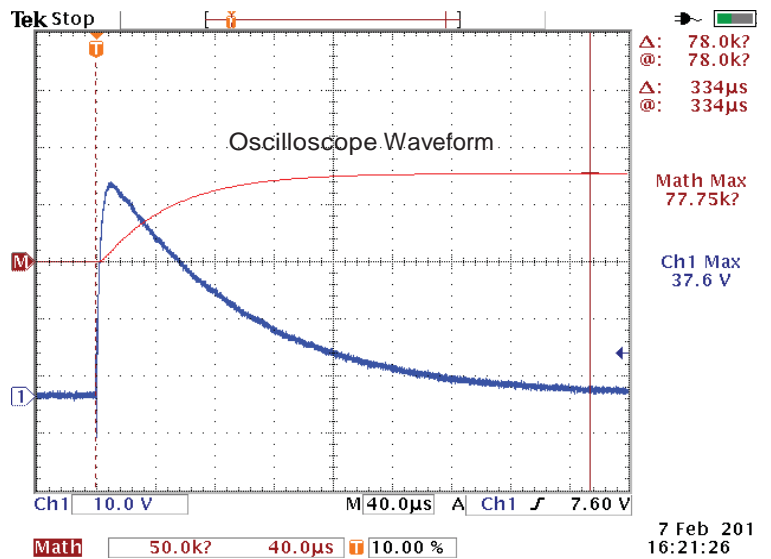
Post Strike Photograph



Pre Strike Resonate Measurement



Channels 1-4 Ground Current



Input Current, kA verse Time, millisecc

Figure A3. Fiberglass substrate configuration performance. Configuration: Painted 2in SansEC

# Fiberglass Panel - Configuration: Painted 2in SansEC

Peak Current, kA: 40

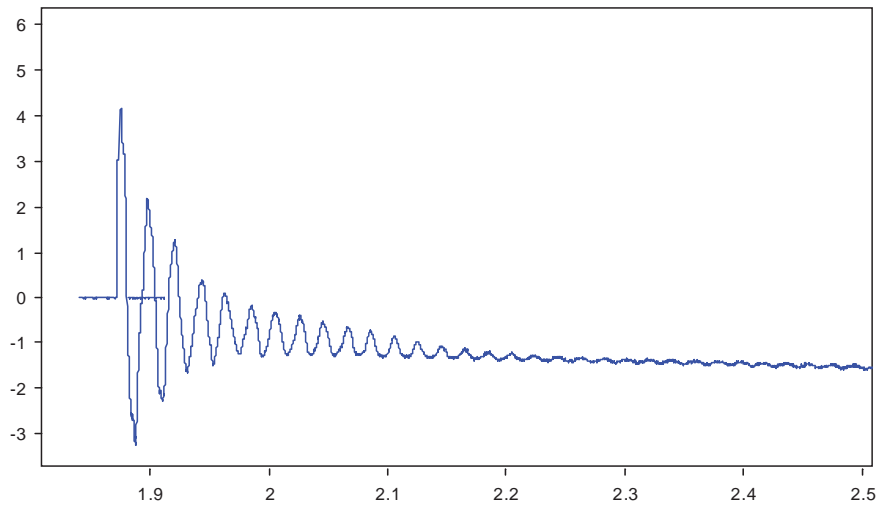


Pre Strike Photograph



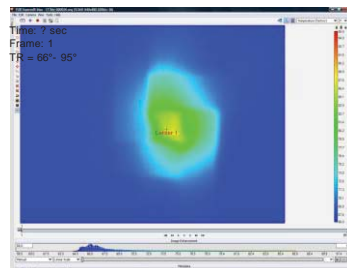
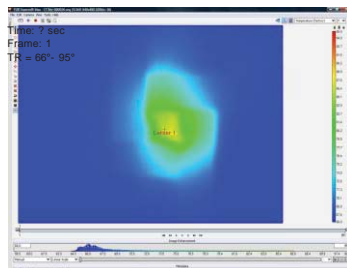
Post Strike Photograph

W2: XY(col(W 1, 1), col(W 1, 2))-06);se thunits('Se conds');se tvunits('m m')



Panel Displacement: Displacement. mm versus Time. sec

(This data is uncorrected for sensor placement angle. The scale factor for corrected data is 0.8572.)

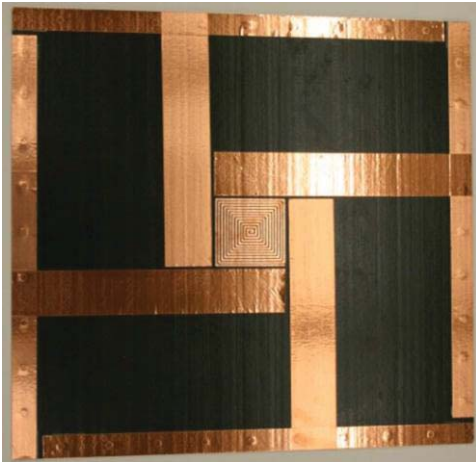


Panel backside IR image at sequential times. Note image has been flipped to provide a top side view.

Figure A 3. Concluded.

# Fiberglass Panel - Configuration: Painted 3in SansEC

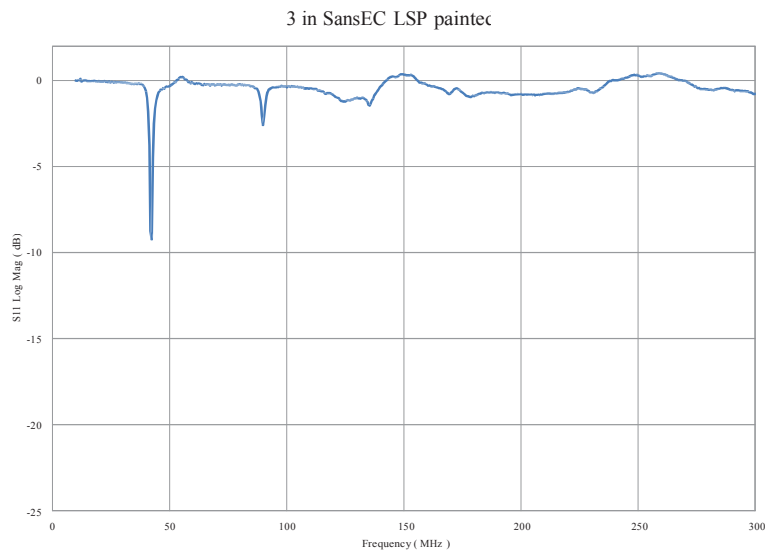
Peak Current, kA: 40



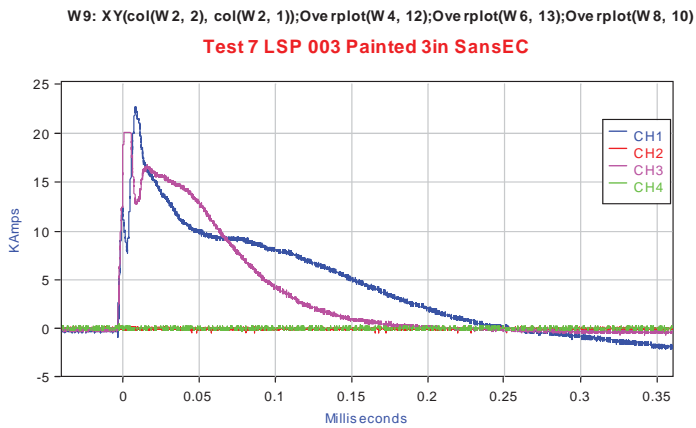
Pre Strike Photograph



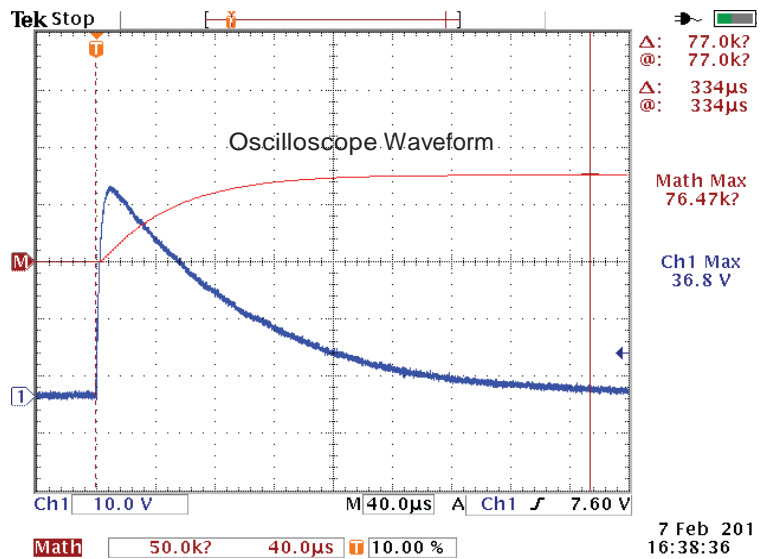
Post Strike Photograph



Pre Strike Resonate Measurement



Channels 1-4 Ground Current

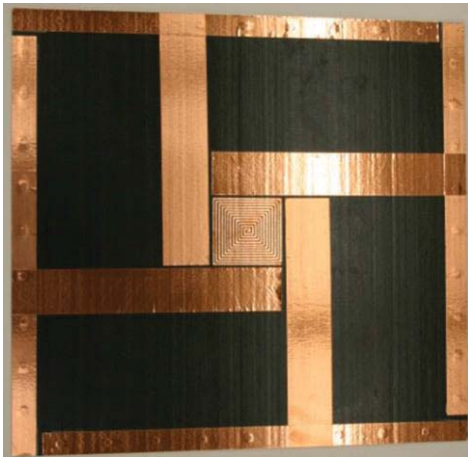


Input Current, kA verse Time, millisecc

Figure A4. Fiberglass substrate configuration performance. Configuration: Painted 3in SansEC

# Fiberglass Panel - Configuration: Painted 3in SansEC

Peak Current, kA: 40

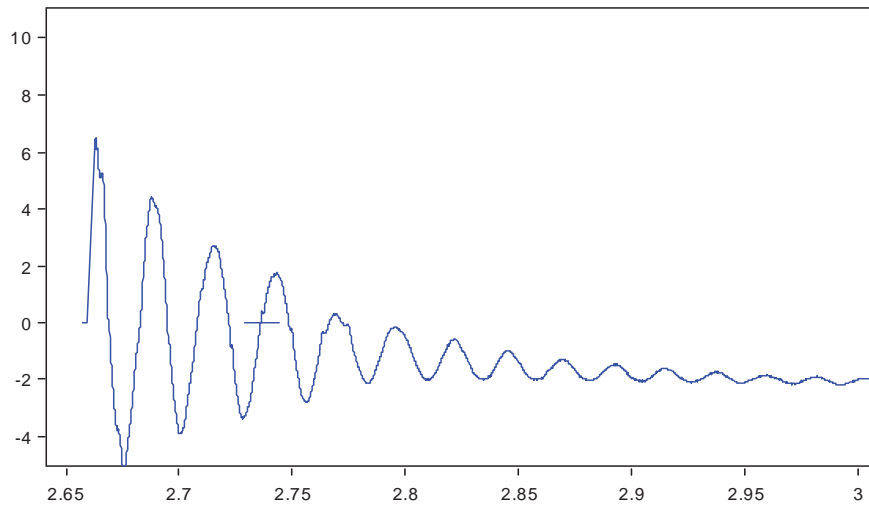


Pre Strike Photograph



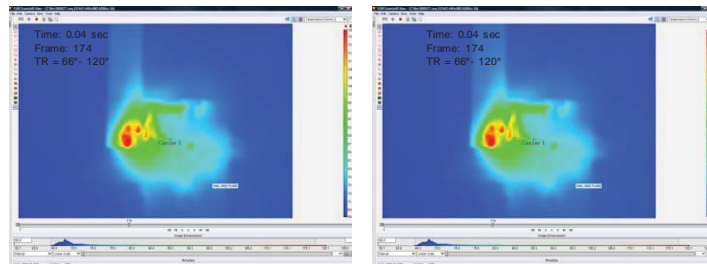
Post Strike Photograph

W2: XY(col(W 1, 1), col(W 1, 2))+.051);se thunits('Se conds');se tvunits('m m')



Panel Displacement: Displacement, mm versus Time, sec

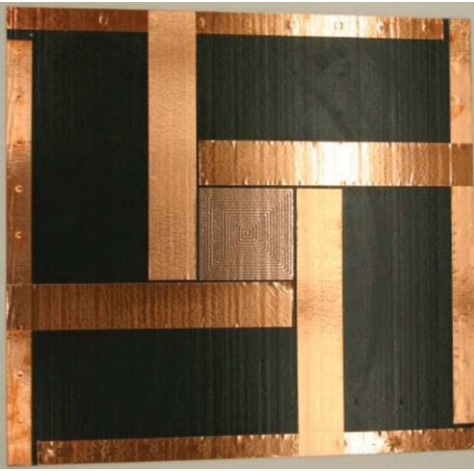
(This data is uncorrected for sensor placement angle. The scale factor for corrected data is 0.8572.)



Panel backside IR image at sequential times. Note image has been flipped to provide a top side view.

Figure A 4. Concluded.

Fiberglass Panel - Configuration: Painted 4in SansEC  
Peak Current, kA: 40

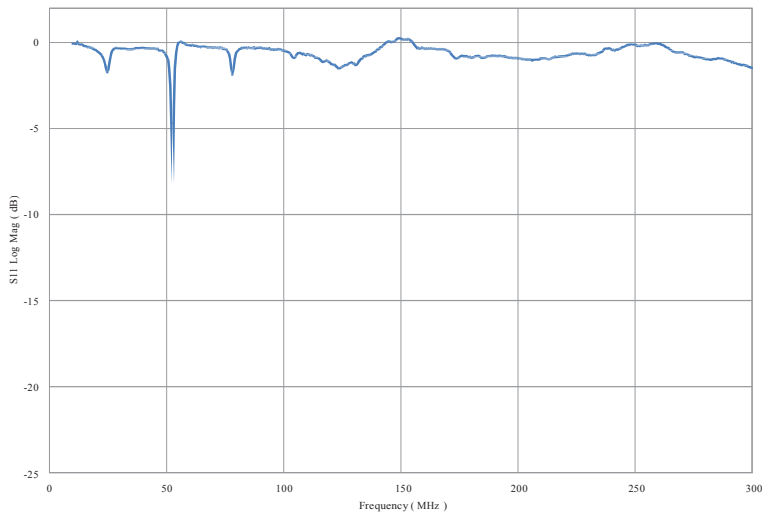


Pre Strike Photograph

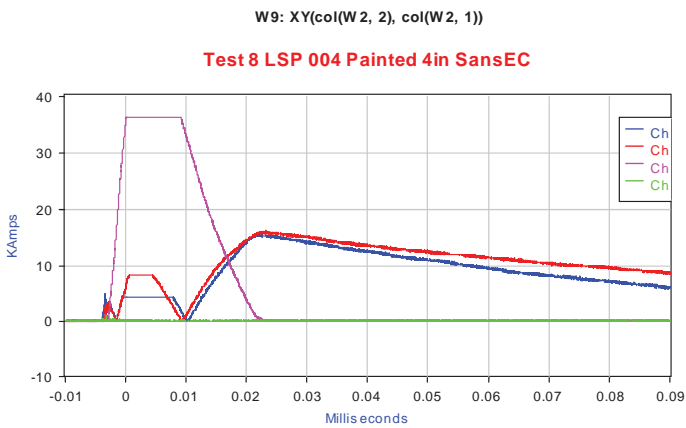


Post Strike Photograph

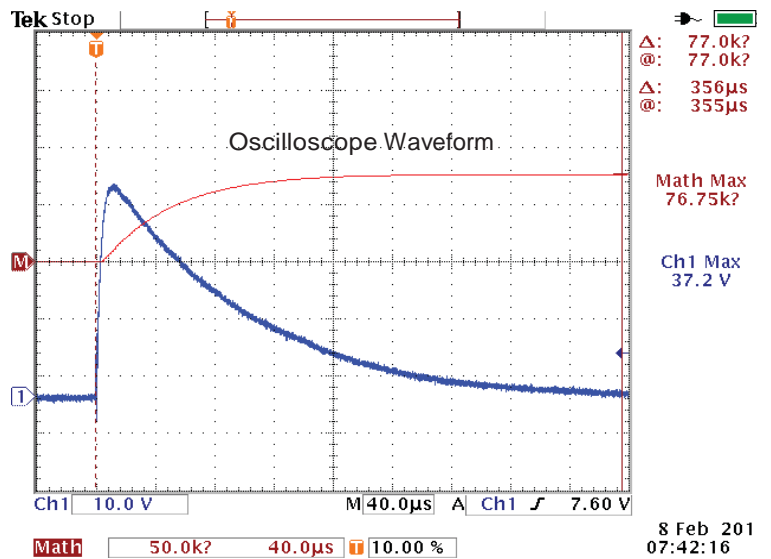
4 in SansEC LSP painted



Pre Strike Resonate Measurement



Channels 1-4 Ground Current

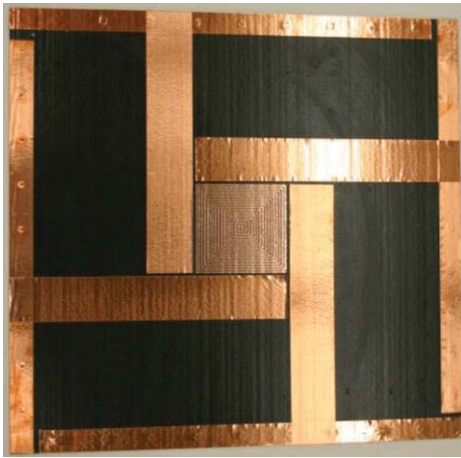


Input Current, kA verse Time, millisecc

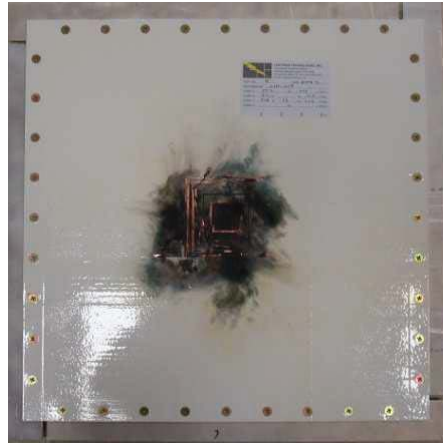
Figure A 5. Fiberglass substrate configuration performance. Configuration: Painted 4in SansEC

# Fiberglass Panel - Configuration: Painted 4in SansEC

Peak Current, kA: 40

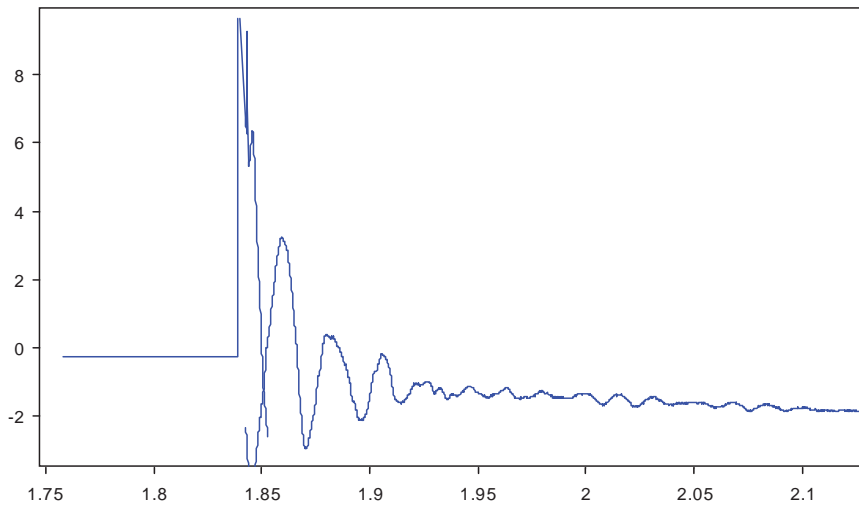


Pre Strike Photograph



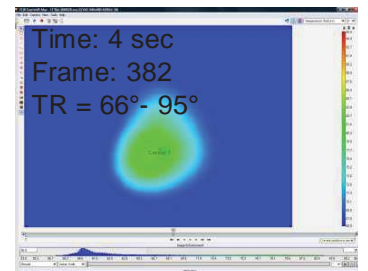
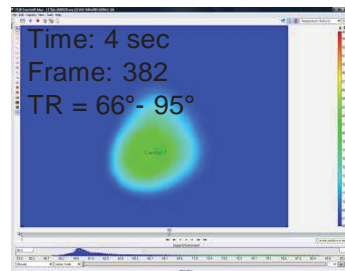
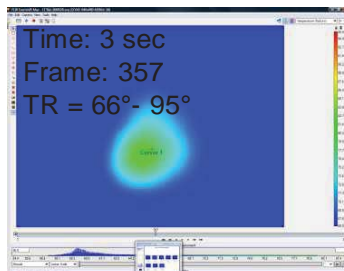
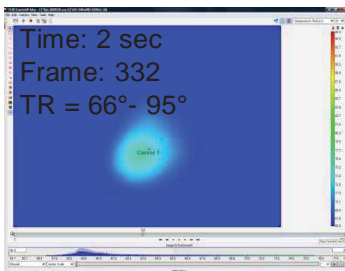
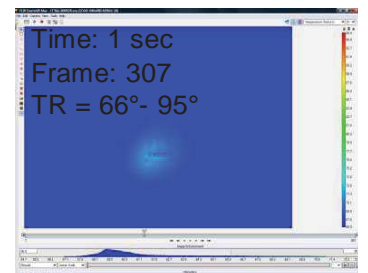
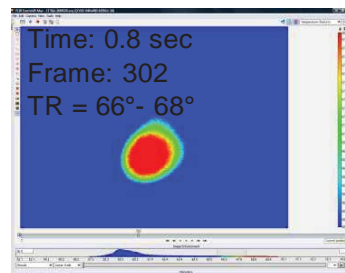
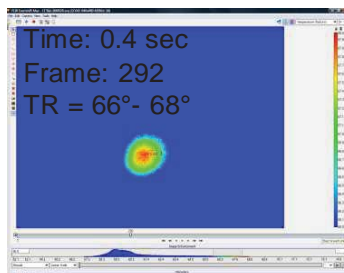
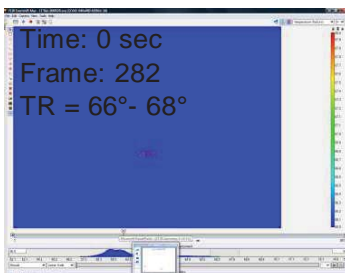
Post Strike Photograph

W2: XY(col(W 1, 1), col(W 1, 2)+1.834);se thunits('Se conds');se tvunits('m m')



Panel Displacement: Displacement. mm versus Time. sec

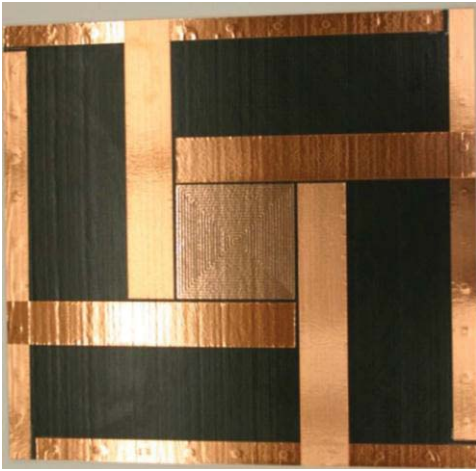
(This data is uncorrected for sensor placement angle. The scale factor for corrected data is 0.8572.)



Panel backside IR image at sequential times. Note image has been flipped to provide a top side view.

Figure A 5. Concluded.

Fiberglass Panel - Configuration: Painted 5in SansEC  
Peak Current, kA: 40

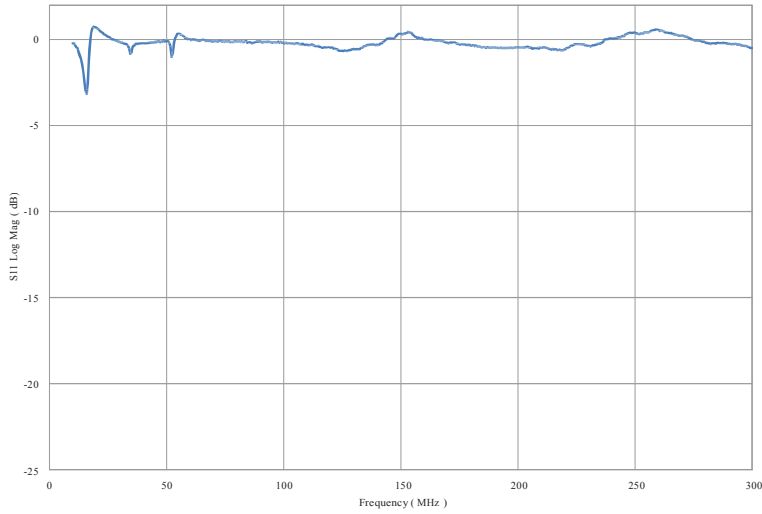


Pre Strike Photograph

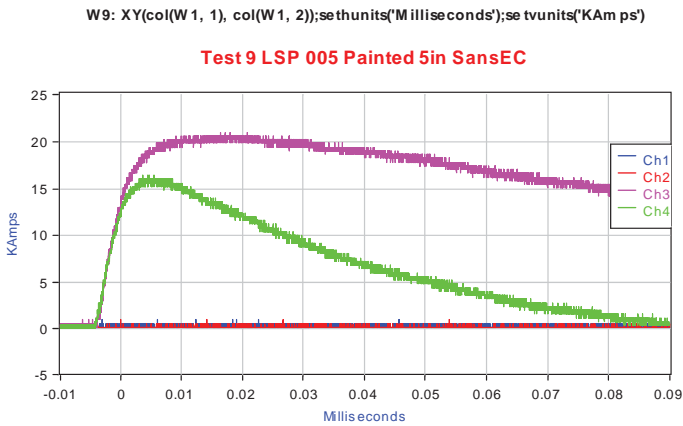


Post Strike Photograph

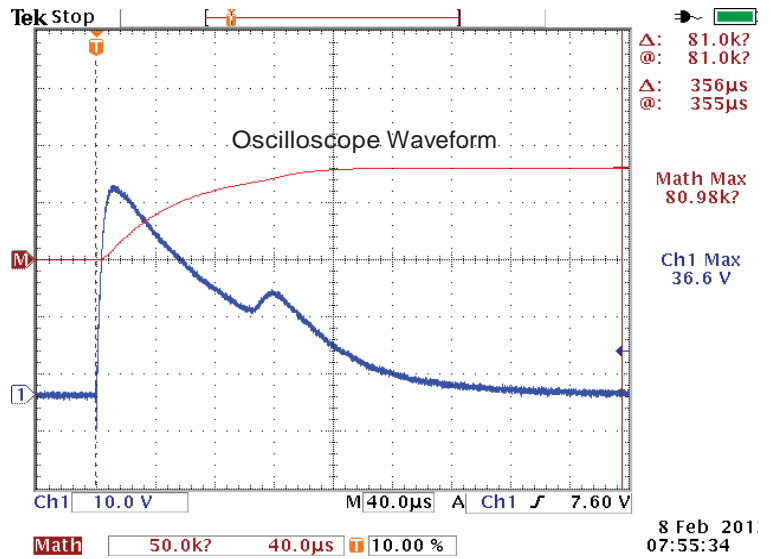
5 in SansEC LSP painted



Pre Strike Resonate Measurement



Channels 1-4 Ground Current

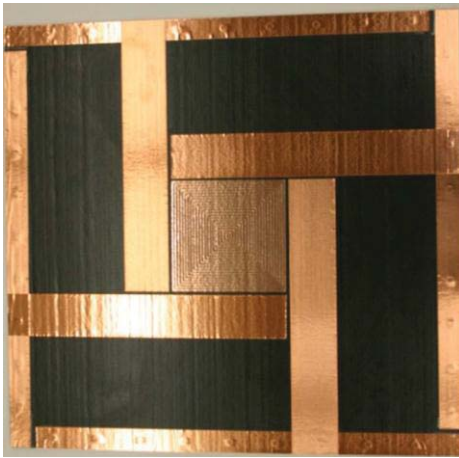


Input Current, kA verse Time, millisecc

Figure A 6. Fiberglass substrate configuration performance. Configuration: Painted 5in SansEC

# Fiberglass Panel - Configuration: Painted 5in SansEC

Peak Current, kA: 40

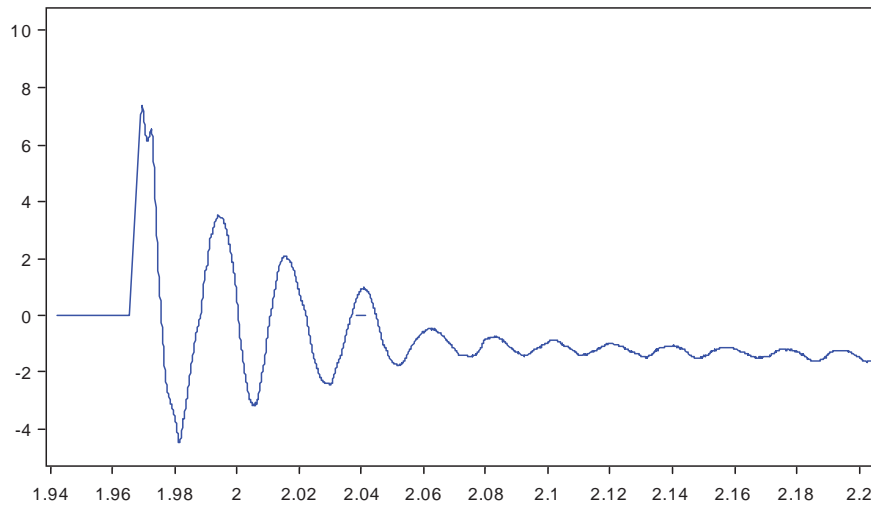


Pre Strike Photograph



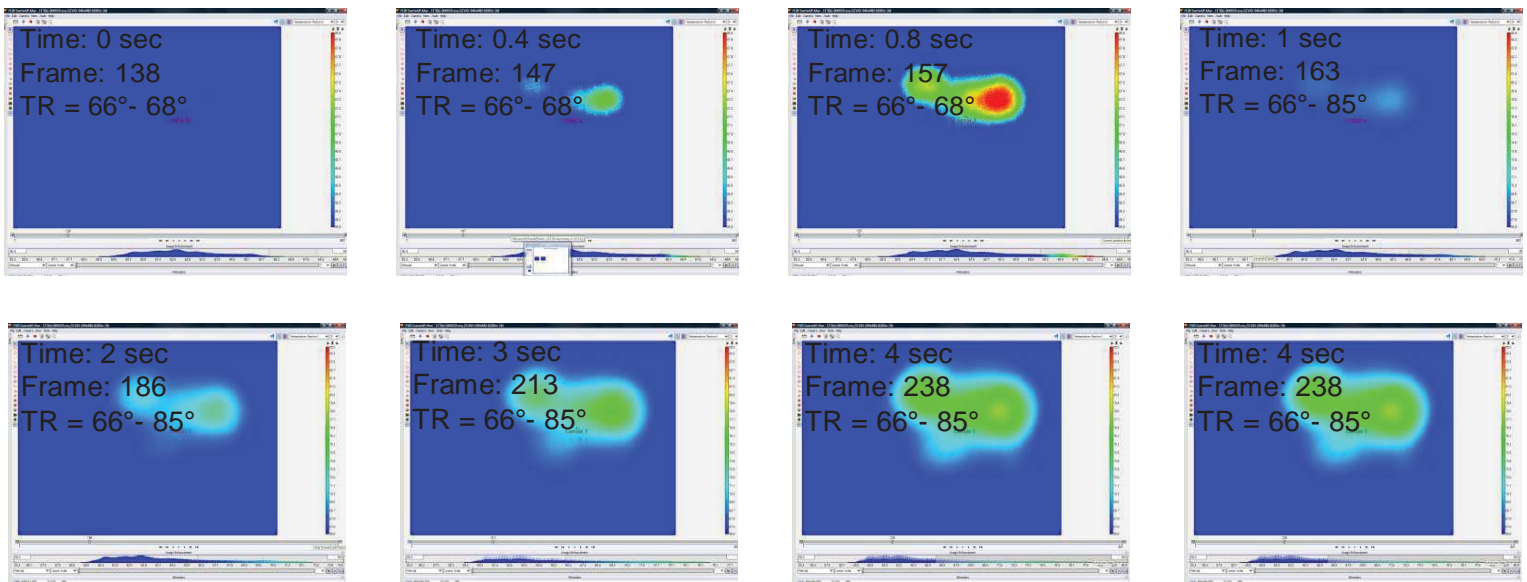
Post Strike Photograph

W2: XY(col(W 1, 1), col(W 1, 2)+1.676);se thunits('Se conds');se tvunits('m m')



Panel Displacement: Displacement, mm versus Time, sec

(This data is uncorrected for sensor placement angle. The scale factor for corrected data is 0.8572.)

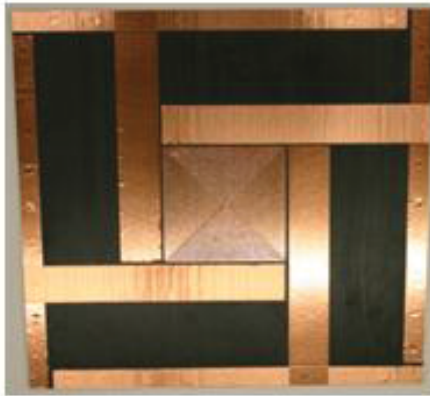


Panel backside IR image at sequential times. Note image has been flipped to provide a top side view.

Figure A 6. Concluded.

Fiberglass Panel - Configuration: Painted 6in SansEC

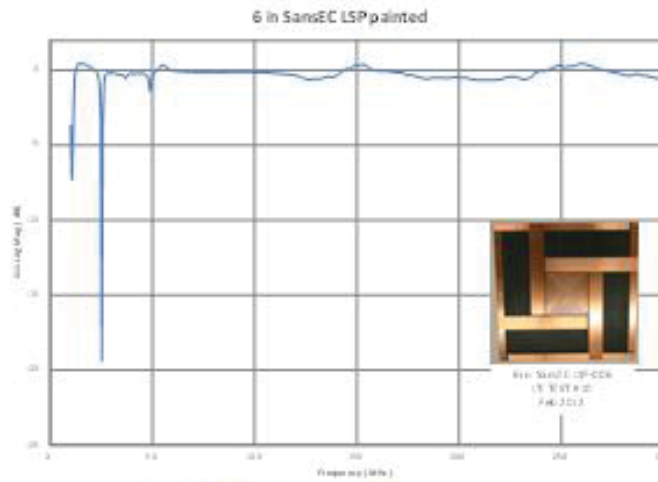
Peak Current, kA: 40



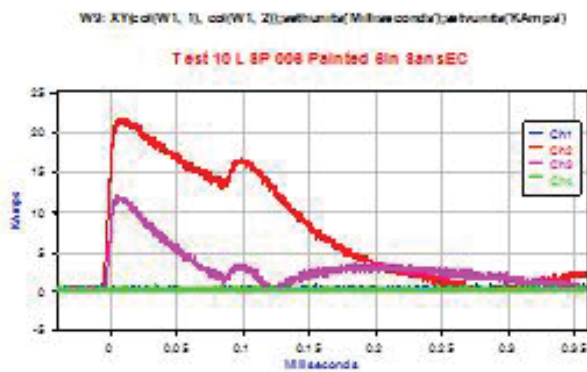
Pre Strike Photograph



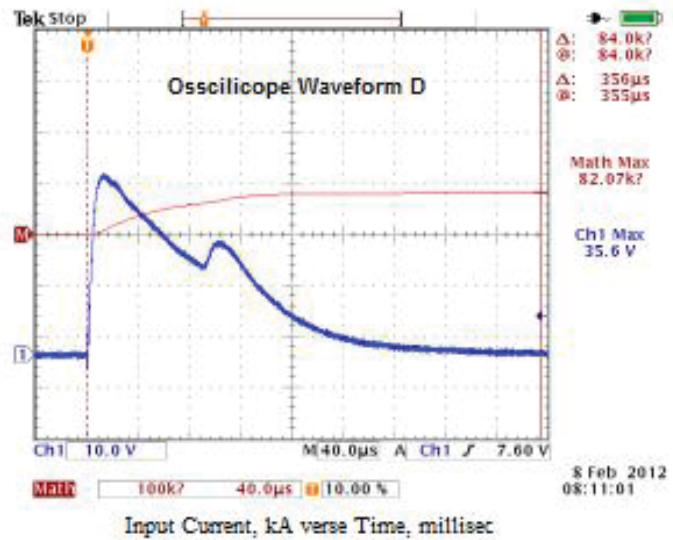
Post Strike Photograph



Pre Strike Resonate Measurement



Channels 1-4 Ground Current



Input Current, kA verse Time, millisec

Figure A.7. Fiberglass substrate configuration performance. Configuration: Painted 6in SansEC

Fiberglass Panel - Configuration: Painted 6in SansEC

Peak Current, kA: 40



Pre Strike Photograph

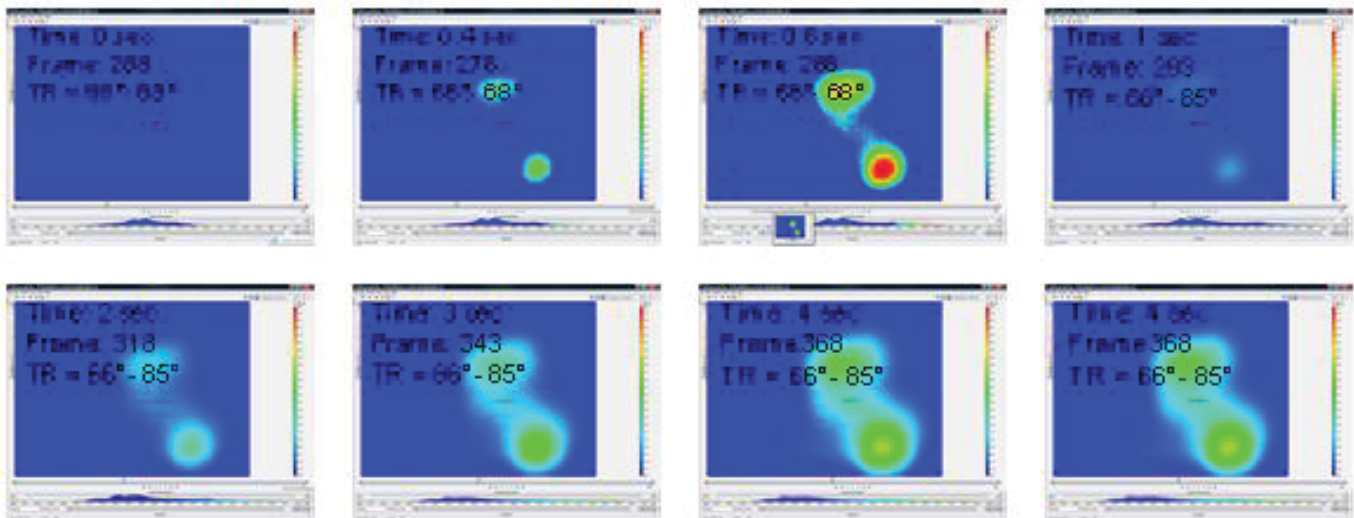


Post Strike Photograph

**Data not Available**

Panel Displacement: Displacement, mm versus Time, sec

(This data is uncorrected for sensor placement angle. The scale factor for corrected data is 0.8572.)



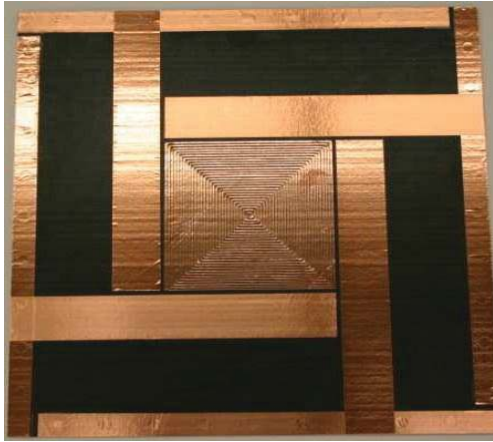
Panel backside IR image at sequential times. Note image has been flipped to provide a top side view.

Figure A. 7. Concluded.



# Fiberglass Panel - Configuration: Painted 7in SansEC

Peak Current, kA: 40

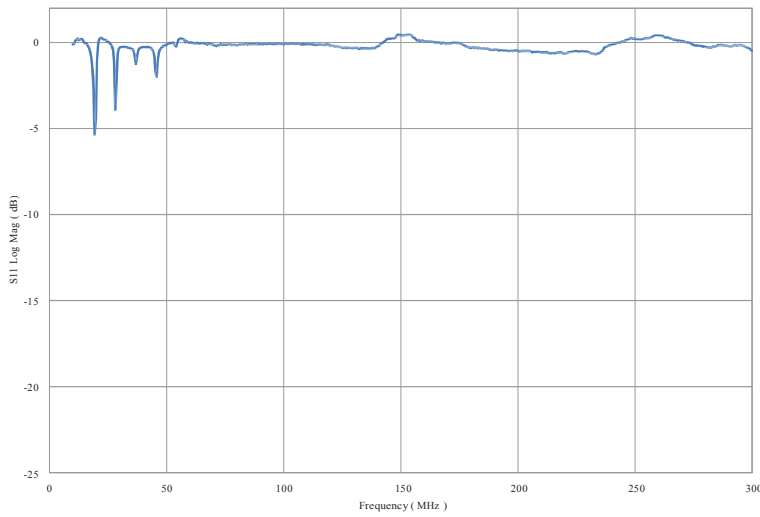


Pre Strike Photograph

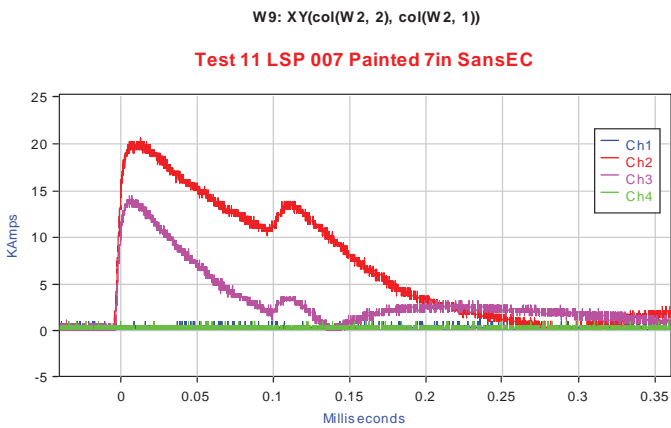


Post Strike Photograph

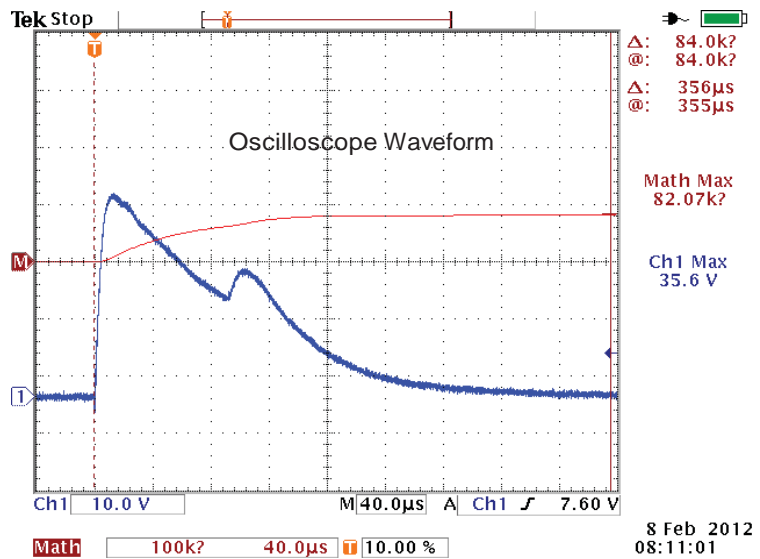
7 in SansEC LSP painted



Pre Strike Resonate Measurement



Channels 1-4 Ground Current

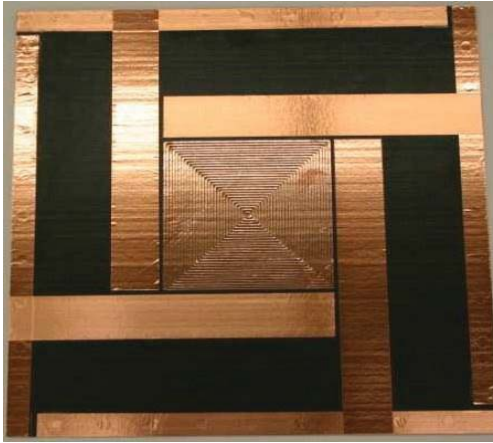


Input Current, kA verse Time, millsec

Figure A 8. Fiberglass substrate configuration performance. Configuration: Painted 7in SansEC

# Fiberglass Panel - Configuration: Painted 7in SansEC

Peak Current, kA: 40

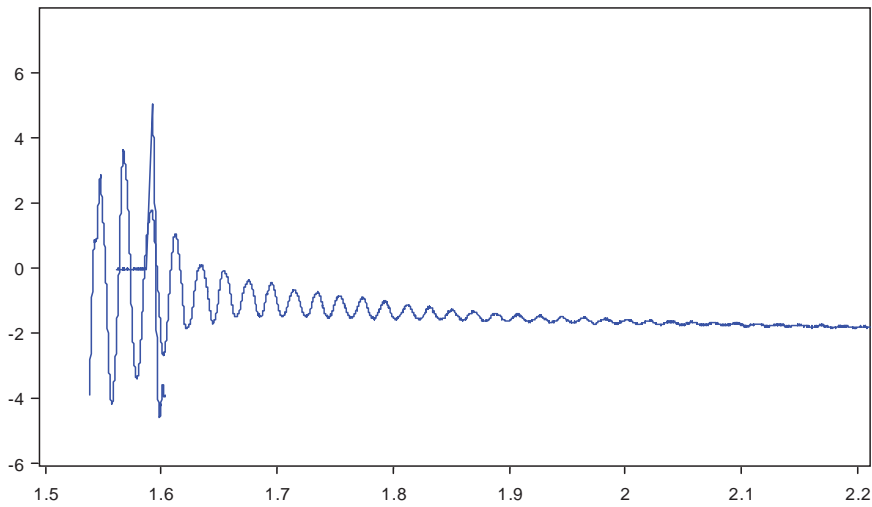


Pre Strike Photograph



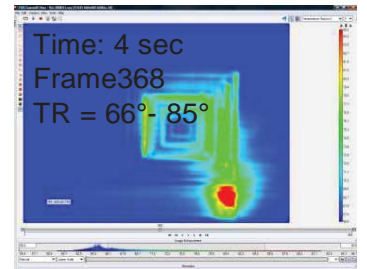
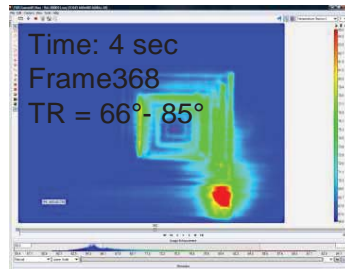
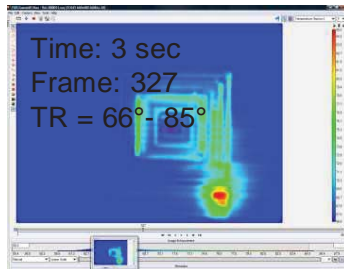
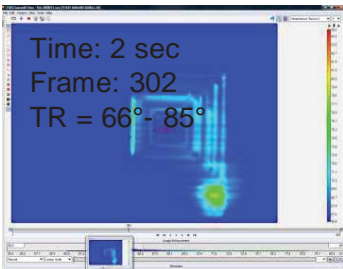
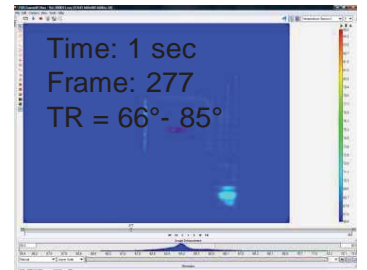
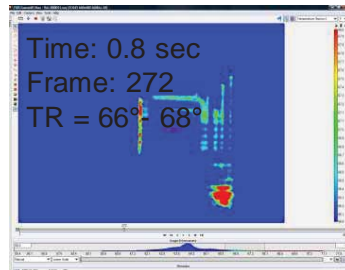
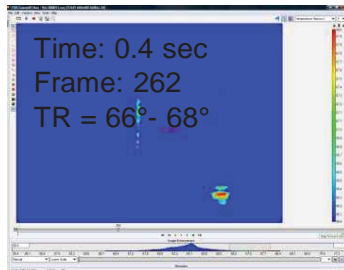
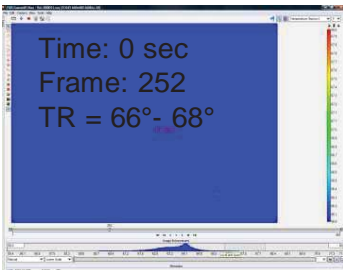
Post Strike Photograph

W2: XY(col(W 1, 1), col(W 1, 2)+0);se thunits('Seconds');se tvunits('m m')



Panel Displacement: Displacement. mm versus Time. sec

(This data is uncorrected for sensor placement angle. The scale factor for corrected data is 0.8572.)

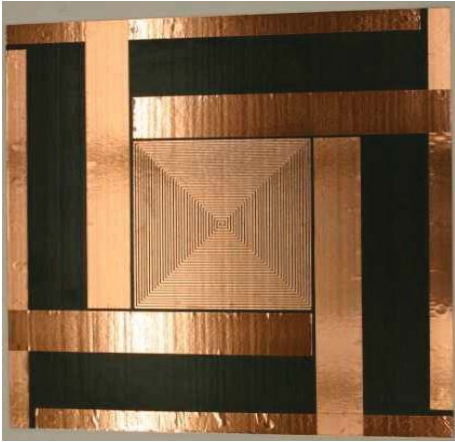


Panel backside IR image at sequential times. Note image has been flipped to provide a top side view.

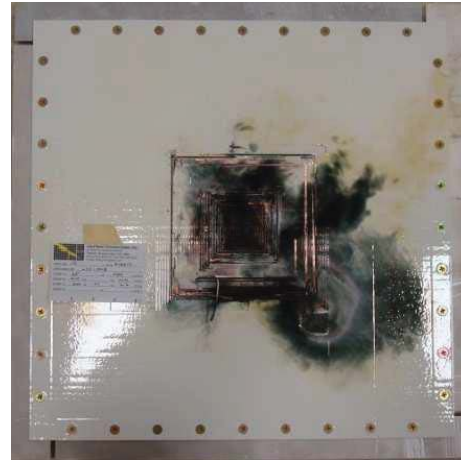
Figure A 8. Concluded.

# Fiberglass Panel - Configuration: Painted 8in SansEC

Peak Current, kA: 40

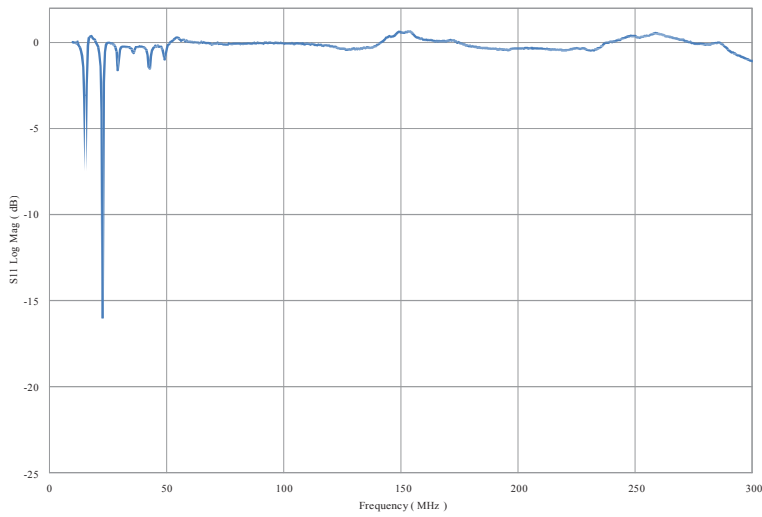


Pre Strike Photograph

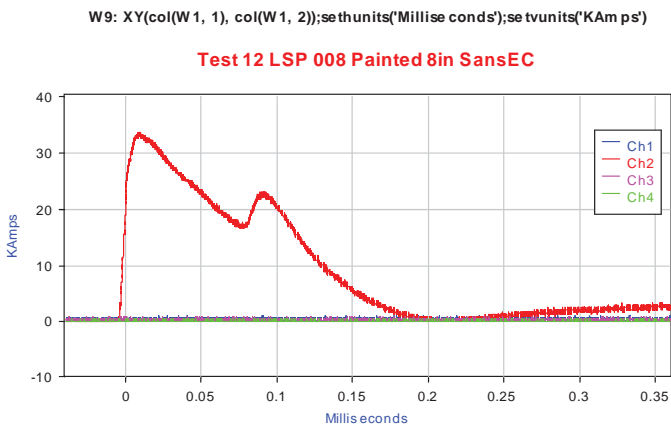


Post Strike Photograph

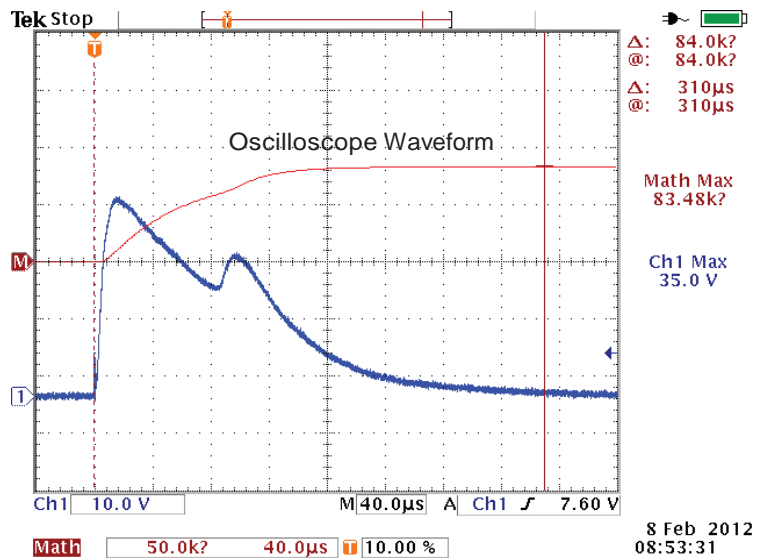
8 in SansEC LSP painted



Pre Strike Resonate Measurement



Channels 1-4 Ground Current

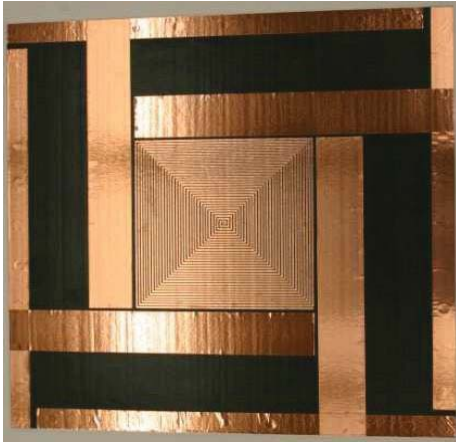


Input Current, kA verse Time, millsec

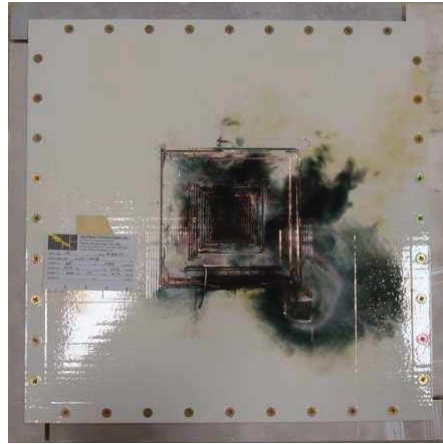
Figure A9. Fiberglass substrate configuration performance. Configuration: Painted 8in SansEC

# Fiberglass Panel - Configuration: Painted 8in SansEC

Peak Current, kA: 40

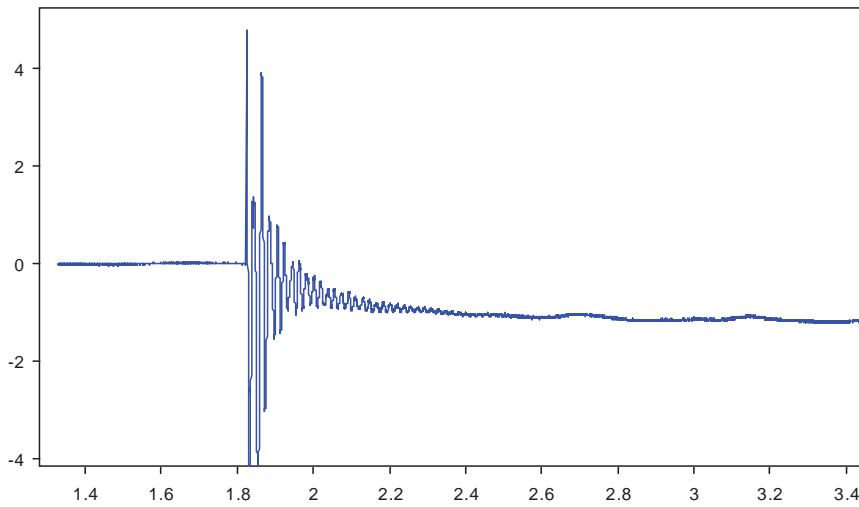


Pre Strike Photograph



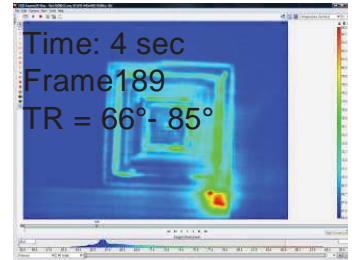
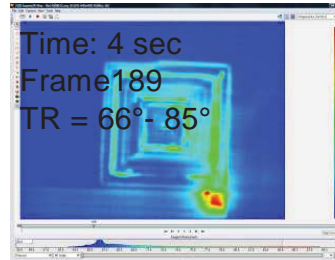
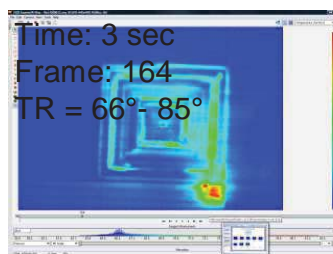
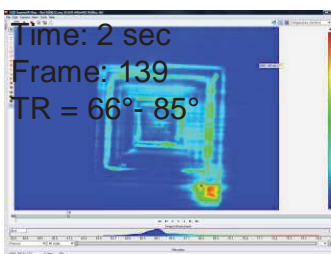
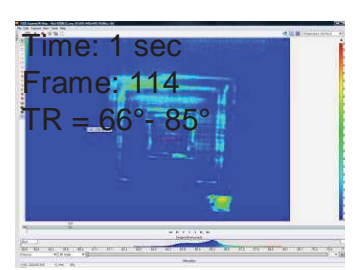
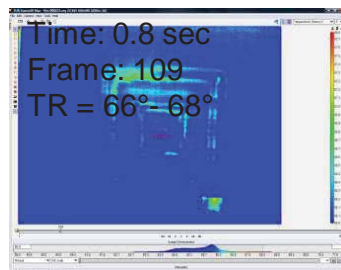
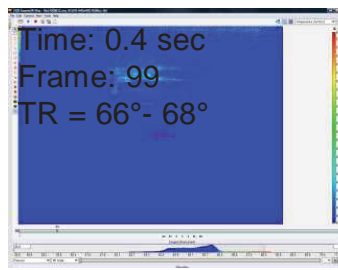
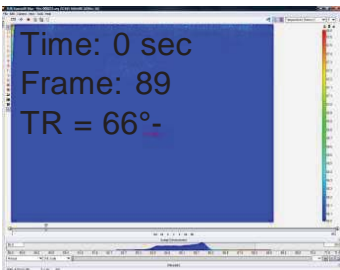
Post Strike Photograph

W2: XY(col(W 1, 1), col(W 1, 2)+.17);sethunits('Seconds');setvunits('m m')



Panel Displacement: Displacement, mm versus Time, sec

(This data is uncorrected for sensor placement angle. The scale factor for corrected data is 0.8572.)



Panel backside IR image at sequential times. Note image has been flipped to provide a top side view.

Figure A9. Concluded.

# Fiberglass Panel - Configuration: Painted 9in SansEC

Peak Current, kA: 40

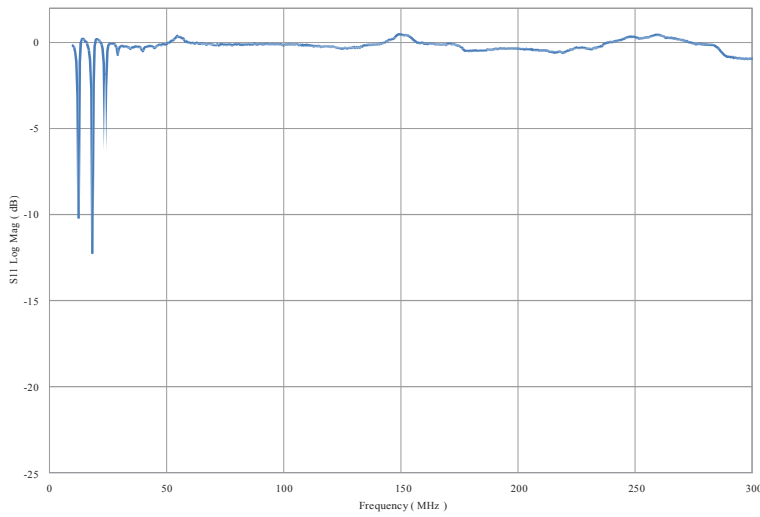


Pre Strike Photograph

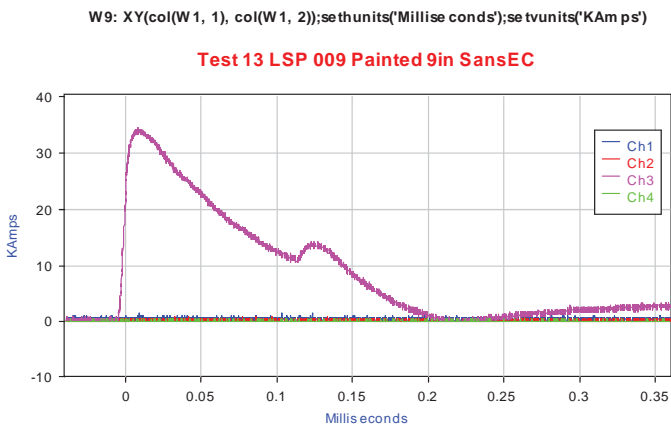


Post Strike Photograph

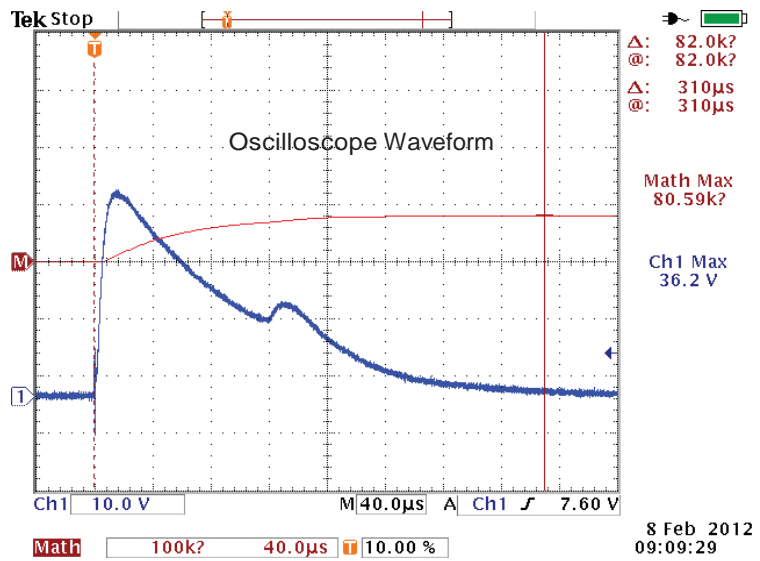
9 in SansEC LSP painted



Pre Strike Resonate Measurement



Channels 1-4 Ground Current



Input Current, kA verse Time, millsec

Figure A 10. Fiberglass substrate configuration performance. Configuration: Painted 9in SansEC

# Fiberglass Panel - Configuration: Painted 9in SansEC

Peak Current, kA: 40

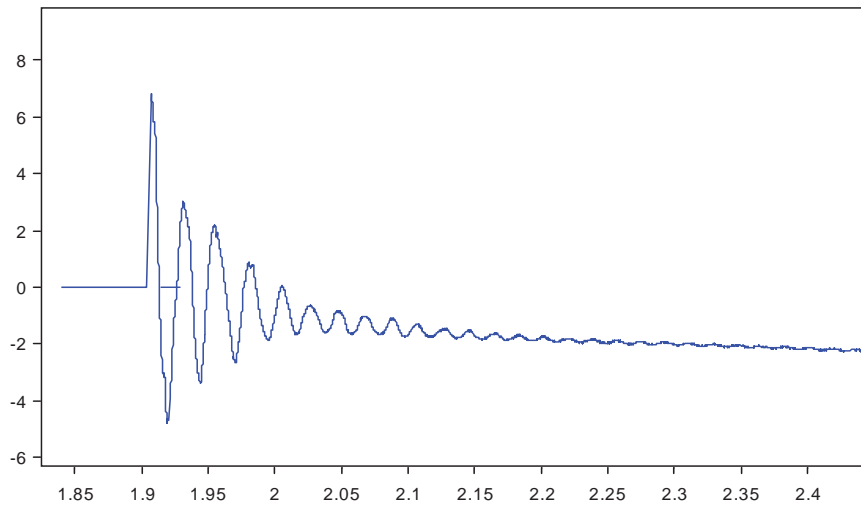


Pre Strike Photograph



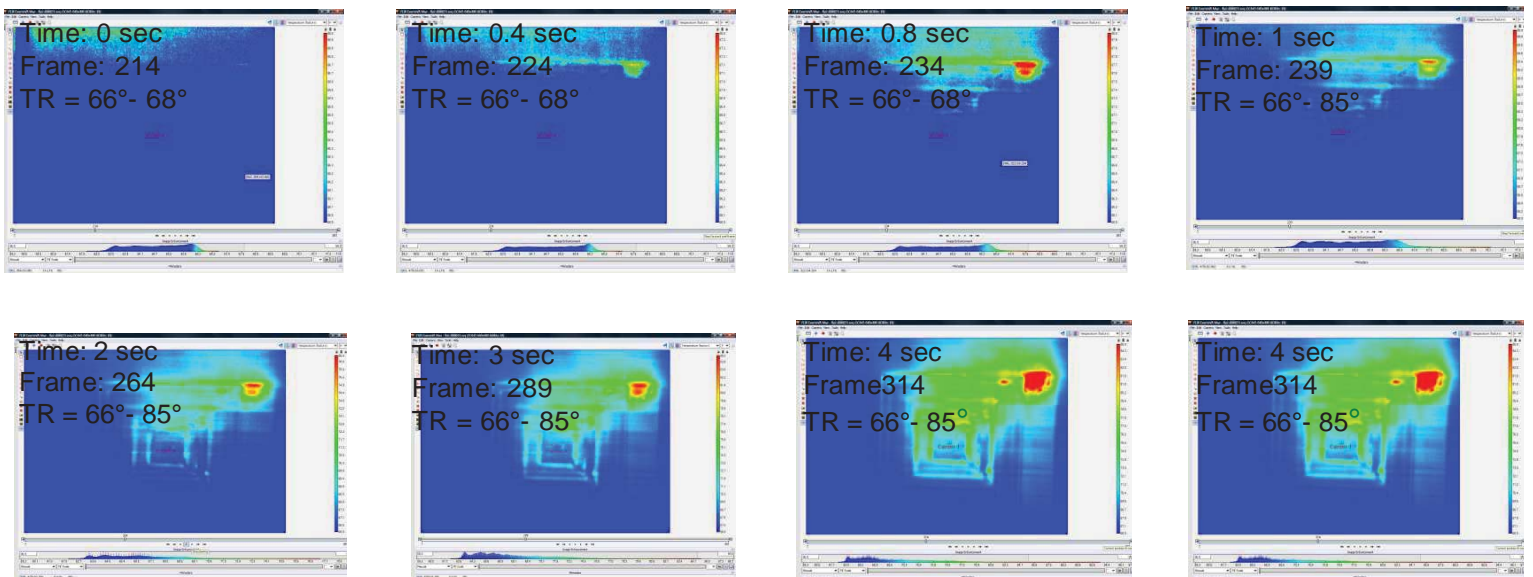
Post Strike Photograph

W2: XY(col(W 1, 1), col(W 1, 2)+1.336);se thunits('Se conds');se tvunits('m m')



Panel Displacement: Displacement, mm versus Time, sec

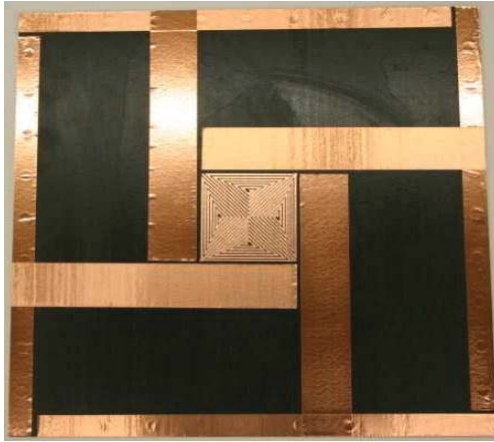
(This data is uncorrected for sensor placement angle. The scale factor for corrected data is 0.8572.)



Panel backside IR image at sequential times. Note image has been flipped to provide a top side view.

Figure A 10. Concluded.

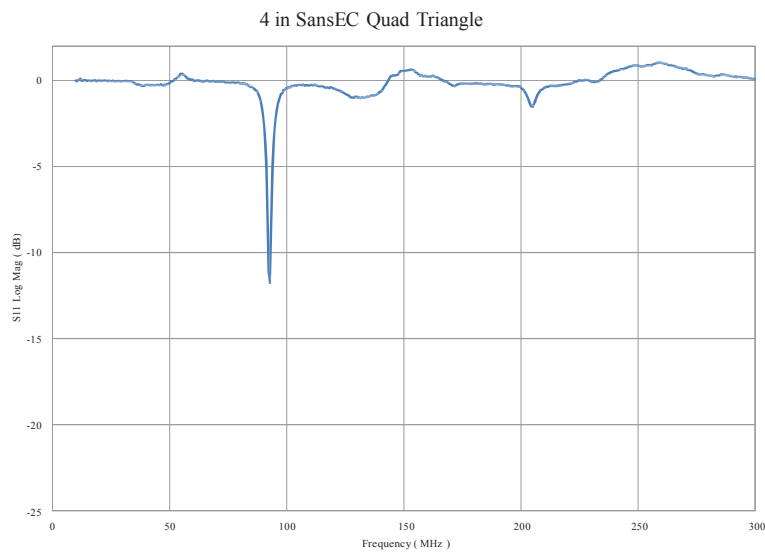
Fiberglass Panel - Configuration: Painted 4in SansEC Quad Triangle  
 Peak Current, kA: 40



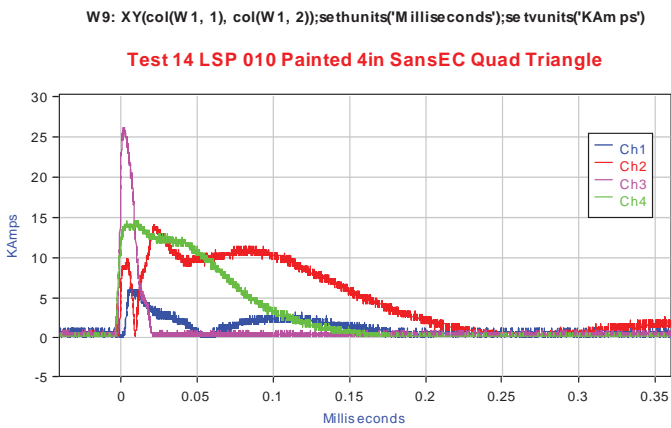
Pre Strike Photograph



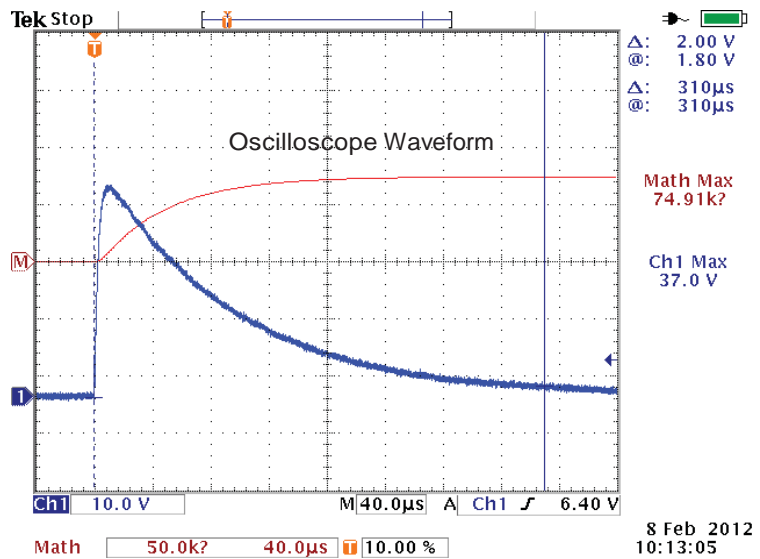
Post Strike Photograph



Pre Strike Resonate Measurement



Channels 1-4 Ground Current

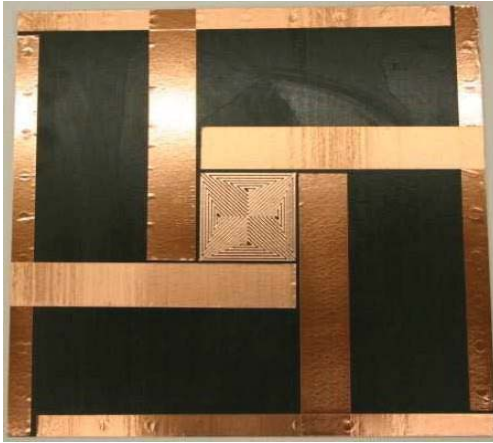


Input Current, kA verse Time, millsec

Figure A 11. Fiberglass substrate configuration performance. Configuration: Painted 4in SansEC Quad Triangle

# Fiberglass Panel - Configuration: Painted 4in SansEC Quad Triangle

Peak Current, kA: 40



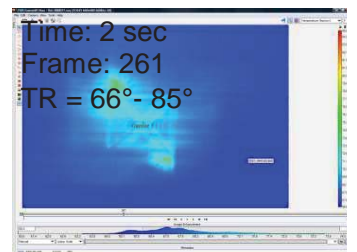
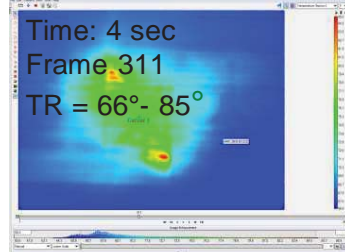
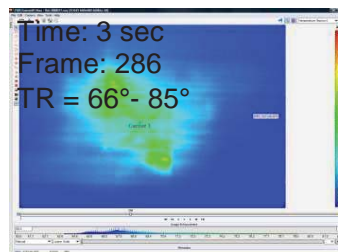
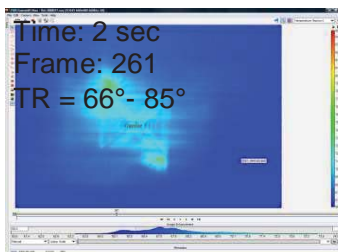
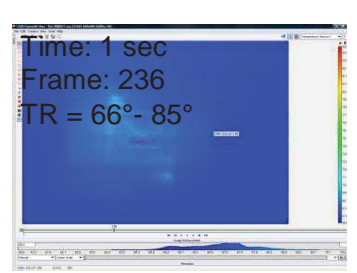
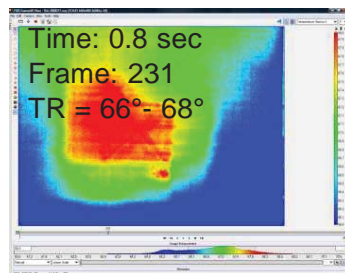
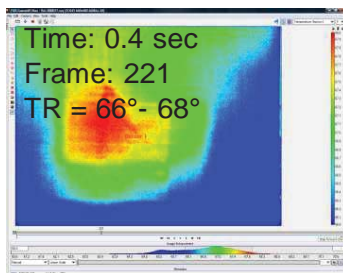
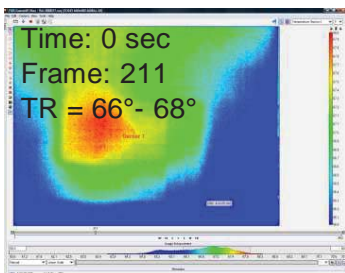
Pre Strike Photograph



Post Strike Photograph

## Data not Available

Panel Displacement: Displacement, mm verses Time, sec  
(This data is uncorrected for sensor placement angle. The scale factor for corrected data is 0.8572.)



Panel backside IR image at sequential times. Note image has been flipped to provide a top side view.  
Figure A 11. Concluded.

Fiberglass Panel - Configuration: Painted 3in SansEC Taper Trace  
 Peak Current, kA: 40

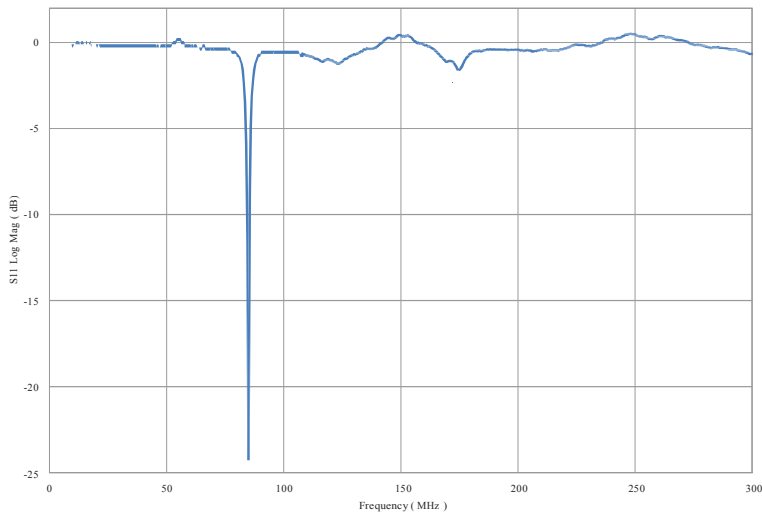


Pre Strike Photograph

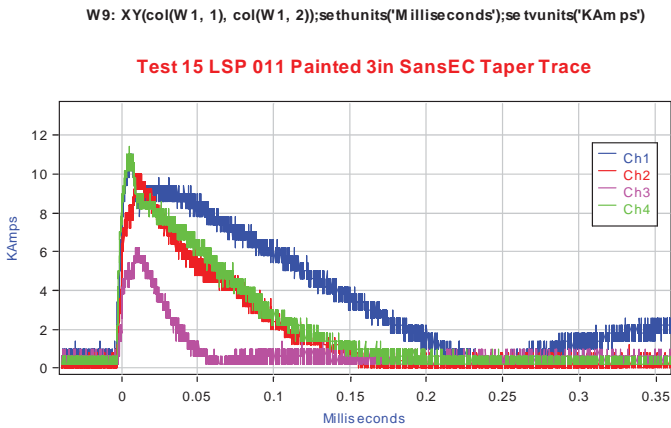


Post Strike Photograph

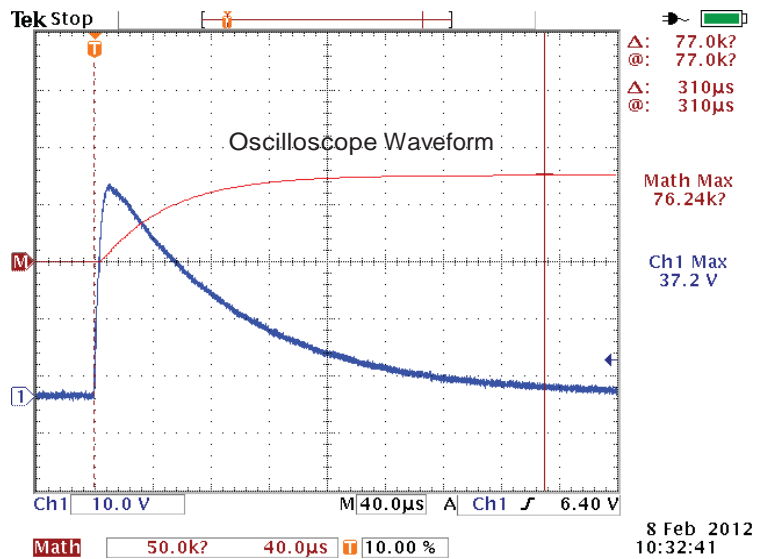
3 in SansEC Tapered Spiral LSP painted



Pre Strike Resonate Measurement



Channels 1-4 Ground Current

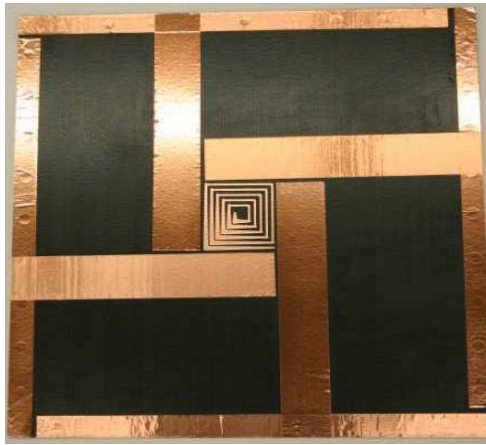


Input Current, kA verse Time, millsec

Figure A 12. Fiberglass substrate configuration performance. Configuration: Painted 3in SansEC Taper Trace

# Fiberglass Panel - Configuration: Painted 3in SansEC Taper Trace

Peak Current, kA: 40

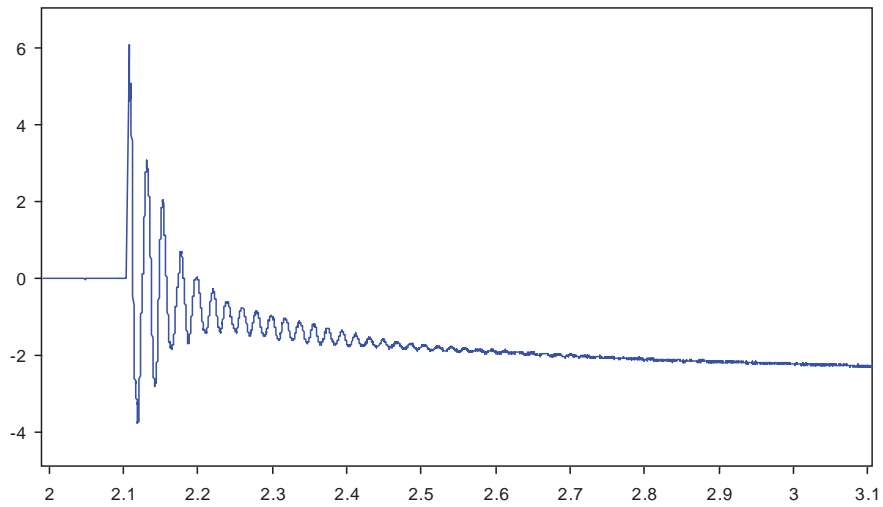


Pre Strike Photograph



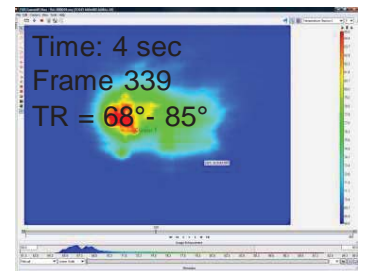
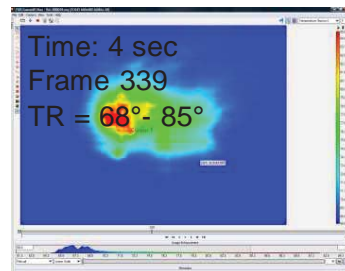
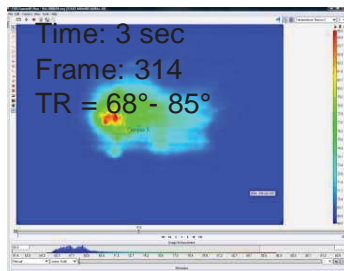
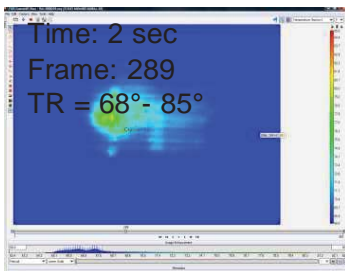
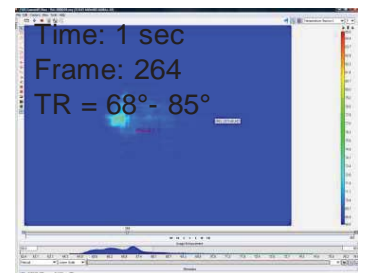
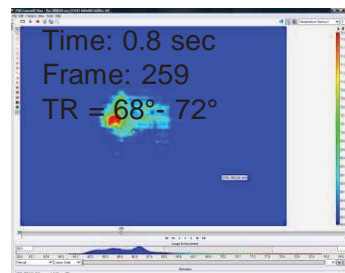
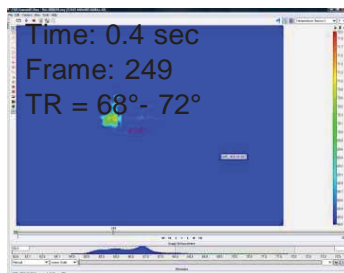
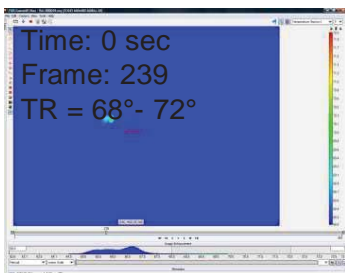
Post Strike Photograph

W2: XY(col(W 1, 1), col(W 1, 2)+.67);sethunits('Seconds');setvunits('m m')



Panel Displacement: Displacement, mm versus Time, sec

(This data is uncorrected for sensor placement angle. The scale factor for corrected data is 0.8572.)

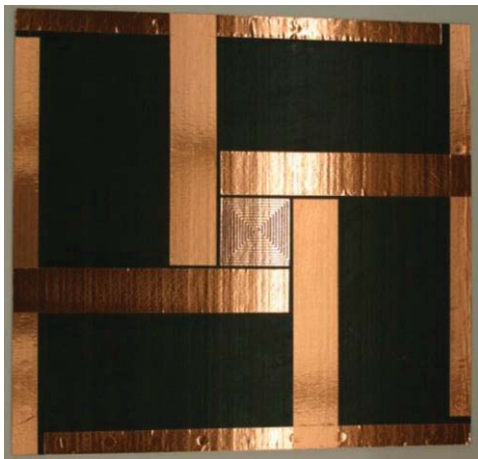


Panel backside IR image at sequential times. Note image has been flipped to provide a top side view.

Figure A 12. Concluded.

# Fiberglass Panel - Configuration: Painted 3in SansEC Dual Trace

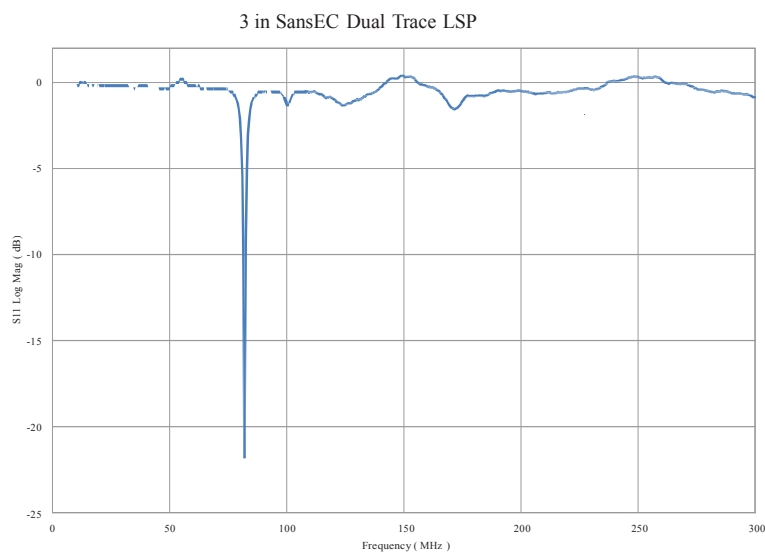
Peak Current, kA: 40



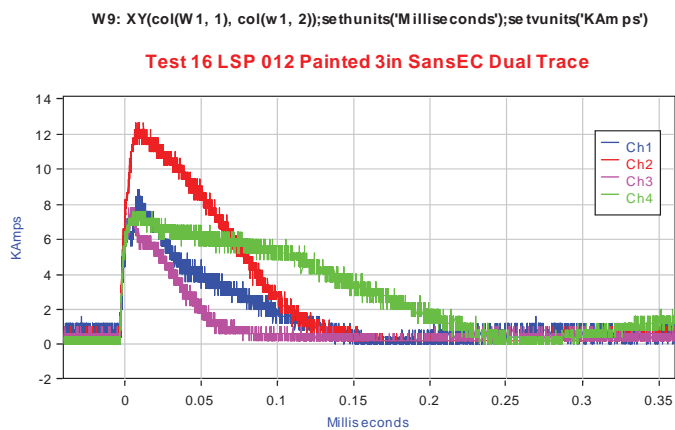
Pre Strike Photograph



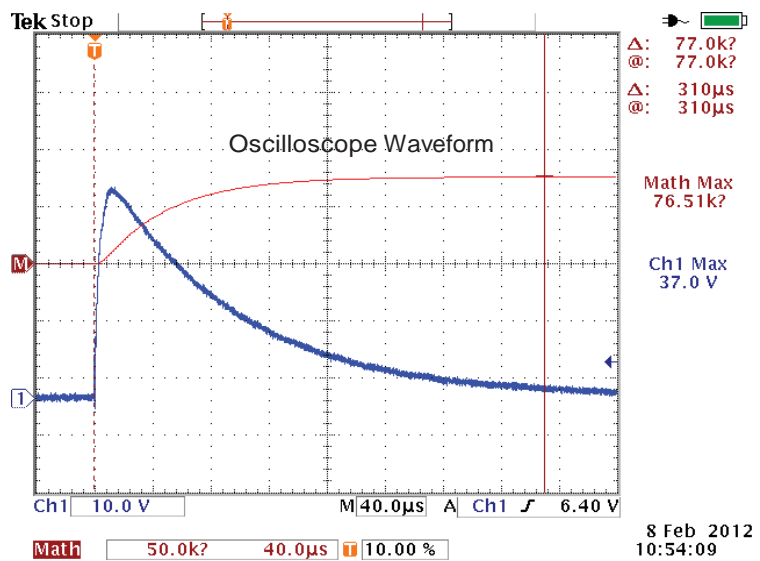
Post Strike Photograph



Pre Strike Resonate Measurement



Channels 1-4 Ground Current

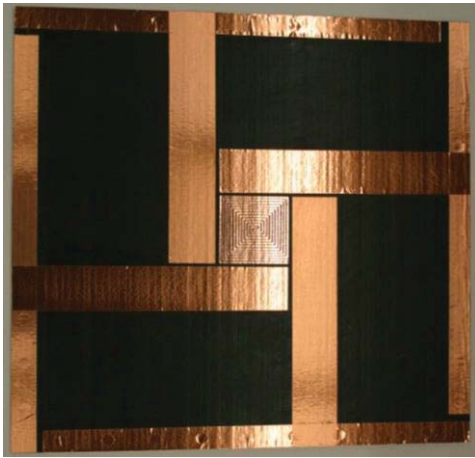


Input Current, kA verse Time, millsec

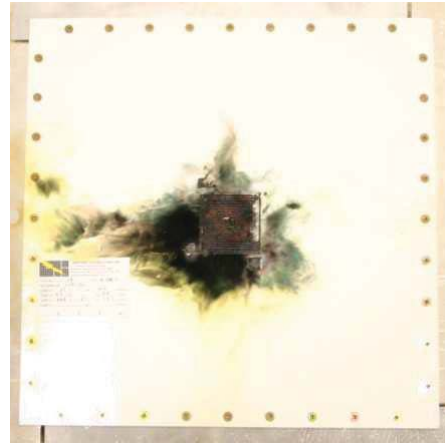
Figure A 13. Fiberglass substrate configuration performance. Configuration: Painted 3in SansEC Dual Trace

# Fiberglass Panel - Configuration: Painted 3in SansEC Dual Trace

Peak Current, kA: 40

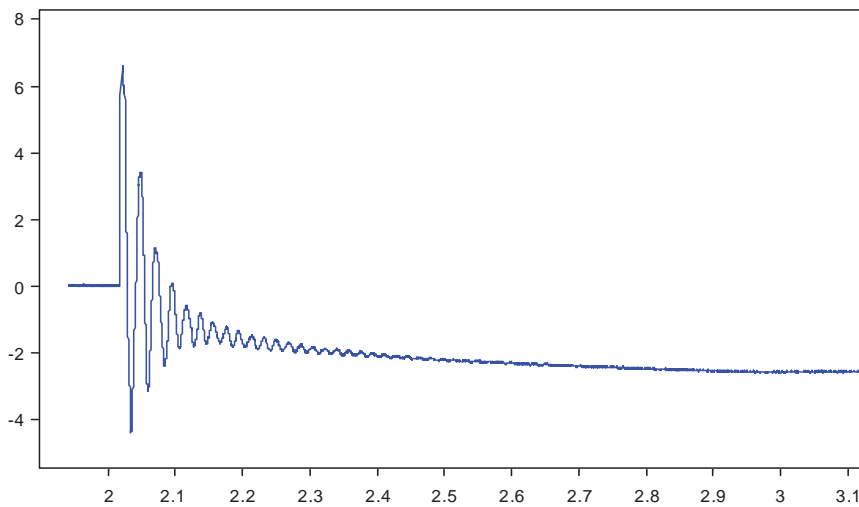


Pre Strike Photograph



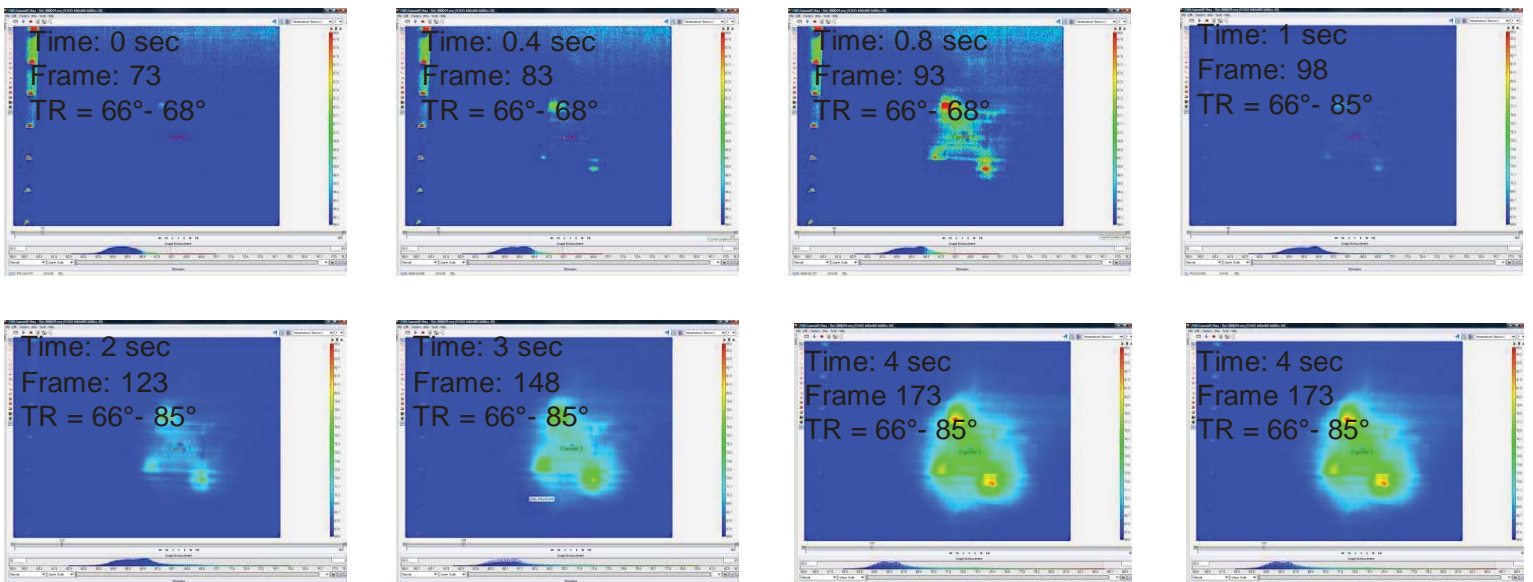
Post Strike Photograph

W2: XY(col(W 1, 1), col(W 1, 2)+1.41);se thunits('Se conds');se tvunits('m m')



Panel Displacement: Displacement, mm versus Time, sec

(This data is uncorrected for sensor placement angle. The scale factor for corrected data is 0.8572.)

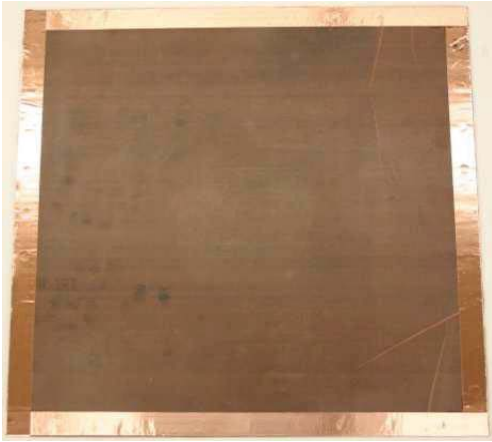


Panel backside IR image at sequential times. Note image has been flipped to provide a top side view.

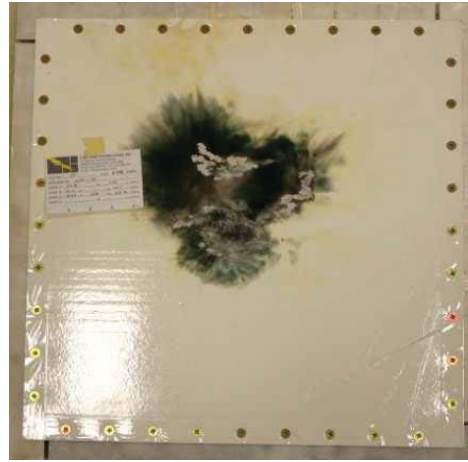
Figure A 13. Concluded.

# Fiberglass Panel - Configuration: Painted Baseline Dexmet Cu Mesh

Peak Current, kA: 40

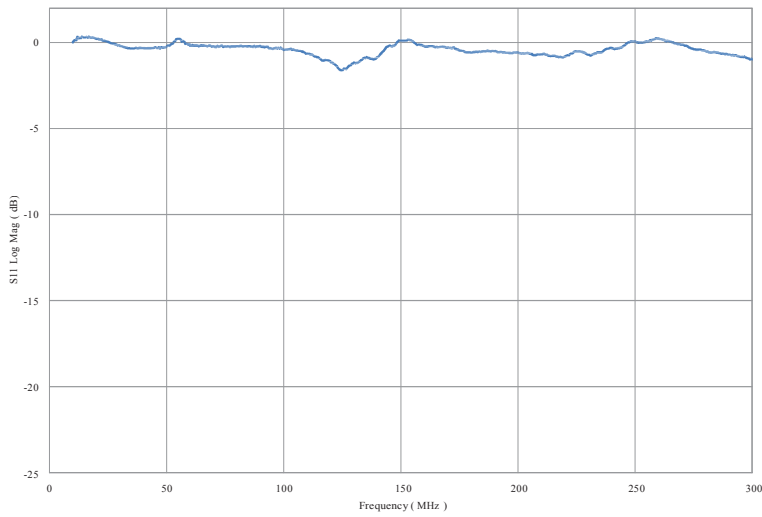


Pre Strike Photograph

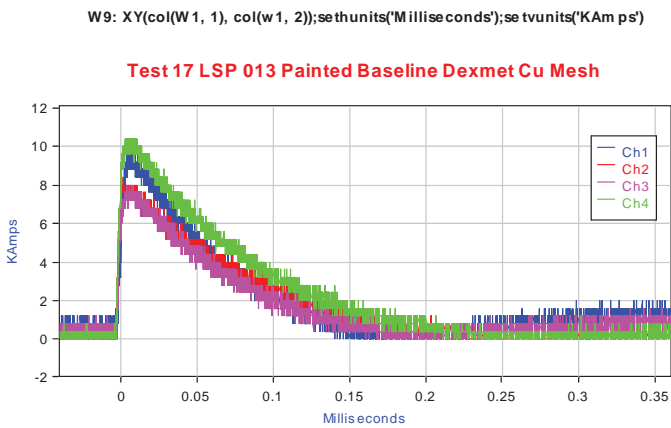


Post Strike Photograph

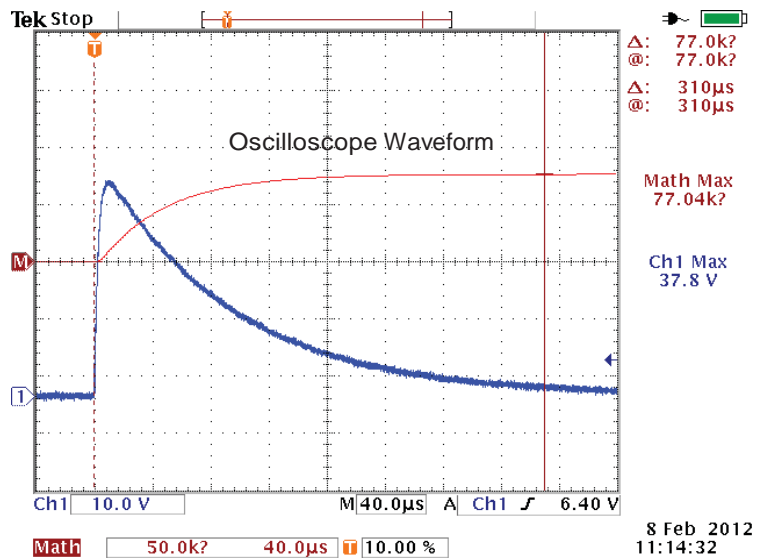
Dexmet Mesh



Pre Strike Resonate Measurement



Channels 1-4 Ground Current

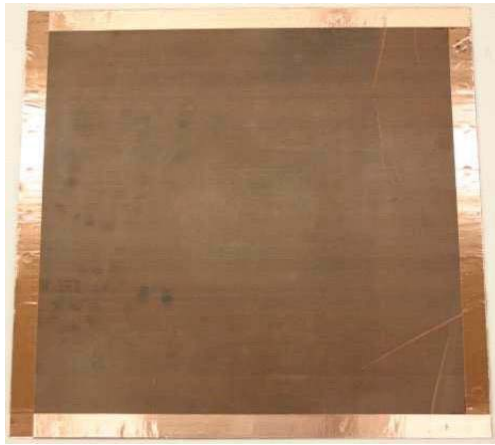


Input Current, kA verse Time, millsec

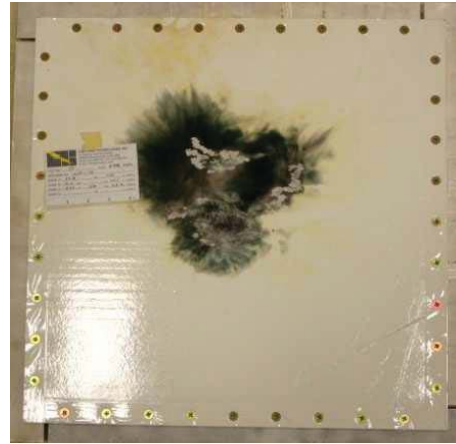
Figure A 14. Fiberglass substrate configuration performance. Configuration: Painted Baseline Dexmet Cu Mesh

# Fiberglass Panel - Configuration: Painted Baseline Dexmet Cu Mesh

Peak Current, kA: 40

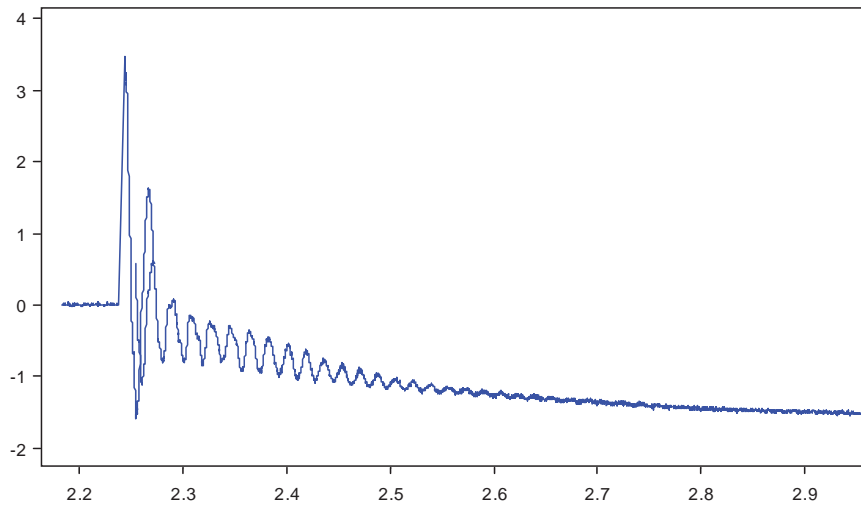


Pre Strike Photograph



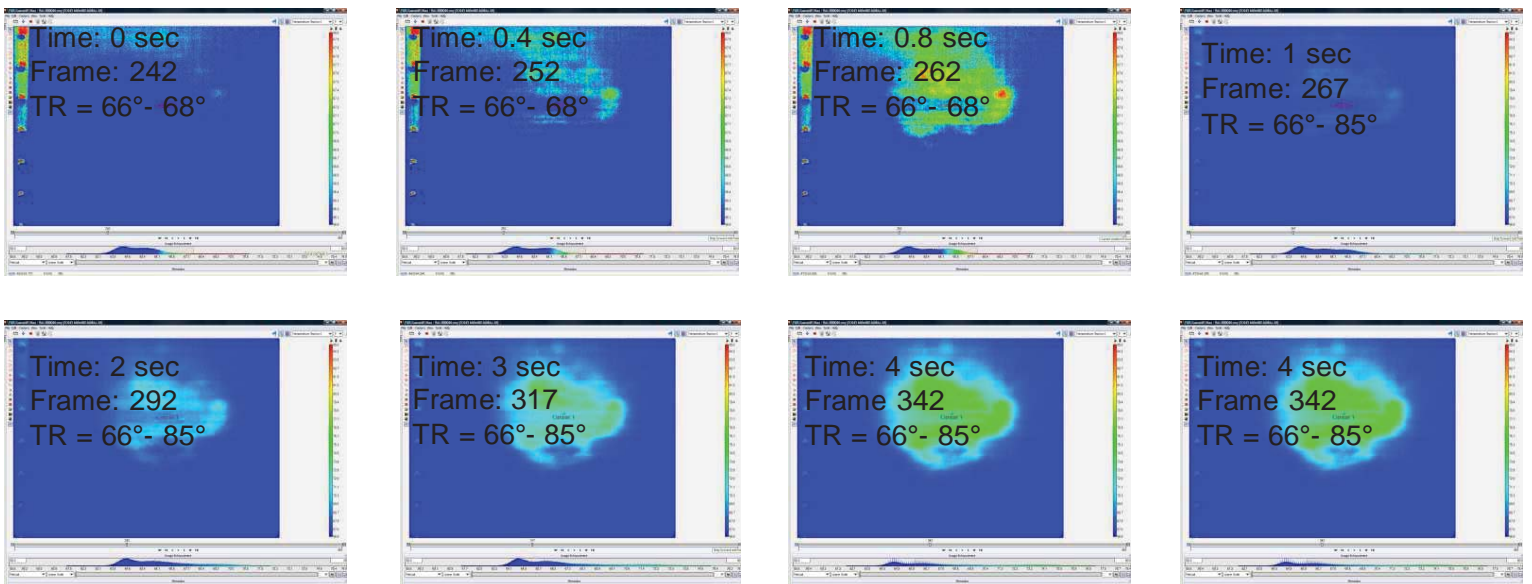
Post Strike Photograph

W2: XY(col(W 1, 1), col(W 1, 2)+2.94);se thunits('Se conds');se tvunits('m m')



Panel Displacement: Displacement, mm versus Time, sec

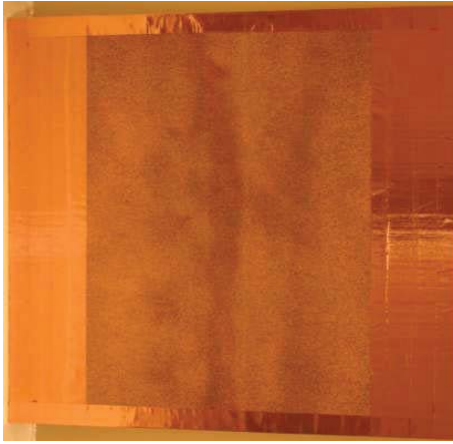
(This data is uncorrected for sensor placement angle. The scale factor for corrected data is 0.8572.)



Panel backside IR image at sequential times. Note image has been flipped to provide a top side view.

Figure A 14. Concluded.

Fiberglass Panel - Configuration: Baseline Plasma Spray Cu  
 Peak Current, kA: 40



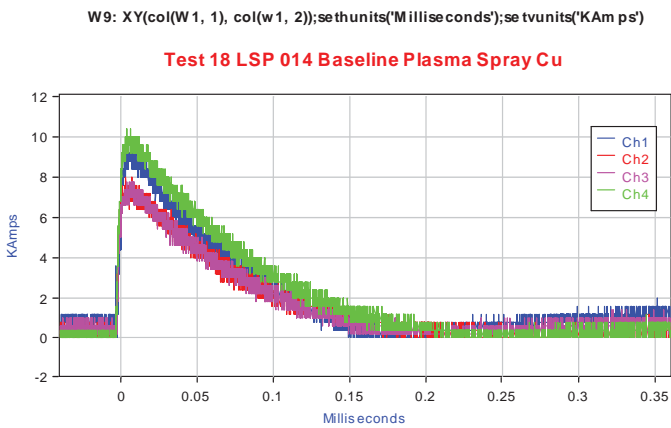
Pre Strike Photograph



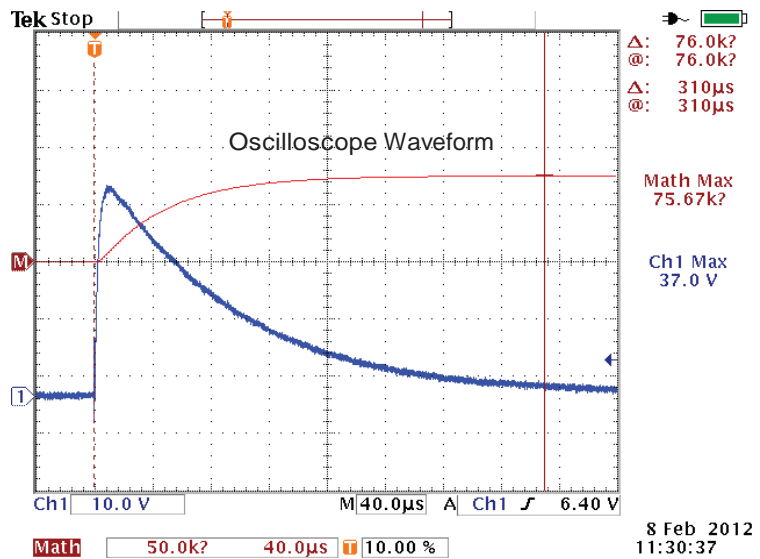
Post Strike Photograph

Data not Available

Pre Strike Resonate Measurement



Channels 1-4 Ground Current

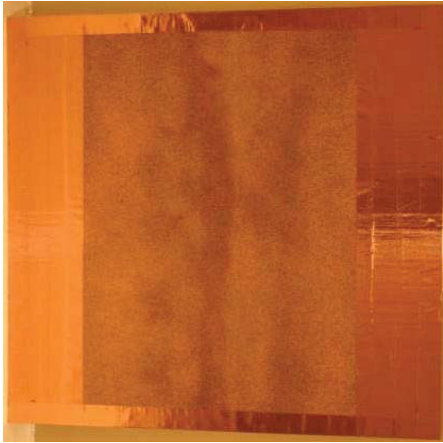


Input Current, kA verse Time, millsec

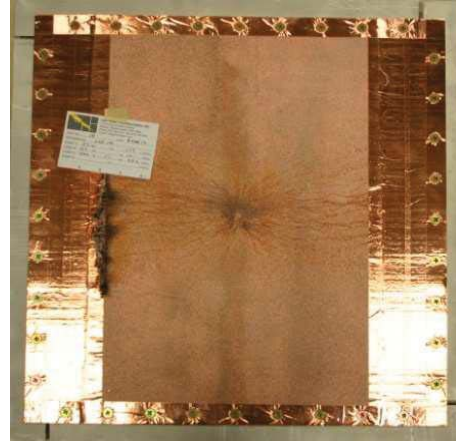
Figure A 15. Fiberglass substrate configuration performance. Configuration: Baseline Plasma Spray Cu

# Fiberglass Panel - Configuration: Baseline Plasma Spray Cu

Peak Current, kA: 40

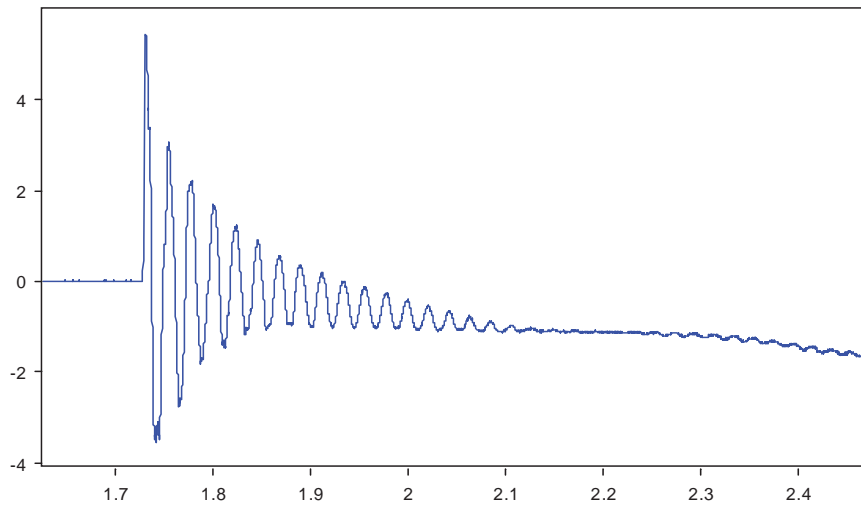


Pre Strike Photograph



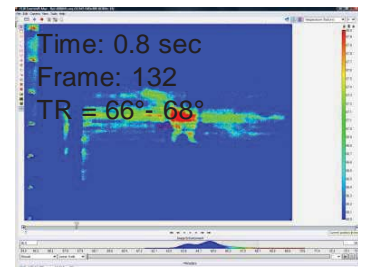
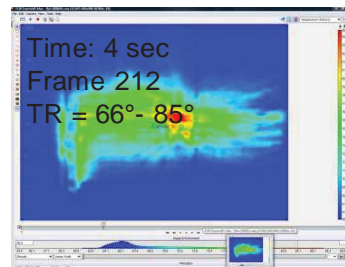
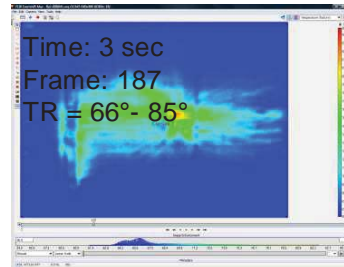
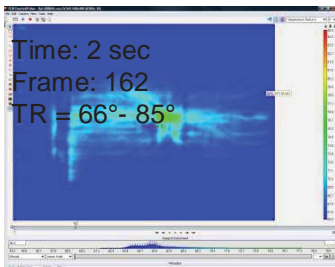
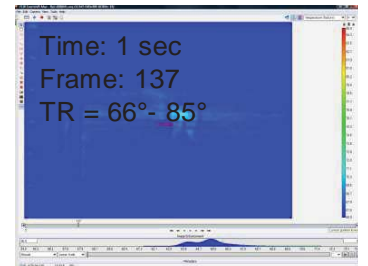
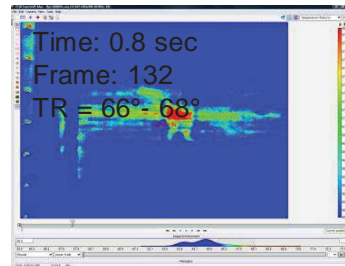
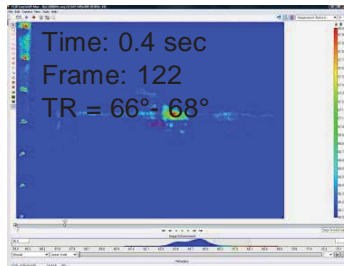
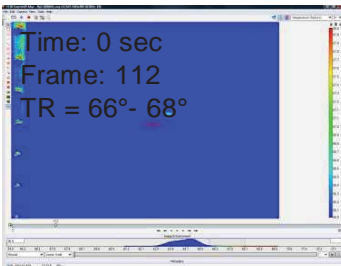
Post Strike Photograph

W2: XY(col(W 1, 1), col(W 1, 2)+.149);se thunits('Se conds');se tvunits('m m')



Panel Displacement: Displacement, mm versus Time, sec

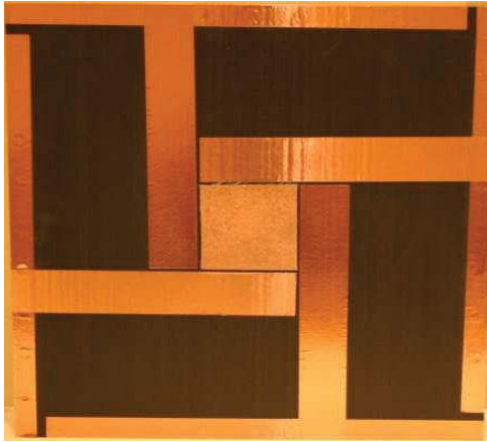
(This data is uncorrected for sensor placement angle. The scale factor for corrected data is 0.8572.)



Panel backside IR image at sequential times. Note image has been flipped to provide a top side view.

Figure A 15. Concluded.

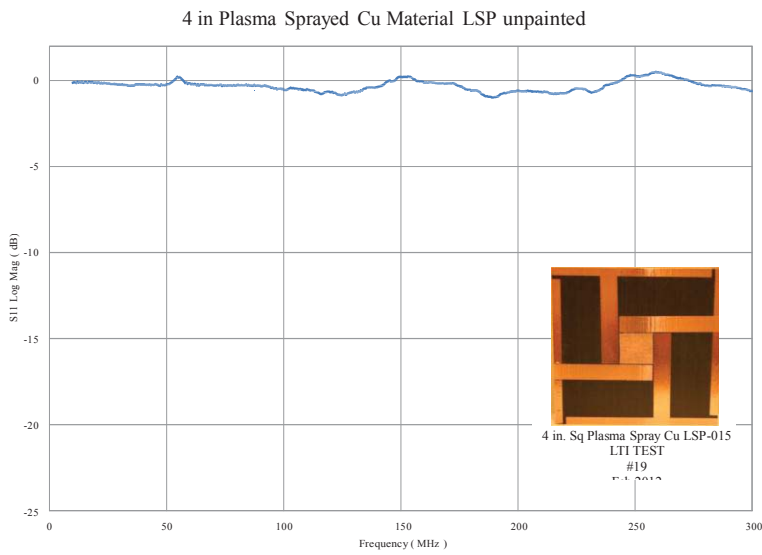
# Fiberglass Panel - Configuration: Unpainted 4in Square Plasma Spray Peak Current, kA: 40



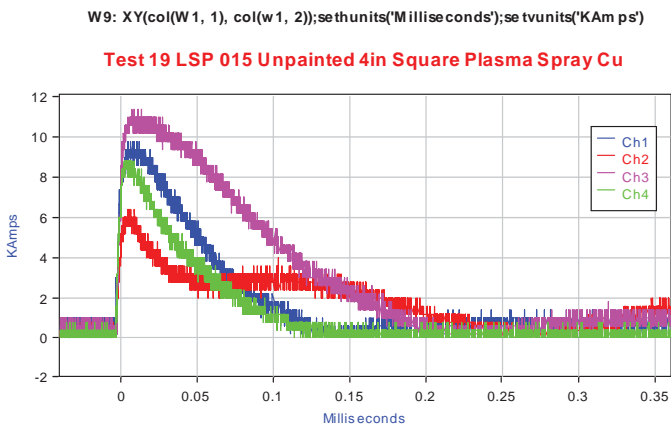
Pre Strike Photograph



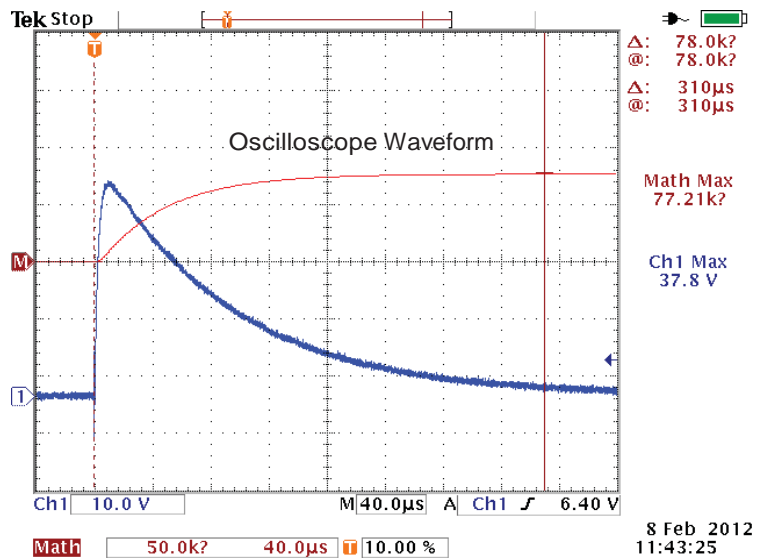
Post Strike Photograph



Pre Strike Resonate Measurement



Channels 1-4 Ground Current

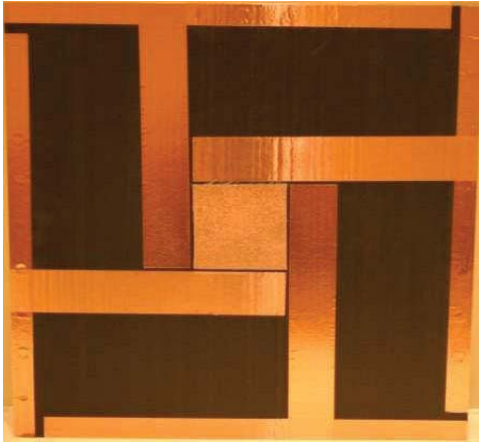


Input Current, kA verse Time, millisecc

Figure A 16. Fiberglass substrate configuration performance. Configuration: Unpainted 4in Square Plasma Spray

# Fiberglass Panel - Configuration: Unpainted 4in Square Plasma Spray

Peak Current, kA: 40



Pre Strike Photograph



Post Strike Photograph

**Data not Available**

Panel Displacement: Displacement, mm versus Time, sec  
(This data is uncorrected for sensor placement angle. The scale factor for corrected data is 0.8572.)

**Data not Available**

Panel backside IR image at sequential times. Note image has been flipped to provide a top side view.

Figure A 16. Concluded.

Fiberglass Panel - Configuration: Unpainted 4in SansEC Plasma  
Peak Current, kA: 40

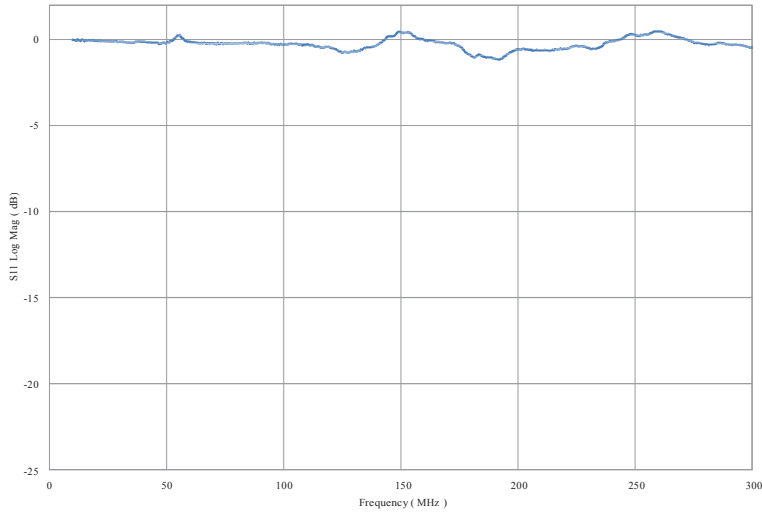


Pre Strike Photograph

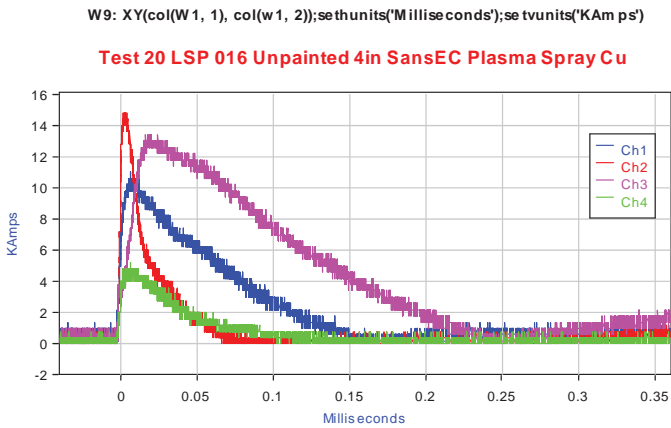


Post Strike Photograph

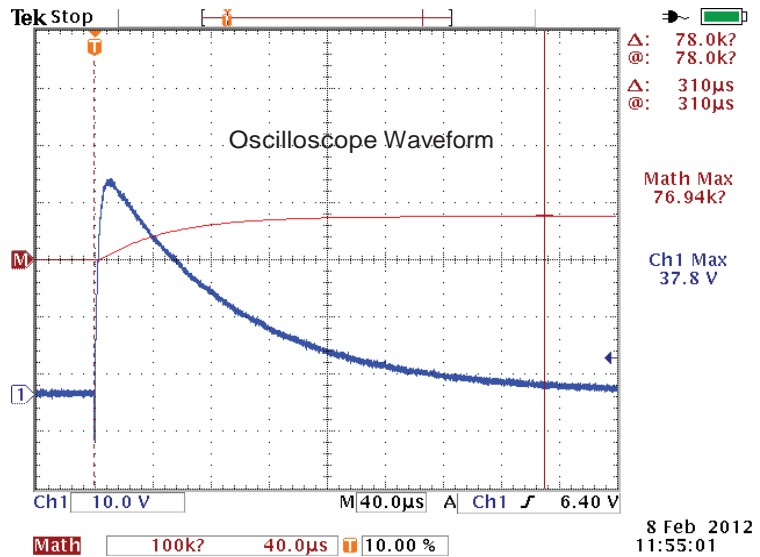
4 in SansEC Plasma Sprayed Cu Material LSP unpainted



Pre Strike Resonate Measurement



Channels 1-4 Ground Current

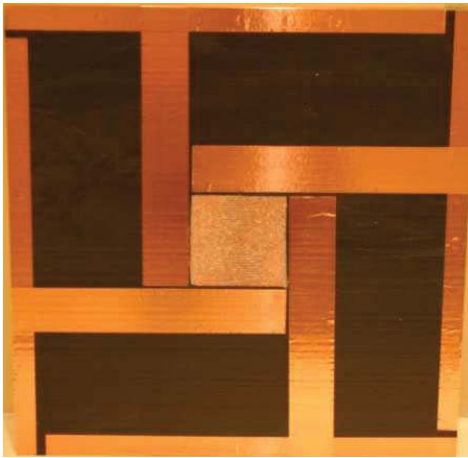


Input Current, kA verse Time, millsec

Figure A 17. Fiberglass substrate configuration performance. Configuration: Unpainted 4in SansEC Plasma Spray

# Fiberglass Panel - Configuration: Unpainted 4in SansEC Plasma

Peak Current, kA: 40

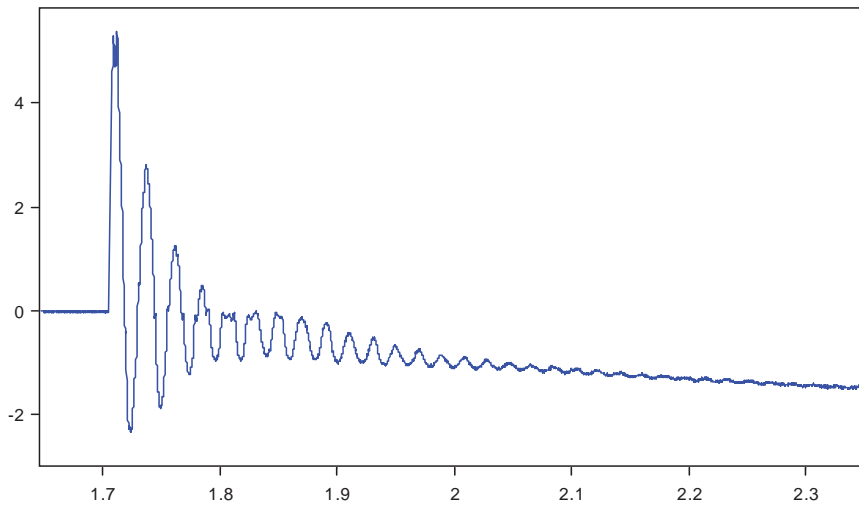


Pre Strike Photograph



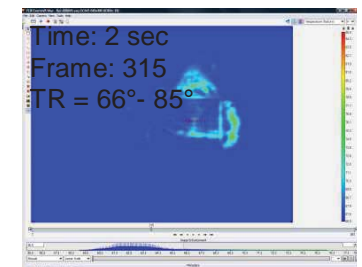
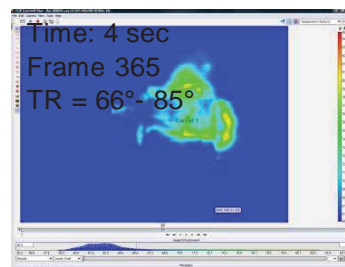
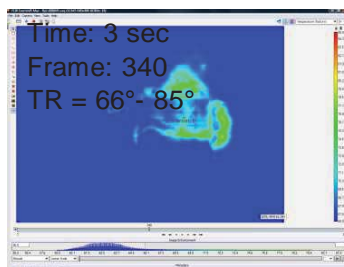
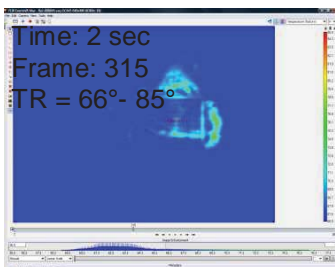
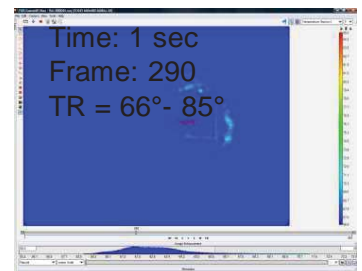
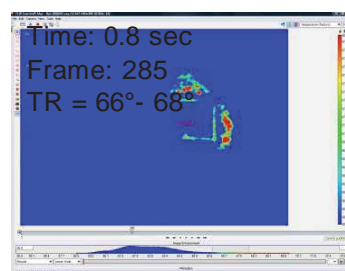
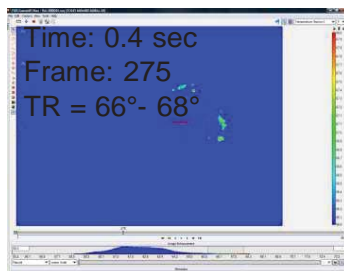
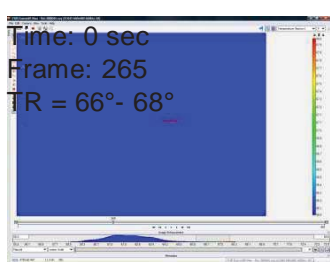
Post Strike Photograph

W2: XY(col(W 1, 1), col(W 1, 2)+2.19);se thunits('Se conds');se tvunits('m m')



Panel Displacement: Displacement, mm versus Time, sec

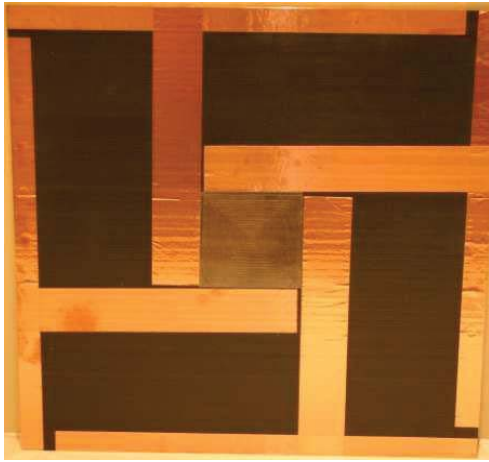
(This data is uncorrected for sensor placement angle. The scale factor for corrected data is 0.8572.)



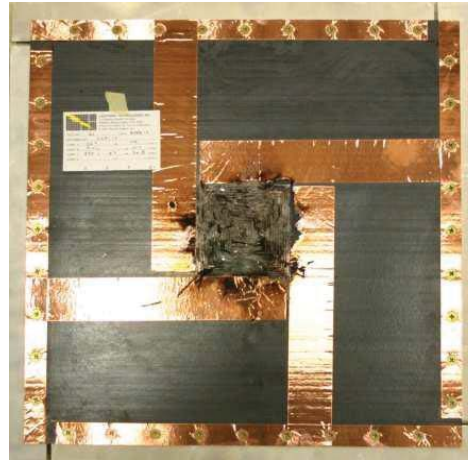
Panel backside IR image at sequential times. Note image has been flipped to provide a top side view.

Figure A 17. Concluded.

Fiberglass Panel - Configuration: Unpainted 4in Dexmet Cu Mesh  
 Peak Current, kA: 40

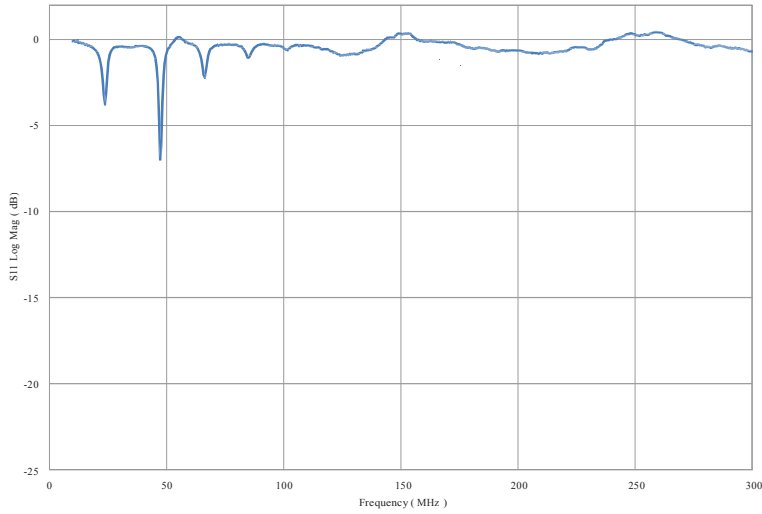


Pre Strike Photograph

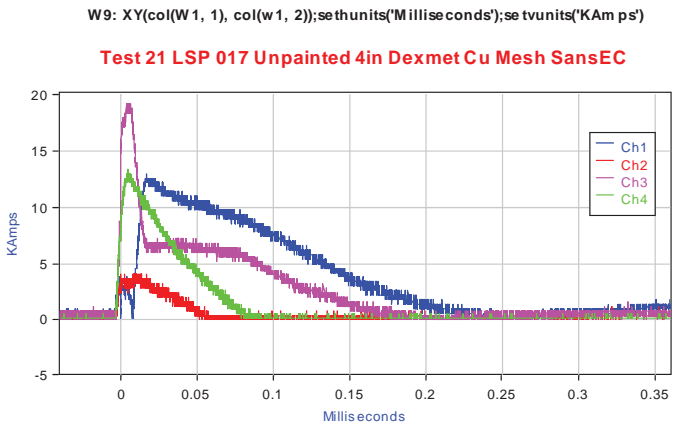


Post Strike Photograph

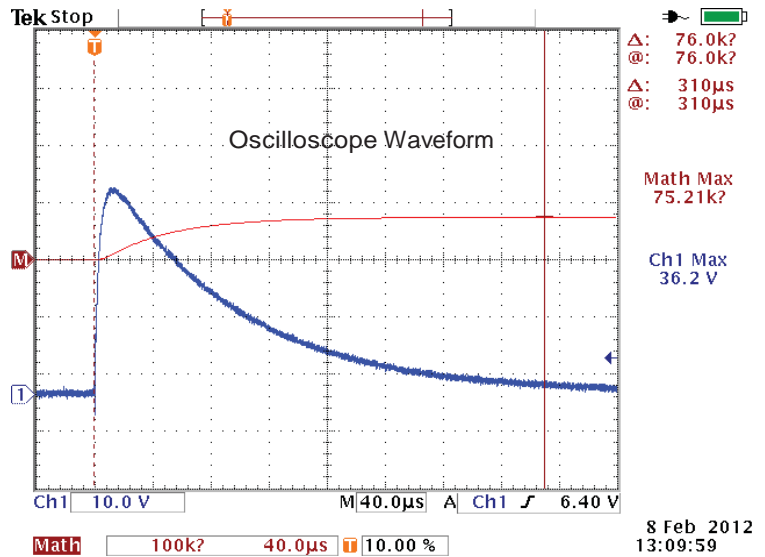
4 in SansEC Dexmet Mesh LSP unpainted



Pre Strike Resonate Measurement



Channels 1-4 Ground Current



Input Current, kA verse Time, millisecc

Figure A 18. Fiberglass substrate configuration performance. Configuration: Unpainted 4in Dexmet Cu Mesh  
 120

# Fiberglass Panel - Configuration: Unpainted 4in Dexmet Cu Mesh

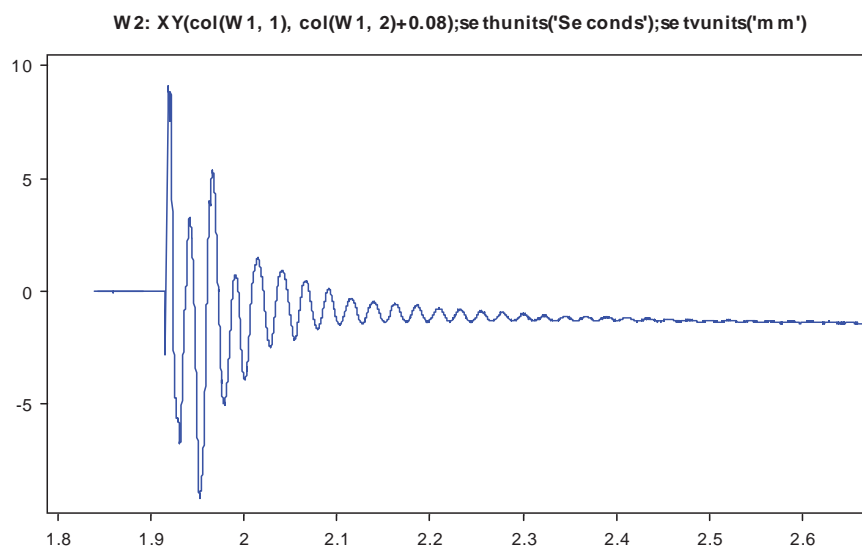
Peak Current, kA: 40



Pre Strike Photograph



Post Strike Photograph



Panel Displacement: Displacement, mm versus Time, sec

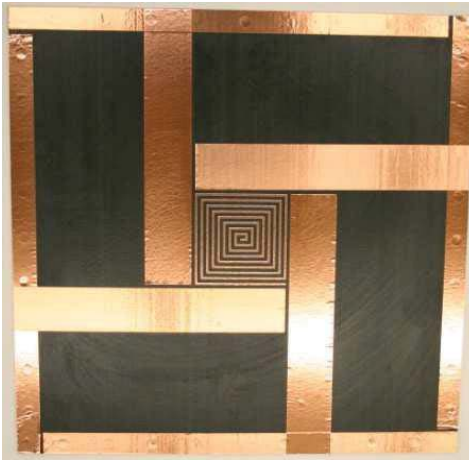
(This data is uncorrected for sensor placement angle. The scale factor for corrected data is 0.8572.)

**Data not Available**

Panel backside IR image at sequential times. Note image has been flipped to provide a top side view.

Figure A 18. Concluded.

Fiberglass Panel - Configuration: Painted 4in Gap Width SansEC  
 Peak Current, kA: 40

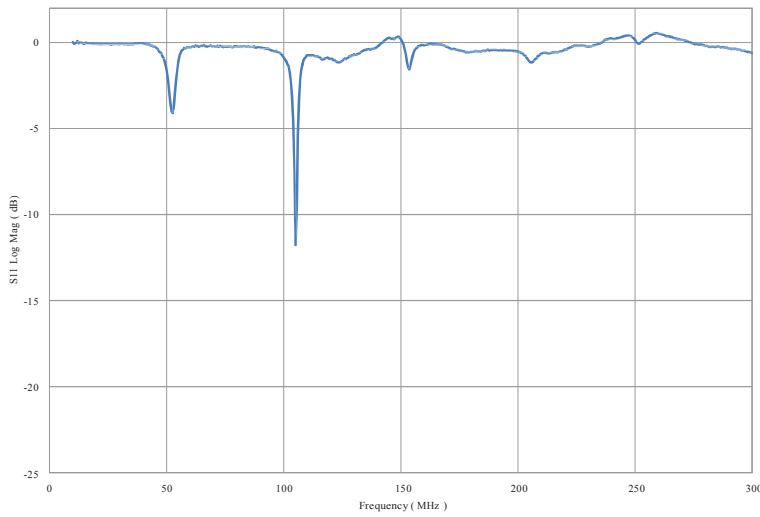


Pre Strike Photograph

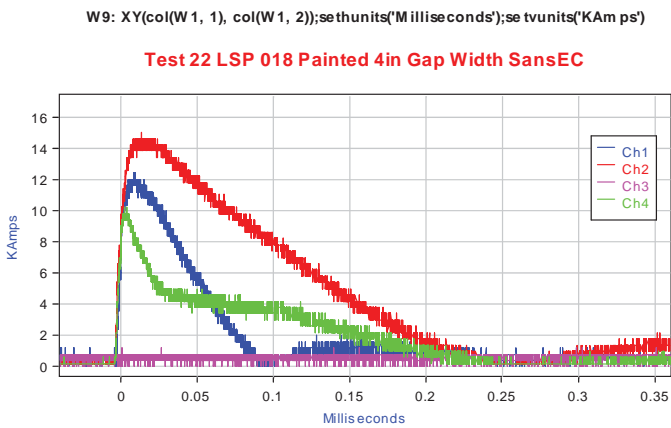


Post Strike Photograph

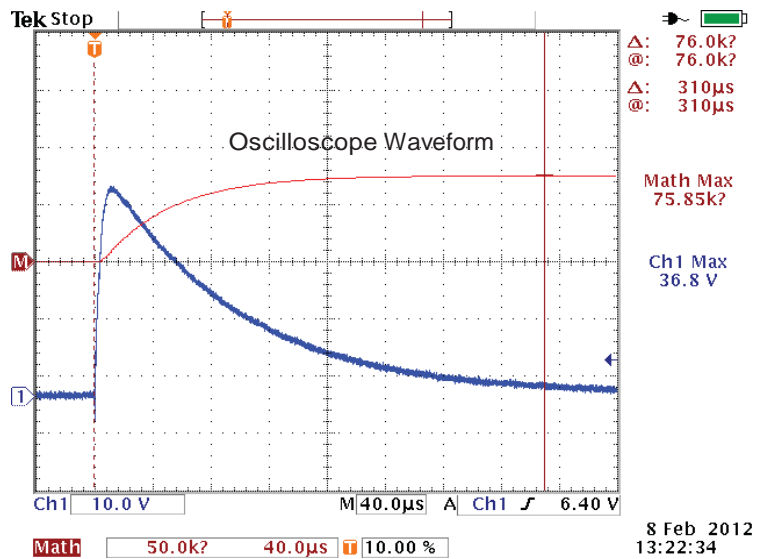
4 in SansEC Gap Width



Pre Strike Resonate Measurement



Channels 1-4 Ground Current



Input Current, kA verse Time, millsec

Figure A 19. Fiberglass substrate configuration performance. Configuration: Painted 4in Gap Width SansEC

# Fiberglass Panel - Configuration: Painted 4in Gap Width SansEC

Peak Current, kA: 40

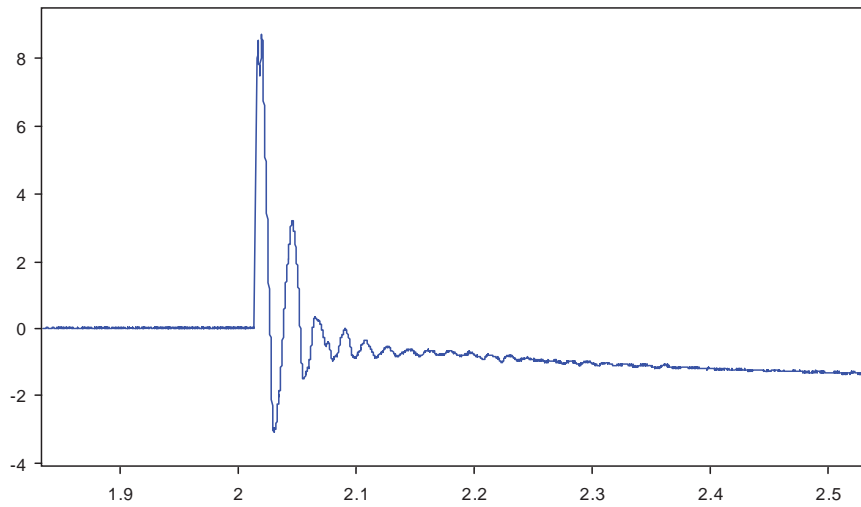


Pre Strike Photograph



Post Strike Photograph

W2: XY(col(W 1, 1), col(W 1, 2)+3.32);se thunits('Se conds');se tvunits('m m')



Panel Displacement: Displacement, mm versus Time, sec

(This data is uncorrected for sensor placement angle. The scale factor for corrected data is 0.8572.)

**Data not Available**

Panel backside IR image at sequential times. Note image has been flipped to provide a top side view.

Figure A 19. Concluded.

Fiberglass Panel - Configuration: Painted 4in Trace Width SansEC  
 Peak Current, kA: 40

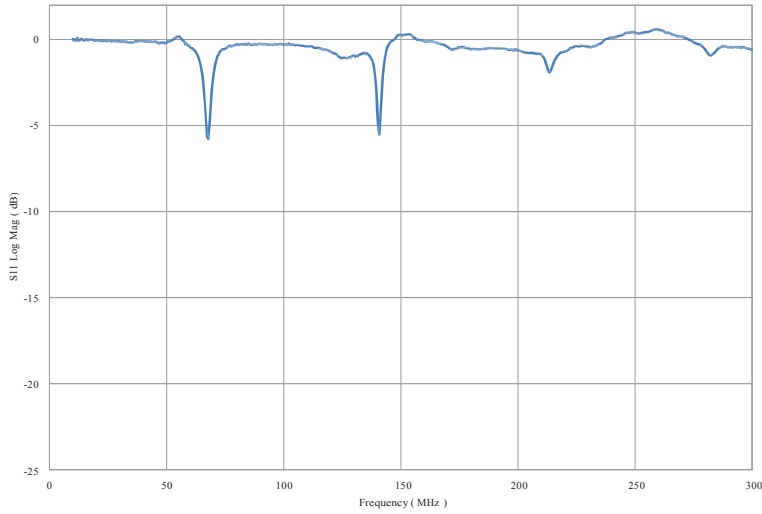


Pre Strike Photograph

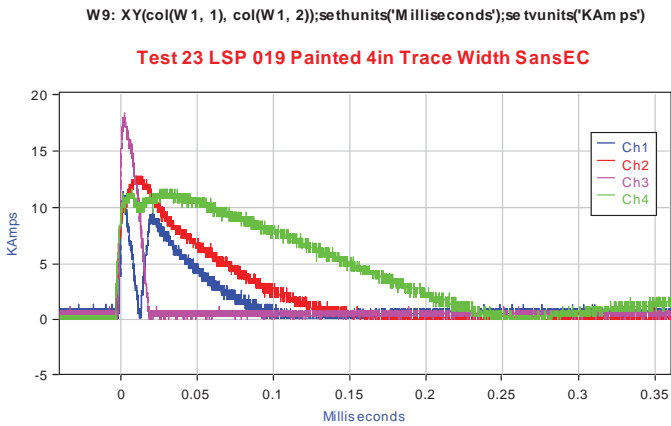


Post Strike Photograph

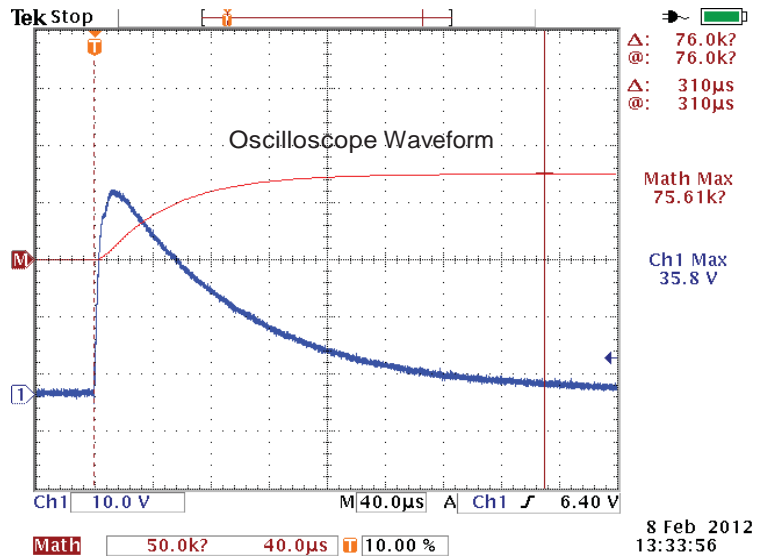
4 in SansEC Trace Width



Pre Strike Resonate Measurement



Channels 1-4 Ground Current



Input Current, kA verse Time, millsec

Figure A 20. Fiberglass substrate configuration performance. Configuration: Painted 4in Trace Width SansEC  
 124

# Fiberglass Panel - Configuration: Painted 4in Trace Width SansEC

Peak Current, kA: 40

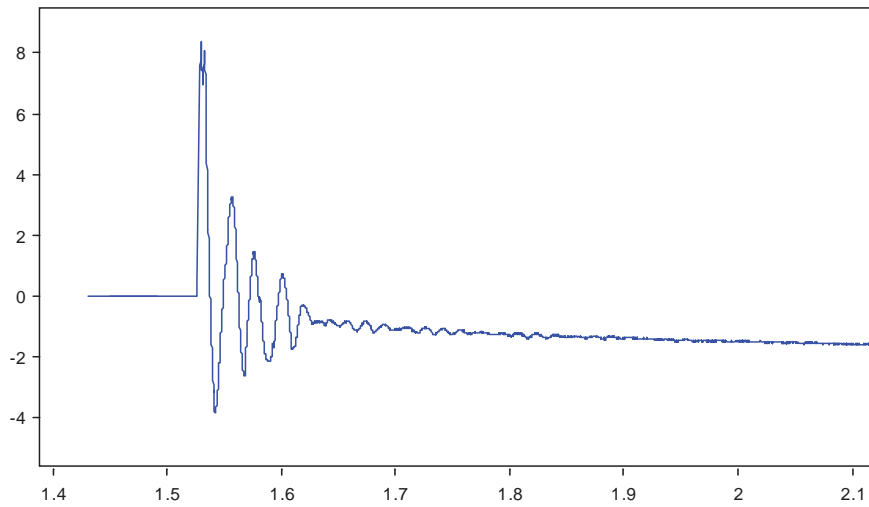


Pre Strike Photograph



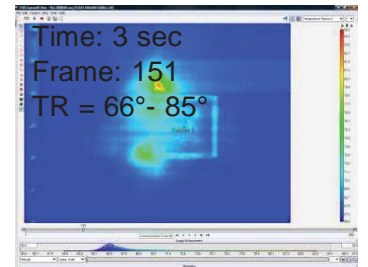
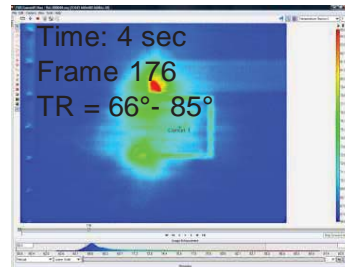
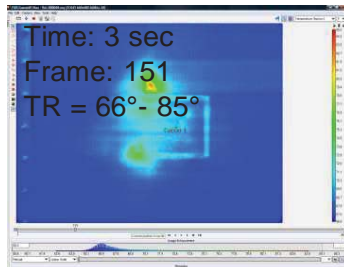
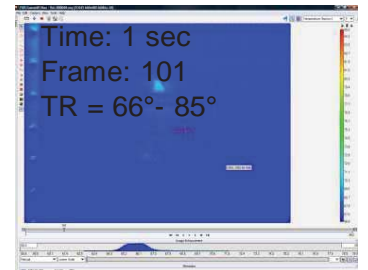
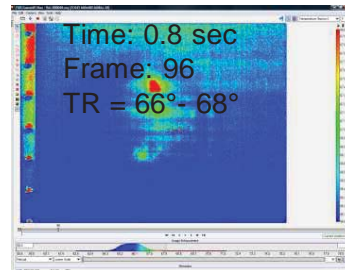
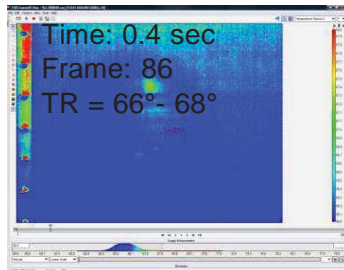
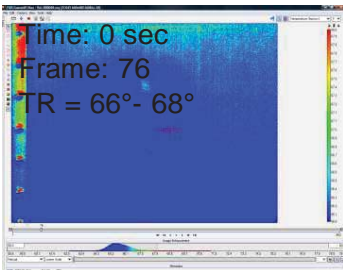
Post Strike Photograph

W2: XY(col(W 1, 1), col(W 1, 2)+2.87);se thunits('Se conds');se tvunits('m m')



Panel Displacement: Displacement, mm versus Time, sec

(This data is uncorrected for sensor placement angle. The scale factor for corrected data is 0.8572.)



Panel backside IR image at sequential times. Note image has been flipped to provide a top side view.

Figure A 20. Concluded.

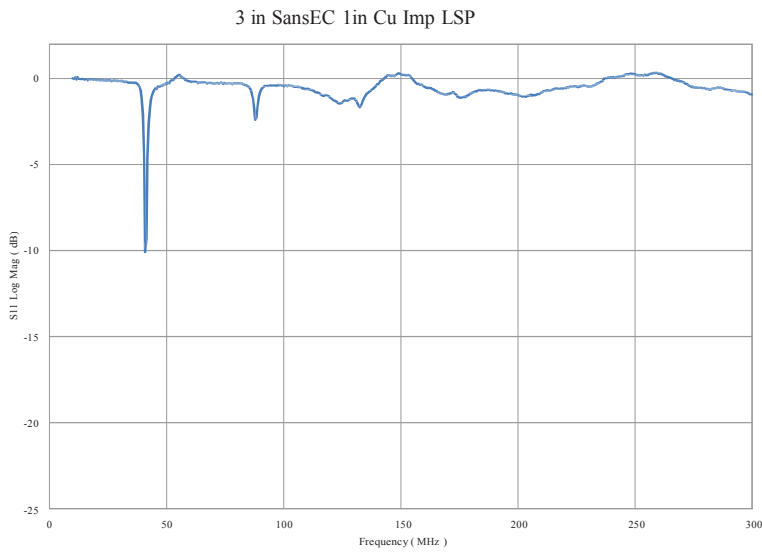
Fiberglass Panel - Configuration: Painted 3in SansEC 1in Cu  
 Peak Current, kA: 40



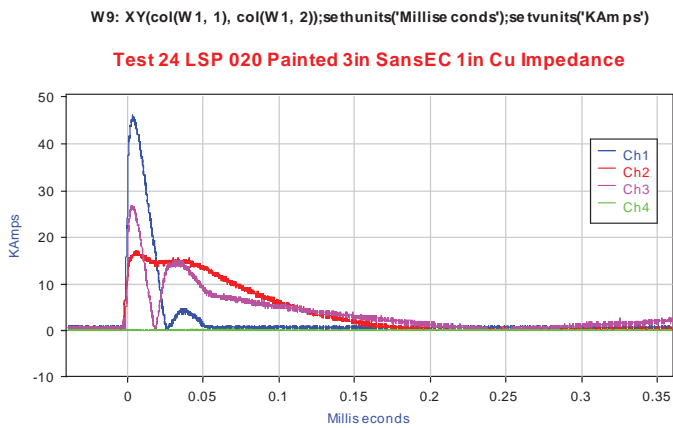
Pre Strike Photograph



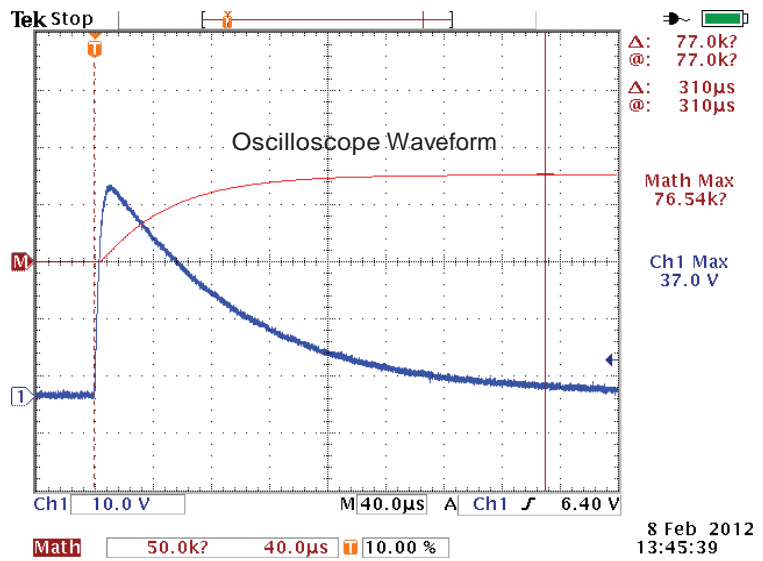
Post Strike Photograph



Pre Strike Resonate Measurement



Channels 1-4 Ground Current

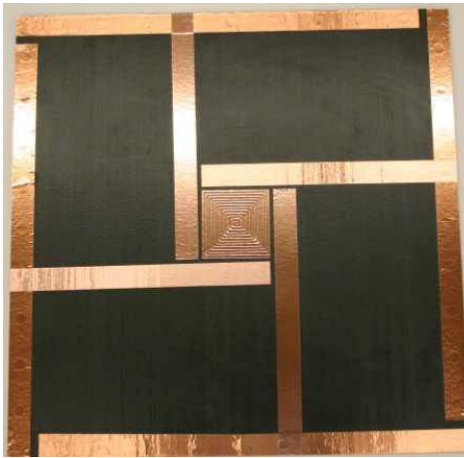


Input Current, kA verse Time, millisecc

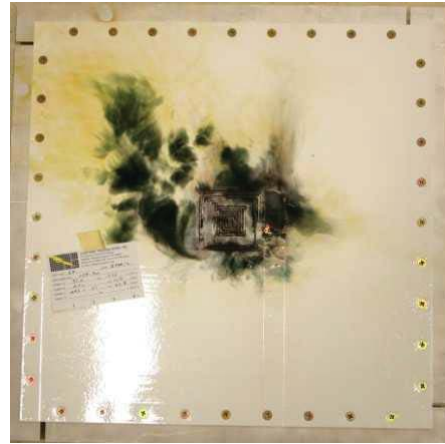
Figure A21. Fiberglass substrate configuration performance. Configuration: Painted 3in SansEC 1in Cu  
 126

# Fiberglass Panel - Configuration: Painted 3in SansEC 1in Cu

Peak Current, kA: 40

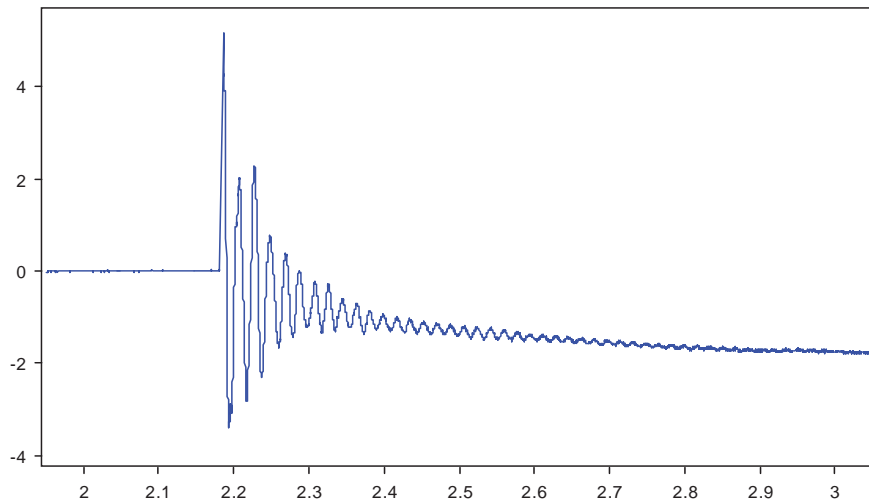


Pre Strike Photograph



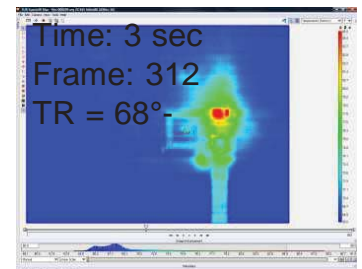
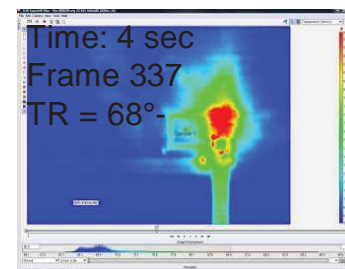
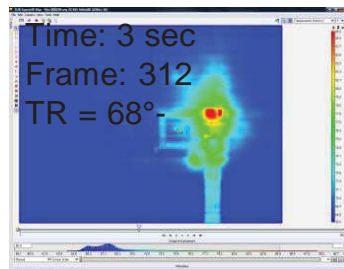
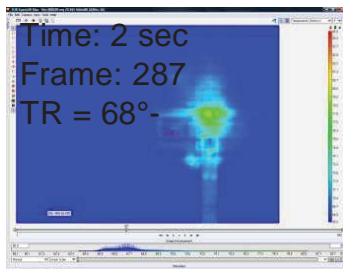
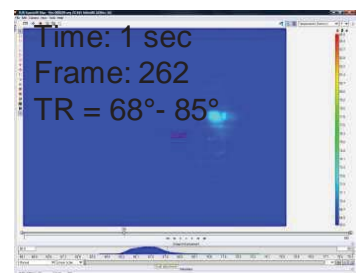
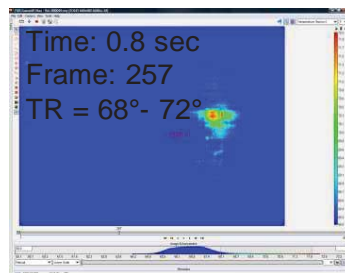
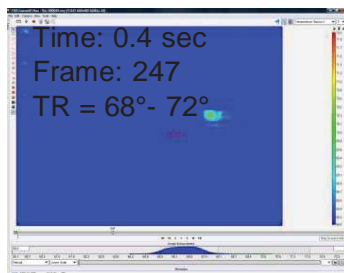
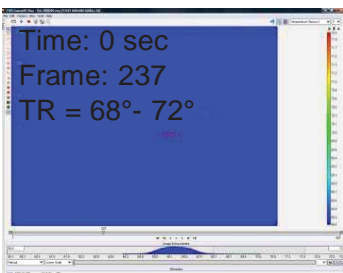
Post Strike Photograph

W2: XY(col(W 1, 1), col(W 1, 2)+0.83);se thunits('Se conds');se tvunits('m m')



Panel Displacement: Displacement, mm versus Time, sec

(This data is uncorrected for sensor placement angle. The scale factor for corrected data is 0.8572.)

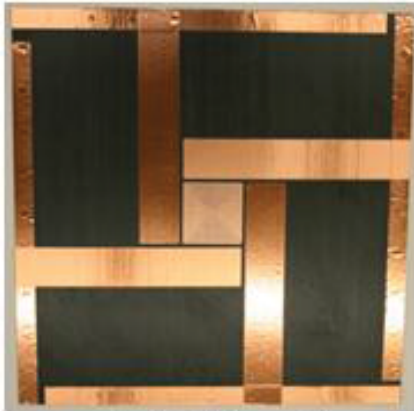


Panel backside IR image at sequential times. Note image has been flipped to provide a top side view.

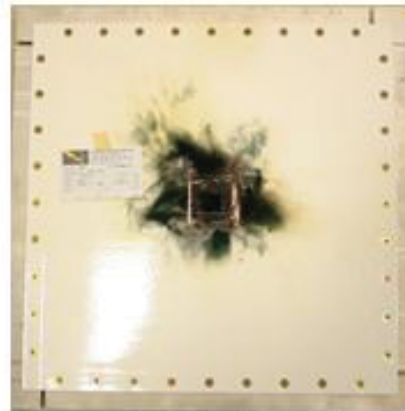
Figure A21. Concluded.

Fiberglass Panel - Configuration: Painted 3in SansEC 2in Cu Impedance

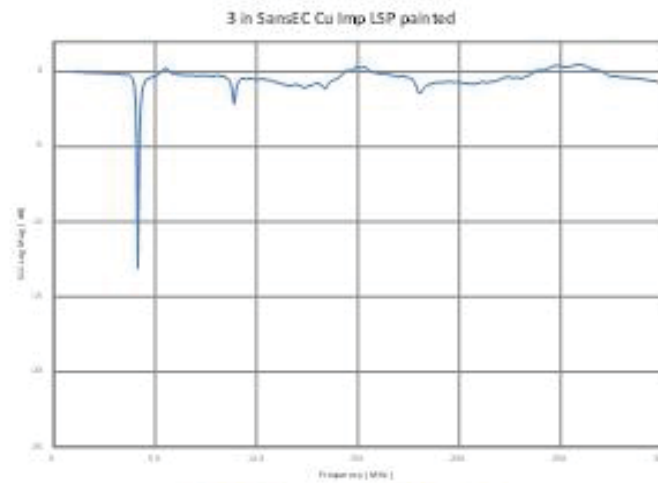
Peak Current, kA: 40



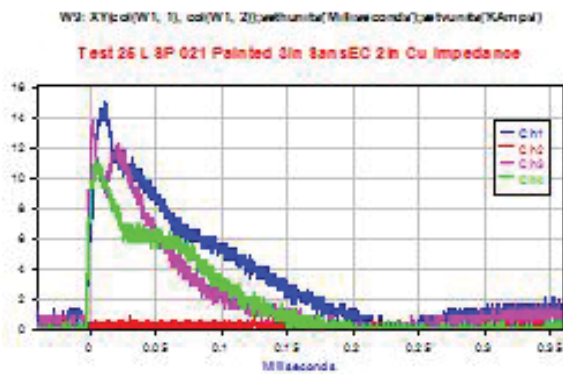
Pre Strike Photograph



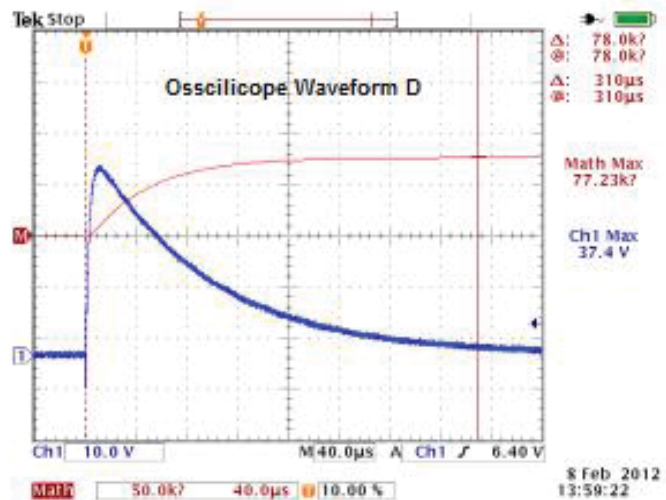
Post Strike Photograph



Pre Strike Resonate Measurement



Channels 1-4 Ground Current



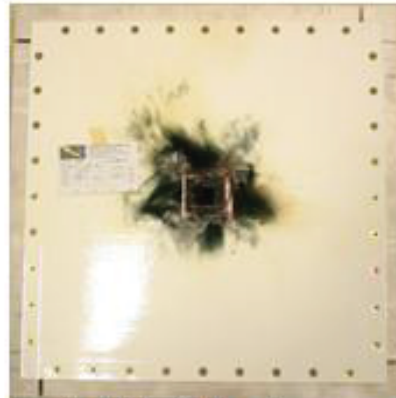
Input Current, kA verse Time, millisc

Figure A.22. Fiberglass substrate configuration performance. Configuration: Painted 3in SansEC 2in Cu

Fiberglass Panel - Configuration: Painted 3in SansEC 2in Cu Impedance  
Peak Current, kA: 40

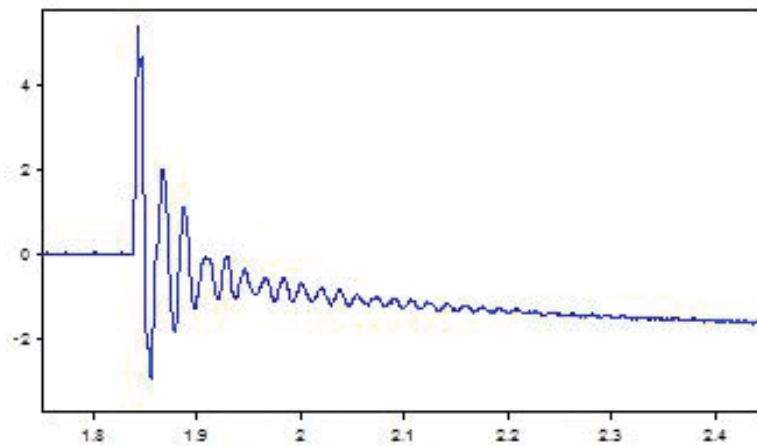


Pre Strike Photograph



Post Strike Photograph

W2: XY(ool(W1, 1), ool(W1, 2)+1.84);sethunits('seconds');setvunits('mm')



Panel Displacement: Displacement, mm versus Time, sec

(This data is uncorrected for sensor placement angle. The scale factor for corrected data is 0.8572.)

**Data not Available**

Panel backside IR image at sequential times. Note image has been flipped to provide a top side view.

Figure A 22. Concluded.

# Fiberglass Panel - Configuration: Painted 3in SansEC 2in Al

Peak Current, kA: 40

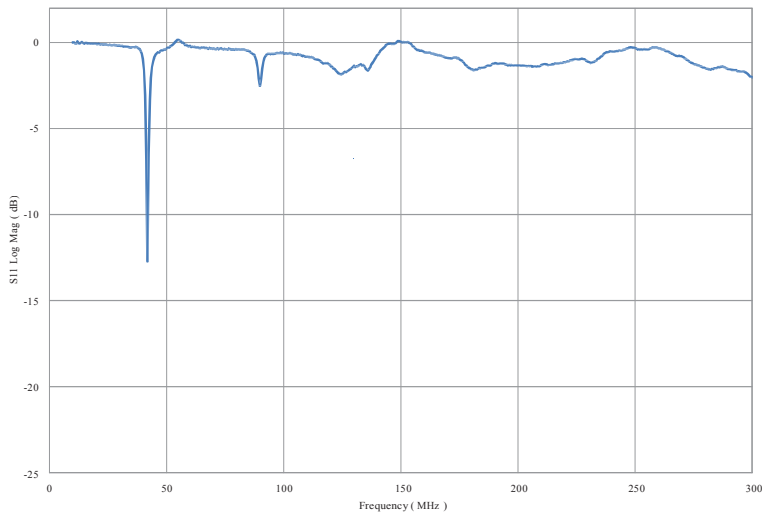


Pre Strike Photograph

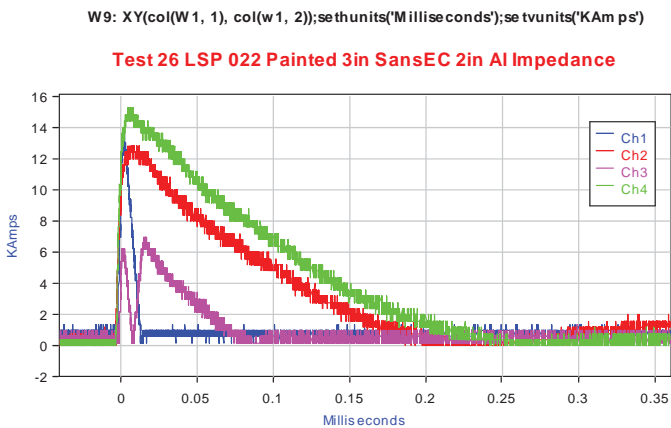


Post Strike Photograph

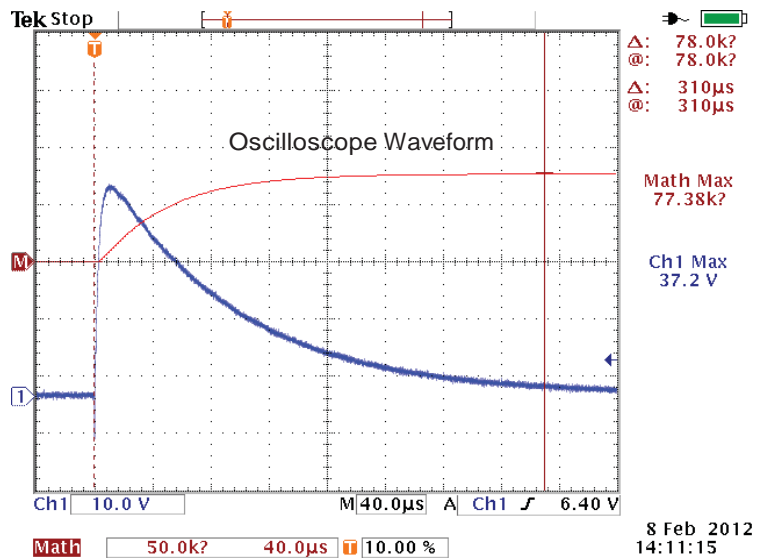
3 in SansEC Al Imp LSP



Pre Strike Resonate Measurement



Channels 1-4 Ground Current



Input Current, kA verse Time, millsec

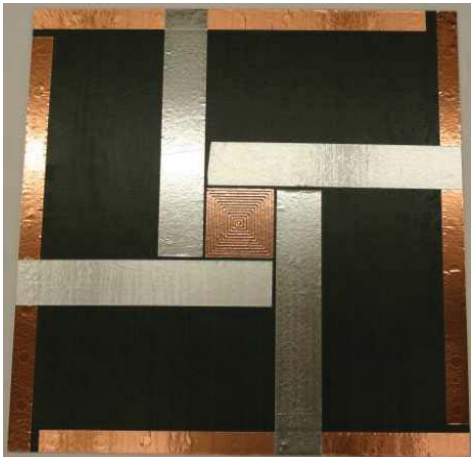
Figure A 23. Fiberglass substrate configuration performance. 130

Configuration: Painted 3in SansEC 2in Al Impedance

8 Feb 2012  
14:11:15

# Fiberglass Panel - Configuration: Painted 3in SansEC 2in Al

Peak Current, kA: 40

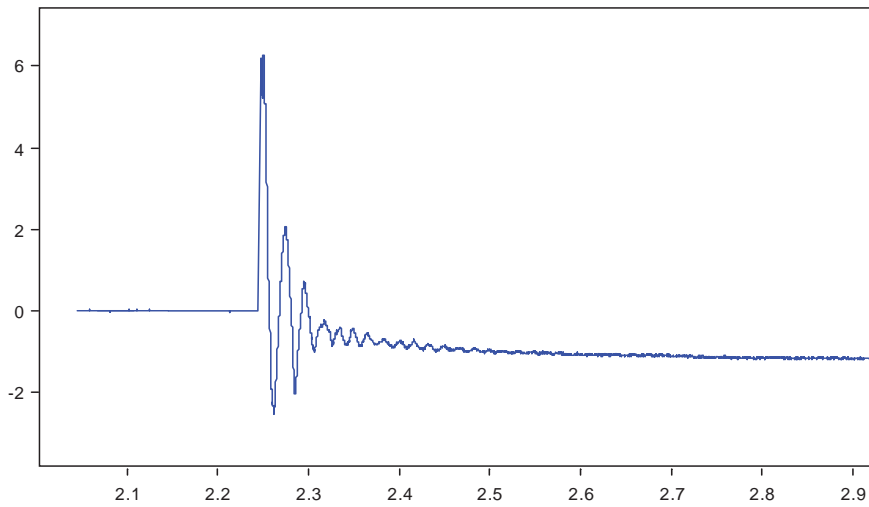


Pre Strike Photograph



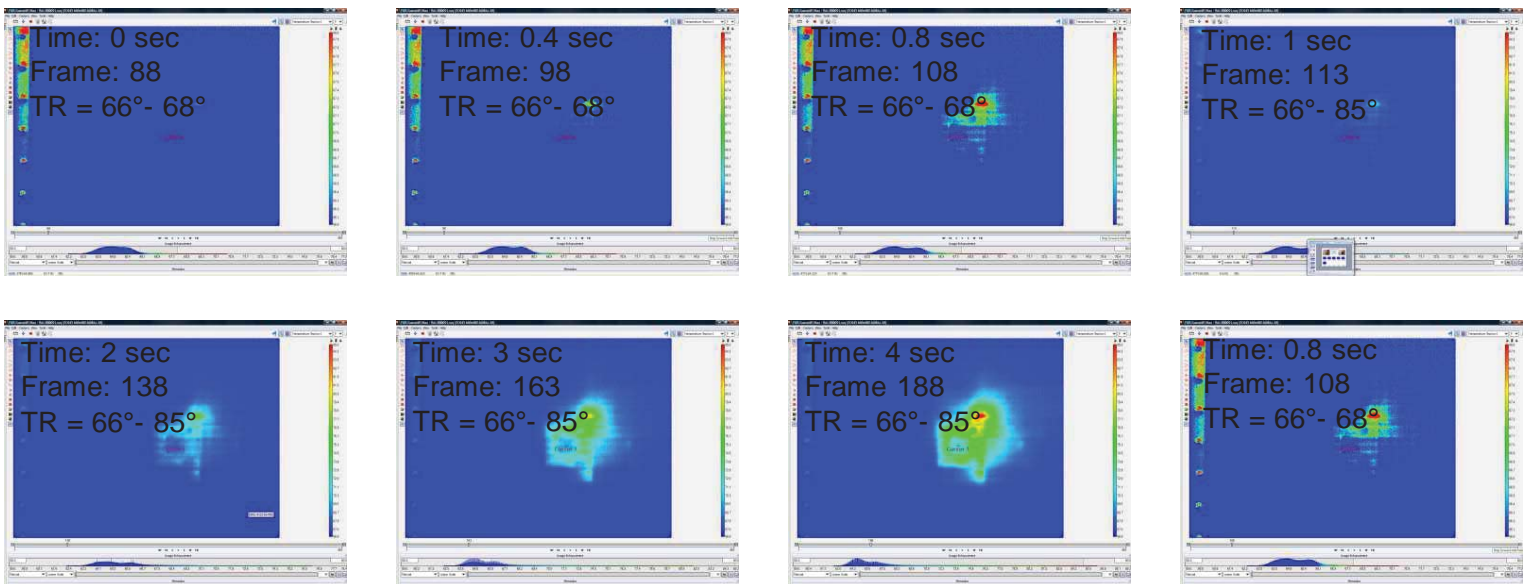
Post Strike Photograph

W2: XY(col(W 1, 1), col(W 1, 2)+3.44);se thunits('Se conds');se tvunits('m m')



Panel Displacement: Displacement, mm versus Time, sec

(This data is uncorrected for sensor placement angle. The scale factor for corrected data is 0.8572.)

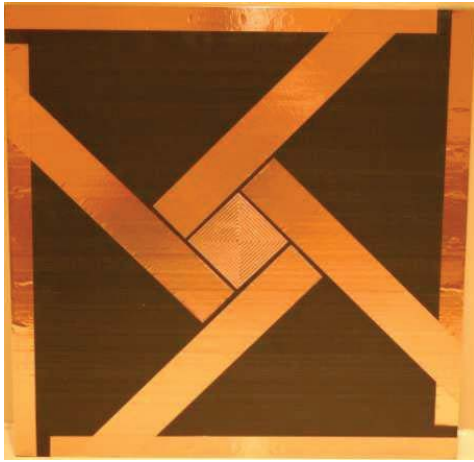


Panel backside IR image at sequential times. Note image has been flipped to provide a top side view.

Figure A 23. Concluded.

# Fiberglass Panel - Configuration: Unpainted 3in SansEC 45 deg

Peak Current, kA: 40

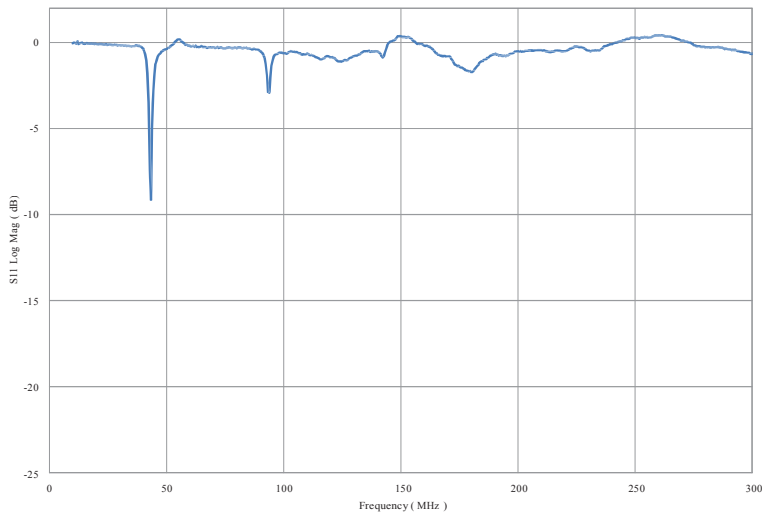


Pre Strike Photograph

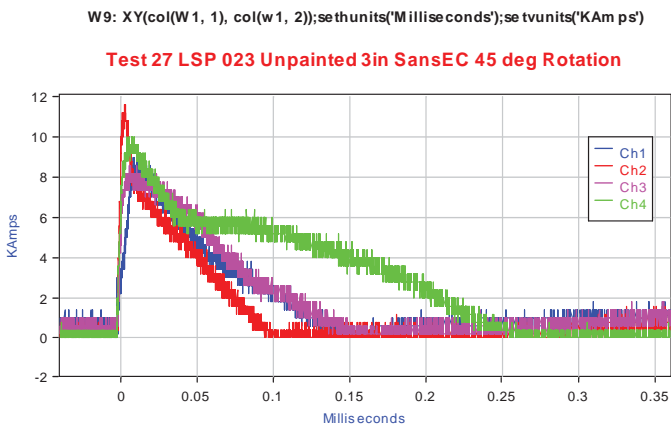


Post Strike Photograph

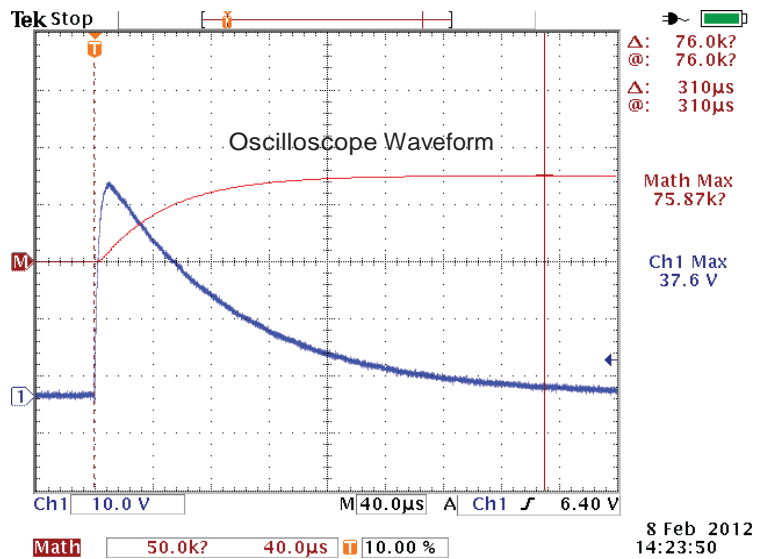
3 in SansEC Rotated LSP unpainted



Pre Strike Resonate Measurement



Channels 1-4 Ground Current

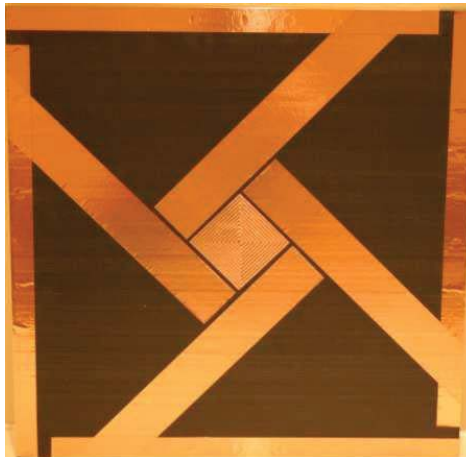


Input Current, kA verse Time, millsec

Figure A24. Fiberglass substrate configuration performance. Configuration: Unpainted 3in SansEC 45 deg

Fiberglass Panel - Configuration: Unpainted 3in SansEC 45 deg

Peak Current, kA: 40

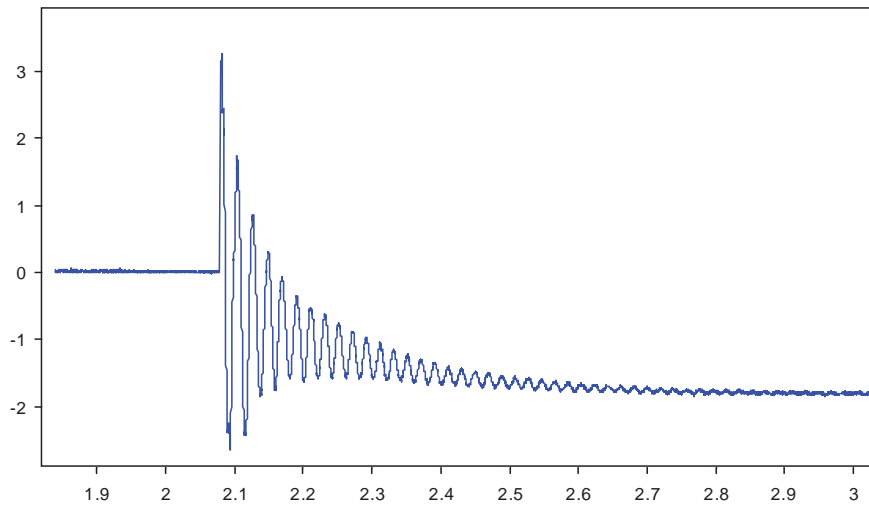


Pre Strike Photograph



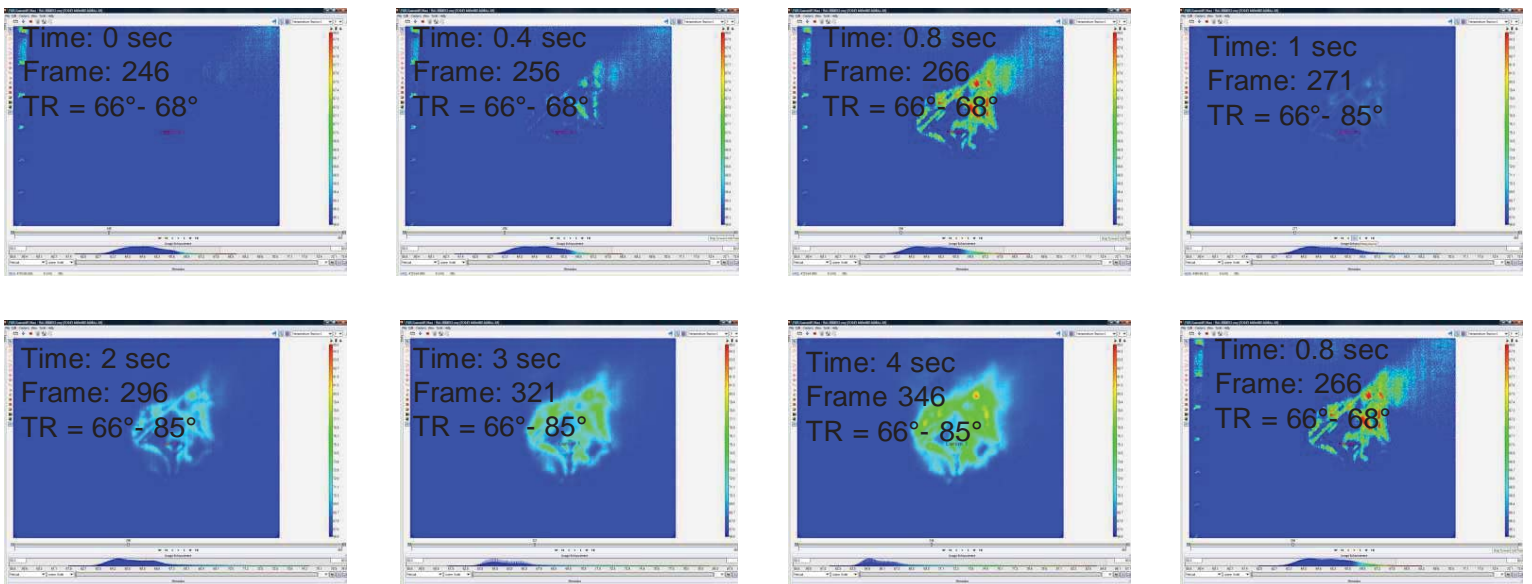
Post Strike Photograph

W2: XY(col(W 1, 1), col(W 1, 2)+0.24);se thunits('Se conds');se tvunits('m m')



Panel Displacement: Displacement, mm versus Time, sec

(This data is uncorrected for sensor placement angle. The scale factor for corrected data is 0.8572.)

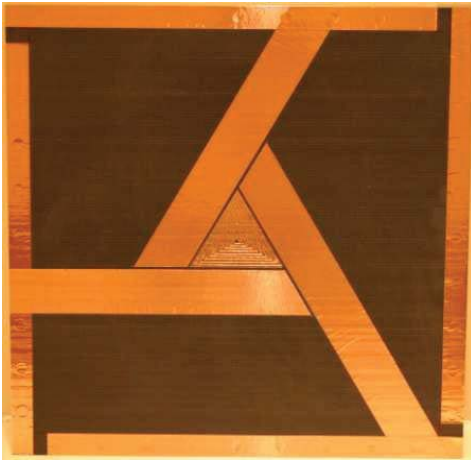


Panel backside IR image at sequential times. Note image has been flipped to provide a top side view.

Figure A 24. Concluded.

# Fiberglass Panel - Configuration: Unpainted 4in Triangular SansEC

Peak Current, kA: 40

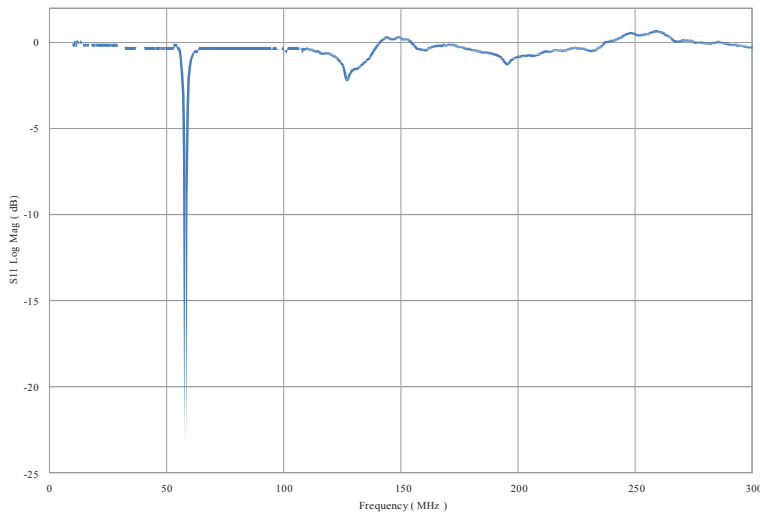


Pre Strike Photograph

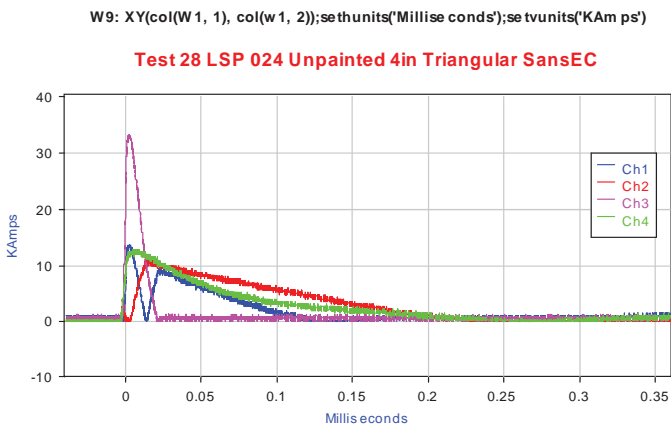


Post Strike Photograph

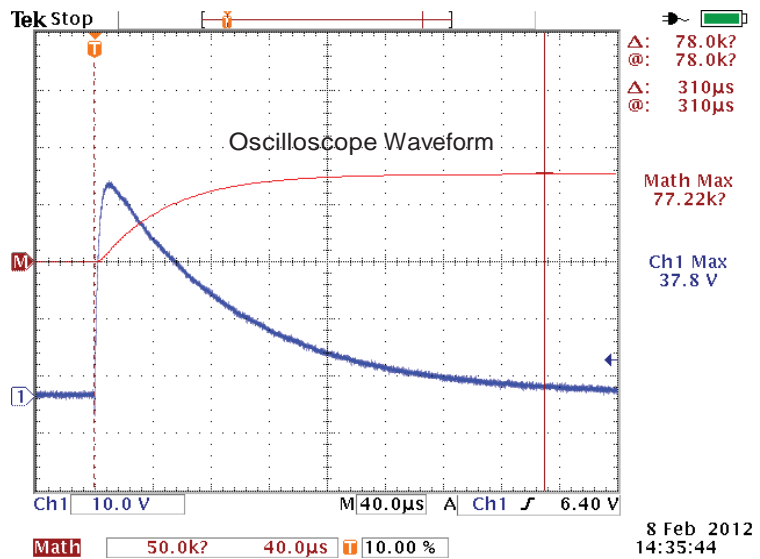
4 in SansEC Triangle LSP



Pre Strike Resonate Measurement



Channels 1-4 Ground Current

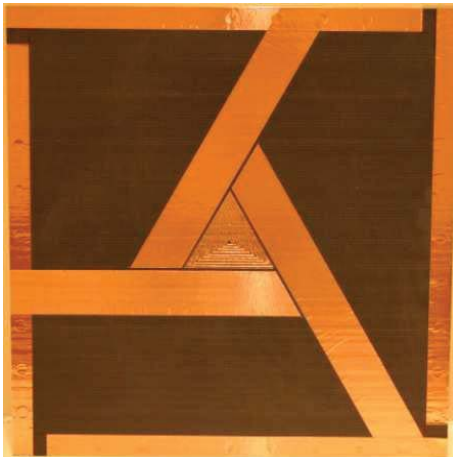


Input Current, kA verse Time, millsec

Figure A25. Fiberglass substrate configuration performance. Configuration: Unpainted 4in Triangular SansEC

# Fiberglass Panel - Configuration: Unpainted 4in Triangular SansEC

Peak Current, kA: 40

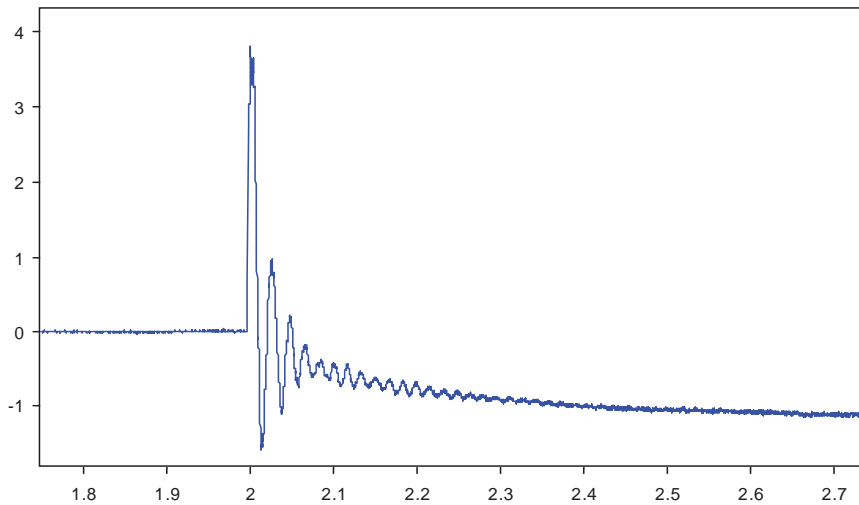


Pre Strike Photograph



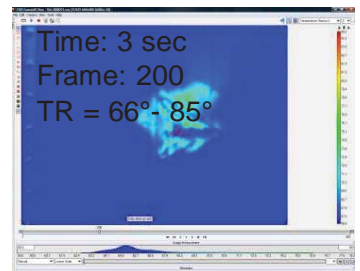
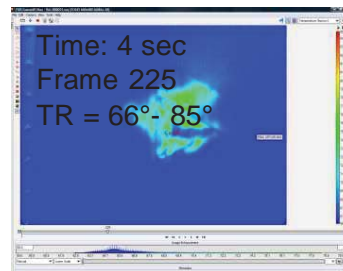
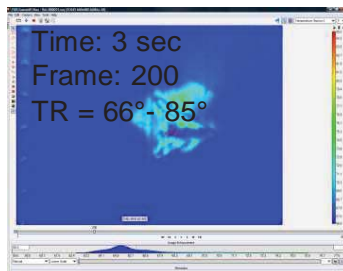
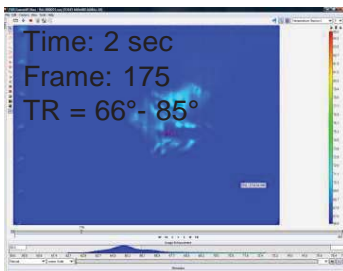
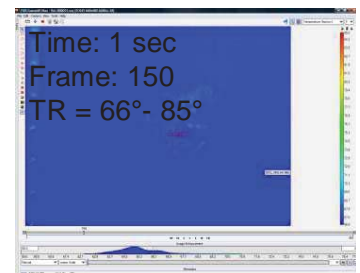
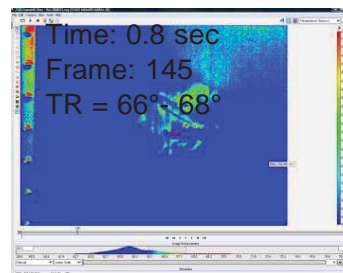
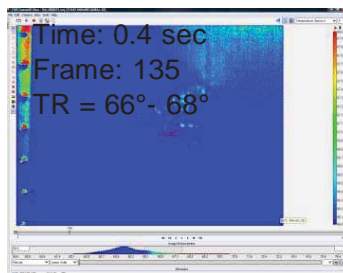
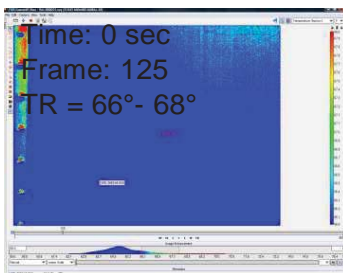
Post Strike Photograph

W2: XY(col(W 1, 1), col(W 1, 2)+4.04);se thunits('Se conds');se tvunits('m m')



Panel Displacement: Displacement, mm versus Time, sec

(This data is uncorrected for sensor placement angle. The scale factor for corrected data is 0.8572.)

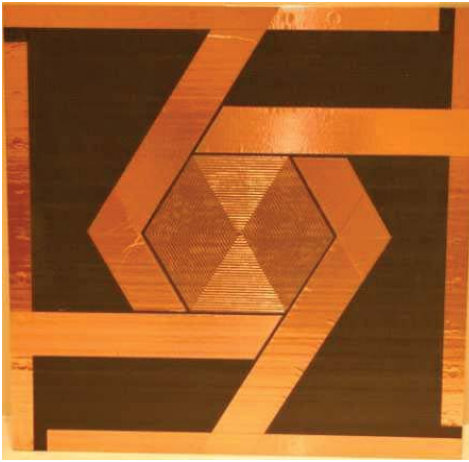


Panel backside IR image at sequential times. Note image has been flipped to provide a top side view.

Figure A 25. Concluded.

# Fiberglass Panel - Configuration: Unpainted 4in Hexagonal SansEC

Peak Current, kA: 40

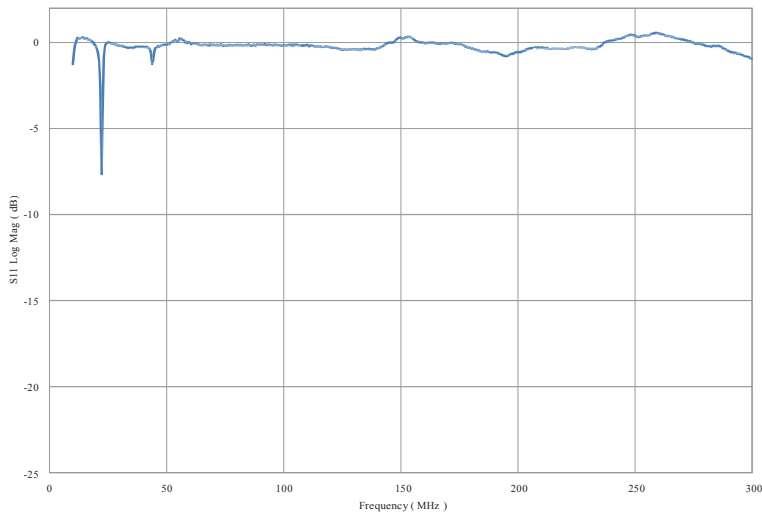


Pre Strike Photograph

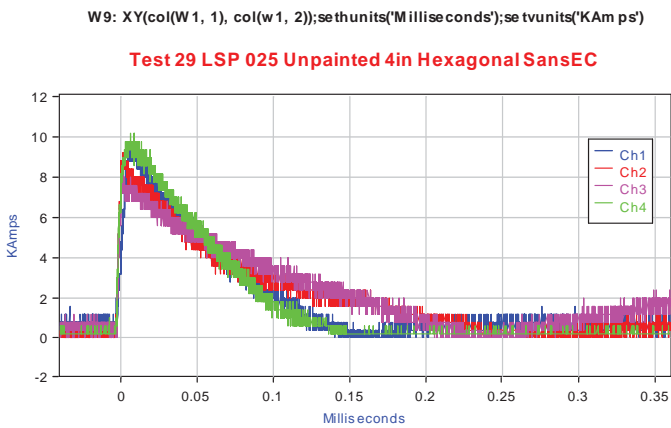


Post Strike Photograph

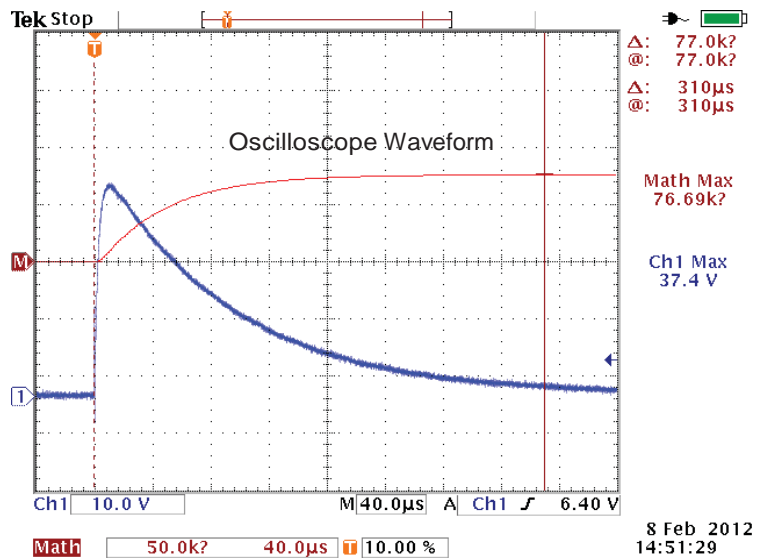
4 in SansEC Hexagon LSP unpainted



Pre Strike Resonate Measurement



Channels 1-4 Ground Current



Input Current, kA verse Time, millsec

Figure A26. Fiberglass substrate configuration performance. 136

Configuration: Unpainted 4in Hexagonal SansEC

# Fiberglass Panel - Configuration: Unpainted 4in Hexagonal SansEC

Peak Current, kA: 40

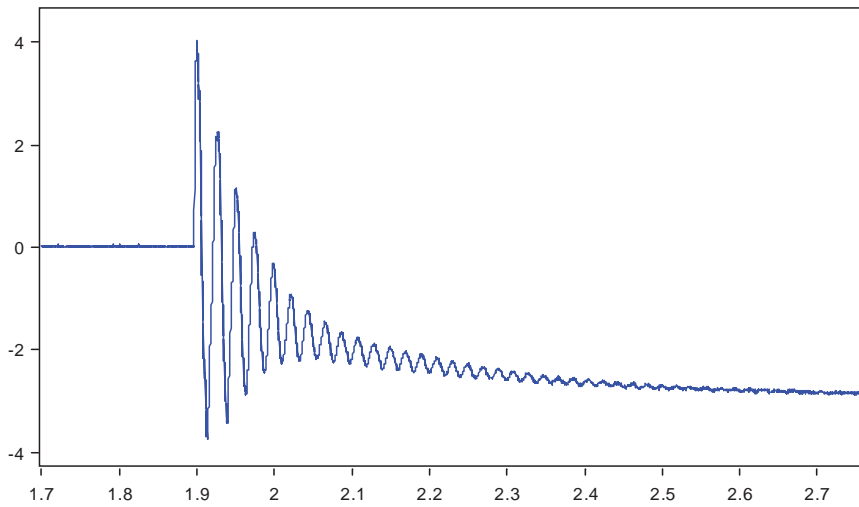


Pre Strike Photograph



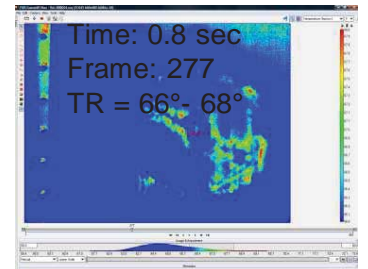
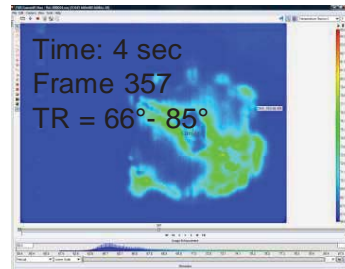
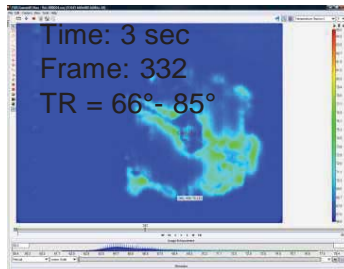
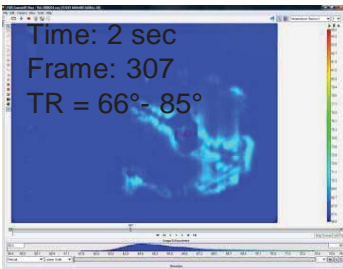
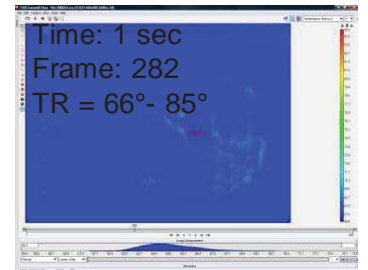
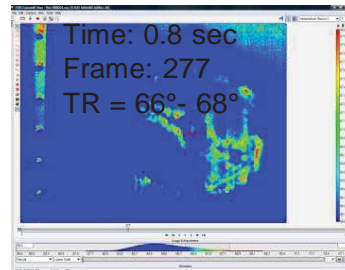
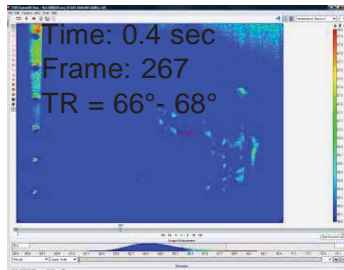
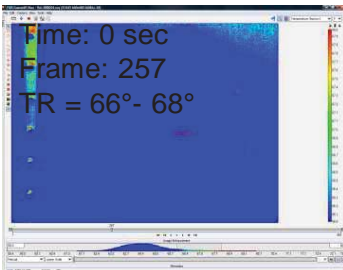
Post Strike Photograph

W2: XY(col(W 1, 1), col(W 1, 2)-0.21);se thunits('Seconds');se tvunits('m m')



Panel Displacement: Displacement, mm versus Time, sec

(This data is uncorrected for sensor placement angle. The scale factor for corrected data is 0.8572.)

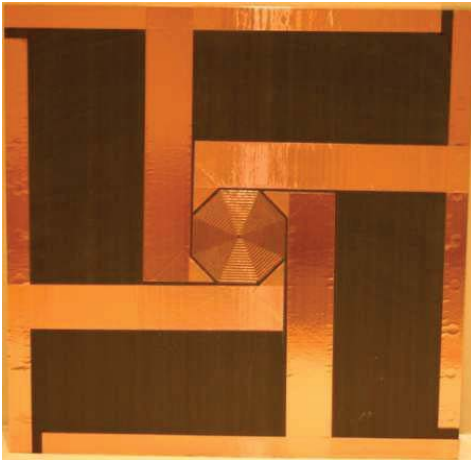


Panel backside IR image at sequential times. Note image has been flipped to provide a top side view.

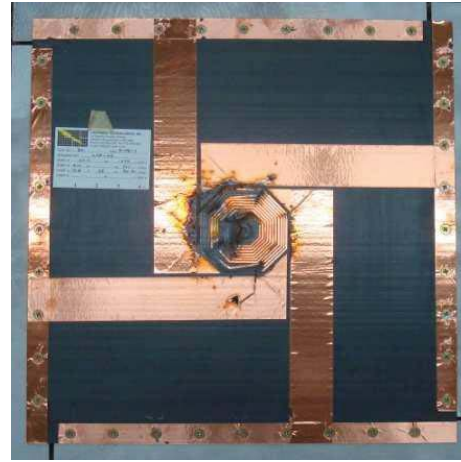
Figure A 26. Concluded.

# Fiberglass Panel - Configuration: Unpainted 2in Octagonal SansEC

Peak Current, kA: 40

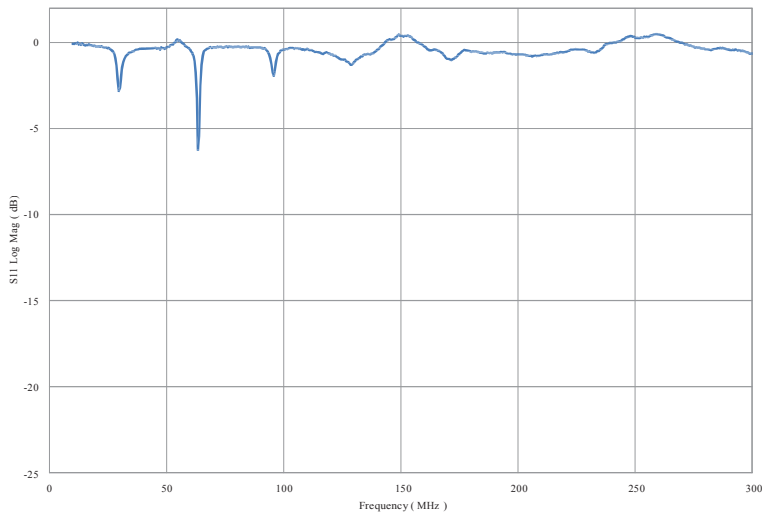


Pre Strike Photograph

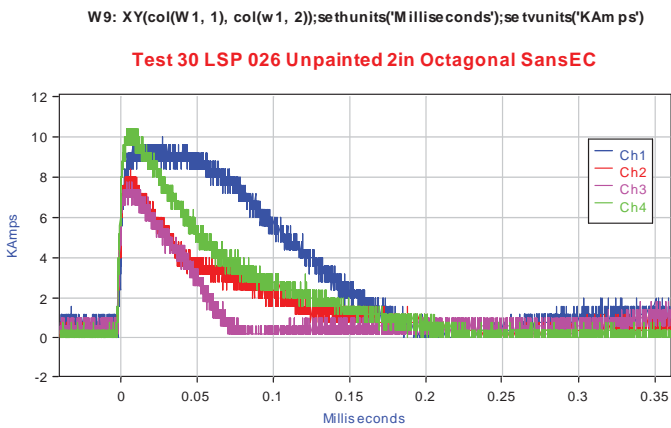


Post Strike Photograph

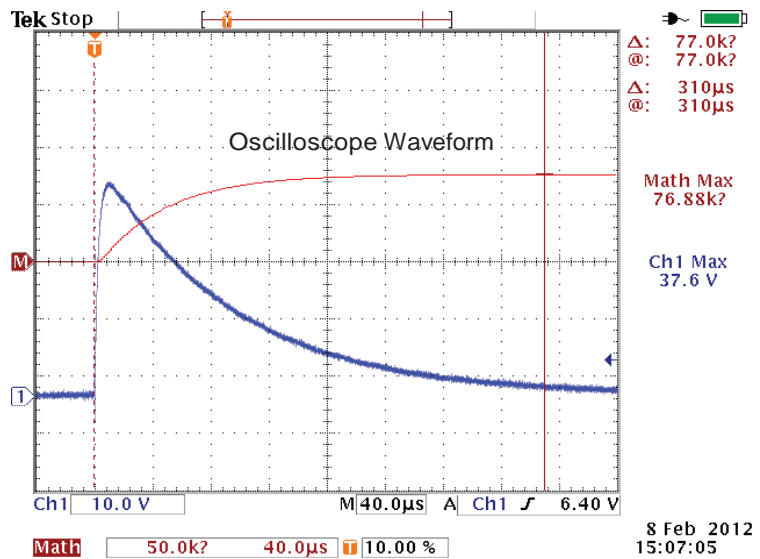
2 inch Octagon Unpainted LSP



Pre Strike Resonate Measurement



Channels 1-4 Ground Current

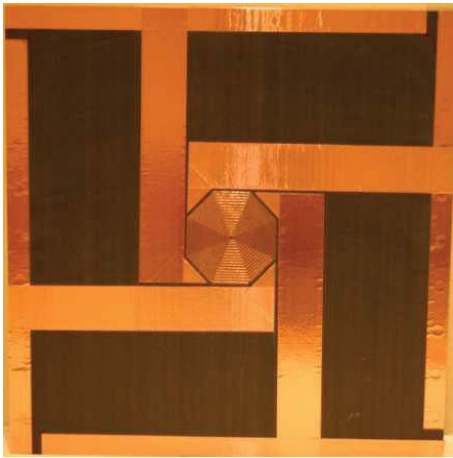


Input Current, kA verse Time, millsec

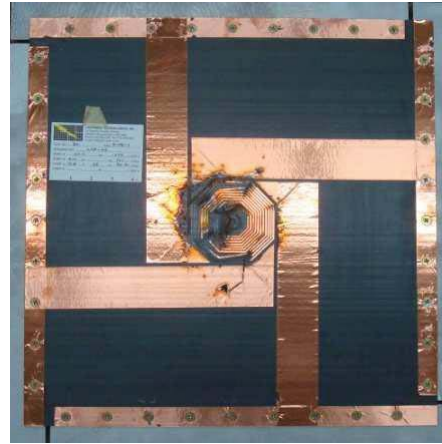
Figure A27. Fiberglass substrate configuration performance. Configuration: Unpainted 2in Octagonal SansEC

# Fiberglass Panel - Configuration: Unpainted 2in Octagonal SansEC

Peak Current, kA: 40

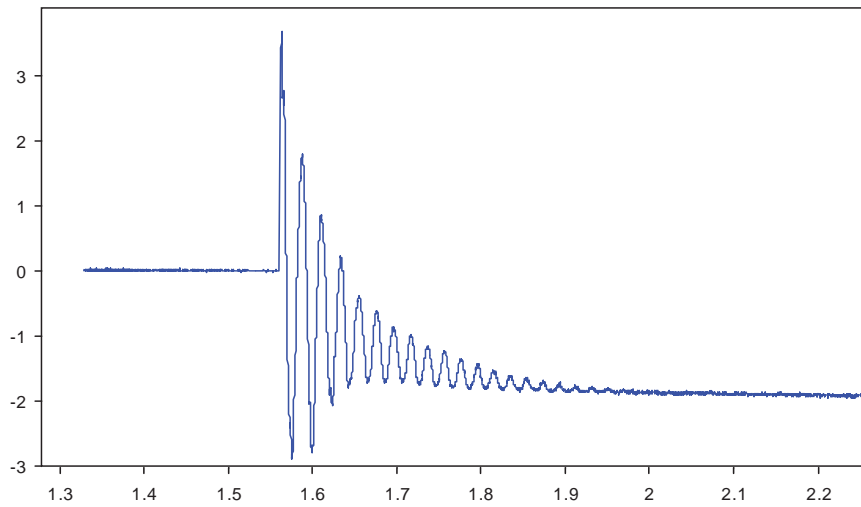


Pre Strike Photograph



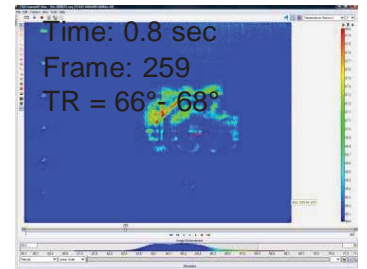
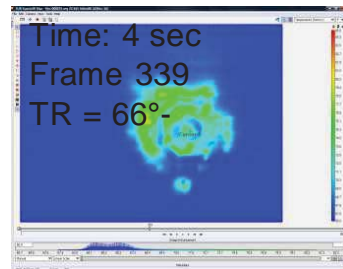
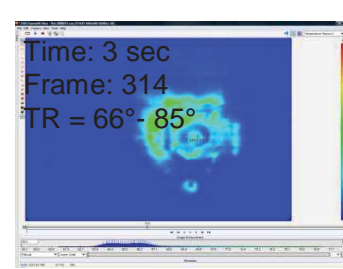
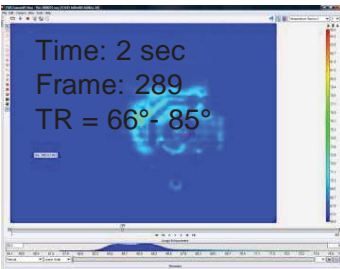
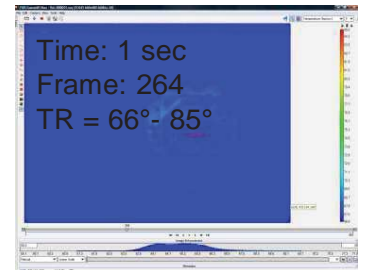
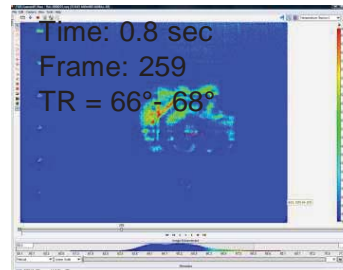
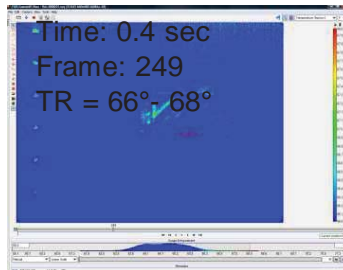
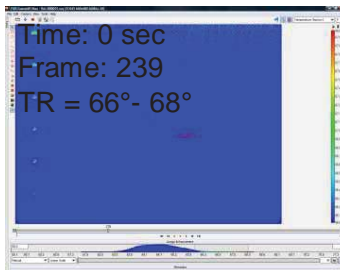
Post Strike Photograph

W2: XY(col(W 1, 1), col(W 1, 2)+0.40);se thunits('Se conds');se tvunits('m m')



Panel Displacement: Displacement, mm versus Time, sec

(This data is uncorrected for sensor placement angle. The scale factor for corrected data is 0.8572.)

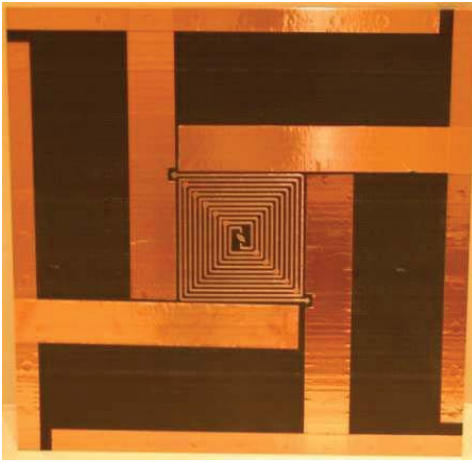


Panel backside IR image at sequential times. Note image has been flipped to provide a top side view.

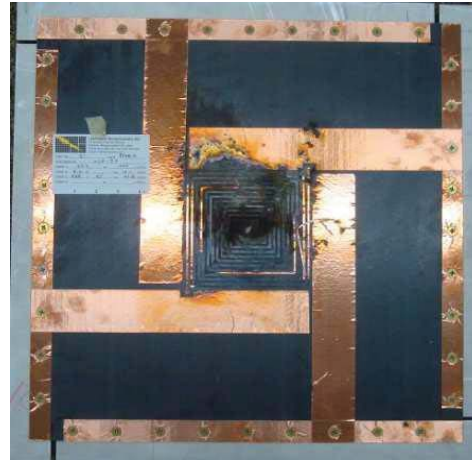
Figure A 27. Concluded.

# Fiberglass Panel - Configuration: Unpainted SansEC Football Stars

Peak Current, kA: 40

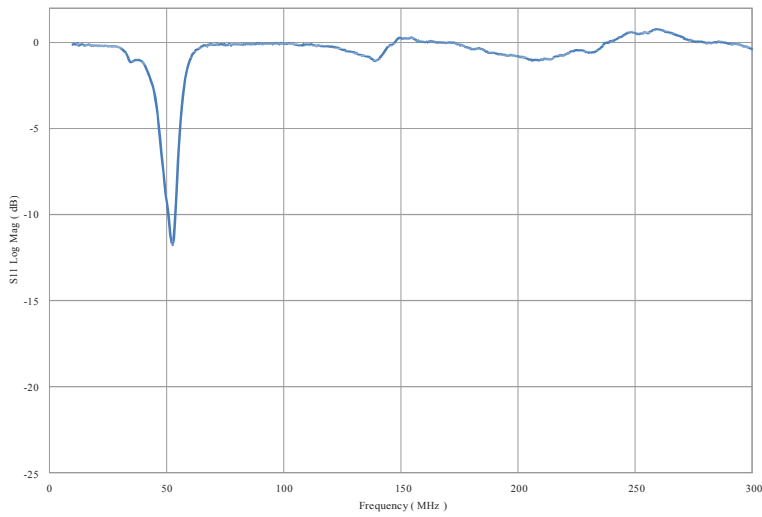


Pre Strike Photograph

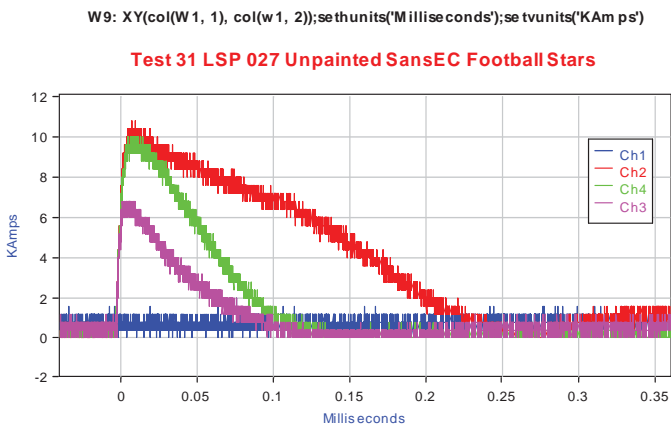


Post Strike Photograph

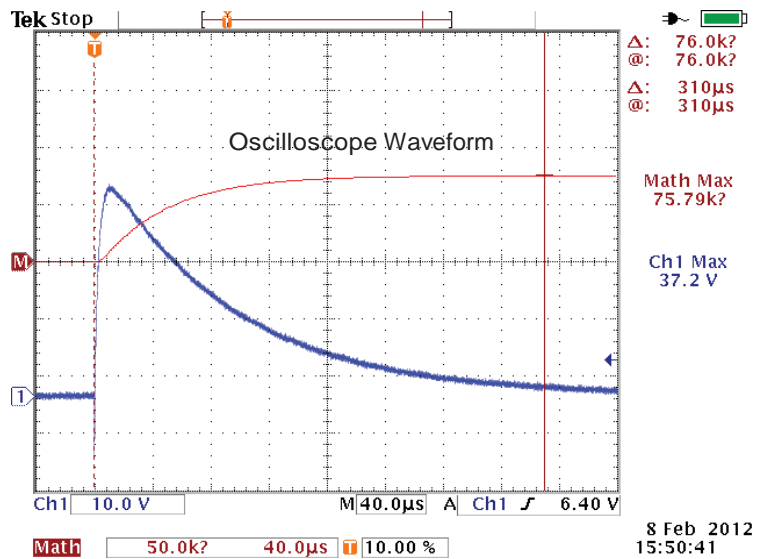
6 in SansEC Dual Spiral Football Stars LSP



Pre Strike Resonate Measurement



Channels 1-4 Ground Current



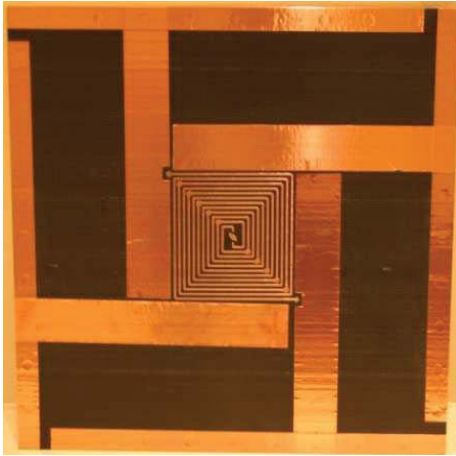
Input Current, kA verse Time, millisecc

8 Feb 2012 15:50:41

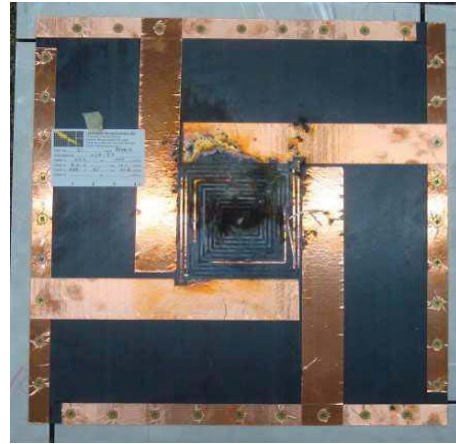
Figure A28. Fiberglass substrate configuration performance. Configuration: Unpainted SansEC Football Stars

# Fiberglass Panel - Configuration: Unpainted SansEC Football Stars

Peak Current, kA: 40

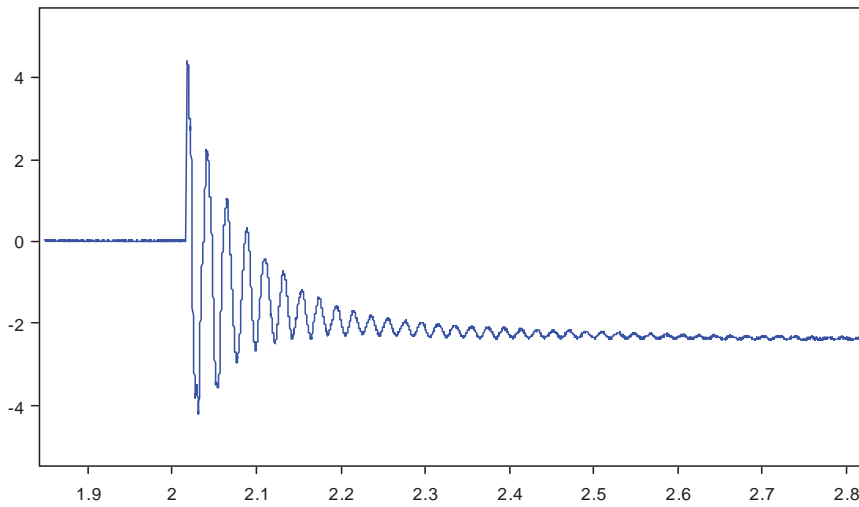


Pre Strike Photograph



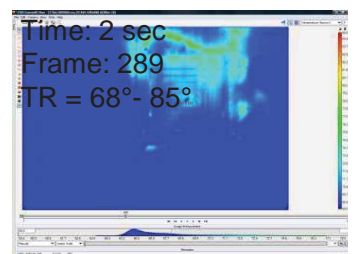
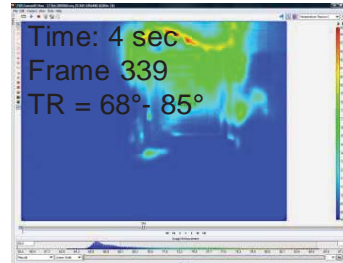
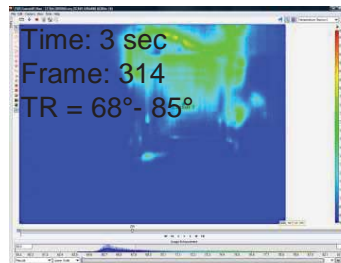
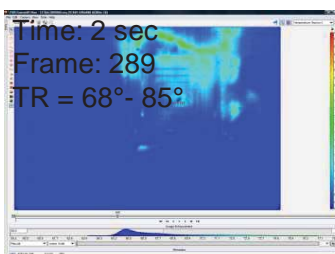
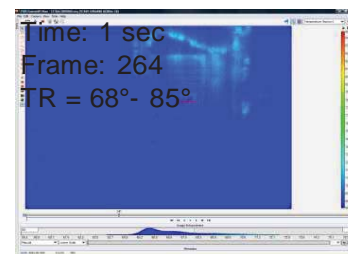
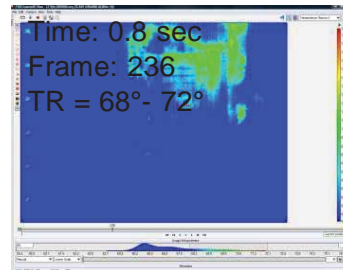
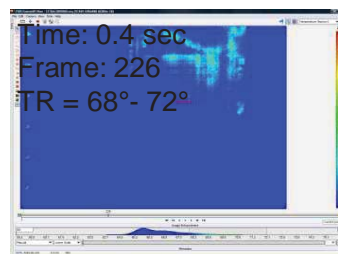
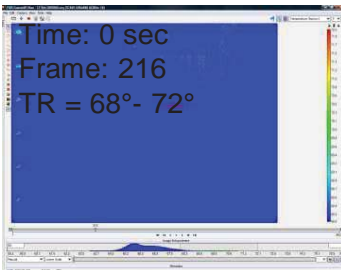
Post Strike Photograph

W2: XY(col(W 1, 1), col(W 1, 2))-0.28);se thunits('Seconds');se tvunits('m m')



Panel Displacement: Displacement, mm versus Time, sec

(This data is uncorrected for sensor placement angle. The scale factor for corrected data is 0.8572.)

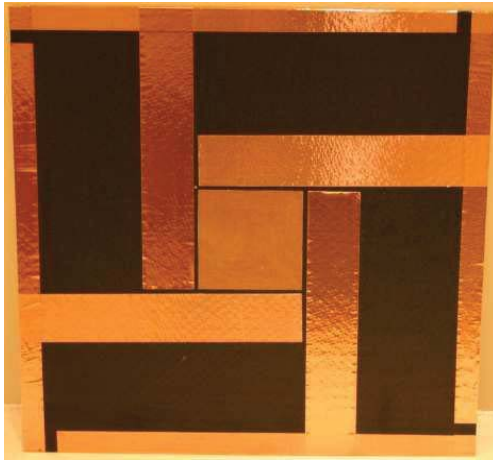


Panel backside IR image at sequential times. Note image has been flipped to provide a top side view.

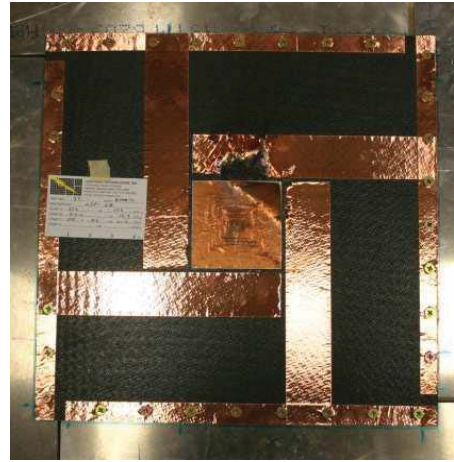
Figure A 28. Concluded.

# Fiberglass Panel - Configuration: Unpainted Carbon Composite

Peak Current, kA: 40

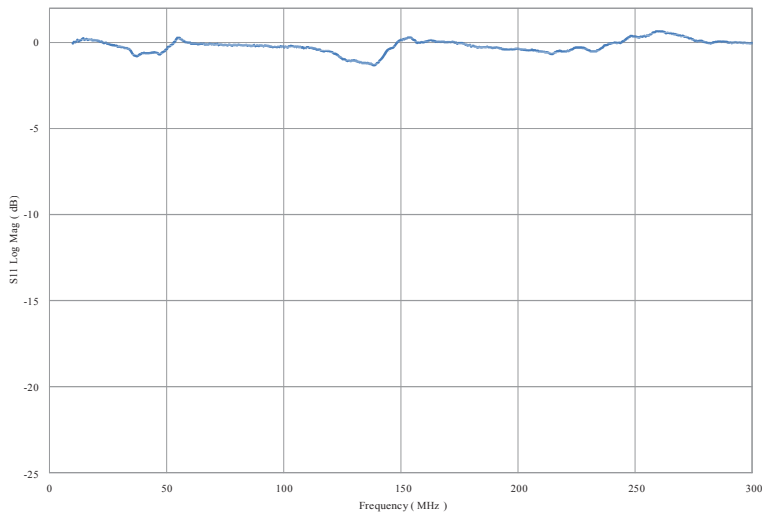


Pre Strike Photograph

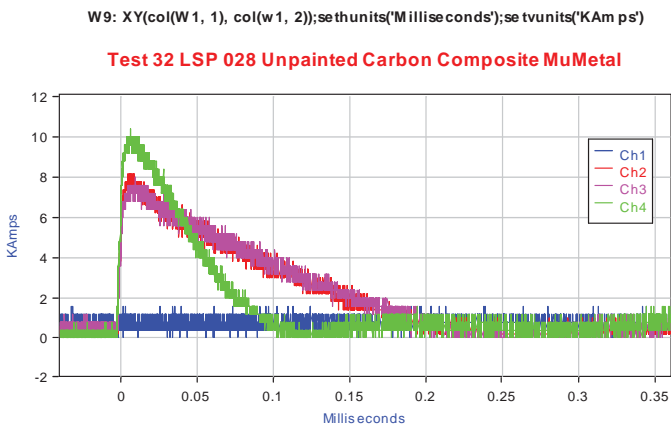


Post Strike Photograph

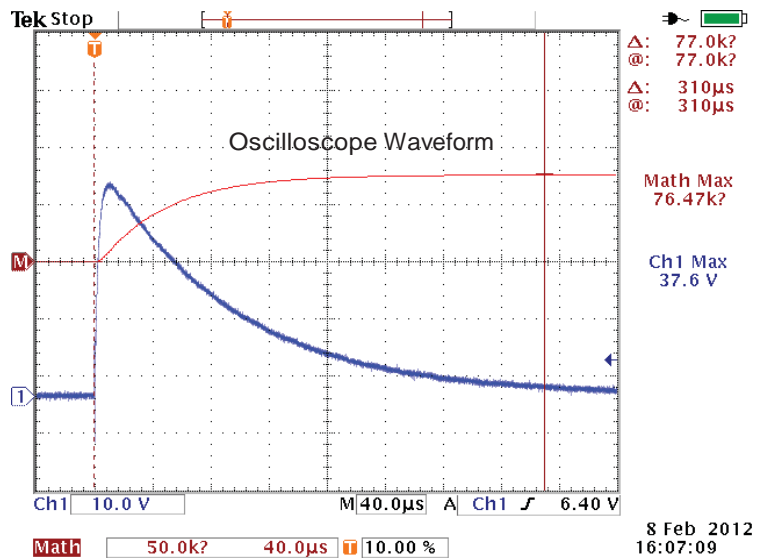
4 in SansEC Carbon Fiber Mu Metal LSP unpainted



Pre Strike Resonate Measurement



Channels 1-4 Ground Current

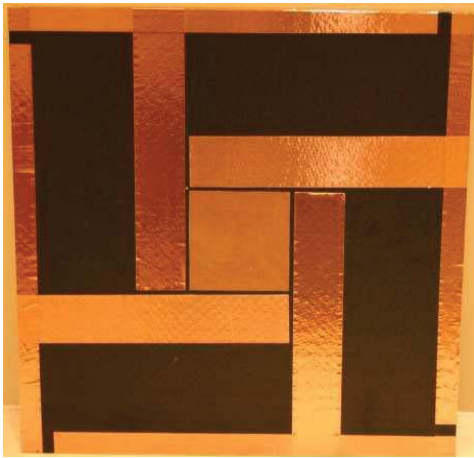


Input Current, kA verse Time, millisecc

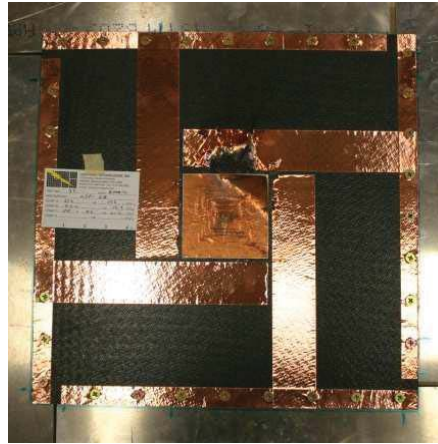
Figure A29. Fiberglass substrate configuration performance. Configuration: Unpainted Carbon Composite

# Fiberglass Panel - Configuration: Unpainted Carbon Composite

Peak Current, kA: 40



Pre Strike Photograph

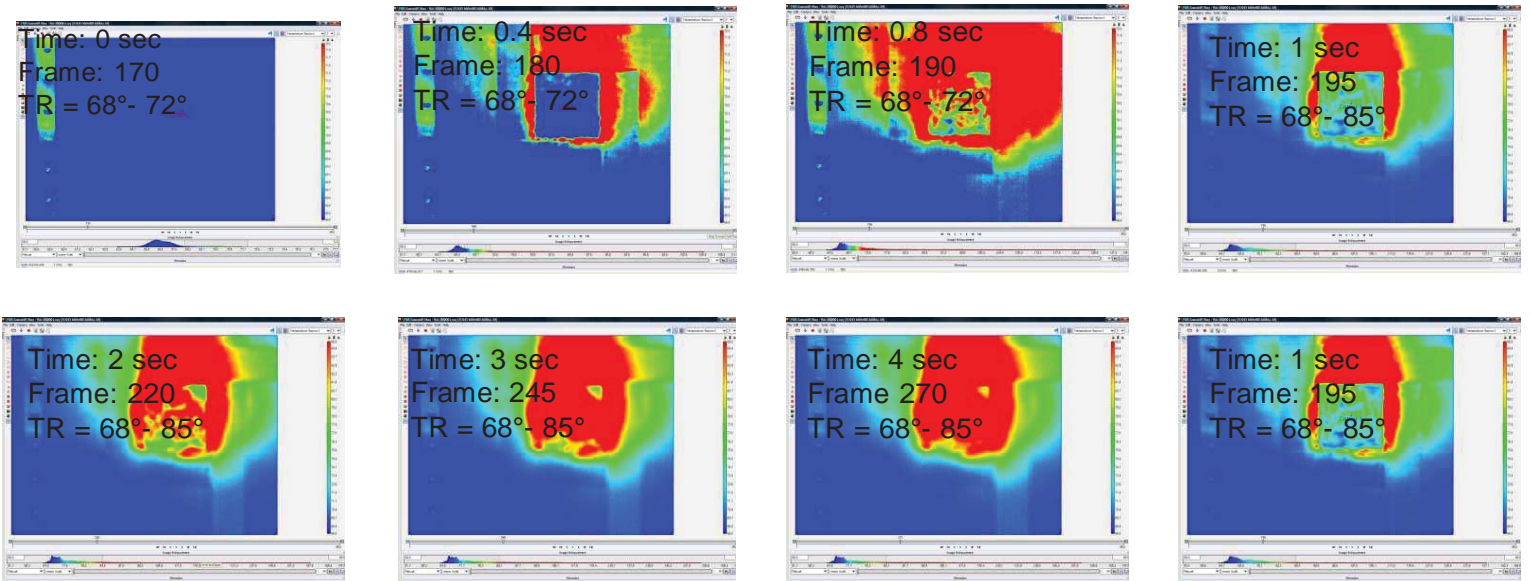


Post Strike Photograph

**Data not Available**

Panel Displacement: Displacement, mm versus Time, sec

(This data is uncorrected for sensor placement angle. The scale factor for corrected data is 0.8572.)

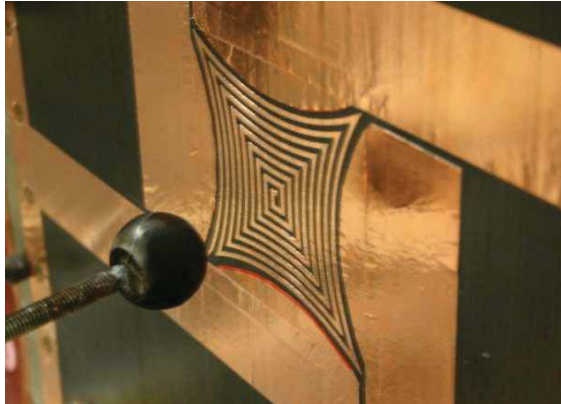


Panel backside IR image at sequential times. Note image has been flipped to provide a top side view.

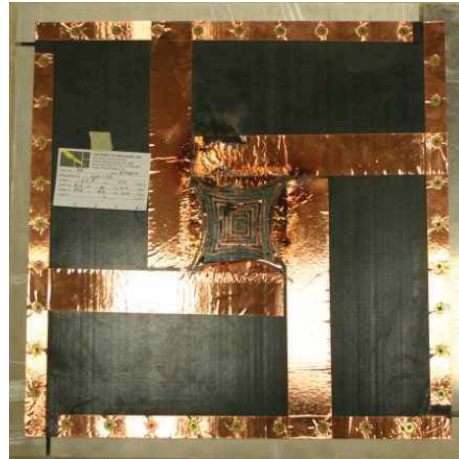
Figure A 29. Concluded.

# Fiberglass Panel - Configuration: Unpainted SansEC Spider Web

Peak Current, kA: 40

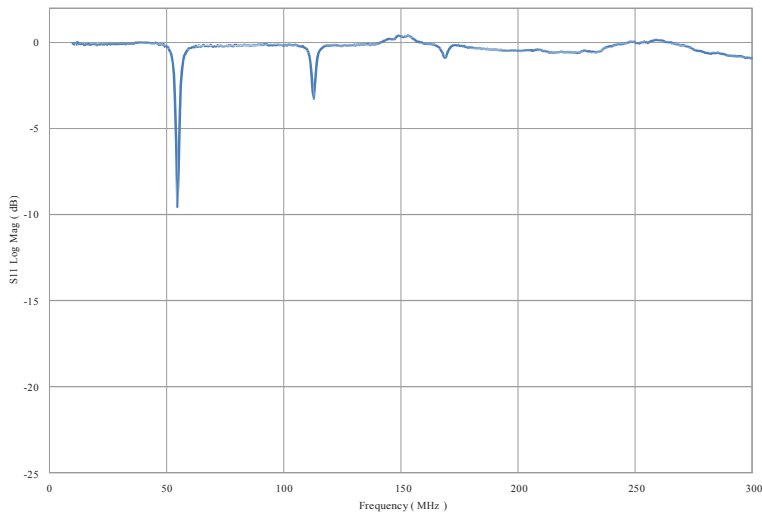


Pre Strike Photograph

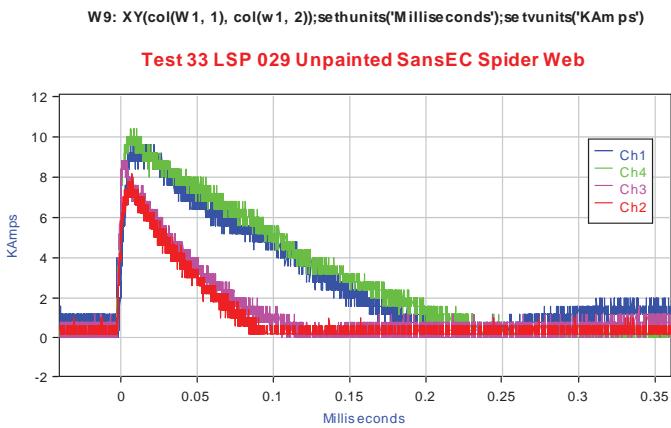


Post Strike Photograph

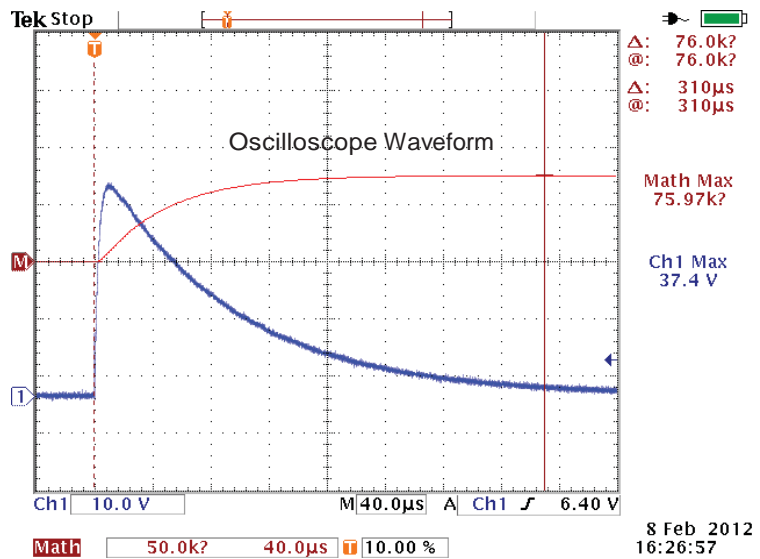
4 in SansEC Single Spider Web LSP



Pre Strike Resonate Measurement



Channels 1-4 Ground Current



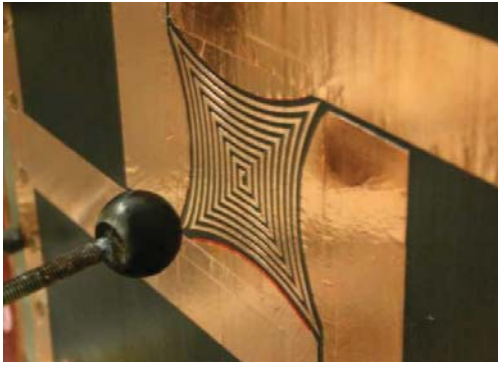
Input Current, kA verse Time, millsec

Figure A 30. Fiberglass substrate configuration performance.

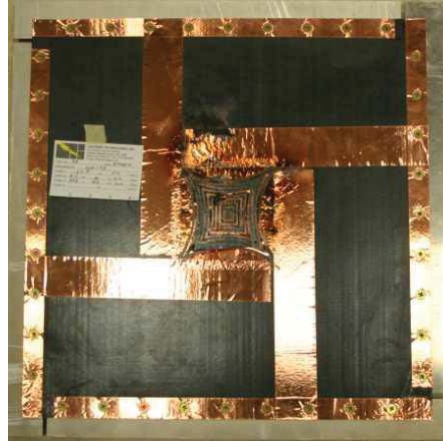
Configuration: Unpainted SansEC Spider Web

# Fiberglass Panel - Configuration: Unpainted SansEC Spider Web

Peak Current, kA: 40

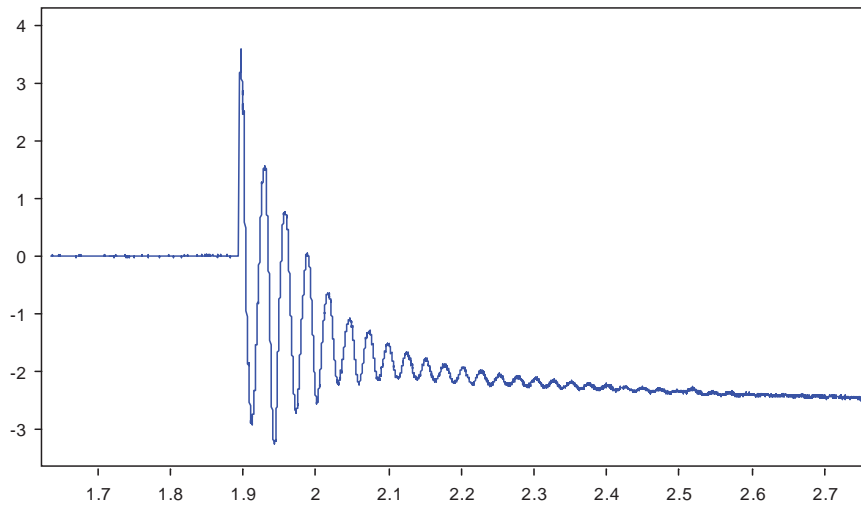


Pre Strike Photograph



Post Strike Photograph

W2: XY(col(W 1, 1), col(W 1, 2)+0.31);se thunits('Se conds');se tvunits('m m')



Panel Displacement: Displacement, mm versus Time, sec

(This data is uncorrected for sensor placement angle. The scale factor for corrected data is 0.8572.)

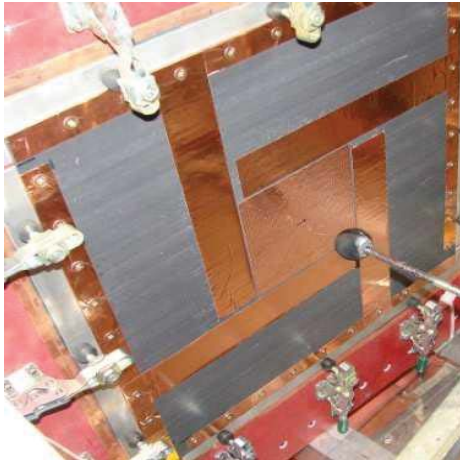
**Data not Available**

Panel backside IR image at sequential times. Note image has been flipped to provide a top side view.

Figure A 30. Concluded.

# Fiberglass Panel - Configuration: Unpainted SansEC Tight Trace

Peak Current, kA: 40



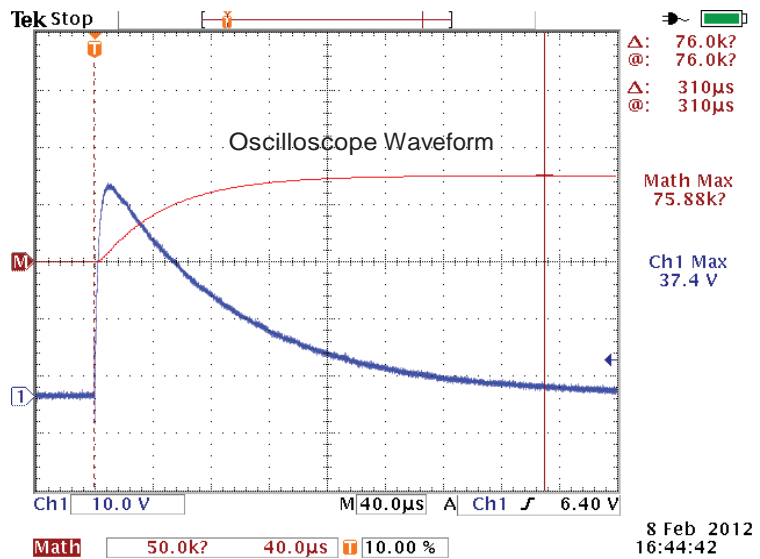
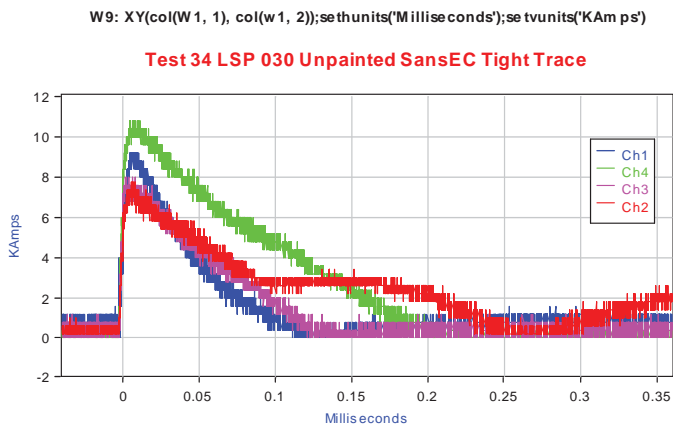
Pre Strike Photograph



Post Strike Photograph

**Data not Available**

Pre Strike Resonate Measurement

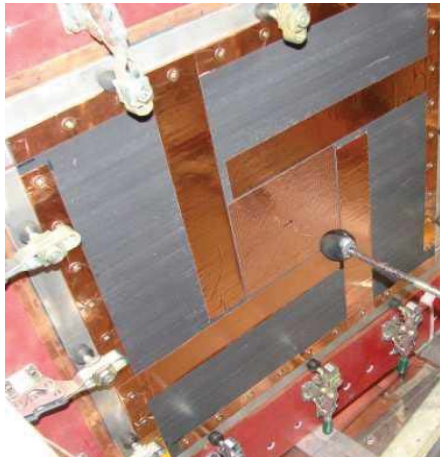


Input Current, kA verse Time, millsec

Figure A31. Fiberglass substrate configuration performance. Configuration: Unpainted SansEC Tight Trace

# Fiberglass Panel - Configuration: Unpainted SansEC Tight Trace

Peak Current, kA: 40

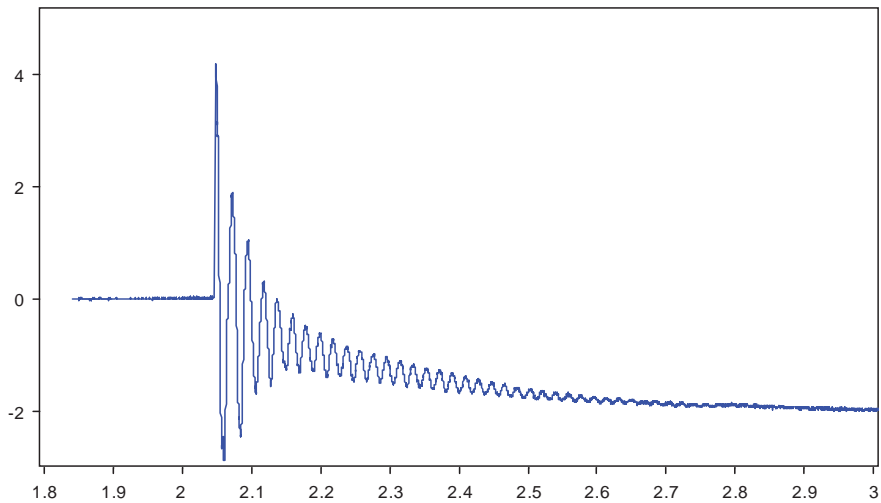


Pre Strike Photograph



Post Strike Photograph

W2: XY(col(W 1, 1), col(W 1, 2)+0.65);se thunits('Se conds');se tvunits('m m')



Panel Displacement: Displacement, mm versus Time, sec

(This data is uncorrected for sensor placement angle. The scale factor for corrected data is 0.8572.)

**Data not Available**

Panel backside IR image at sequential times. Note image has been flipped to provide a top side view.

Figure A 31. Concluded.

# CFRP Panel - Configuration: Painted, No Protection

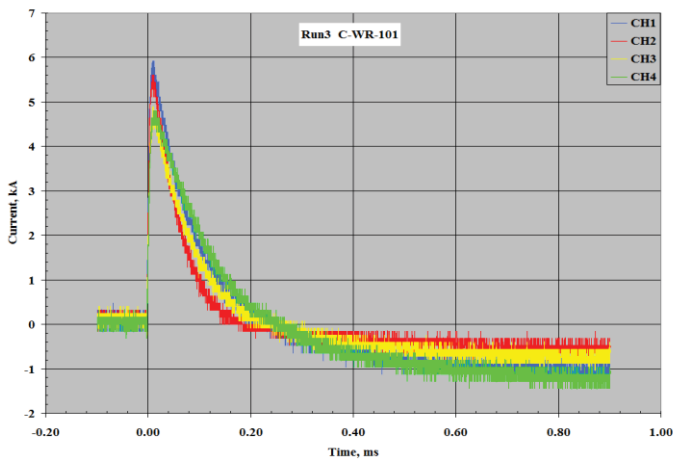
Peak Current, kA: 20



Pre Strike Photograph



Post Strike Photograph



Channels 1-4 Ground Current

Data not Available

Panel Displacement: Displacement, mm versus Time, sec

Data not Available

Panel backside IR image at sequential times. Note image has been flipped to provide a top side view.

Figure A 32 . CFRP substrate configuration performance. Configuration: Painted, No Protection

# CFRP Panel - Configuration: Painted, No Protection

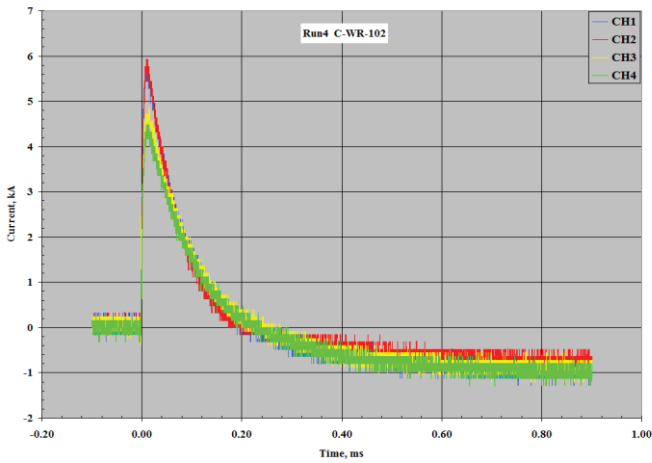
Peak Current, kA: 20



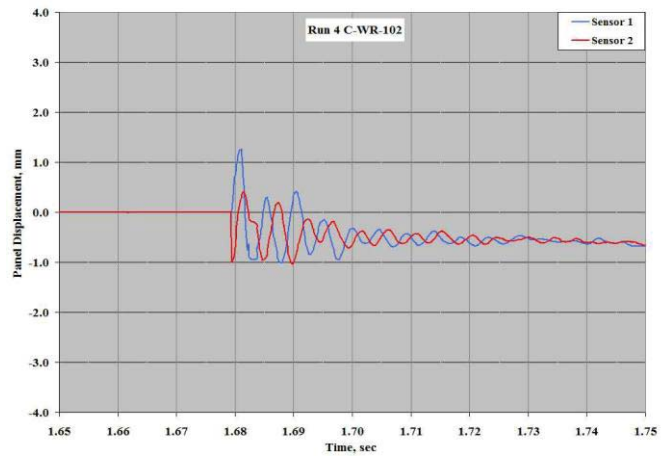
Pre Strike Photograph



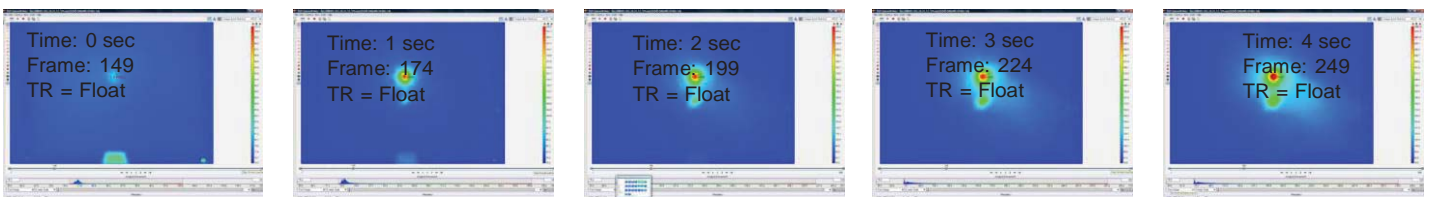
Post Strike Photograph



Channels 1-4 Ground Current



Panel Displacement: Displacement, mm versus Time, sec



Panel backside IR image at sequential times. Note image has been flipped to provide a top side view.

Figure A 33 . CFRP substrate configuration performance. Configuration: Painted, No Protection

# CFRP Panel - Configuration: Painted, No Protection

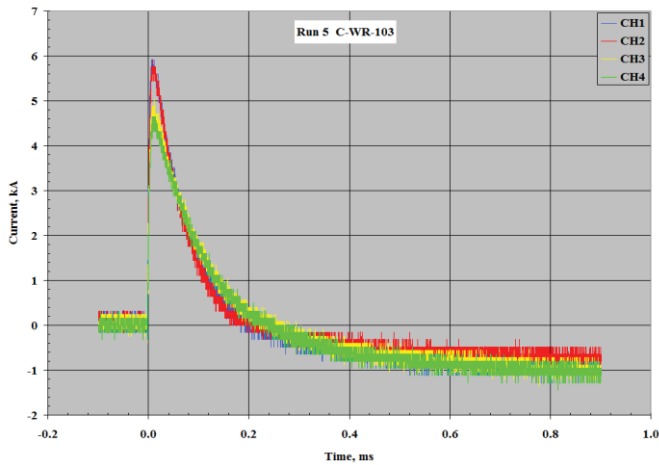
Peak Current, kA: 20



Pre Strike Photograph



Post Strike Photograph



Channels 1-4 Ground Current

**Data not Available**

Panel Displacement: Displacement, mm versus Time, sec



Panel backside IR image at sequential times. Note image has been flipped to provide a top side view.

Figure A 34 . CFRP substrate configuration performance. Configuration: Painted, No Protection

# CFRP Panel - Configuration: Painted, No Protection

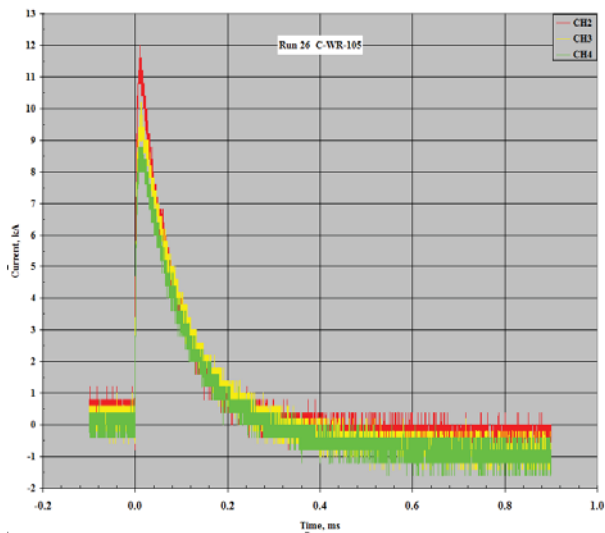
Peak Current, kA: 40



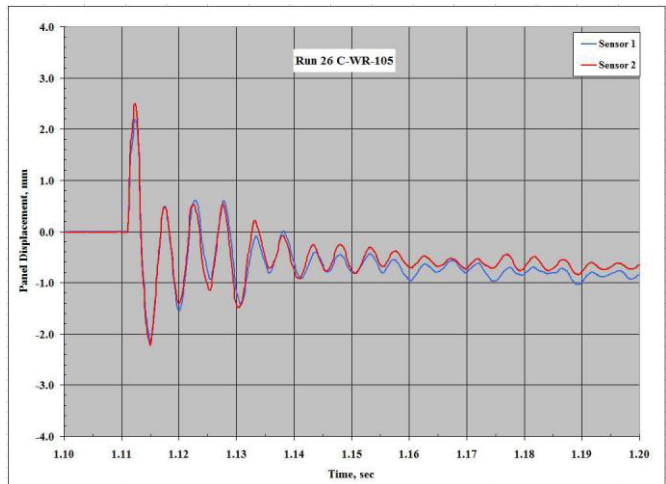
Pre Strike Photograph



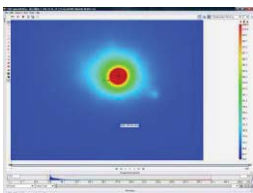
Post Strike Photograph



Channels 1-4 Ground Current



Panel Displacement: Displacement, mm versus Time, sec



Panel backside IR image at sequential times. Note image has been flipped to provide a top side view.

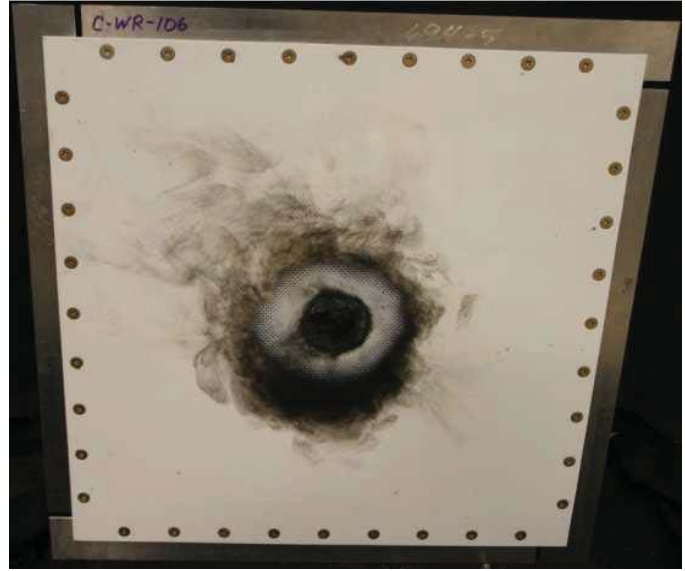
Figure A 35. CFRP substrate configuration performance. Configuration: Painted, No Protection

# CFRP Panel - Configuration: Painted, No Protection

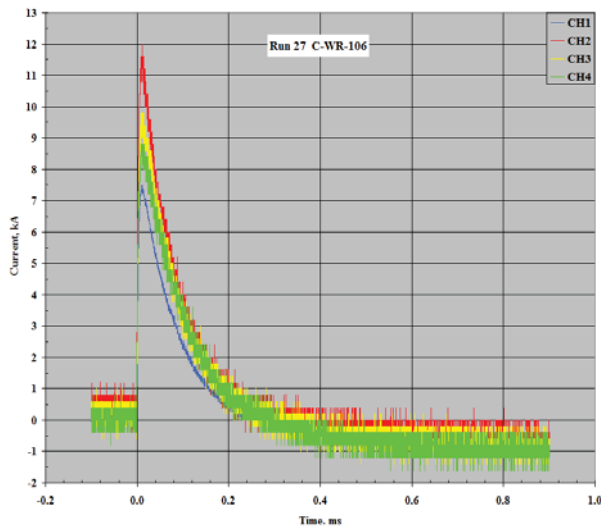
Peak Current, kA: 40



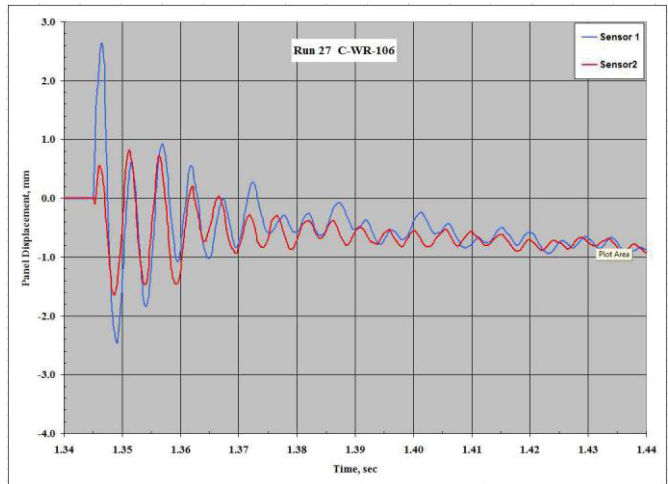
Pre Strike Photograph



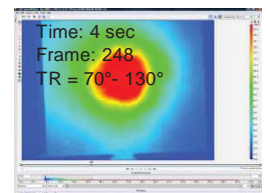
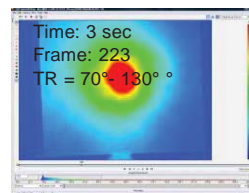
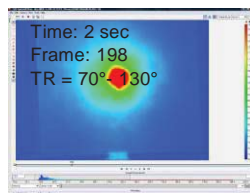
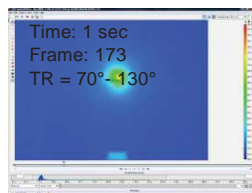
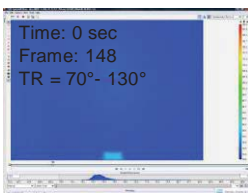
Post Strike Photograph



Channels 1-4 Ground Current



Panel Displacement: Displacement, mm versus Time, sec

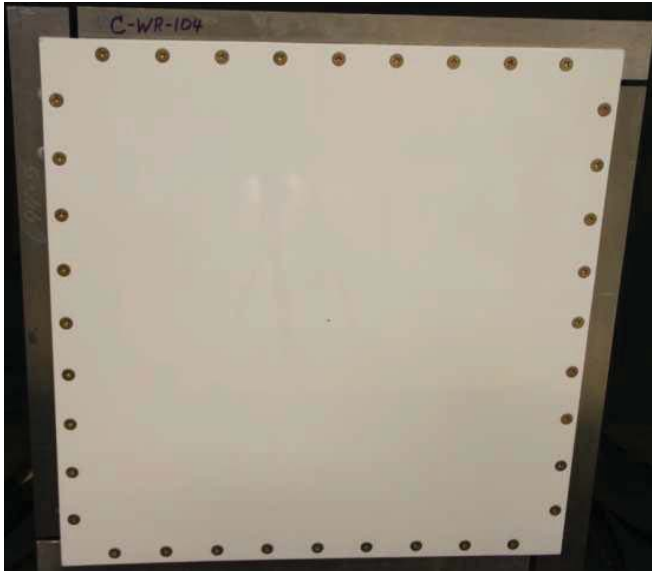


Panel backside IR image at sequential times. Note image has been flipped to provide a top side view.

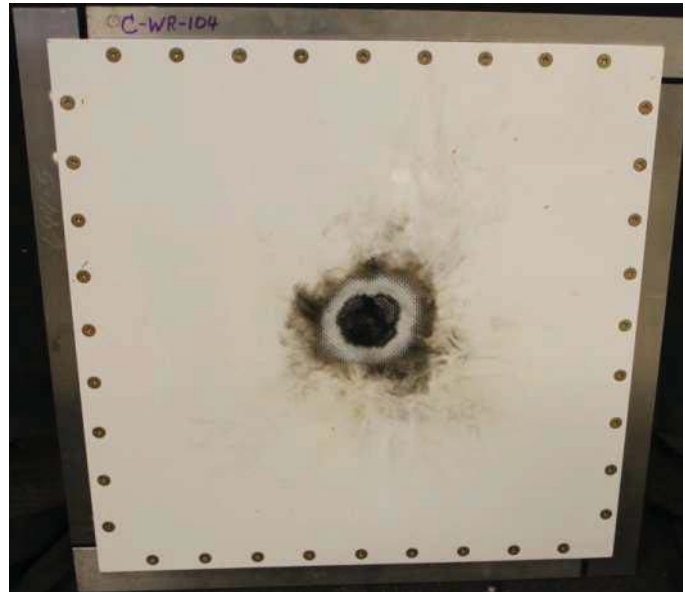
Figure A 36. CFRP substrate configuration performance. Configuration: Painted, No Protection

# CFRP Panel - Configuration: Painted, No Protection

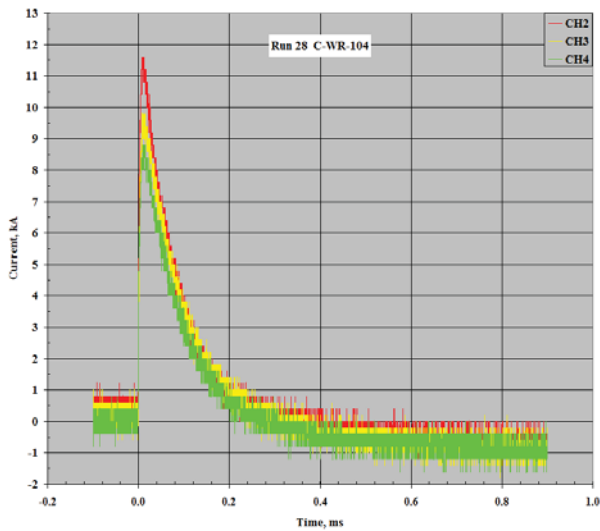
Peak Current, kA: 40



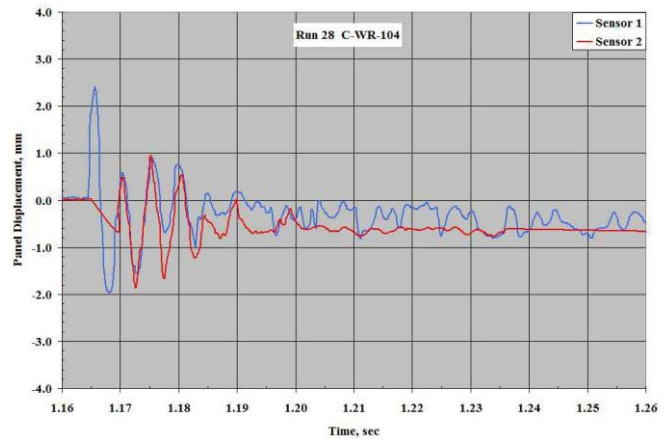
Pre Strike Photograph



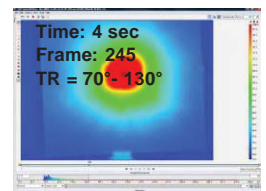
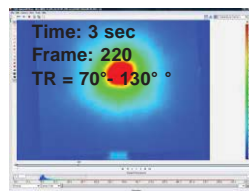
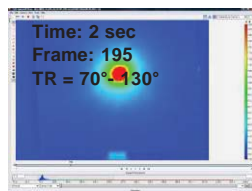
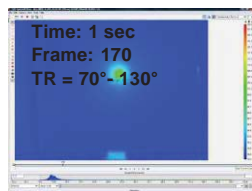
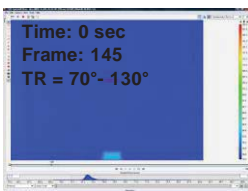
Post Strike Photograph



Channels 1-4 Ground Current



Panel Displacement: Displacement, mm versus Time, sec



Panel backside IR image at sequential times. Note image has been flipped to provide a top side view.

Figure A 37. CFRP substrate configuration performance. Configuration: Painted, No Protection

# CFRP Panel - Configuration: Painted, No Protection

Peak Current, kA: 100



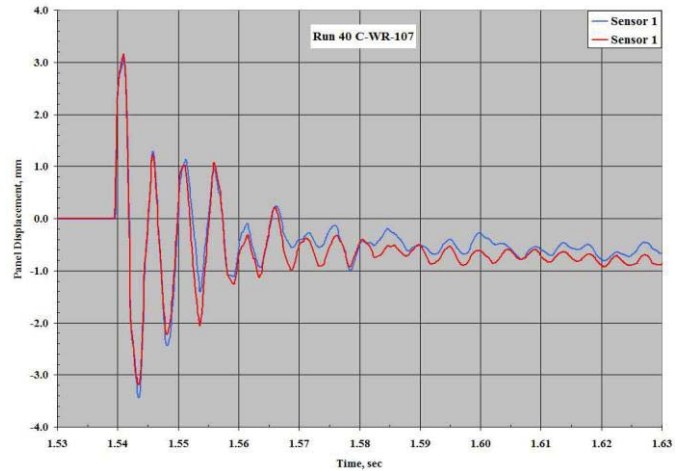
Pre Strike Photograph



Post Strike Photograph

**Data not Available**

Channels 1-4 Ground Current



Panel Displacement: Displacement, mm versus Time, sec

**Data not Available**

Panel backside IR image at sequential times. Note image has been flipped to provide a top side view.

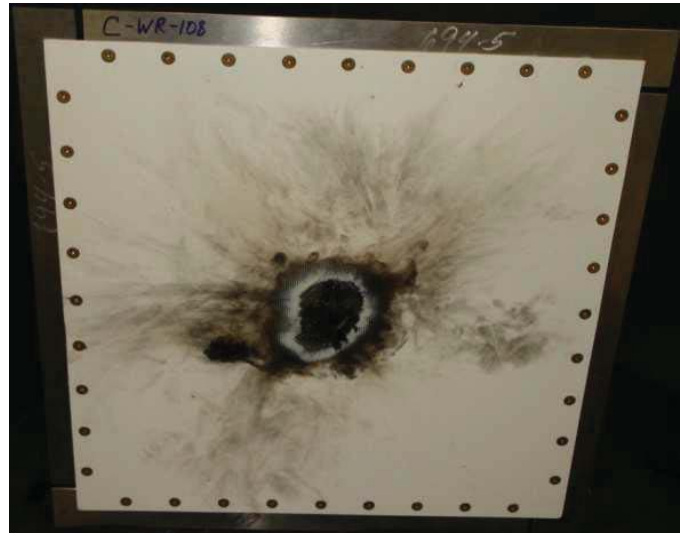
Figure A 38. CFRP substrate configuration performance. Configuration: Painted, No Protection

# CFRP Panel - Configuration: Painted, No Protection

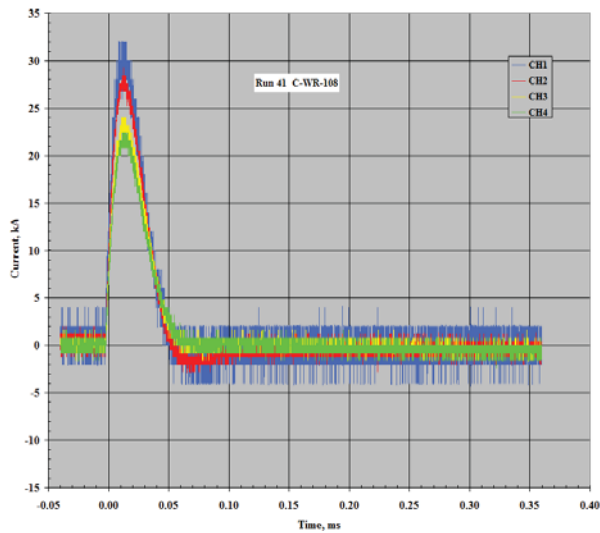
Peak Current, kA: 100



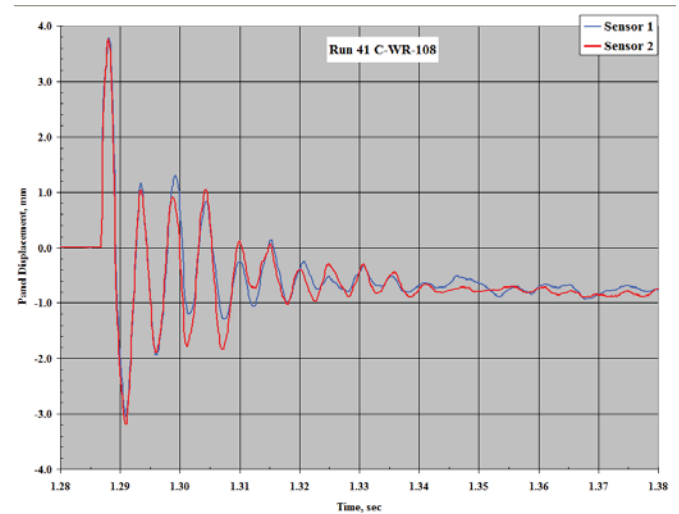
Pre Strike Photograph



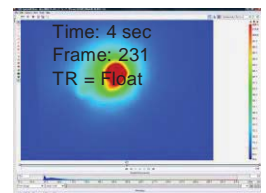
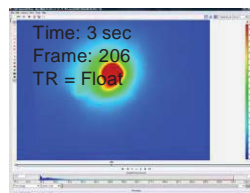
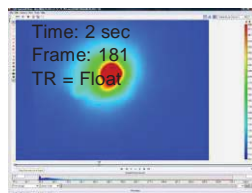
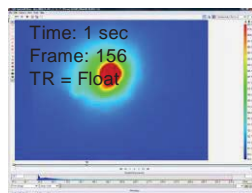
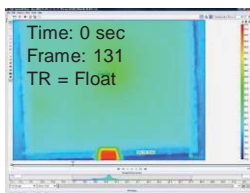
Post Strike Photograph



Channels 1-4 Ground Current



Panel Displacement: Displacement, mm versus Time, sec



Panel backside IR image at sequential times. Note image has been flipped to provide a top side view.

Figure A 39. CFRP substrate configuration performance. Configuration: Painted, No Protection

# CFRP Panel - Configuration: Painted, No Protection

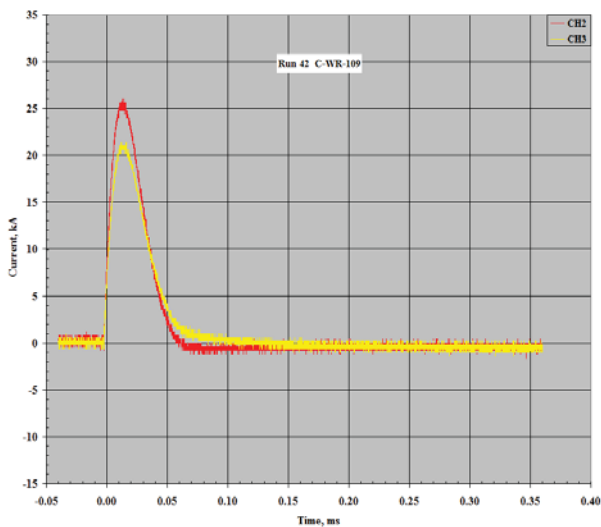
Peak Current, kA: 100



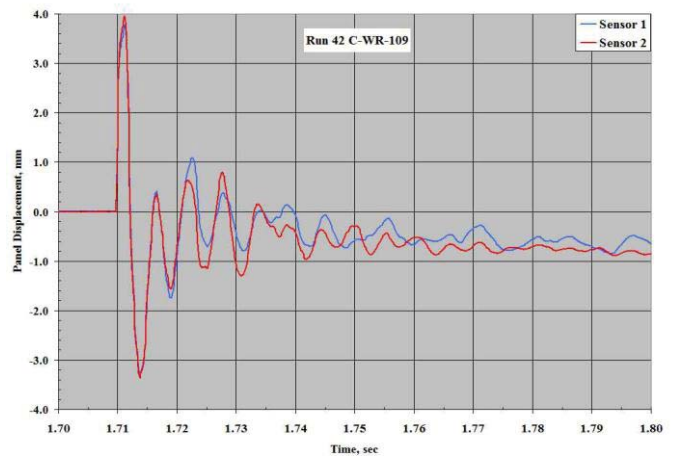
Pre Strike Photograph



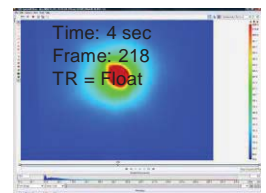
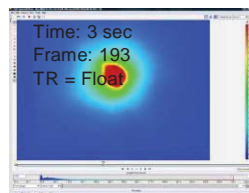
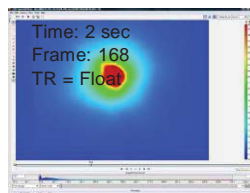
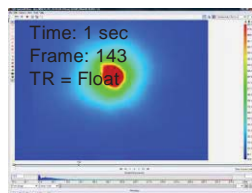
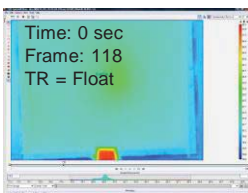
Post Strike Photograph



Channels 1-4 Ground Current



Panel Displacement: Displacement, mm versus Time, sec



Panel backside IR image at sequential times. Note image has been flipped to provide a top side view.

Figure A 40. CFRP substrate configuration performance. Configuration: Painted, No Protection

# CFRP Panel - Configuration: Painted with Protecting ECF

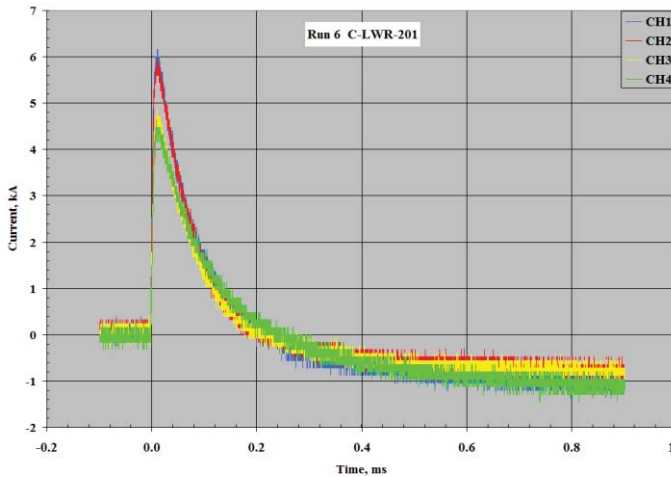
Peak Current, kA: 20



Pre Strike Photograph



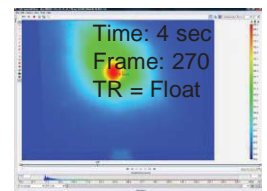
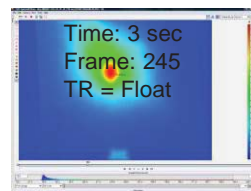
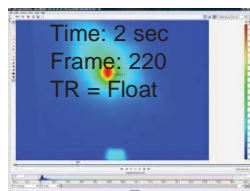
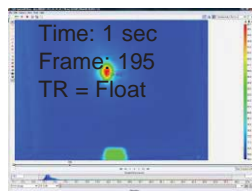
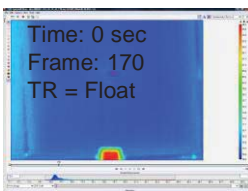
Post Strike Photograph



Channels 1-4 Ground Current

**Data not Available**

Panel Displacement: Displacement, mm versus Time, sec



Panel backside IR image at sequential times. Note image has been flipped to provide a top side view.

Figure A 41 . CFRP substrate configuration performance. Configuration: Painted with Protecting ECF

# CFRP Panel - Configuration: Painted with Protecting ECF

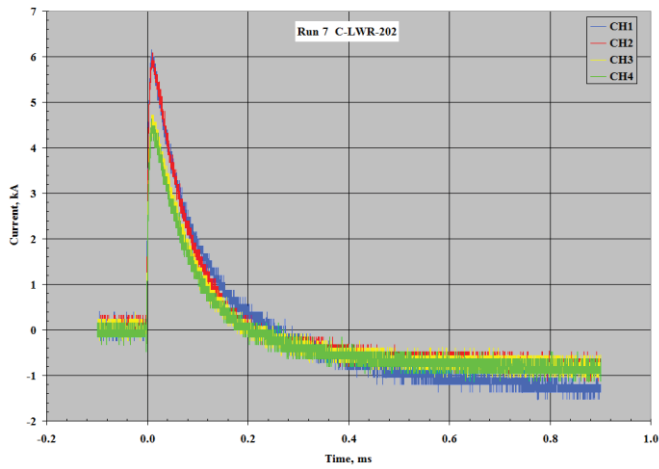
Peak Current, kA: 20



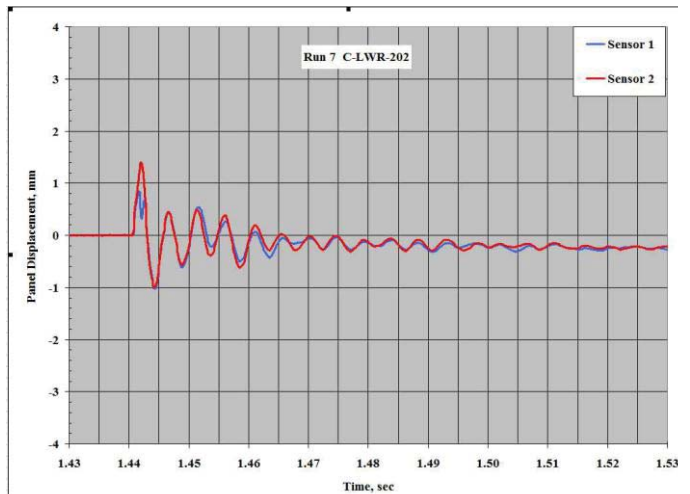
Pre Strike Photograph



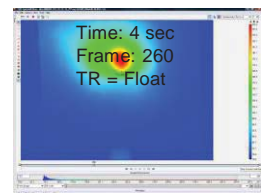
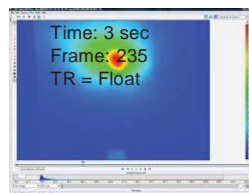
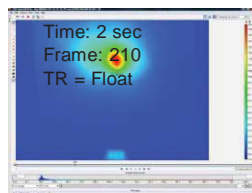
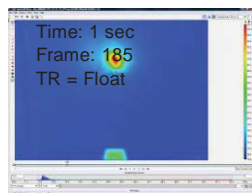
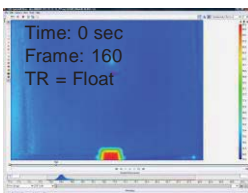
Post Strike Photograph



Channels 1-4 Ground Current



Panel Displacement: Displacement, mm versus Time, sec



Panel backside IR image at sequential times. Note image has been flipped to provide a top side view.

Figure A 42. CFRP substrate configuration performance. Configuration: Painted with Protecting ECF

# CFRP Panel - Configuration: Painted with Protecting ECF

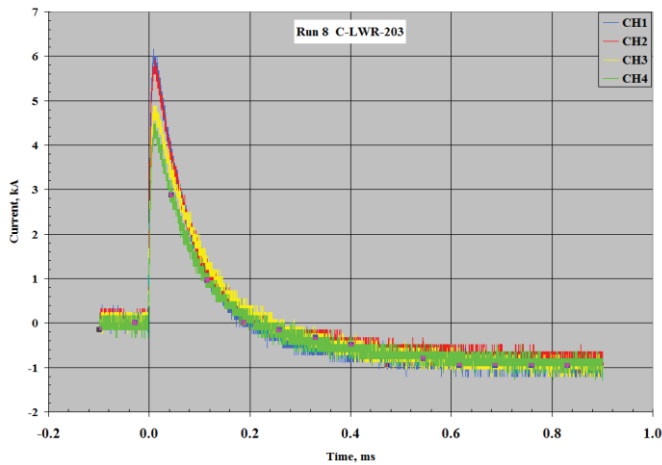
Peak Current, kA: 20



Pre Strike Photograph



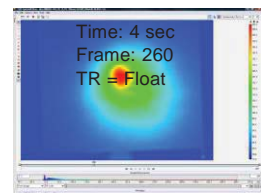
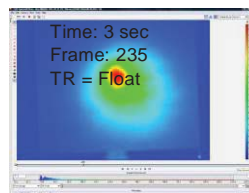
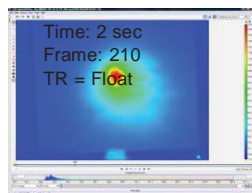
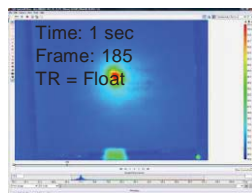
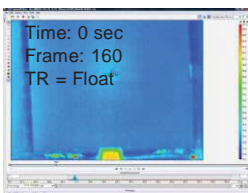
Post Strike Photograph



Channels 1-4 Ground Current

**Data not Available**

Panel Displacement: Displacement, mm versus Time, sec



Panel backside IR image at sequential times. Note image has been flipped to provide a top side view.

Figure A 43 . CFRP substrate configuration performance. Configuration: Painted with Protecting ECF

# CFRP Panel - Configuration: Painted with Protecting ECF

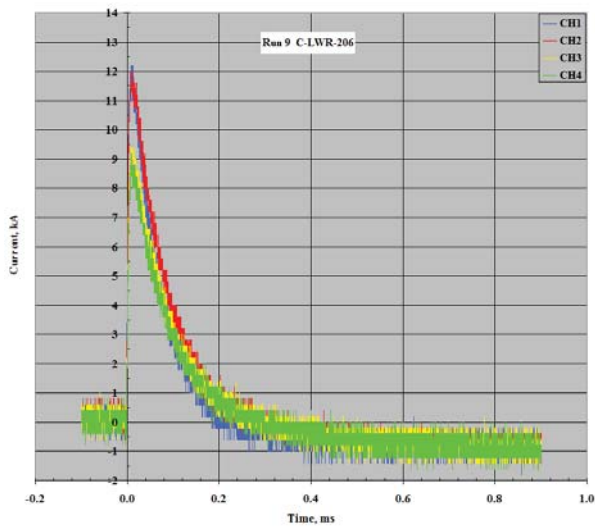
Peak Current, kA: 40



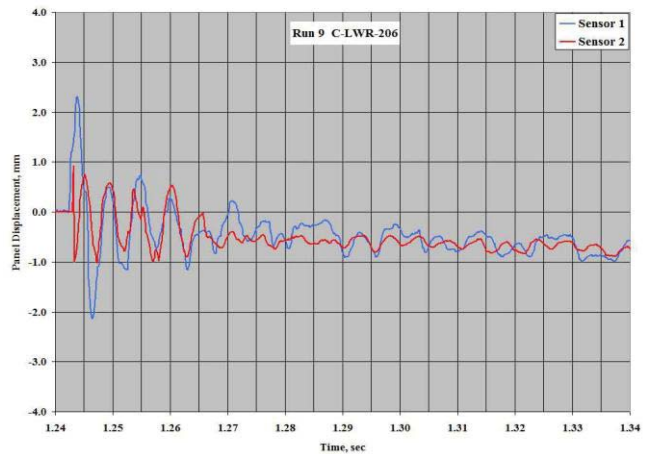
Pre Strike Photograph



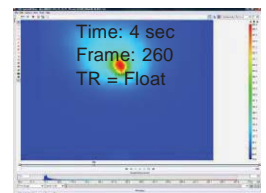
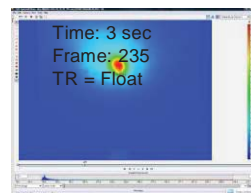
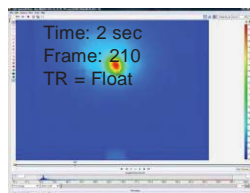
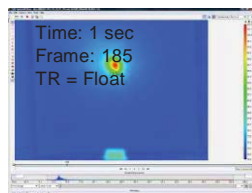
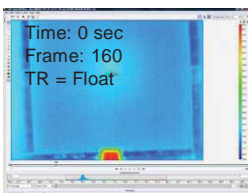
Post Strike Photograph



Channels 1-4 Ground Current



Panel Displacement: Displacement, mm versus Time, sec



Panel backside IR image at sequential times. Note image has been flipped to provide a top side view.

Figure A 44. CFRP substrate configuration performance. Configuration: Painted with Protecting ECF

# CFRP Panel - Configuration: Painted with Protecting ECF

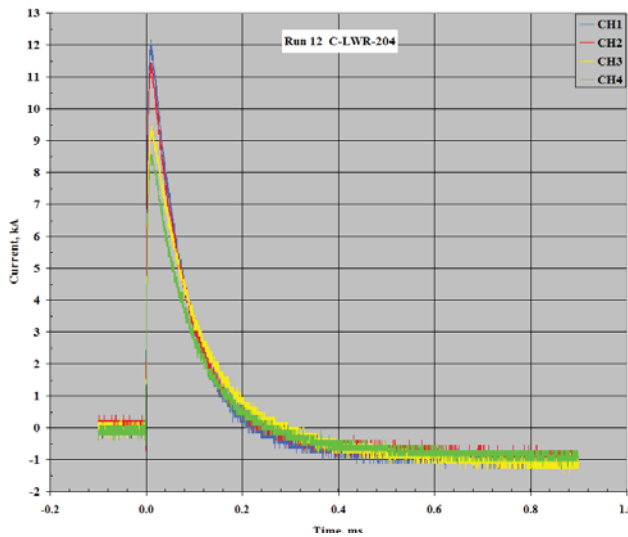
Peak Current, kA: 40



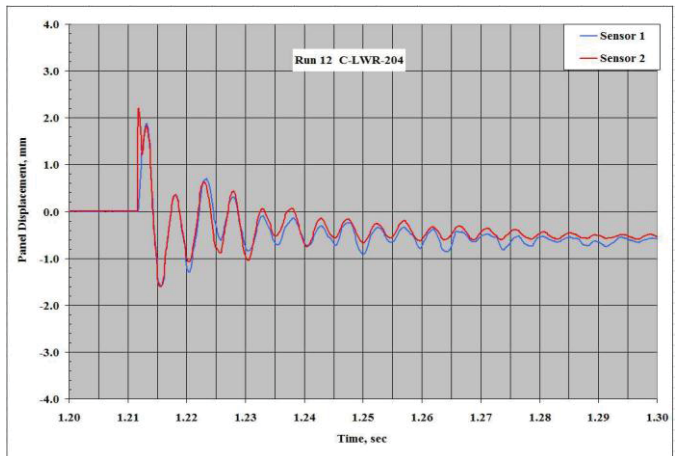
Pre Strike Photograph



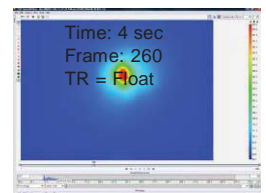
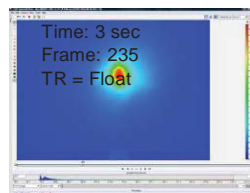
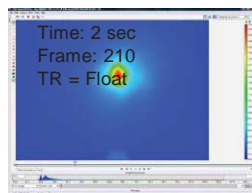
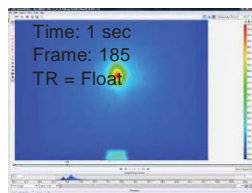
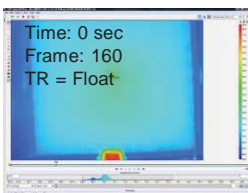
Post Strike Photograph



Channels 1-4 Ground Current



Panel Displacement: Displacement, mm versus Time, sec



Panel backside IR image at sequential times. Note image has been flipped to provide a top side view.

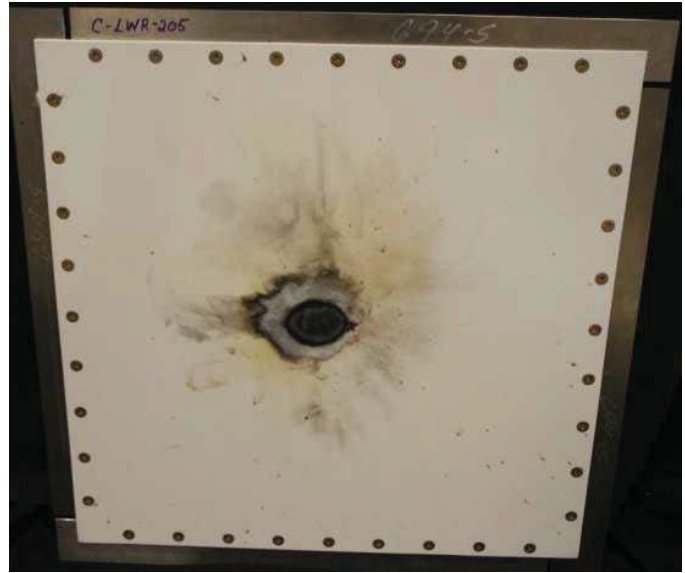
Figure A 45. CFRP substrate configuration performance. Configuration: Painted with Protecting ECF

# CFRP Panel - Configuration: Painted with Protecting ECF

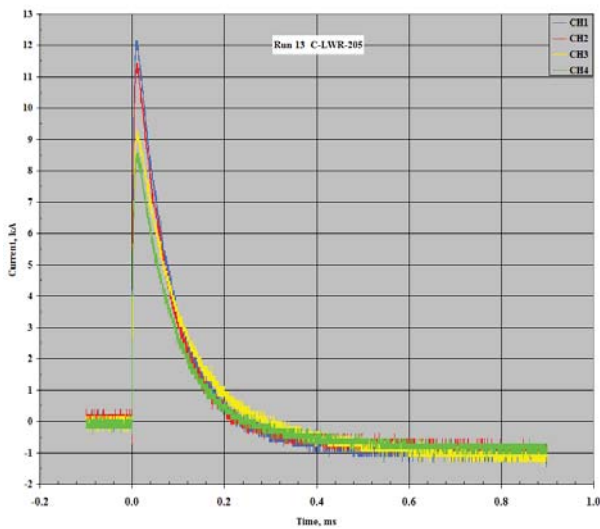
Peak Current, kA: 40



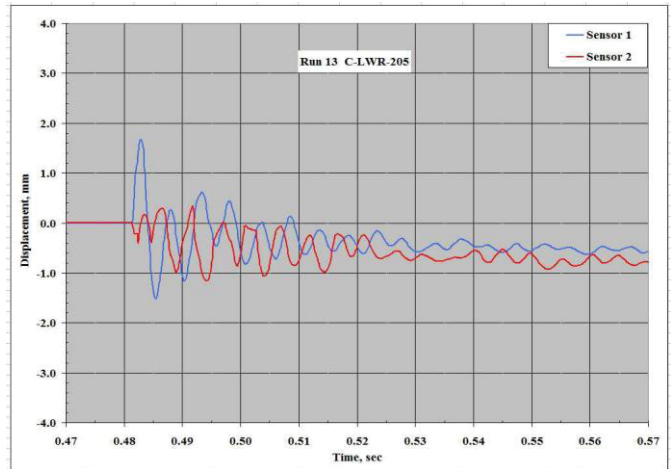
Pre Strike Photograph



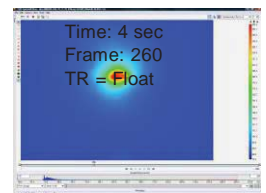
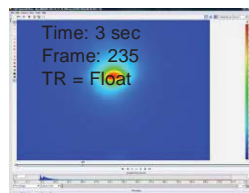
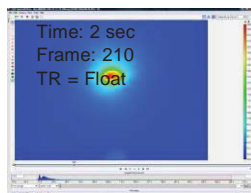
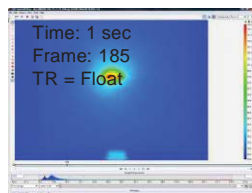
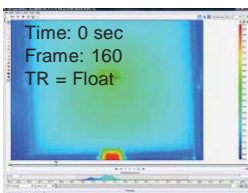
Post Strike Photograph



Channels 1-4 Ground Current



Panel Displacement: Displacement, mm versus Time, sec

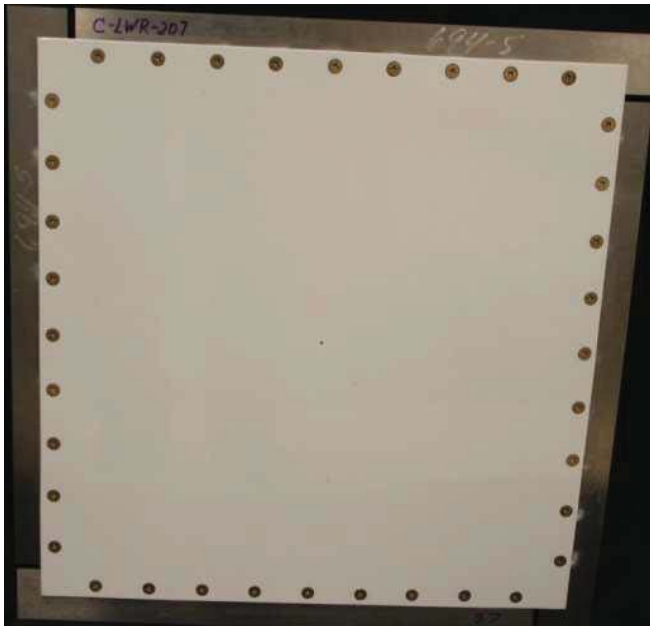


Panel backside IR image at sequential times. Note image has been flipped to provide a top side view.

Figure A 46. CFRP substrate configuration performance. Configuration: Painted with Protecting ECF

# CFRP Panel - Configuration: Painted with Protecting ECF

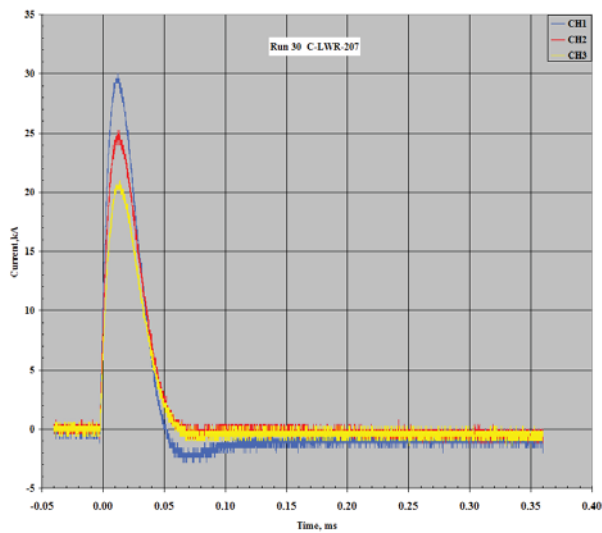
Peak Current, kA: 100



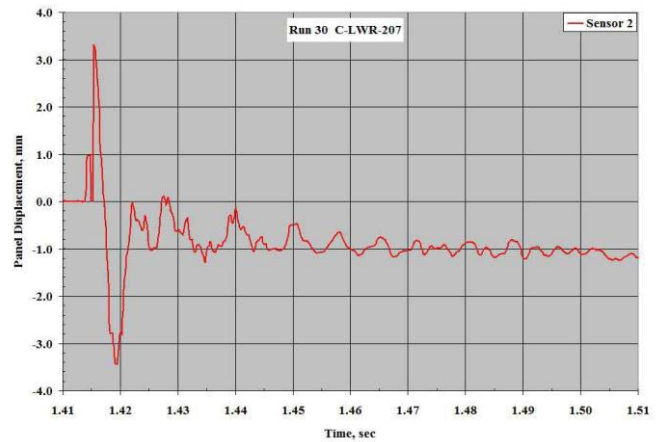
Pre Strike Photograph



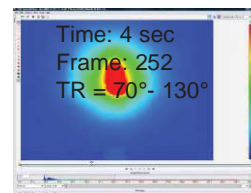
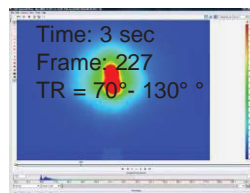
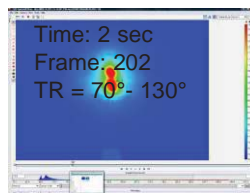
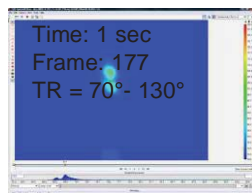
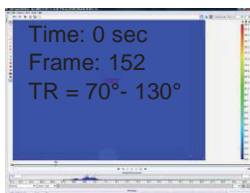
Post Strike Photograph



Channels 1-4 Ground Current



Panel Displacement: Displacement, mm versus Time, sec



Panel backside IR image at sequential times. Note image has been flipped to provide a top side view.

Figure A 47. CFRP substrate configuration performance. Configuration: Painted with Protecting ECF

# CFRP Panel - Configuration: Painted with Protecting ECF

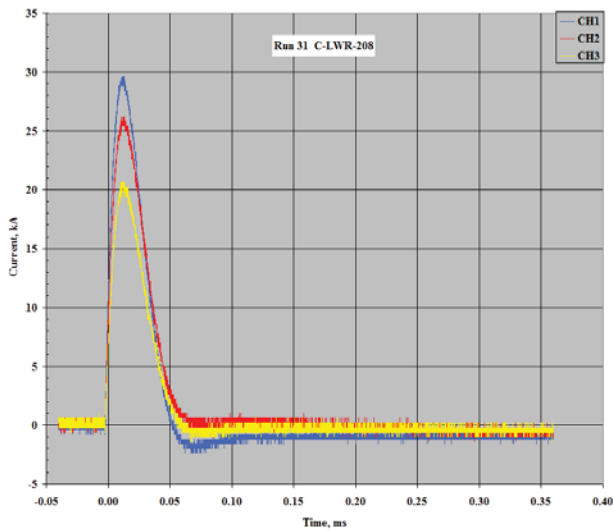
Peak Current, kA: 100



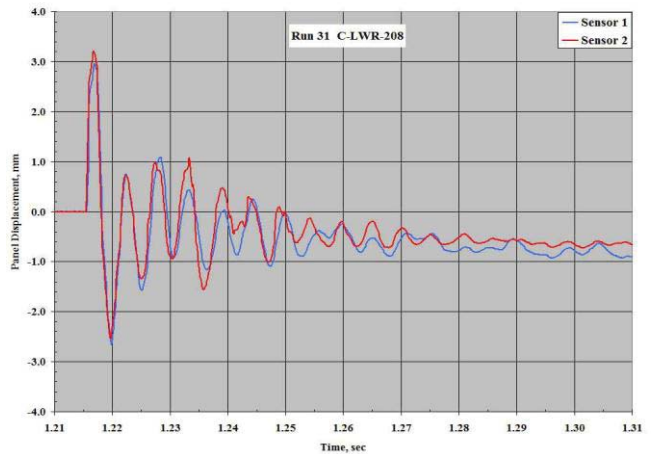
Pre Strike Photograph



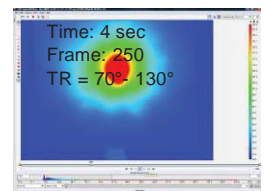
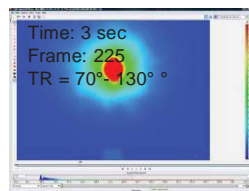
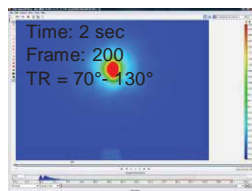
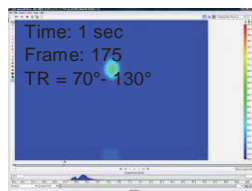
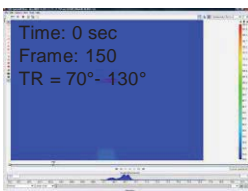
Post Strike Photograph



Channels 1-4 Ground Current



Panel Displacement: Displacement, mm versus Time, sec



Panel backside IR image at sequential times. Note image has been flipped to provide a top side view.

Figure A 48. CFRP substrate configuration performance. Configuration: Painted with Protecting ECF

# CFRP Panel - Configuration: Painted with Protecting ECF

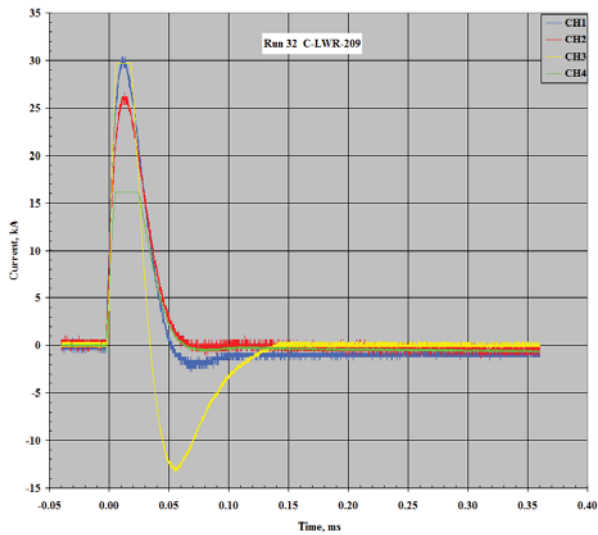
Peak Current, kA: 100



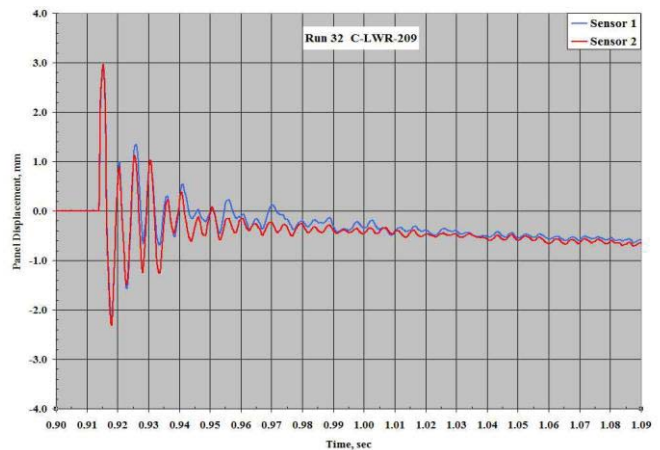
Pre Strike Photograph



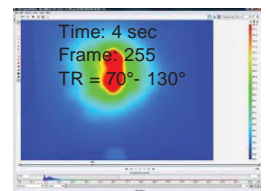
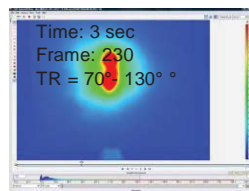
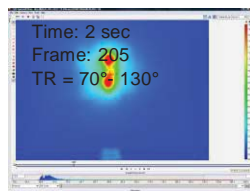
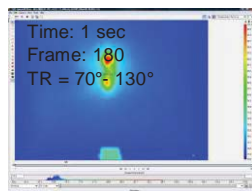
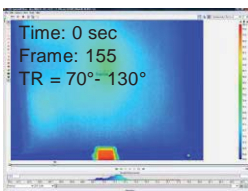
Post Strike Photograph



Channels 1-4 Ground Current



Panel Displacement: Displacement, mm versus Time, sec



Panel backside IR image at sequential times. Note image has been flipped to provide a top side view.

Figure A 49. CFRP substrate configuration performance. Configuration: Painted with Protecting ECF

# CFRP Panel - Configuration: Painted with Protecting ECF

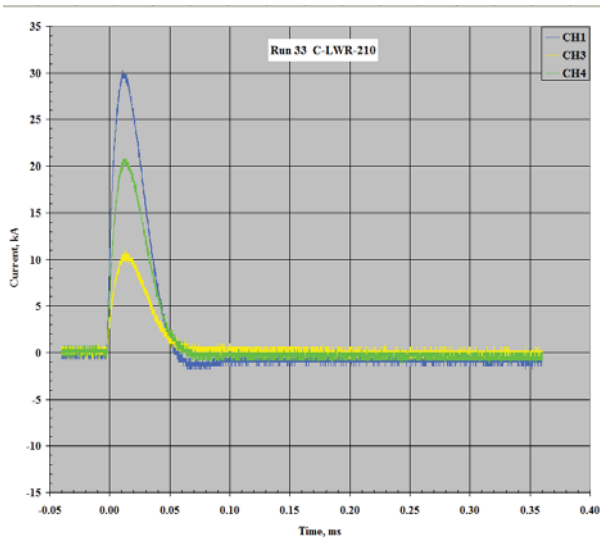
Peak Current, kA: 100



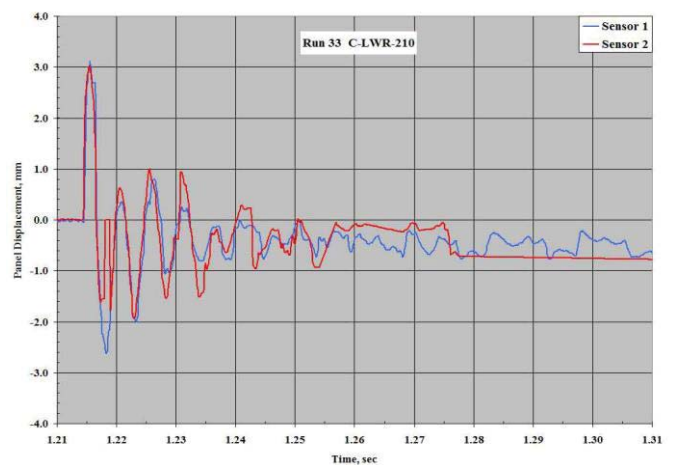
Pre Strike Photograph



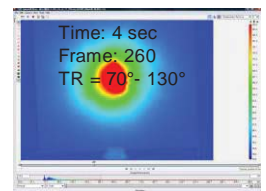
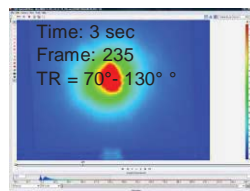
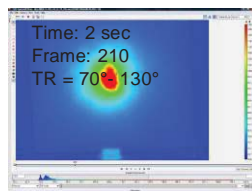
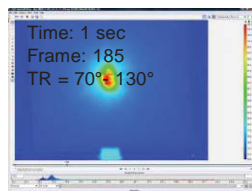
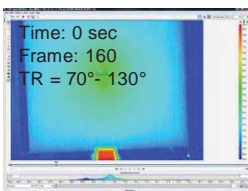
Post Strike Photograph



Channels 1-4 Ground Current



Panel Displacement: Displacement, mm versus Time, sec



Panel backside IR image at sequential times. Note image has been flipped to provide a top side view.

Figure A 50. CFRP substrate configuration performance. Configuration: Painted with Protecting ECF

# CFRP Panel - Configuration: Painted with Protecting ECF

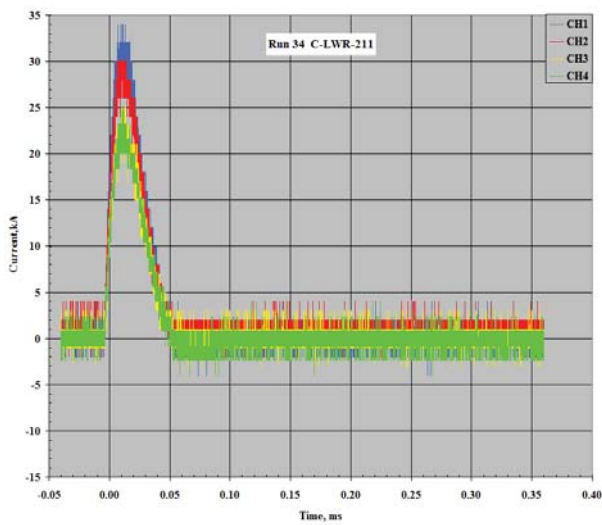
Peak Current, kA: 100



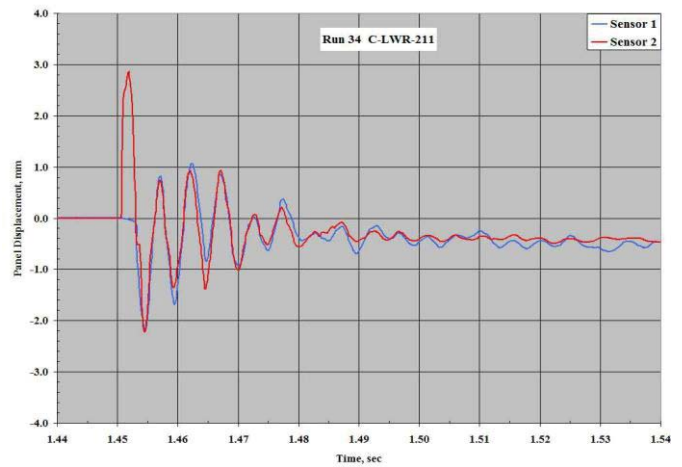
Pre Strike Photograph



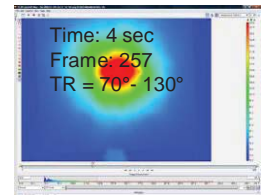
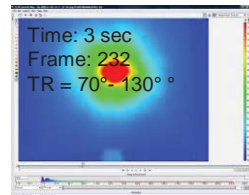
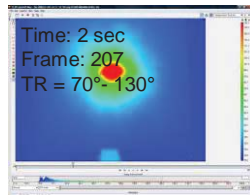
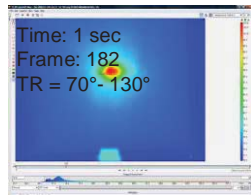
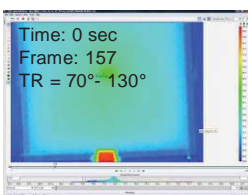
Post Strike Photograph



Channels 1-4 Ground Current



Panel Displacement: Displacement, mm versus Time, sec



Panel backside IR image at sequential times. Note image has been flipped to provide a top side view.

Figure A 51 . CFRP substrate configuration performance. Configuration: Painted with Protecting ECF

# CFRP Panel - Configuration: Painted with Protecting ECF

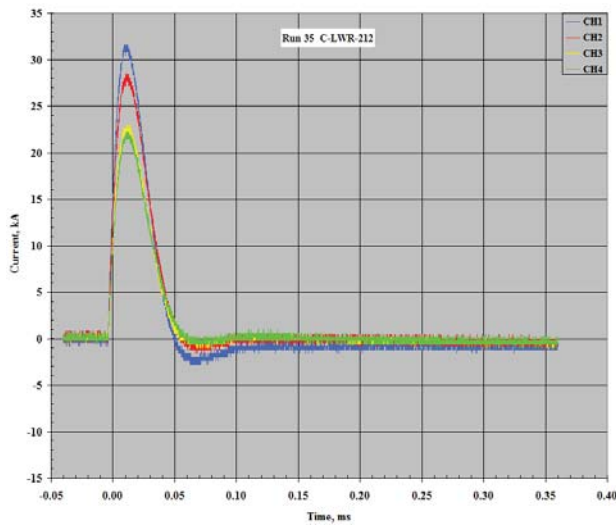
Peak Current, kA: 100



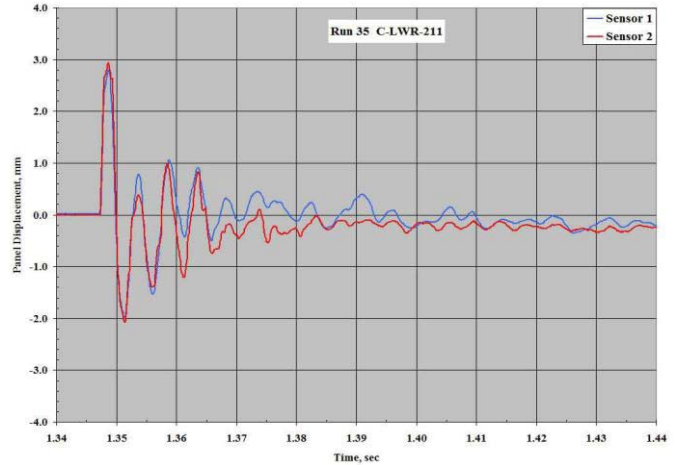
Pre Strike Photograph



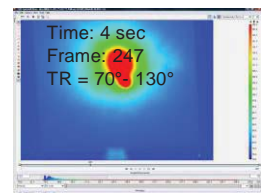
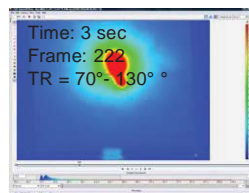
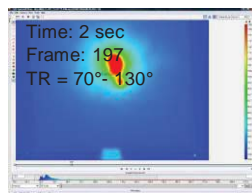
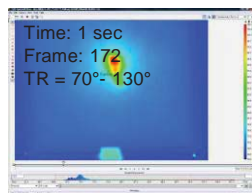
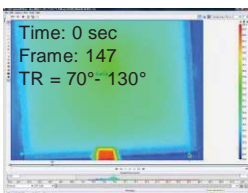
Post Strike Photograph



Channels 1-4 Ground Current



Panel Displacement: Displacement, mm versus Time, sec



Panel backside IR image at sequential times. Note image has been flipped to provide a top side view.

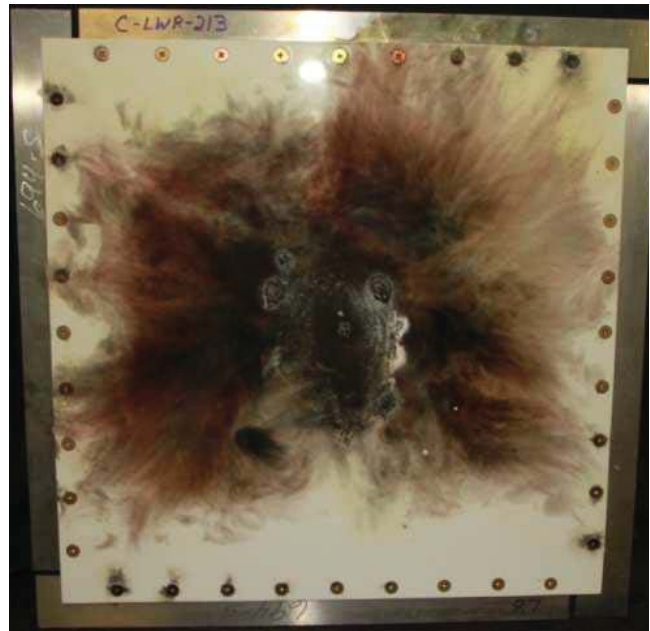
Figure A 52. CFRP substrate configuration performance. Configuration: Painted with Protecting ECF

# CFRP Panel - Configuration: Painted with Protecting ECF

Peak Current, kA: 200



Pre Strike Photograph



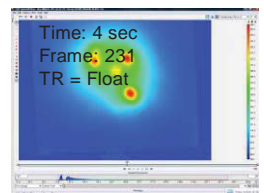
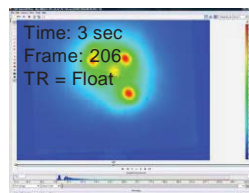
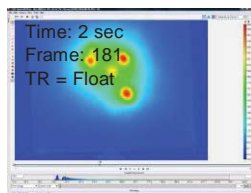
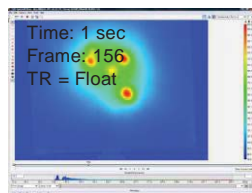
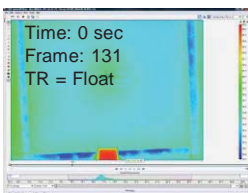
Post Strike Photograph

**Data not Available**

**Data not Available**

Channels 1-4 Ground Current

Panel Displacement: Displacement, mm versus Time, sec



Panel backside IR image at sequential times. Note image has been flipped to provide a top side view.

Figure A 53 . CFRP substrate configuration performance. Configuration: Painted with Protecting ECF

# CFRP Panel - Configuration: Painted 8 in SansEC

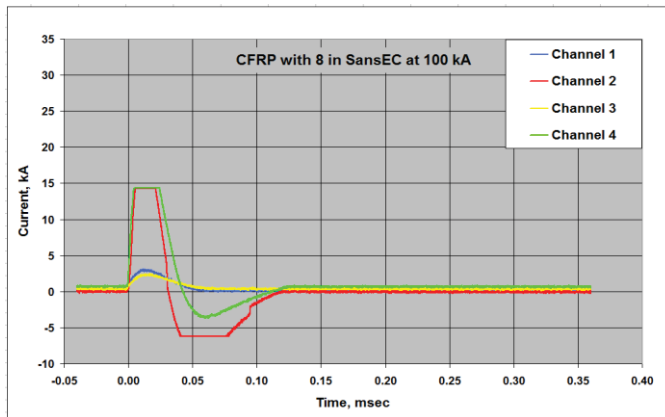
Peak Current, kA: 100



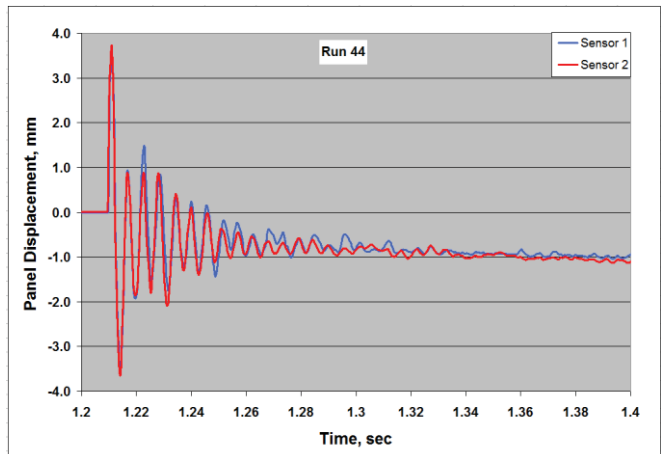
Pre Strike Photograph



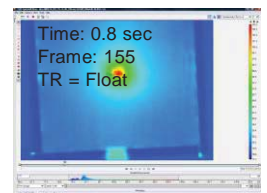
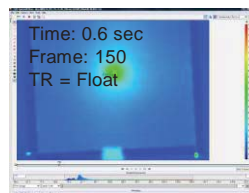
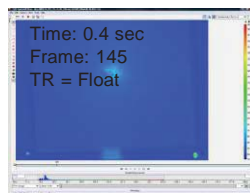
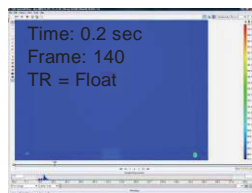
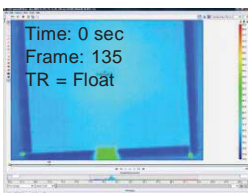
Post Strike Photograph



Channels 1-4 Ground Current



Panel Displacement: Displacement, mm versus Time, sec



Panel backside IR image at sequential times. Note image has been flipped to provide a top side view.

Figure A 54. CFRP substrate configuration performance. Configuration: Painted 8 in SansEC

CFRP Panel - Configuration: Painted 9 in SansEC

Peak Current, kA: 100



Pre Strike Photograph



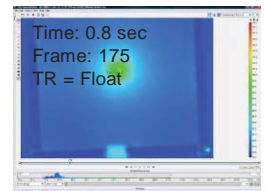
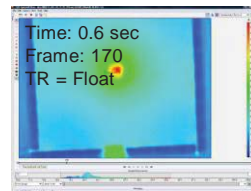
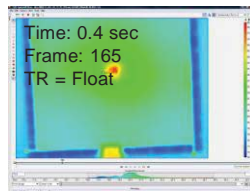
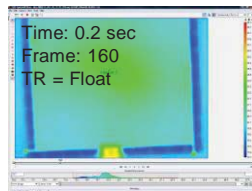
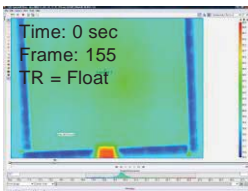
Post Strike Photograph

**Data not Available**

**Data not Available**

Channels 1-4 Ground Current

Panel Displacement: Displacement, mm versus Time, sec



Panel backside IR image at sequential times. Note image has been flipped to provide a top side view.

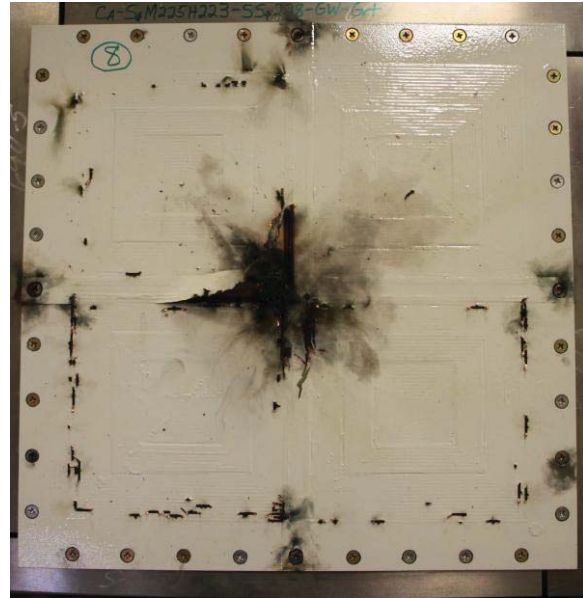
Figure A 55 . CFRP substrate configuration performance. Configuration: Painted 9 in SansEC

# CFRP Panel - Configuration: 2x2 8 in SansEC array with Mu-Metal

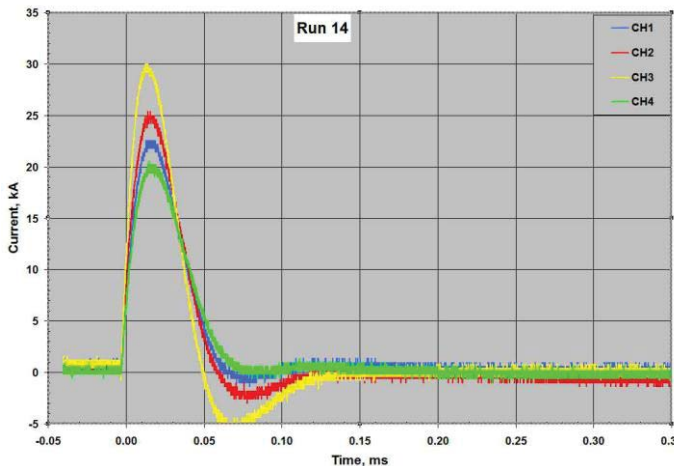
Peak Current, kA: 100



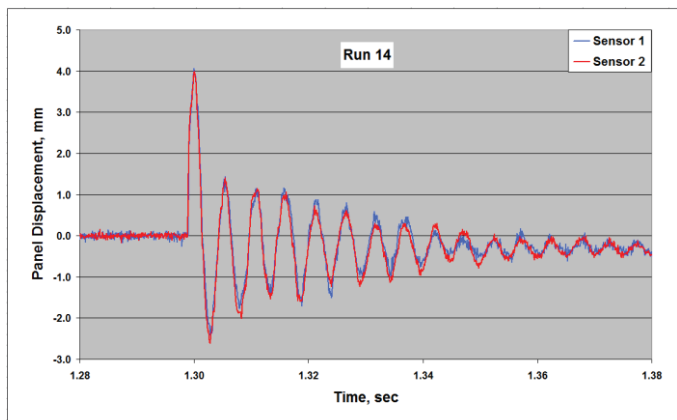
Pre Strike Photograph



Post Strike Photograph



Channels 1-4 Ground Current



Panel Displacement: Displacement, mm versus Time, sec

Figure A 56 . CFRP substrate configuration performance. Configuration: 2x2 8 in SansEC array with Mu-Metal

## 16.0 REFERENCES

- [1] Long, M. W.; and Narciso, J. D.: *Probabilistic Design Methodology for Composite Aircraft Structure*. DOT/FAA/AR-99/2 Report, No. ADA365683, 1999.
- [2] Nobuo Takeda, Shu; and Minakuchi, Yoji Okabe; *Smart Composite Sandwich Structures for Future Aerospace Application -Damage Detection and Suppression: a Review*. Journal of Solid Mechanics and Materials Engineering, Vol. 1, No. 1, 2007, pp. 3-17.
- [3] Fhisher, Franklin A.; Plumer, J. Anderson; and Perala, Rodney A.; *Lightning Protection of Aircraft*, 2nd Ed., Chapter 3. Lightning Technologies Inc., Pittsfield, 2004.
- [4] Meo, U. Polimeno M.: *Detecting barely visible impact damage detection on aircraft composites structures*, Composite Structures, Vol. 91, Issue 4, Pages 398-402, Dec 2009.
- [5] Mielnik, Jr., John J.; *Open Circuit Resonant Sensors for Composite Damage Detection and Diagnosis*. NASA/CR-2011-216884, 2011.
- [6] Kent, Renee M.; and Murphy, Dennis A.: *Health Monitoring System Technology Assessments - Cost Benefits Analysis*. NASA/CR-2000-209848, January, 2000.
- [7] Society of Automotive Engineers: *Aircraft Lightning Test Method*, SAE ARP5416. Revised January, 2013.
- [8] Chuantong Wang; Woodard, S.E.; Taylor, B.D.; *Sensing of Multiple Unrelated Tire Parameters using Electrically Open Circuit Sensors having no Electrical Connections*, Sensors Applications Symposium, 2009. SAS 2009. IEEE , vol., no., pp.142-147, 17-19 Feb. 2009. Web. 19 Aug. 2010.
- [9] Shrader, Robert L; *Electronic Communication*, Fifth Edition. New York: McGraw-Hill, 1985.
- [10] John J. Mielnik, Jr., *Open Circuit Resonant Sensors for Composite Damage Detection and Diagnosis*, NASA/CR-2011-216884, 2011.
- [11] Shukla, Neeraj KR., Shilpi Birla, and R.K.Singh, *New Modeling Technology for Spiral Inductors for Ultra Wideband Applications*, IACSIT International Journal of Engineering and Technology Vol. 2, No.1, ISSN: 1793-8236, February, 2010.
- [12] Chen, Wai-Kai; *RF Passive IC Components*, The VLSI Handbook. Boca Raton, FL: CRC, 2000.
- [13] Yue, Patrick C., and Simon S. Wong; *Physical Modeling of Spiral Inductors on Silicon*. IEEE Transactions on Electron Devices 47.3 (2000): 560-68. IEEE Xplore. Web. 12 Aug. 2010.
- [14] Greenhouse, H. M.; *Design of Planar Rectangular Microelectronic Inductors*. IEEE Transactions on Parts, Hybrids, and Packaging PHP-10.2 (1974): 101-09. Web. 12 Aug. 2010.
- [15] Mohan, Sunderarajan S., Maria Del Mar Hershenson, Stephen P. Boyd, and Thomas H. Lee. *Simple Accurate Expressions for Planar Spiral Inductances*, IEEE Journal Of Solid-State Circuits 34.10 (1999): 1420-421. 10 Sept. 2010.
- [16] C.R. Neagu, H.V. Jansen, A. Smith, J.G.E. Gardeniers, M.C. Elwenspoek, *Characterization of a Planar Microcoil for Implantable Microsystems, Sensors and Actuators* , Volume 62, Issues 1-3, Proceedings of Eurosensors X, July 1997, Pages 599-611.
- [17] Balakrishnan, A.; Palmer, W.D.; Joines, W.T.; Wilson, T.G.; *Inductance of Planar Rectangular-Spiral Strip Conductors for Low-Profile Inductors*, Power Electronics Specialists Conference, 1992. PESC '92 Record., 23rd Annual IEEE , vol., no., pp.1401-1408 vol.2, 29 Jun-3 Jul 1992.

- [18] "Missouri S&T." *Missouri S&T, Electromagnetic Compatibility Laboratory*. Web. 11 Aug. 2010.
- [19] Foundations of Mathematics Sylvain Poirier, Le Havre, France, Nov 18, 2013.
- [20] Boylestead, Robert L. *Introductory Circuit Analysis*. Prentice Hall, Roald K. Wangsness, *Electromagnetic Fields (2nd Edition)*, , Wiley, 1986.
- [21] Tipler, Paul (2004). *Physics for Scientists and Engineers: Electricity, Magnetism, Light, and Elementary Modern Physics (5th ed.)*. W. H. Freeman.
- [22] Paul, Clayton R. (2001). *Fundamentals of Electric Circuit Analysis*. John Wiley & Sons.
- [23] Ralph Morrison, *Grounding and Shielding Techniques in Instrumentation* Wiley-Interscience (1986).
- [24] Robert B. Northrop, *Introduction to instrumentation and measurements*, CRC Press, 1997.
- [25] Jackson, John David (1999). *Classical Electrodynamics (3rd ed. ed.)*. New York: Wiley.
- [26] Herbert P. Neff, *Basic Electromagnetic Fields*.
- [27] Magdy F. Iskander, *Electromagnetic Fields and Waves*.
- [28] 1856 paper by Kohlrausch and Weber.
- [29] Purcell, E. *Electricity and Magnetism (2nd ed.)*. Cambridge University Press (2011).
- [30] Laura J. Smith, Kenneth L. Dudley, and George N. Szatkowski, *Computational Electromagnetic Modeling of SansEC Sensors*, 27th International Review of Progress in Applied Computational Electromagnetics, Williamsburg, VA, Mar. 27-31, 2011.
- [31] Chuantong Wang, Woodard, S.E., and Taylor, B.D.; , *Sensing of Multiple Unrelated Tire Parameters using Electrically Open Circuit Sensors having no Electrical Connections*, IEEE Sensors Applications Symposium, New Orleans, 2009, pp.142-147.
- [32] Stanley E. Woodard, Chuantong Wang, and Bryant D. Taylor, *Wireless Temperature Sensing using Temperature-Sensitive Dielectrics within Responding Electric Fields of Open-Circuit Sensors having no Electrical Connections*, Measurement Science and Technology, Vol. 21, No. 7, July 2010.
- [33] Stanley E. Woodard, *SansEC Sensing Technology — A New Tool for Designing SpaceSystems and Components*, Aerospace Conference, 2011 IEEE, Big Sky, 2011, pp.1-11.
- [34] EMSS, *FEKO Comprehensive Electromagnetic Solutions User's Manual*, EM Software & Systems-S.A. (Pty) Ltd. 32 Techno Avenue, Technopark, Stellenbosch, 7600, South Africa, 2011.
- [35] Thomas Boundreau, "CFR NPRM-Airworthiness Standards; Rain and Hail Ingestion Standards," Federal Aviation Administration, Docket No. 28652, No. 96-12, Vol. 61, No. 155, August 9, 1996.
- [36] Allen H. Meitzler, Ann Arbor, and George S. Saloka, Ford Motor Company, Dearborn, Mich, *Resonant Cavity Flexible, Fuel Sensor and System*, U.S. Patent No.5361035, Nov. 1, 1994.
- [37] Mohammadali Ansarizadehm, Alper Ozturk, and Robert Paknys, *Using FEKO for Electromagnetic Analysis of Carbon-Fiber Composite Structures*, 27th International Review of Progress in Applied Computational Electromagnetics, Williamsburg, VA, Mar. 27-31, 2011.

- [38] Dennis Roach, Larry Dorrell, Jeff Kollgaard, Tom Dreher, *Improving Aircraft Composite Inspections Using Optimized Reference Standards*, FAA Airworthiness Assurance NDI Validation Center / Sandia National Laboratories, 98AEMR-34, SAND-98-2022C, CONF-981115, 1998.
- [39] Dave Galella; *FAA Inspection Research Activities for Composite Materials*, The 2006 Composite Damage Tolerance & Maintenance Workshop, July 20, 2006.
- [40] Laura J. Smith, Kenneth L. Dudley, and George N. Szatkowski; *Computational Electromagnetic Modeling of SansEC Sensors*, 27th International Review of Progress in Applied Computational Electromagnetics, Williamsburg, VA, Mar. 27-31, 2011.
- [41] Stanley E. Woodard and Bryant D. Talyor, *Magnetic Field Response Measurement Acquisition System*, NASA/TM-2005-213518, 2005.
- [42] Kenneth L. Dudley, George N. Szatkowski, Chuantong Wang, Laura J. Smith, Larry A. Ticatch, John J. Mielnik, Sandra V. Koppen, Jay J. Ely, Truong X. Nguyen ; *Damage Detection Response Characteristics of Open Circuit Resonant (SansEC) Sensors*, 2013 International Conference on Lightning and Static Electricity (ICOLSE), Seattle, USA, 18-20 September 2013.
- [43] Kovach, D.; Griess, K.: *LSP Composite Substrate Manufacturing Processing Guide*. NASA Document Number: DOC-128694, The Boeing Company, June 2011.
- [44] Kovach, D.; Griess, K.: *LSP Composite Substrate NDE Assessment Manual*. NASA Document Number: DOC-128695, The Boeing Company, June 2011.
- [45] Kovach, D.; Erickson, G.: *LSP Composite Substrate Lightning Test Operations Manual*. NASA Document Number: DOC-128696, The Boeing Company, September 2011.
- [46] Kovach, D.; Erickson, G.: *LSP Composite Substrate Destructive Evaluation Test Assessment Manual*. NASA Document Number: DOC-128697, The Boeing Company, July 2011.
- [47] Day, A.; Griess, K.: *LSP Composite Substrate Test Bed Design*. NASA Document Number: DOC-128698, The Boeing Company, September 2011.
- [48] Le Vine, David M.: *Review of Measurements of the RF Spectrum of Radiation from Lightning*. NASA TM-87788, March 1986.
- [49] Chemartin, L.; Lalande, P.; Peyrou, B.; Chazottes, A.; Elias, P.Q.; Delalondre, C.; Cheron, B.G.; Lago, F.: *Direct Effects of Lightning on Aircraft Structure: Analysis of the Thermal, Electrical and Mechanical Constraints*. Journal AerospaceLab AL05-09, Dec 2012.
- [50] Salah, L.; Kurupparachige, C.; Salagame, R.: *NASA LSP Composite Substrate Destructive Evaluation Test*. CAMP-RP-2013-027, NIAR, June 2013.
- [51] Sharpe, Harlan E.: *Panel Shielding Effectiveness Testing Reverb Method*. ENV-RP-2013-001 N/C, NIAR, June, 2013.

REPORT DOCUMENTATION PAGE			Form Approved OMB No. 0704-0188		
<p>The public reporting burden for this collection of information is estimated to average 1 hour per response, including the time for reviewing instructions, searching existing data sources, gathering and maintaining the data needed, and completing and reviewing the collection of information. Send comments regarding this burden estimate or any other aspect of this collection of information, including suggestions for reducing this burden, to Department of Defense, Washington Headquarters Services, Directorate for Information Operations and Reports (0704-0188), 1215 Jefferson Davis Highway, Suite 1204, Arlington, VA 22202-4302. Respondents should be aware that notwithstanding any other provision of law, no person shall be subject to any penalty for failing to comply with a collection of information if it does not display a currently valid OMB control number.</p> <p><b>PLEASE DO NOT RETURN YOUR FORM TO THE ABOVE ADDRESS.</b></p>					
1. REPORT DATE (DD-MM-YYYY) 01-11-2014		2. REPORT TYPE Technical Publication		3. DATES COVERED (From - To)	
4. TITLE AND SUBTITLE  Open Circuit Resonant (SansEC) Sensor Technology for Lightning Mitigation and Damage Detection and Diagnosis for Composite Aircraft Applications			5a. CONTRACT NUMBER		
			5b. GRANT NUMBER		
			5c. PROGRAM ELEMENT NUMBER		
			5d. PROJECT NUMBER		
6. AUTHOR(S)  Szatkowski, George N.; Dudley, Kenneth L.; Smith, Laura J.; Wang, Chuantong; Ticatch, Larry A.			5e. TASK NUMBER		
			5f. WORK UNIT NUMBER  648987.02.04.07.20		
			8. PERFORMING ORGANIZATION REPORT NUMBER  L-20473		
7. PERFORMING ORGANIZATION NAME(S) AND ADDRESS(ES) NASA Langley Research Center Hampton, VA 23681-2199			8. PERFORMING ORGANIZATION REPORT NUMBER		
9. SPONSORING/MONITORING AGENCY NAME(S) AND ADDRESS(ES) National Aeronautics and Space Administration Washington, DC 20546-0001			10. SPONSOR/MONITOR'S ACRONYM(S)  NASA		
			11. SPONSOR/MONITOR'S REPORT NUMBER(S)  NASA/TP-2014-218554		
12. DISTRIBUTION/AVAILABILITY STATEMENT Unclassified - Unlimited Subject Category 01 Availability: NASA STI Program (757) 864-9658					
13. SUPPLEMENTARY NOTES					
14. ABSTRACT  Traditional methods to protect composite aircraft from lightning strike damage rely on a conductive layer embedded on or within the surface of the aircraft composite skin. This method is effective at preventing major direct effect damage and minimizes indirect effects to aircraft systems from lightning strike attachment, but provides no additional benefit for the added parasitic weight from the conductive layer. When a known lightning strike occurs, the points of attachment and detachment on the aircraft surface are visually inspected and checked for damage by maintenance personnel to ensure continued safe flight operations. A new multi-functional lightning strike protection (LSP) method has been developed to provide aircraft lightning strike protection, damage detection and diagnosis for composite aircraft surfaces. The method incorporates a SansEC sensor array on the aircraft exterior surfaces forming a "Smart skin" surface for aircraft lightning zones certified to withstand strikes up to 100kA peak current. SansEC sensors are open-circuit devices comprised of conductive trace spiral patterns sans (without) electrical connections. The SansEC sensor is an electromagnetic resonator having specific resonant parameters (frequency, amplitude, bandwidth & phase) which when electromagnetically coupled with a composite substrate will indicate the electrical impedance of the composite through a change in its resonant response.					
15. SUBJECT TERMS  Aircraft lightning; Composite damage; SansEC; Smartskin					
16. SECURITY CLASSIFICATION OF:			17. LIMITATION OF ABSTRACT	18. NUMBER OF PAGES	19a. NAME OF RESPONSIBLE PERSON
a. REPORT	b. ABSTRACT	c. THIS PAGE			STI Help Desk (email: help@sti.nasa.gov)
U	U	U	UU	179	19b. TELEPHONE NUMBER (Include area code) (757) 864-9658